Redox Flow Batteries: From Vanadium to Earth abundant organic molecules (Quinones)

F. Javier Vázquez Galván

Doctoral thesis

Redox Flow Batteries: From Vanadium to Earth abundant organic molecules (Quinones)

Author: F. Javier Vázquez Galván

Director: Dr. Joan Ramon Morante

UNIVERSITAT DE BARCELONA

Redox Flow Batteries: From Vanadium to Earth abundant organic molecules (Quinones)

Programa de doctorado en Nanociencias

Autor: F. Javier Vázquez Galván

Director:Dr. Joan Ramon Morante

Co-Director: Dra. Cristina Flox Donoso

Lugar donde se ha llevado a cabo la tesis

UNIVERSITAT DE BARCELONA

"Art is never finished, only abandoned"

Leonardo Da Vinci

Acknowledgements

To my mother,

Table of content

1 Scope of the Thesis.....12

2 Redox Flow Batteries.....14

2.1 What is a Redox Flow Battery? 14

2.2 Types of Redox Flow Batteries.....15

2.3 Advantages and disadvantages 15

2.4 Applications of Redox Flow batteries 16

2.5 Evolution of Redox flow batteries.....17

2.6 Redox flow batteries configuration 23

2.6.1 Various Redox flow batteries.....26

2.6.1.1 Iron/chromium 26

2.6.1.2 Bromine/polysulfide.....27

2.6.1.3 All-vanadium 28

2.6.1.4 Vanadium/bromine.....29

2.6.1.5 Hydrogen-based systems 29

2.6.1.6 Hybrid redox flow batteries 30

2.6.1.6.1 Zinc/bromine. 30

2.6.1.6.2 Soluble lead acid 31

2.6.1.6.3 All iron 31

2.6.1.6.4 All-copper.....32

2.6.1.7 Non-aqueous redox flow batteries 32

2.6.1.8 Other configurations.....34

2.7 All Vanadium Redox Flow Batteries 34

2.7.1 Cell potential 36

2.7.2 Operating Cell Voltage 37

2.7.3 Cell Components and Design Requirements 38

2.7.4 Cost analysis 39

3 Experimental Methodology 43

3.1 Felt treatments 43

3.2 Synthesis methods 43

3.2.1 TiO_2 synthesis.....44

3.2.1.1 Defective TiO_2.....46

3.2.1.2 Nitrided TiO_2.....46

3.2.2 CeO_2 synthesis.....46

3.3 Membrane pretreatments 47

3.4 Three electrode system configuration 48
3.4.1 Rotating disk set-up 49
3.4.2 Electrode's electrical measurement 50
3.5 Single cell device set-up 51
3.6 Characterization techniques 53
3.6.1 "In-operando" reference electrode 54
3.6.2 UV-visible spectroscopy 55
3.6.3 Scanning electron microscope 55
3.6.4 X-ray diffraction 56
3.6.5 X-ray photoelectron spectroscopy 57
4 Vanadium Redox Flow Batteries: Architecture enhancement 59
4.1 Reference electrode implementation into a single cell for *"in-situ"* measurements 59
4.1.1 Electrochemical characterization 60
4.1.2 Single cell evaluation 64
4.1.3 Conclusions 68
5 Vanadium Redox Flow Batteries: Electrolyte Enhancements 69
5.1 Thermally Stable Positive Electrolyte with a Superior Performance in All-Vanadium Redox Flow Batteries 69
5.1.1 Characterization 71
5.1.1.1 Electrochemical characterization 73
5.1.2 Single cell performance 75
5.1.3 Conclusions 78
6 Vanadium Redox Flow Batteries: Electrode Enhancements 79
6.1 Electrodes developed 81
6.1.1 Titanium dioxide (TiO_2) 83
6.1.1.1 Characterization 84
6.1.1.1.1 Electrochemical characterization 86
6.1.1.2 Single cell performance 89
6.1.2 Reduced titanium dioxide (TiO_2-H) 91
6.1.2.1 Characterization 92
6.1.2.1.1 Electrochemical characterization 95
6.1.2.2 Single cell performance 99
6.1.3 Nitrided titanium dioxide (TiO_2-N) 106

6.1.3.1 Characterization 108
6.1.3.1.1 Structural characterization 108
6.1.3.1.2 Chemical Characterization 111
6.1.3.1.3 Electrochemical characterization 116
6.1.3.2 Single cell performance 122
6.1.3.3 Mechanism proposed 128
6.1.4 Cerium oxide (CeO_2) 131
6.1.4.1 Characterization 133
6.1.4.1.1 Electrochemical characterization 135
6.1.4.2 Single cell performance 140
6.2 Conclusions 146
6.3 Vanadium redox flow batteries perspective. 148
7 Organic Redox Flow Batteries 150
7.1 Current trend in Redox Flow Batteries 150
7.2 Rise of the organic active materials 150
7.3 Quinones as electroactive molecules 152
7.3.1 Selection criteria for electrolyte 156
7.3.2 Cathodic electroactive species 162
7.3.2.1 Electrodes enhancement 162
7.3.2.1.1 Characterization 163
7.3.2.1.2 Electrochemical characterization 167
7.3.3 Anodic electroactive species 176
7.3.3.1 Electrode enhancement 177
7.3.3.1.1 Characterization 177
7.3.3.1.2 Electrochemical characterization 181
7.3.4 Single cell performance 187
7.3.4.1 Carbon-based electrodes 187
7.3.4.1.1 1,4-benzoquinone (+) vs. anthraquinone 2,7- Disulfonic acid disodium salt (-) 188
7.3.4.1.2 1,2-benzoquinone (+) vs. anthraquinone 2,7- Disulfonic acid disodium salt (-) 193
7.3.4.1.3 Sodium 4,5-dihydroxybenzene-1,3-disulfonate (+) vs. anthraquinone 2,7- Disulfonic acid disodium salt (-) 195
7.3.4.2 Enhanced carbon-based electrodes 199
7.3.4.2.1 Sodium 4,5-dihydroxybenzene-1,3-disulfonate (+) vs. anthraquinone 2,7- Disulfonic acid disodium salt (-) 199
7.4 Conclusions 204
7.5 Perspective of Organic Redox Flow Devices 206

8 Conclusions 208

9 Appendix 213

9.1 Kinetics of redox reactions 213

9.1.1 One step, one-electron process 213

9.1.2 Implications of Butler-Volmer model for the one-step, one-electron process 216

9.1.2.1 Equilibrium conditions. The exchange current 216

9.1.2.2 The current-overpotential equation 217

9.1.2.3 Approximate Form of the i-η Equation 218

9.1.2.3.1 Tafel plots 218

9.1.2.4 Effects of Mass Transfer 220

9.1.3 Multistep mechanisms 223

9.1.3.1 Rate-determining electron transfer 224

9.1.3.2 Multistep Process at Equilibrium 225

9.1.3.3 Quasirreversible and Irreversible Multistep Processes 227

9.2 Active surface area 229

9.3 Transport phenomena 230

9.3.1 Rotating disk electrode 231

9.3.1.1 Solution of the Convective-Diffusion Equation 232

9.3.1.2 General Current-Potential Curves at the RDE 233

9.3.2 Electrolyte flow 235

9.3.3 Reactant concentration effects 238

10 References 240

1 Scope of the Thesis

Along this Thesis dissertation book, which is focused on the topic of Redox Flow Batteries, many efforts have been done in order to improve different aspects of the all-Vanadium Redox Flow batteries (VRFBs) technology, as monitoring each battery compartment, increasing operational temperature range, enhancing negative electrode to reduce side reactions and charge transfer towards V^{3+}/V^{2+} redox reaction and also modifying positive electrode to obtain a faster VO_2^{+}/VO^{2+} redox reaction. Vanadium technology was chosen over all redox flow technologies due to its mature development reaching the barrier to commercial breakthrough. The main targeted aspects about VRFBs have been:

- Reference electrode implementation into a single cell device (battery) to study separately anolyte and catholyte in real working conditions. This set-up allows following the contribution of each one of the electrodes separately, and consequently knowing the limiting factor in the battery, in order to improve them.

- Electrolyte modifications with catalytic quantities of an additive allowing a larger vanadium ion concentration being able to be solved into the electrolyte, as well as increase the operational temperature window. These improvements are done in order to increase the energy density of the system, and also allow the battery to work in a wider temperature range to adapt this system to broader climate areas without temperature control.

- Electrodes enhancement:

  Initially, we will focus our attention into electrode modifications to enhance their electrochemical properties. Firstly, increasing functional groups on the electrode's surface, this makes them more electroactive towards vanadium redox reactions. Secondly, different catalysts are deposited to obtain faster vanadium redox reactions on a carbon-based structure (as graphite felt or carbon felt).

  - Anode, main lacks are large ohmic overpotential due to competing side reaction.

    - It has been done an exhaust study of different structures of the same material, as it is nanoparticles (NPs), single-nanorods (SNRs) and multi-nanorods assembly (MNRs).

    - Graphite and/or carbon felt enhancement using the synthesis of different catalyst (TiO_2, TiO_2:H, TiO_2:N, O and N groups) which help not only to make the negative redox reaction (V^{3+}/V^{2+}) faster and reduce the voltage drop, but also avoid

side reactions (gas evolution) as can be hydrogen evolution reaction (HER). All of these help to elevate the reachable energy and power densities of the battery.

- Cathode, which lacks of a fast kinetics.
    - Deposition of a catalyst over graphite felt, as it is ceria (CeO_2), to aid the positive redox reaction (VO_2^+/VO^{2+}) making it faster, as well as improve the efficiencies and accessible capacity of the battery.

Despite the fact that the systems described previously were already proposed several decades ago, they are still the subject of current research. These systems show several inconvenient related to the vanadium abundance, the cost of it, as well as the geopolitical impact caused by its mining. As a consequence, the implementation of organic redox active species is a first step in order to avoid these disadvantages. Organic molecules are abundant, tunable by synthetic pathways and an improved kinetic with the possibility of having two-electron transfer process (as happens to quinones)[1,2]. Such a battery has the potential to meet the demanding cost, durability, eco-friendliness, and sustainability requirements for grid-scale electrical energy storage.

Furthermore, this system has been studied targeting on a Quinone-based redox flow battery. After the selection of the catholyte (benzoquinone-based molecules as p-benzoquinone, o-benzoquinone and disodium 4,5-dihydroxy-1,3-benzenedisulfonate) and the anolyte (Anthraquinone-2,7-disulfonic acid disodium salt) in a methanosulfonic acid solvent, the next step has been improving the electrode technology on both single cell compartments to promote positive and negative redox reactions. In order to do that surface modification has been done, by means of nitrogen and oxygen functionalization using different methods. Finally, it has been commented the present of all-Vanadium and Aqueous Organic Redox Flow Batteries, as well as some future perspective of both technologies.

2 Redox Flow Batteries

2.1 What is a Redox Flow Battery?

Redox flow batteries represent one class of electrochemical energy storage devices. The name "redox" refers to chemical reduction and oxidation reactions employed in the RFB to store energy in liquid electrolyte solutions, separate by a membrane[3,4], which flow through a battery of electrochemical cells during charge and discharge (**Figure 2.1**).

During discharge, an electron is released via an oxidation reaction from a high chemical potential state on the negative or anode side of the battery. The electron moves through an external circuit to do useful work. Finally, the electron is accepted via a reduction reaction at a lower chemical potential state on the positive or cathode side of the battery. The direction of the current and the chemical reactions are reversed during charging[5].

The total difference in chemical potential between the chemical states of the active elements on the two sides of the battery determines the electromotive force (emf or voltage) generated in each cell of the battery. The voltage developed by the RFB is specific to the chemical species involved in the reactions and the number of cells that are connected in series. The current developed by the battery is determined by the number of atoms or molecules of the active chemical species that are reacted within the cells as a function of time. The power delivered by the RFB is the product of the total current and total voltage developed in the electrochemical cells. The amount of energy stored in the RFB is determined by the total amount of active chemical species available in the volume of electrolyte solution present in the system.

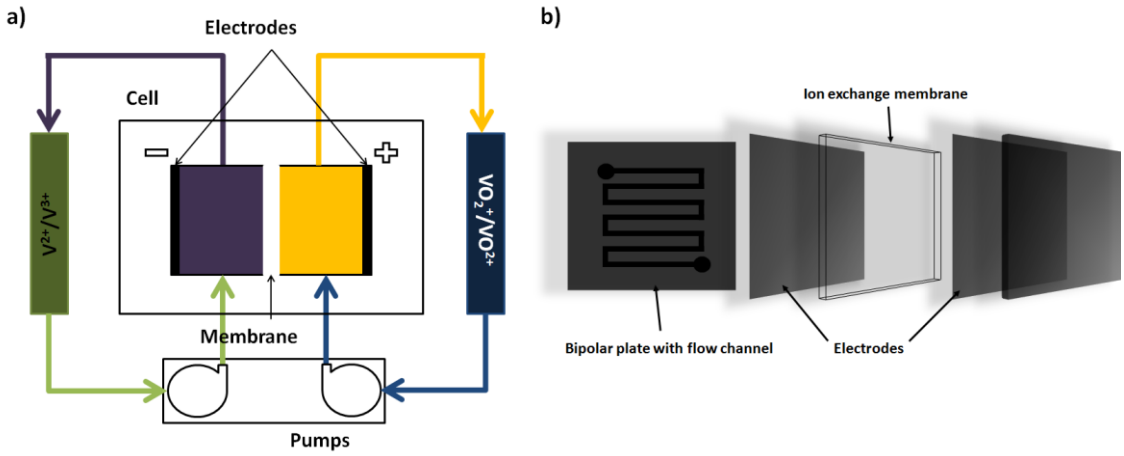

Figure 2.1. – a) Diagram of a RFB energy storage system: RFB stack and electrolyte are separated. **b)** Diagram of a RFB cell with membrane, electrodes and bipolar plates with parallel-channels layout for flow distribution.

2.2 Types of Redox Flow Batteries

RFB's can be divided into two categories[6]:

1) True redox flow batteries, where all of the chemical species active in storing energy are fully dissolved in solution at all times. Examples of true RFB's include the vanadium-vanadium and iron-chromium systems. True RFB's achieve the complete separation of power and energy, along with the full advantages.

2) Hybrid redox flow batteries, where at least one of the chemical species is plated as a solid in the electrochemical cells during charge. Examples of hybrid RFB's include the zinc-bromine and zinc-chlorine systems. In hybrid RFB's, complete separation of power and energy is not achieved, because energy is stored in the metal which is plated in the electrochemical stack during charge. Other examples of hybrid batteries are metal-air batteries[7] or semi-solid redox flow batteries[8]

Larger energy storage capacity requires a larger stack, so the distinction of the hybrid RFB from integrated cell architectures is only partly achieved.

2.3 Advantages and disadvantages

The separation of power and energy is a key distinction of RFB's, compared to other electrochemical storage systems. As described above, the system energy is stored in the volume of electrolyte, which can easily and economically be in the range of kilowatt-hours to 10's of megawatt-hours, depending on the size of the storage tanks. The power capability of the system is determined by the size of the stack of electrochemical cells, which is the electrodes total area. The amount of electrolyte flowing in the electrochemical stack at any moment is rarely more than a fraction of the total amount of electrolyte in the tanks (for energy ratings corresponding to discharge at rated power for two to eight hours). Flow can easily be stopped during a fault condition. As a result, system vulnerability to uncontrolled energy release in the case of RFB's is limited by system architecture just to a small percentage of the total energy stored. This feature is in contrast with packaged, integrated cell storage architectures (lead-acid, NAS, Li Ion), where the full energy of the system is connected at all times and available for discharge. It makes them more vulnerable to a system failure.

Redox flow batteries have one main architectural disadvantage compared with integrated cell architectures of electrochemical storage. RFB's tend to have lower volumetric energy densities (15-25 WhL^{-1}) than integrated cell architectures (250–693 WhL^{-1} for Li-ion), especially in the high power, short duration applications. This is due to the volume of electrolyte flow delivery and control components of the system, which is not used to store energy. In spite of this, RFB's are available with system footprint below the EPRI substation target of <500 ft^2 / MWh.

2.4 Applications of Redox Flow batteries

Flow batteries are normally considered for relatively large (1 kWh – 10 MWh) stationary applications[6]:

- **Load balancing** – where the battery is connected to an electrical grid to store excess electrical power during off-peak hours and release electrical power during peak demand periods. The common problem limiting the use of most flow battery chemistries in this application is their low areal power (operating current density) which translates into a high cost of power.
- **Storing energy from renewable sources** such as wind or solar for discharge during periods of peak demand.
- **Peak shaving**, where spikes of demand are met by the battery.
- **Uninterruptible power supply (UPS)**, where the battery is used if the main power fails to provide an uninterrupted supply.
- **Power conversion** – The electrolyte/s may be charged using a given number of cells and discharged with a different number, because all cells share the same electrolyte/s. Because the voltage of the battery is proportional to the number of cells used the battery can therefore act as a very powerful DC–DC converter. In addition, if the number of cells is continuously changed (on the input and/or output side) power conversion can also be AC/DC, AC/AC, or DC–AC with the frequency limited by that of the switching gear.
- **Electric vehicles** – Because flow batteries can be rapidly "recharged" by replacing the electrolyte, they can be used for applications where the vehicle needs to take on energy as fast as a combustion engine vehicle. A common problem found with most RFB chemistries in the EV applications is their low energy density which translated into a short driving range. Flow batteries based on highly soluble halides are a notable exception.
- **Stand-alone power system** – An example of this is in cell phone base stations where no grid power is available. The battery can be used alongside solar or wind power sources to compensate for their fluctuating power levels and alongside a generator to make the most efficient use of it to save fuel. Currently, flow batteries are being used in solar micro grid applications throughout the Caribbean.

Furthermore, economically convenient and technically competitive storage solutions must ensure not only response time and storage capacity suitable for meeting both the generation and grid needs but, must also show a long lifetime and be able to withstand many charge/discharge cycles. Present-day technologies are characterized by different levels of development and are suitable for different storage and localization needs[9,10]. Modular technologies such as redox flow battery (RFB) offer the capability of high power rating, long energy storage time and excellent response time: full power can be delivered in few seconds.

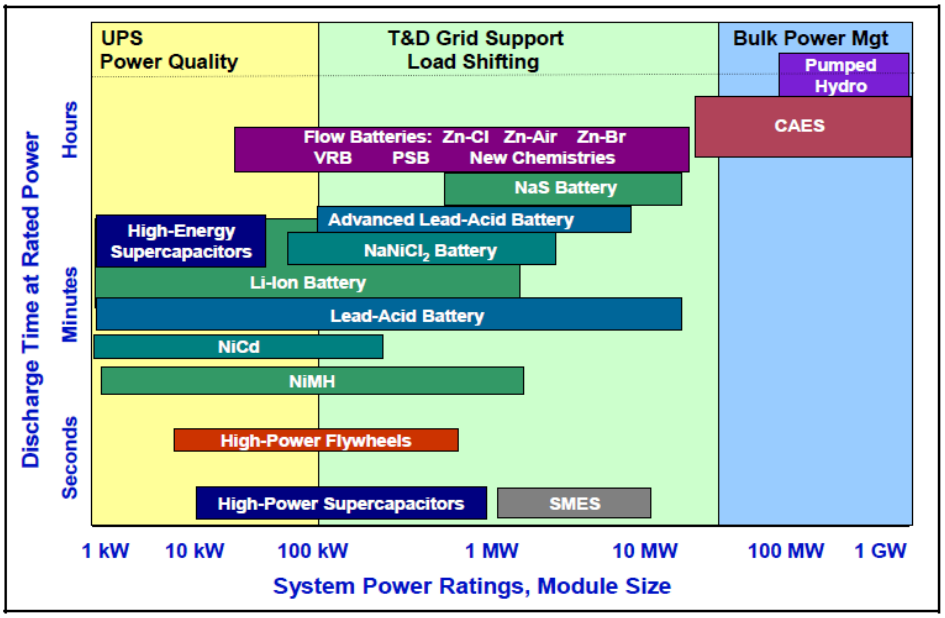

Figure 2.2. – Comparison of discharge time and power rating for various EES technologies [Courtesy of EPRI].

Among electrochemical systems, redox flow batteries (RFBs) represent one of the most recent technologies and a highly promising choice for grid energy storage[11]. They are electrochemical energy conversion devices, which exploit redox processes of species in solution in fluid form, stored in external tanks and introduced into the RFB when needed. The most appealing features of this technology are: scalability and flexibility, independent sizing of power and energy, high round-trip efficiency, high depth of discharge (DOD), long durability and fast responsiveness[12]. Such features allow for wide ranges of operational powers and discharge periods (**Figure 2.2**), making them ideal for assisting electricity generation from renewable sources. Redox flow batteries are suitable for energy storage applications with power ratings from 10's of kW to 10's of MW and storage durations of 2 to 10 hours.

2.5 Evolution of Redox flow batteries

Since the 70s new systems for electrochemical energy storage have been researched due to a great interest by NASA. For some of the systems such as redox flow batteries, development has now reached the commercial stage. Redox flow battery differs from the usual storage system in the energy-active compounds are not stored within the battery container, but separately in a liquid reservoir.

The system is shockingly simple. It consists of two tanks, each containing an active species in different oxidation states. Each fluid passes in a half-cell, divided by a membrane, and is returned to the reservoir. In the half-cell there is electrochemical

exchange with the electrodes which permits the output or input of current, for example:

$$\mathbf{Fe^{3+} + e^{-} = Fe^{2+}}(+) \text{ And } \mathbf{Cr^{2+} = Cr^{3+} + e^{-}}(-)$$

Usually the four species (ions) are in solution and sometimes gaseous elements are involved due to side reactions involving gas evolution reactions. In other cases, metallic species are deposited in one half-cell. Such systems are referred to as being "*hybrid*" or "*redox-hybrid*"[13].

During the 70s to 80s there was an enormous effort developing the redox flow battery technology, as a result of the NASA investment on this technology. In **Figure 2.3** there is an overview of this redox flow cell evolution. In 1971, Ashimura and Miyake published in Denki Kagaru an article dealing with the polarization characteristics of redox pair Fe^{3+}/Fe^{2+} type fuel cell cathodes at a flow-through porous carbon electrode as well as its regeneration[14].

In 1973 the National Aeronautics and Space Administration (NASA) founded the Lewis research center with the object of researching electrically rechargeable redox flow cells. NASA also established some contracts with Exxon Company[15], Giner Ind. and Gel Inc for the hybrid version and with Ionics Inc. for membrane development[16].

From 1973 to 1979, the Lewis research center produced several reports about redox flow batteries, covering the following topics:

i) Screening of redox couples.
ii) Electrochemical diagnostics.
iii) Kinetics problems.
iv) Membrane development.
v) Carbon based electrodes.
vi) Components screening and life testing.
vii) System studies.
viii) Hydrodynamics.
ix) Models.
x) Electrocatalysis.

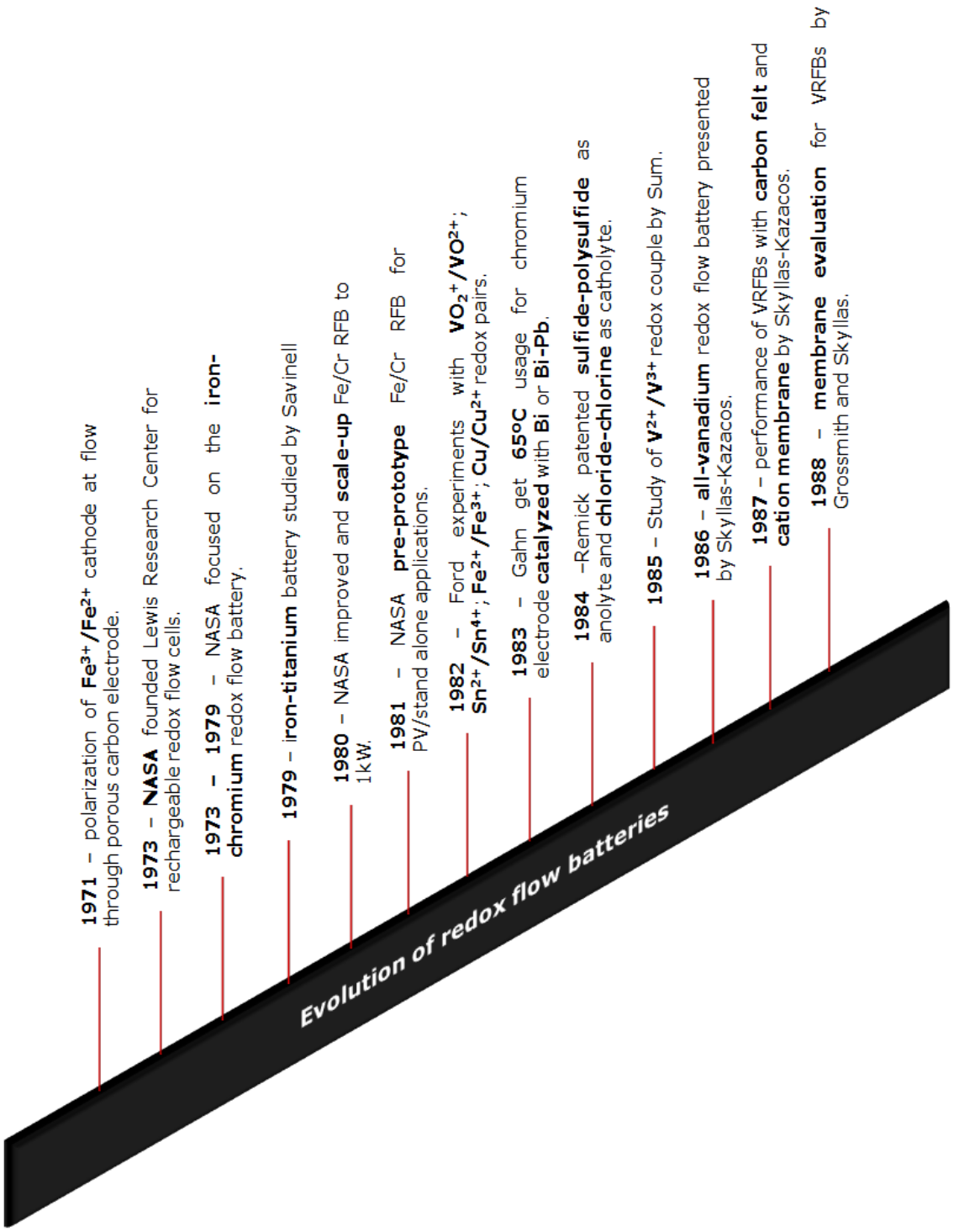

Figure 2.3 – Timeline of redox flow batteries initial development during 70s to 80s.

Many redox pairs were tested, titanium (Ti^{3+}/TiO^{2+}), iron (Fe^{2+}/Fe^{3+}), chromium (Cr^{2+}/Cr^{3+}). From all of these, the iron-chromium system seemed to be the most promising for the global reaction and much effort was invested in this direction.

$$\mathbf{Fe^{3+} + Cr^{2+} \leftrightarrow Fe^{2+} + Cr^{3+}}$$

During this period also contributions were done from Beccu (Battelle Institute, Geneva, Switzerland)[17], which examined the redox systems regarding secondary batteries; Warshay, which estimated the costs of electrochemical energy storage[18]; Wever- The G.E.L. iron redox cell did a report of initial cycling tests[19]; and from Zito (The iron-redox battery in a large solar-photovoltaic application).

In 1979, Roy and Kaplan analyzed the performance capabilities of redox flow storage. In this period there were also some NASA patents on electrically rechargeable redox flow cells[20], as well as on gel as battery membranes and electrochemical cells for rebalancing a redox flow system. Moreover, Savinell et. al. studied the characteristics of a iron/titanium battery system.

In early 80s a patent was granted to Giner Inc. on catalyst surfaces for the chromous/chromic redox couple in the iron-chromium flow cell and iron hybrid flow cell[21]. Mine while, some evaluations of chromium and titanium redox systems by Nozaki and coworkers[22], as well as, a new report from NASA concerning a redox system based on Fe and Cr chlorides[23] and another about improvement and scale-up redox storage systems up to 1kW.

In 1981, NASA presented a pre-prototype redox storage system, based on iron-chromium, for a photovoltaic stand-alone application[24]. Some other contribution was made by Savinell researching factors that affects the performance of the iron-redox battery, enhancing the performance of the Ti^{3+}/Ti^{4+} couple[25] and evaluating a hybrid redox-halogen (Cr-chlorine) for use in energy storage devices. A theoretical study, relating flow-through and flow-by porous electrodes for redox energy storage, was published by Trainham and Newman at Berkeley[26]. Advances in membrane technology were done by NASA[27].

In January 1982, two Japanese patents by the Agency of Industrial Science and Technology were issued. The first was for manganese (cathode) -chromium (anode) system and the second was for chromium or titanium couple with bromine, obtaining a battery output of 0.9 V when applying 10 mA/cm^2. In a report by Roberts Zn-Br batteries were reviewed[27]. Giner Inc. presented data about the development of Cr^{3+}/Cr^{2+} redox reactions in the iron-chromium battery[28]. Savinell et al. described the operating performance of an iron-titanium stationary redox battery in the presence of lead[29]. Catalytic electrodes (ZrC electrodes) for redox flow cell energy storage devices were studied[30]. Ford published experiments regarding redox cell using VO_2^+/VO^{2+}--Sn^{2+}/Sn^{4+}, VO_2^+/VO^{2+}--Fe^{2+}/Fe^{3+} and VO_2^+/VO^{2+}--Cu/Cu^{2+}[31]. Also a singular manner of recharging redox batteries was proposed by Denno utilizing ocean thermal energy.

In 1983, at the 18th IECEC Conference Gahn discussed a small cell using mixed reactant solutions at 65ºC, with a chromium electrode catalyzed with Bi or Bi-Pb[31].

In 1984, an improved mathematical model of the iron-chromium redox battery was made by Fedkiw. This was based on the porous electrode theory and incorporates redox kinetics, mass transfer, and ohmic effects, as well as the parasitic hydrogen reaction which occurs in the chromium electrode[32]. Voltage drop and electrical resistivity measurements of ion-exchange membranes used in redox flow batteries were studied by Ohya[33]. Remick patented a cell using sulfide-polysulfide as anolyte and chloride-chlorine as catholyte[34]. Reactivation of complex compound by amines

taking place in the redox reaction was the topic of a German patent by Cheng and Reiner.

In 1985, Sumitomo Electric Industries patented a general system of flow batteries with a separator made of a cation-exchange membrane. Chen and Hollax patented an iron-chromium type redox battery using thallium and gold electrocatalysts[34]. The Mitsui Engineering and Shipbuilding Co. Ltd. Patented a system for the determination of the state of charge of a redox flow battery[35]. A study of the V^{2+}/V^{3+} redox couple for flow cell application was done by Sum[36]. The iron-chromium, with graphite electrodes, redox battery was studied by Aldaz[37]. Moreover, the Sumitomo Electric Industries Ltd. Patented a redox flow battery with cylindrical electrodes built from porous carbon fibers[38]. An investigation of the VO_2^+/VO^{2+} system for use in the positive half-cell of a redox flow battery was done by Sum and coworkers[39]. Additionally, Three Sumitomo patents appeared in the second hal of 1985. The first was for a redox flow battery with new flexible electrodes made of metal wires coated with carbon/graphite and embedded in conductive rubber[40]. The second described a redox flow system with pipeline made from plastic with low oxygen permeability[41]. The Third is about a nonionic surfactant was added to the catholyte and anolyte, thus increasing the charge-discharge efficiency[42]. A redox flow system using iron-chromium couples and all chromium electrolytes was described by Doria[43]. A redox cell containing couples of vanadium and molybdenum ions was studied by Kummer (Ford Motor Company)[44].

In 1986, a new all-vanadium redox flow battery was presented by Skyllas-Kazacos, which is the starting point of our research plan[45]. Nozaki (Mitsui) reported studies of a secondary redox flow battery (hybrid) with chromium and halogen couples showing a voltage of 1.2 V[46]. Swette (Giner Inc.) studied the characterization of gold electrocatalysts for iron-chromium redox batteries[47].

In 1987, Exchange current densities of the Fe^{2+}/Fe^{3+} couple was studied by Mathur[48]. The Fe-Cr redox flow battery prototypes, with graphite plates and deflectors to promote turbulent flow of the electrolyte, were studied by Climent and Garces[49,50]. More importantly, the performance of an all-vanadium redox flow cell with carbon felt electrodes and cation selective membrane was described by Skyllas-Kazacos[51].

New characteristics of an all-vanadium redox flow battery were described by Rychcik in early 1988[52]. A 10 kW Fe-Cr redox flow battery with an 80% energy efficiency and 300 cycle life was described by Shimizu[53]. Besides, the application of conductive organic polymers to battery electrodes was reviewed by Duic[54]. A general evaluation test of four advanced 10 kW batteries (Na-S, Zn-Cl, Zn-Br and Fe-Cr redox flow) was done by Takahasi[55]. The same year, a new structure for flowing electrolyte and its distribution in an efficient manner was patented by Shimuzu[56]. Moreover, the evaluation of membranes for an all-vanadium redox cell was done by Grossmith and Skyllas[57].

In 1990, a 1 MW/4MWh zinc-bromine RFB system was installed in Japan[5]. At present, the zinc-bromine RFB is being developed by ZBB Energy Corporation, RedFlow Ltd., and Premium Power. The battery modules are expandable from 50 kWh to 500 kWh and are available for commercial and utility applications.

From 1993 to present (**Figure 2.4**), the VRFB has been commercialized for various applications, such as load-leveling, power quality control and renewable coupling. More than 20 large-scale plants have been installed globally by manufacturers[58]. The considerable progress of the VRFB has been assisted by improvements in electrode[59–65] and membrane materials[66–73].

Bromine-polysulphide RFB systems were developed by Regenesys Technologies (UK) at Innogy plc between 1991 and 2004[74–76] A 1 MW pilot plant at Abershaw power state in South Walles was demonstrated and successfully tested. The construction of 15 MW/120 MWh demonstration plants started at Little Barford in the early 2000s[75,76]. The bromine-polysulphide technology has been one of the largest scaled-up RFB systems, driven by the moderate cost of non-catalyzed electrodes and especially the low-cost of the electrolyte components which are available from multiple sources on a tonnage scale. Full production-scale modular cell stacks were proven on a pilot plant but commercial scale was ceased due to changes of the holding company policy. Regenesys technology was acquired by VRB Power Systems Inc. in 2004 and was subsequently acquired by Prudent Energy (China) in 2009.

Several membrane-free flow batteries, such as soluble lead-acid[77–79], zinc-nickel[80–82] and zinc-cerium types[83,84] have been developed since 2004. These batteries utilize a single electrolyte and therefore do not require an ion-exchange membrane taking as an advantage the lower cost and greater simplicity over other flow battery systems[78]. Among these undivided systems, some were reported to have excellent round-trip DC energy efficiency >80% and a cycle life above 1000 cycles[80]. More recently, two types of lithium flow batteries storing energy so-called "flowable" electrode materials[85] and an aqueous positive electrolyte[86,87] have been introduced, reporting a discharge cell voltage of 3.8 V and energy density per electrolyte volume of 397 Wh/L, which are attractive for electric vehicle applications.

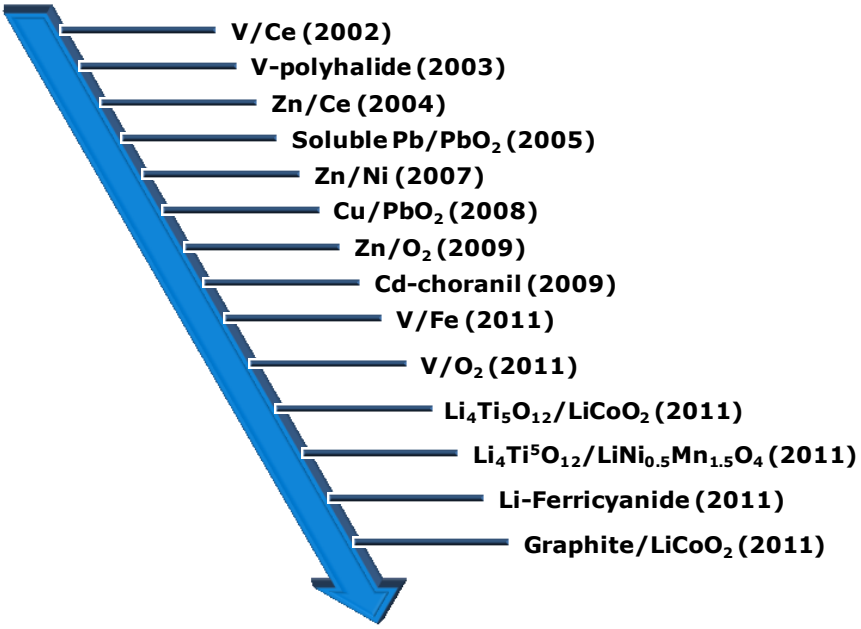

Figure 2.4 – Latest progressions on new redox flow batteries.

2.6 Redox flow batteries configuration

Redox flow batteries can be classified by active species or solvent (aqueous or non-aqueous respectively). **Figure 2.5** shows a generic RFB system. In the discharge mode, an anolyte solution flows through a porous electrode and reacts to generate electrons, which are conducted through the external circuit. The charge-carrying species are then transported to a separator (ion exchange membrane (IEM) or nano-porous membrane), which separates the anolyte and catholyte solutions. Typically for the anode (negative electrode) and the cathode (positive electrode), respectively, the general reactions can be written as:

$$\mathbf{A^{n+} + xe^- \rightarrow A^{(n-x)+}\ and\ A^{(n-x)+} \rightarrow A^{n+} + xe^-\ (n > x)}$$

$$\mathbf{B^{m+} - ye^- \rightarrow B^{(m+y)+}\ and\ B^{(m+y)+} \rightarrow B^{m+} - ye^-\ (m > y)}$$

The key transport mechanisms are shown in **Figure 2.6** for this generic system. The dominant losses in these systems, other than charge transfer reaction kinetics, are related to the charge and mass transport in the electrolyte and separator,

which are discussed in turn later on. Additionally, a key factor in many of these systems is the crossover of ions or molecules through the separator, depending on the current and membrane permeability. The polarization curve is composed by ohmic, mass-transport and/or kinetic losses. The first part of the curves, shown in **Figure 2.6**, the overpotential generated is kinetically limited. The middle part of the curves is dominated by ohmic or ionic-conduction losses, while the last part of the curves is typically a signature of reactant mass-transport limitations.

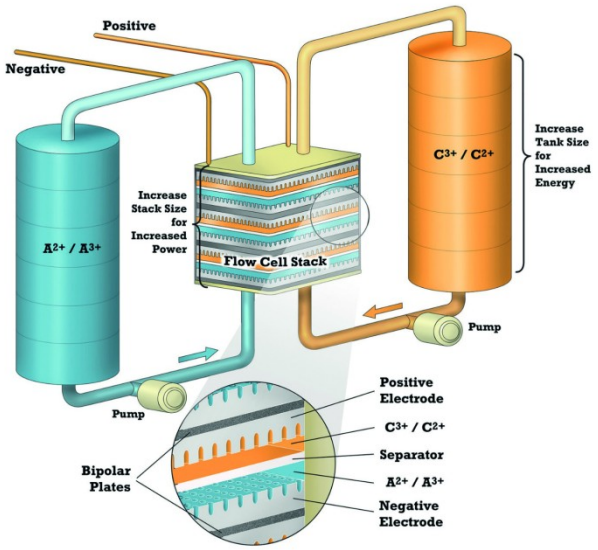

Figure 2.5 – Scheme of a redox flow battery[88].

The arrangement of individual cells in series can be done to increase the overall stack voltage. Generally, stacks are arranged in a bipolar fashion so that current flows in series from one cell to the next.

The electrodes in most RFB configurations are not required to undergo physical changes such as phase change or intercalation/de-intercalation during operation because the changes are occurring in the dissolved reactants in the solution phase adjacent to the solid-electrode surface. Though there are exceptions to this formulation. Side reactions can, of course, complicate design and operation, but if the reactions proceed as intended, degradation of the electrode surface need not proceed as a matter of course. The decoupling of storage and reaction in RFB systems is an advantage in terms of flexibility, but it complicates their designs relative to conventional batteries and adds a mechanical balance-of-plant element for pumping the often highly corrosive liquid electrolyte. As a result, their specific mass and volumetric energy densities are much lower than conventional batteries. A RFB configuration can nevertheless exceed the performance of other grid-storage technologies and does not require specific geographical sitting, as pumped hydroelectric and compressed-air energy storage (CAES) do.

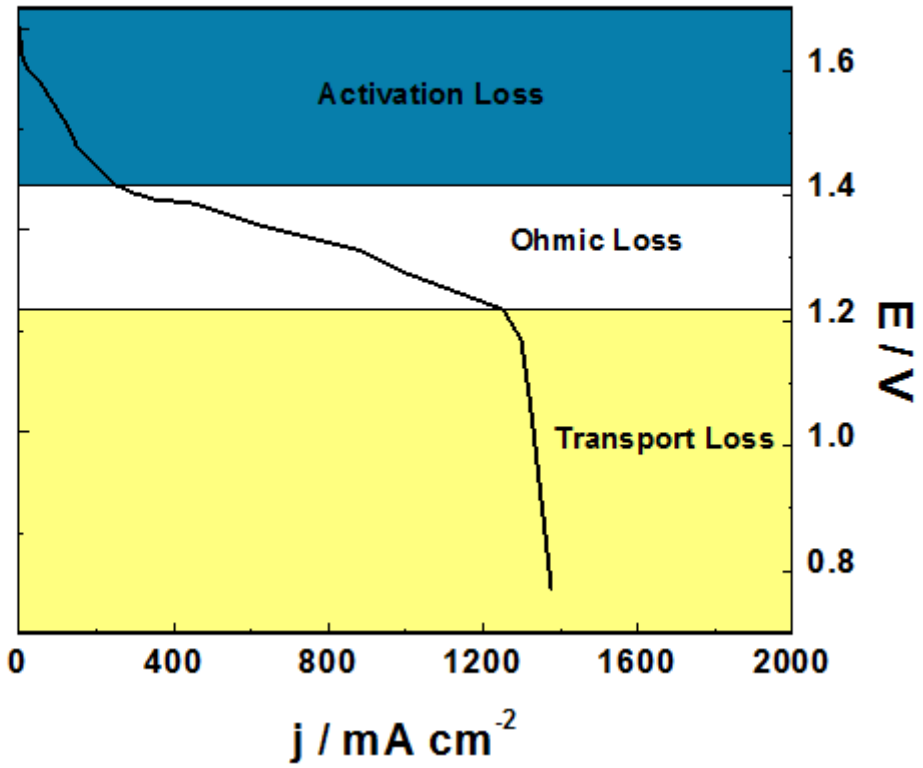

Figure 2.6 – Polarization curve of an all vanadium RFB using 1 M $VOSO_4$ in 3 M H_2SO_4 and Nafion 117 membrane. Electrode area = 4 cm^2.[89,90]

Additionally, RFBs offer the important advantage that power and energy output are independent variables since the power is determined by the reactor size and the amount of energy depends on the reactant chosen, their concentration, and the size of the reactant tanks[51,91]. The amount of energy that can be stored in a conventional sealed battery is generally limited by the effective path length for diffusion and migration in the direction normal to the current collector. Making the electrode thicker will add to the amount of active material, but one experiences diminishing return in terms of energy extraction, because of diffusion and ohmic losses in these systems.

Most RFB systems currently require two separate electrolyte tanks, one for the anolyte and another for the catholyte. This ensures that the potentials at each electrode are close to the reversible potential for each of the half-cell reactions are minimized. This does, however, add to the size and cost of the system, and it also requires a uniform delivery of the dissolved species to the entire surface area as oftentimes most of the convective flow is parallel to the electrode surface rather than being flowed directly through it.

The key costs of RFBs are the active material stored in the electrolyte and the electrochemical cell itself. The construction costs of the cell scale with the total power requirement of the application, but these costs are directly rated to the specific power of the device itself. i.e. how effectively the materials are utilized.

While RFBs ought to be able to operate at relatively high current densities, as convection can be employed to deliver reactants to the electrode surface, RFBs have typically been operated at current densities consistent with conventional batteries without convection. It is anticipated that electrolyte improvements in power density, thereby reducing considerably cell material costs.

2.6.1 Various Redox flow batteries

Several battery technologies have been considered for grid-based storage in recent decades. Traditional rechargeable batteries have been modified and optimized for grid-based storage and are being deployed in some installations, including lead-acid, nickel-based, and lithium-ion batteries. However, we turn our attention to RFBs, which have been demonstrated on the order of 100 kW to 10 MW. RFBs are generally categorized based upon the anolyte and catholyte that comprise the form of energy storage of the system. Configurations with the same element but different oxidation states, such as all-vanadium, as well as different active species in the anolyte and catholyte are used. In this section, we introduce the various important RFB types and briefly some of the advantages, disadvantages and challenges of each one.

2.6.1.1 Iron/chromium

Modern development of what we might term as RFB began with the development of an iron/chromium system (Fe/Cr) in the 1970s at NASA, which demonstrated a 1kW/13kWh system for a photovoltaic-array application[92,93]. The Fe/Cr system is based upon an aqueous solution of a ferric/ferrous redox couple at the positive electrode (Fe^{2+}/Fe^{3+}), while the negative electrolyte is a mixture of chromic and chromous ions (Cr^{2+}/Cr^{3+}). Most systems use hydrochloric acid as the supporting electrolyte. The charge transfer reactions at each electrode are

$$\mathbf{Fe^{2+} \leftrightarrow Fe^{3+} + e^{-}, E^{0} = 0.77\ V\ vs.\ NHE} \quad \textbf{(2.1)}$$

and

$$\mathbf{Cr^{2+} \leftrightarrow Cr^{3+} + e^{-}, E^{0} = -0.41\ V\ vs.\ NHE} \quad \textbf{(2.2)}$$

The system can operate with an IEM/separator and low-cost carbon-felt electrodes. Both charge-transfer reactions require only a single electron transfer, which is expected to simplify charge transfer and result in reasonable surface over-potentials without specific electrocatalysts. Indeed, the iron redox couple is highly reversible on carbon or graphite electrodes, but the chromium redox couple has significantly slower kinetics and does require electrocatalysts. This system has a

relatively low open circuit potential (OCP), between 0.90 and 1.20 V with 19.1 WhL^{-1}, and designers must endure crossover of iron to the chromium stream and vice versa. Some Japanese companies built similar batteries by licensing the NASA patents, but have not shown improvement in the low output voltage and efficiency[13].

2.6.1.2 Bromine/polysulfide

The bromine/polysulfide RFB was patented by Remick then extensively studied by Regenesys Technology[94] from 1993 until 2006 when it was acquired by VRB Power Systems. To date, three series of bromine/polysulfide RFB systems have been developed, including 5, 20 and 100 kW class systems. A commercial size 15 MW system was successfully demonstrated. This plant used up to 120 modules, and 200 bipolar electrodes with and energy storage capacity up to 12 MWh and two 1800 m^3 electrolyte storage tanks[95].

In the bromine/polysulfide system, the positive electrolyte is sodium bromide, and the negative electrolyte is sodium polysulfide, though, the counter ion could be replaced with another cation. The key attributes of this system are that species that comprise the two electrolytes are abundant and reasonably inexpensive. Moreover, they are highly soluble in aqueous electrolytes, which reduce the volume of electrolyte that is required to store a given quantity of charge. At the positive electrode three bromide ions combine to form the tribromide ion.

$$\mathbf{3Br^- \leftrightarrow Br_3^- + 2e^-, E^0 = 1.09\ V\ vs.\ NHE} \quad \textbf{(2.3)}$$

At the negative electrode, the sulfur in solution is shuttled between polysulfide and sulfide

$$\mathbf{2S_2^{2-} \leftrightarrow S_4^{2-} + 2e^-, E^0 = -0.265\ V\ vs.\ NHE} \quad \textbf{(2.4)}$$

In this system with a cell voltage of 1.54 V, all of the electroactive species are anions, so a cation-exchange membrane is needed to prevent mixing of the anolyte and catholyte streams. Charge is carried via sodium ions through the membrane. When activated carbon/polyolefin composite electrodes were used in this system, the voltage increased from 1.7 to 2.1 V (20-30 WhL^{-1}) during charging process due to adsorption of bromine in the activated carbon[96]. This system is prone to crossover and mixing of the electrolytes, can lead to the precipitation of sulfur species and the formation of H_2S and Br_2.

2.6.1.3 All-vanadium

In both of the systems described above, a chief of concern and liability is the incompatibility between, and sensitivity of, the two electrolyte streams to contamination from the other. If a species crosses over and reacts irreversibly with elements in the opposite stream, it comprises not just an efficiency loss on that particular charge/discharge cycle, but a loss of capacity and degradation in the overall performance of the system, which may result in expensive electrolyte separation and reactant recovery. To this end, it is helpful to develop a system with more than two oxidation states of the same element, wherein crossover only represents an efficiency loss as no species are irreversibly consumed or removed from their reactive electrolytic solution. The all-vanadium system employs the V(II)/V(III) redox couple at the negative electrode and the V(IV)/V(V) at the positive electrode, generally identified to exist in the form of VO^{2+} and VO_2^+.

$$\mathbf{V^{2+} \leftrightarrow V^{3+} + e^{-}, E^{0} = -0.26\ V\ vs.\ NHE} \quad \textbf{(2.5)}$$

$$\mathbf{VO^{2+} + H_2O \leftrightarrow VO_2^{+} + 2H^{+} + e^{-}, E^{0} = 1.00\ V\ vs.\ NHE} \quad \textbf{(2.6)}$$

In this case, the 1.4 V cell voltage can generate a 25-35 WhL^{-1} of energy density. The current is maintained by the migration of protons across the membrane separator. While it is nominally the change in the oxidation state of vanadium on either side of the membrane that stores and releases charge, there is a change in the pH of the solution over the course of a charge and discharge cycle. While crossover of the different oxidation states of vanadium comprises an efficiency loss, the proper forms can be regenerated electrochemically, which eases the stringency of maintenance requirements.

While exploratory research on vanadium as a redox couple began at NASA[97], the all vanadium redox flow battery (VRFB) was invented and developed by Maria Skyllas-Kazacos and her co-workers at the University of New South Wales[45,51,98]. Research has continued on this technology since that time. As a promising technology for storing intermittent renewable energy, VRFB systems have received perhaps the most attention of all RFBs[39,51,99]. In fact, prototypes up to the range of MW in power and MWh in energy storage capacity have been demonstrated[70,100,101]. Skyllas-Kazacos developed a 5-10 kW VRFB stacks.

While energy density is not necessarily a primary concern for stationary, grid applications, nonetheless, the VRFB energy density is limited by the solubility of vanadium in the electrolyte stream and precipitation can occur. The solubility limits depend upon both acid concentration and temperature[102].

2.6.1.4 Vanadium/bromine

Because there are limits to how much vanadium can be stored in solution in the VRFB system, some of the same researchers who pioneered the work on the VRFB cell noted that vanadium solubility could be boosted in the presence of halide ions. In this case, during charging the bromide ions in the positive half-cell undergo oxidation to what is assumed to be the polyhalide ion Br_2Cl^-. The formal potential of this couple is about 1.3 V more positive than the V^{2+}/V^{3+} couple[103–105]. The researchers were able to show significantly higher solubility in this system, where vanadium/bromide solutions with nearly twice the solubility on a molar basis relative to vanadium sulfate solutions was demonstrated. The higher solubility of vanadium/bromine results in higher energy densities (35-70 Wh/L) compared to the VRFB systems (25-35 Wh/L). However, the potential concern of vanadium/bromine redox systems is toxic bromine vapor emissions during operation, and thus Skyllas-Kazacos also used bromine complexing agents including tetrabutylammonium bromine, polyethylene glycol, N-methyl-N-ethyl morpholinium bromide, and N-methyl-N-ethyl pyrrolidinium bromide to decrease or eliminate bromine vapor emissions during operation[106]. Generally, the Coulombic efficiency increases with increasing current density due to lower self-discharge through the membrane. However, it decreases as temperature increases due to more rapid diffusion of vanadium and polybromide ions through the membrane.

2.6.1.5 Hydrogen-based systems

A fuel cell takes a fuel, normally hydrogen, and an oxidant, typically air, and produces electricity and water. A typical fuel cell produces a voltage from 0.6 V to 0.7 V with 2-3 $kWhL^{-1}$, hydrogen oxidizes at the anode according to the reaction

$$\mathbf{H_2 \leftrightarrow 2H^+ + 2e^-, E^0 = 0\ V\ vs.\ NHE} \qquad \textbf{(2.7)}$$

and, at the cathode, oxygen is reduced

$$\mathbf{4H^+ + 4e^- + O_2 \leftrightarrow 2H_2O\ , E^0 = 1.229\ V\ vs.\ NHE} \qquad \textbf{(2.8)}$$

If one were to design a system where the fuel cell acts in both the charge and discharge directions (i.e. a reversible or regenerative fuel cell), then a RFB system would exist. Such a RFB system has been examined both with the same and different stacks for charge and discharge[107–109]. This system is inherently different from the RFBs discussed above since the reactants are in the gas phase not liquid storage in a tank, and thus hydrogen compression or novel hydrogen storage materials are needed. Although mass transfer is typically rapid, the oxygen reactions are known to be very sluggish and result in very large overpotentials[110], thereby rendering the overall efficiency of the system to be very low. To enhance as well as drive down cost of the hydrogen/oxygen system, strategies including

looking at alkaline media, high temperatures, and closed systems with oxygen and not air. Also, because of the difficulty associated with finding robust and effective oxygen reduction/evolution catalysts, different oxidants have been examined including bromine and chlorine, both of which react rapidly on carbon surfaces[111–113].

2.6.1.6 Hybrid redox flow batteries

There are other battery configurations that share a development heritage and some common issues with what we would classify as RFBs in that the active material can be introduced to, or removed from, the electrochemical cell without disassembling the cell structure, but which do not store all of the active material in a liquid or gaseous form per se. As such, we might consider them semi-flow cells with electrochemical reactions that are more complicated than simply shuttling between the oxidation states of a single species.

2.6.1.6.1 Zinc/bromine.

The prototypical hybrid RFB is the zinc/bromine system[114]. In this system, electrolyte solutions containing the reactive species are stored in external tanks and circulated through each cell in the stack, but the zinc forms an electrodeposit. At the positive electrode, bromide ions are transformed to bromine and back, see Eq. **(2.3)**. It is important to note that the bromine ions can combine with bromine molecules to generate the tribromide ion[115].

$$\mathbf{Br_2 + 2e^- \leftrightarrow 2Br^-, E^0 = 1.087\ V\ vs.\ NHE} \qquad \textbf{(2.9)}$$

which primarily occurs in liquid bromine. In this system, relatively high concentrations of Br^- and Br_2 can be utilized, enhancing both reaction kinetics and energy density. The toxicity of Br_2 can be mitigated by the use of complexing agents[115], but the effect of complexing agents on kinetics has not been studied quantitatively, particularly strongly acidic supporting electrolyte.

At the negative electrode, zinc metal is dissolved and redeposit,

$$\mathbf{Zn \leftrightarrow Zn^{2+} + 2e^-, E^0 = -0.76\ V\ vs.\ NHE} \qquad \textbf{(2.10)}$$

To prevent self-discharge by combination of zinc and bromine, separate flowing streams o aqueous zinc bromide and bromine circulate in separate loops, separated by and IEM or a micro porous film[115].

The metal negative electrode allows for a compact electrode, thus increasing the energy density (15.7–39 Wh/L). In addition, the zinc/bromine system has a high

cell voltage (1.8 V), good reversibility, and expectations of low material costs. However, the demonstration of zinc/bromine has been limited due to material corrosion, dendrite formation and electrical shorting, high self-discharge rates, low energy efficiencies, and short cycle life. RedFlow Ltd. Successfully demonstrated a zinc/bromine RFB unit up to MW size with an energy efficiency of nearly 74% in Australia[116]. The cell architecture was designed to optimize plating and deplating efficiency of zinc during charging and discharging operations. Derivatives of the zinc/bromine system include other halogens such as zinc/chlorine, which typically have similar performance and issues[116].

2.6.1.6.2 Soluble lead acid

A soluble form of the lead-acid battery has also been considered[116]. The charge transfer reactions as written are the same as in a traditional sealed lead-acid battery configuration. Lead-acid batteries do not shuttle the same ion between the negative and positive electrode. That is, Pb^{2+} is introduced an removed from solution at the negative electrode as lead is dissolved and plated,

$$\mathbf{Pb \leftrightarrow Pb^{2+} + 2e^{-}, E^{0} = -0.13\ V\ vs.\ NHE} \qquad \mathbf{(2.11)}$$

but at the positive electrode, lead ions combine with water to produce lead dioxide and protons,

$$\mathbf{Pb^{2+} + 2H_2O \leftrightarrow PbO_2 + 4H^{+} + 2e^{-}, E^{0} = 1.49\ V\ vs.\ NHE} \qquad \mathbf{(2.12)}$$

As lead ions are produced in the oxidation step at the negative electrode and produced in the reduction step at the positive electrode on discharge with a 1.78 V cell potential and 167 $WhKg^{-1}$. There is not any a risk of crossover lowering the overall efficiency of the system. As long as the solid forms of lead and lead oxide are maintained at the negative and positive electrodes, circulation of electrolyte can maintain the open circuit potential (OCP) of the battery and allow grater specific cell performance than with sealed or flooded lead-acid cells, assuming minimal weight and volume of the external storage tank. As with other hybrid flow configurations, there are risks associated with maintaining the morphology of the solid phase as material can detach or grow across the separator gap to cause short-circuit problems.

2.6.1.6.3 All iron

Similar to the all-vanadium RFB, the all-iron system[117,118] involves only a single element, where on one electrode iron (II) goes to iron (III), Eq. **(2.1)**, and on the other plating of iron occurs

$$\mathbf{Fe \leftrightarrow Fe^{2+} + 2e^{-}, E^{0} = -0.3\ V\ vs.\ NHE} \qquad \textbf{(2.13)}$$

Obtaining a nominal cell potential of 1.21 V and an energy density of 11.5 Wh L^{-1} Due to single species, crossover is not as much a concern although it is still a current inefficiency. This system has some of the same issues as the other hybrid batteries including getting uniform plating of the metal, thereby need precise pH control and supporting electrolyte. However, iron does not have the extensive dendrite problems of zinc. The benefits of the cell are also that the materials are nonhazardous and inexpensive. These are balanced by the fact that the overall cell voltage is relatively low and hydrogen generation can occur, although iron is a poor hydrogen evolution catalyst.

2.6.1.6.4 All-copper

In the all-copper RFB the chemistry of the Cu^{0}-Cu(I)-Cu(II) system is employed to store and deliver electricity within the battery[119], as shown in Equations **(2.14)** and **(2.15)**. The fresh electrolyte, which is initially composed by cuprous chloro-complexes, is transformed into cupric chloro-complexes in the positive half-cell and electro-deposited as copper on the negative electrode surface during charge. Therefore, during discharge, the cupric ions formed in the positive half-cell electrolyte are transformed again to Cu^{+} ions, while the stripping of the copper deposit occurs in the negative side.

$$\mathbf{Cu^{+} \leftrightarrow Cu^{2+} + e^{-}} \qquad \mathbf{E^{0} = 0.521\ V\ vs.\ NHE} \qquad \textbf{(2.14)}$$

$$\mathbf{Cu^{+} + e^{-} \leftrightarrow Cu^{0}} \qquad \mathbf{E^{0} = 0.153\ V\ vs.\ NHE} \qquad \textbf{(2.15)}$$

The potential difference between these two kinetically facile reactions in highly concentrated chloride media is around 0.7 V and 20 WhL^{-1} energy density, according to previous electrochemical studies of copper-chloride electrolytes in aqueous or deep eutectic solvents[120,121].

2.6.1.7 Non-aqueous redox flow batteries

The use of non-aqueous electrolytes in RFB configurations has been considered because of the higher cell potentials that are possible when one is not concerned by the breakdown of the aqueous electrolyte. In addition, many couples and reactants are much more soluble in non-aqueous solvents. However, the challenges of low electrolyte conductivities, stability and cost limit the development of non-aqueous RFB systems.

As an example, the zinc/cerium has been worked on by Plurion Limited. As with the zinc/bromine cell, the negative electrode dissolves and plates zinc, Eq. **(2.10)**, and at the positive electrode, cerium is shuttled between Ce (III) and Ce (IV).

$$\mathbf{Ce^{3+} \leftrightarrow Ce^{4+} + e^{-}, E^{0} = 1.75\ V\ vs.\ NHE} \qquad \textbf{(2.16)}$$

The developers claim a cell potential of approximately 2.5 V on charging, but it drops below 2 V during discharge with an energy density from 37.5 to 120 Wh/L. The high operating potential window is achieved by using methane sulfonic acid rather than pure water as the solvent, thus minimizing decomposition of water into hydrogen and oxygen, as well as aiding in zinc plating. The redox reaction of Ce^{3+}/Ce^{4+} is kinetically slow and Ce^{3+} has a low diffusivity[83,122]. High acid strength facilitates the solubility of Ce^{4+}. However, the solubility of Ce^{3+} decreases at higher acid concentrations. Other electrochemical couples including zinc/chlorine[122], zinc/ferricyanide, and vanadium/cerium[122] have been considered. While non-aqueous electrolytes generally imply higher costs than aqueous electrolytes and must be vetted for environmental and chemical compatibility, the expansion of the operating potential window is attractive, as the cell potential difference has a direct impact on the amount of power that can be delivered for a specified current density.

Other examples of non-aqueous RFBs include that of Matsuda et al.[123] who demonstrated a redox system based on $[Ru(bpy)_3]^{2+}/[Ru(bpy)_3]^{3+}$ (bpy is bipyridine) as the anolyte and $[Ru(bpy)_3]^{+}/[Ru(bpy)_3]^{2+}$ as the catholyte in acetonitrile (CH_3CN) with tetraethylammonium tetrafluoroborate ($TEABF_4$) as the supporting electrolyte. This system yielded an open circuit potential of 2.6 V, with and energy efficiency of 40%. Chakrabarti et al. evaluated a redox system based on a ruthenium acetylacetonate, obtaining a cell potential of 1.77 V[124]. Yamamura et al.[125] studied a non-aqueous system which used various uranium beta-diketonates with the cell potentials of about 1 V.

Recently, Thompson and co-workers demonstrated a redox flow system using $M(acac)_3$ (M= V, Cr or Mn, and acac is acetylacetonate) with at least three different oxidation states[126–128]. The vanadium and chromium acetylacetonate systems showed higher open circuit potentials, 2.2 and 3.4 V, respectively, compared to around 1.26 V for the aqueous VRFB system. However, crossover and ohmic losses due to the large distances between positive and negative electrodes limited the Coulombic efficiency. Although the $Mn(acac)_3$ system show a lower open circuit potential (1.1 V) than that of $V(acac)_3$, $Cr(acac)_3$, and VRFB, it exhibits better reversibility both for Mn(II)/Mn(III) and Mn(III)/Mn(IV) redox couple, with a columbic efficiency approaching 97% in a static H-type cell. Shinkle et al. studied the degradation mechanism in the non-aqueous V(acac)3 redox systems[129], and showed that environmental oxygen and water are associated with side reactions that affect the long-term charge-discharge response of the battery.

2.6.1.8 Other configurations

There is a recent interest in the development of the lithium-air battery, which operates with a static lithium negative electrode, as might be found in a lithium-ion or lithium-polymer battery. Lithium ions combine with oxygen from air to form lithium oxide at the positive electrode on discharge, while oxygen is regenerated during charge. Kraytsberg and Ein-Eli provide an overview of the technology[130]. There are many challenges with such a battery system, such as ensuring proper isolation of the negative electrode structure that provides for facile oxygen transport and reversible oxide formation and stripping. However, the promise for high energy density and low material costs suggest tremendous research opportunities.

Another recent flow-cell concept was invented by Yet-Ming Chiang's group at MIT described by Duduta et al.[85,131] They proposed using typical intercalation electrode materials as active material for a lithium rechargeable battery, but providing the active material in slurry that can be mechanically pumped in and out of a reaction chamber. In the paper describing the concept, they note that they will be able to store much higher concentrations of active material in the solid component of the slurry than can be stored as ions dissolved in electrolyte (up to 24 M), thereby increasing the energy density well beyond what could be achieved in traditional RFBs.

2.7 All Vanadium Redox Flow Batteries

This battery employs the same metal in both half-cells. The negative half-cells employ V^{2+}/V^{3+} redox couple whereas the positive half-cell uses VO^{2+}/VO_2^{+} redox couple. Both vanadium redox couple show sufficient kinetics in sulfuric acid supporting electrolyte. Electrical balance is achieved by the migration of proton across the membrane splitting the electrolytes. The charge-discharge reactions of the VRFB are:

Negative electrode.

$$\mathbf{V^{2+} \leftrightarrow V^{3+} + e^{-},\ E^{0} = -0.26\ V\ vs.\ NHE} \qquad \textbf{(2.17)}$$

Positive electrode.

$$\mathbf{VO^{2+} + H_2O \leftrightarrow VO_2^{+} + 2H^{+} + e^{-},\ E^{0} = 1.0\ V\ vs.\ NHE} \qquad \textbf{(2.18)}$$

The standard open-circuit cell voltage is 1.26 V. It is reported that under actual cell conditions of using 2 M $VOSO_4$ in 2.5 M H_2SO_4 electrolyte, the cell open-circuit potential is 1.35 V at 50% state of charge and 1.60 V in a fully charged state[132]. The system can be operated over a temperature range of 10-40ºC[132,133].

The VRFB was studied in detail by the group of Skyllas-Kazacos[36,39,67,69–72,99,100,102–104,45,105,106,132–135,51,59–63,65] and by industrial organizations[136] in Japan during the 1980s and 90s. Since 2002 significant research and development has been spread

world-wide, especially in China[66,101,137], USA[97,138,139] and Europe[139]. The advantages possessed by VRFB can be summarized as follows:

i) Employing the same element in both half-cells and utilizing four different oxidation states of vanadium in solution, in comparison to the Fe/Cr system, the VRFB eliminates the problem of cross contamination by diffusion of different redox ions across the membrane. Even if ions crossover occurs, the electrolytes can be regenerated by mixing and doing electrolysis without complicated chemical treatments.
ii) The relatively fast kinetics of the vanadium redox couples allow high charge and voltage efficiencies to be obtained, the overall energy efficiency from an initial 71% up to 90% has been reported with a 1 kW VRFB stack.
iii) There is an extremely low rate of gas evolution during the charge rates associated with rapid charging cycles.
iv) It can be fully-charged and deeply discharged, within the limits of the capacity of the electrolytes, as well as, being cycled from any state of charge or discharge without permanent damage to the cell or electrolytes.
v) A reusable electrolyte leads to a long cycle life and reduces cost of the system. These advantages and its flexibility make the VRFB a promising technology for large-scale storage of renewable energy.

For practical applications, however, the VRFB system faces several challenges. One of the major challenges is its low specific energy density (25-30 Wh/Kg) compared to other batteries for energy storage. The energy density in a VRFB depends on the concentration of vanadium species but there is limited vanadium solubility in H_2SO_4, when the vanadium ion concentration is above 2 M, V_2O_5 precipitations occurs in the positive electrolyte at a temperature above 40ºC. Similarly, a vanadium sulfate precipitate appears in the negative electrolyte below 10ºC[102,140,141]. Even with the positive effects of the additives[142], the vanadium concentration is still limited to 1 to 1.5 M for most practical batteries.

Much effort has been focus on increase the energy density of this technology. For example, Skyllas-Kazacos et al.[102] reported that the VO_2^+ concentration can be increased up to 3 M without any precipitation at 40ºC when a sulfuric acid concentration is higher than 5 M and, by using a concentration of 7 M SO_4^{2-} as the medium, an even higher 5.4 M VO_2^+ solution is claimed to be stable for period of over 30 days at >50ºC, but increasing the concentration of sulfuric acid caused a decrease in solubility of $VOSO_4$ at low temperature (<10ºC).

Recently, Yang et al.[143] reported that, in 10 M HCl supporting electrolytes, more than 2.3 M vanadium (V^{2+}, V^{3+}, VO^{2+}, VO_2^+) are all stable for 15 days over a temperature range of 0-50ºC. Despite these efforts to improve the solubility of vanadium, the stability of vanadium ions is determined by a number of influential factors such as solution temperature, the concentration of supporting electrolyte, additives and state of charge. Hence low energy density still remains a major challenge for the VRFB system, as stability needs to be further improved and also allows these batteries to work at large current densities without large polarization

happening. Moreover, hydrogen evolution reaction occurring in the negative side of the battery remains a mayor challenge to overcome, as well as, increases the V^{2+}/V^{3+} redox reaction kinetics to not be the limiting factor of the working cell.

A schematic representation and working principle of the VRFB is shown in **Figure 2.7.** As with other redox flow battery systems, the VRFB is made up of a cell or stack, the size of which determines the power rating of the system (kW), electrolytes in external reservoirs the determine the energy rating (kWh), and a control system that ensures operation within safe limits to ensure a long cycle life.

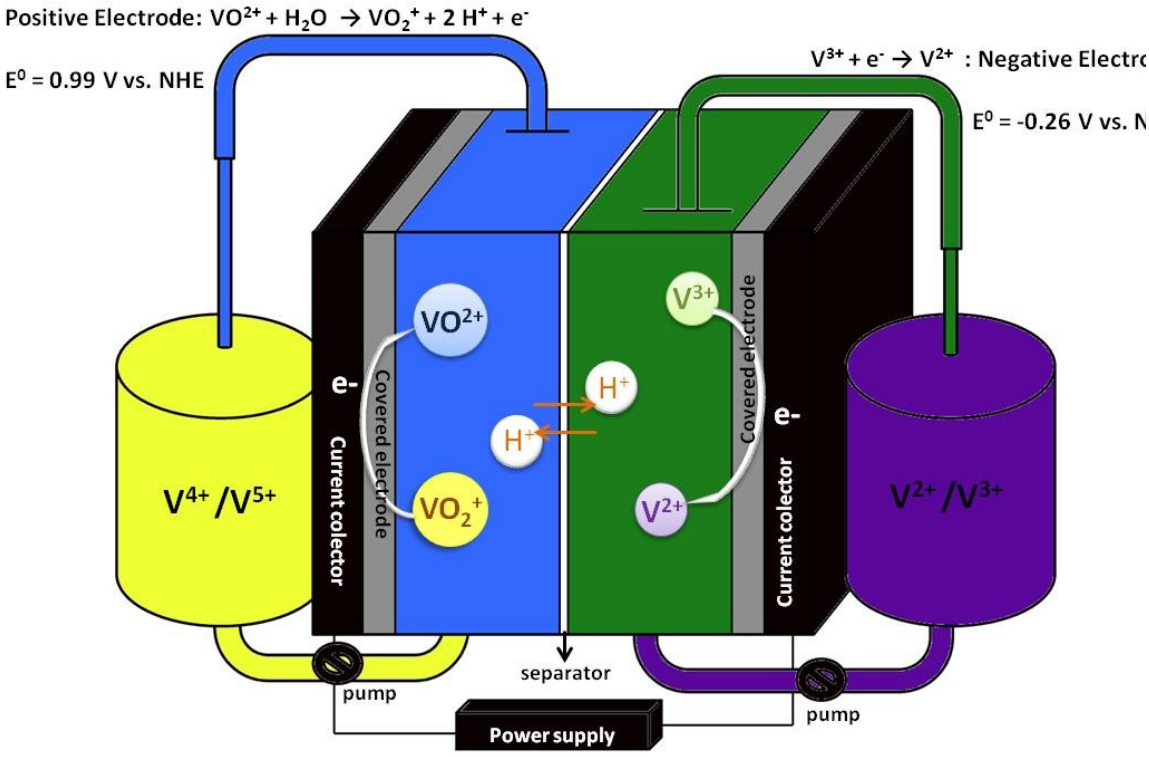

Figure 2.7. Schematic representations of the VRFB.

2.7.1 Cell potential

The standard cell potential (E^0) is the difference of the two electrode potentials (positive or cathode and negative or anode), which forms the voltage of that cell. The cell potential can be defined by the following equation:

$$\mathbf{E^0(Cell) = E^+ - E^-} \qquad \textbf{(2.19)}$$

Where E^0 (Cell) is the standard cell potential (under 1M, 1 bar and at an ambient temperature), E^+ is the standard reduction potential for the reaction occurring at the positive half-cell, and E^- is the standard reduction potential for the oxidation

half reaction occurring at the negative half-cell. The Nernst potentials for the two reduction reactions (**(2.20)** and **(2.21)**) that take place in each half cell of the VRFB can be represented as follows:

Positive half cell

$$\mathbf{E^{+} = E^{0+} - \frac{RT}{F} \ln \left[\frac{[VO^{2+}]}{[VO_2^{+}][H^{+}]^2} \right]} \qquad \textbf{(2.20)}$$

Negative half cell

$$\mathbf{E^{-} = E^{0-} - \frac{RT}{F} \ln \left[\frac{[V^{2+}]}{[V^{3+}]} \right]} \qquad \textbf{(2.21)}$$

Where R= 8.314472 J $K^{-1}mol^{-1}$ is the Universal Gas Constant, F= 96485 C mol^{-1} is Faraday's constant, T is the temperature [K], [V] are the concentrations of the different vanadium species in solution, $[H^{+}]$ is the hydrogen-ion concentration in the positive half-cell electrolyte, and E^{0+} and E^{0-} are the standard half-cell potentials for the positive and negative half-cell reactions, respectively.

2.7.2 Operating Cell Voltage

In practical systems, the actual cell potential during discharge is lower than the theoretical cell potential due to the internal resistance of the cell (internal loss). This internal loss is caused due to factors such as activation polarization, concentration polarization and ohmic potential drop (caused by current flow through resistive components). The overall cell potential can be described at any moment in time during the operation of the cell as follows:

$$\mathbf{E_{cell} = E^{+} - E^{-} - \eta^{+} - \eta^{-} - iR_{Cell}} \qquad \textbf{(2.22)}$$

Where E^{+} is the positive half-cell potential during charge (oxidation of V^{4+} to V^{5+} at the positive electrode), E^{-} is the negative half-cell potential during charge (reduction of V^{3+} to V^{2+} at the negative electrode), η^{-} is the activation overpotential for negative half-cell reactions [V], η^{+} is the concentration overpotential at the positive half-cell reactions [V], i is the current density [A cm^{-2}], and R_{Cell} is the ohmic resistance of the cell [Ω cm^2].

During charging, the cell voltage is higher than the theoretical cell potential as a result of all of the losses that impact on the overall voltage and energy efficiency of the battery during charge-discharge cycling. It is therefore desirable to reduce all of the voltage losses so as to maximize energy efficiency. Ohmic losses can be minimized by selecting membrane and electrode materials with low electrical resistance, by reducing the internal spacing and by minimizing contact resistances. Activation overvoltage losses can be reduced by using electrode materials with

good electrocatalytic properties for the vanadium redox couple reactions, while concentration overvoltage can be minimized by employing mass transfer enhanced electrodes, high flow rates and ensuring good electrolyte flow distribution. In the following sections is studied the cell resistance while modifying the base electrode, graphite or carbon felt, with materials such as TiO_2, TiO_2:H and TiO_2:N synthesized coatings, as well as Atomic layer deposited (ALD) CeO_2. The results indicated that the voltage drop varied with respect to the materials properties. Materials with a larger electrochemical active area, high conductivity, and a hydrophilic nature showed a higher specific capacitance and energy storage efficiency with lower internal resistance. Besides, the material/component selections for cell preparation as well as cell design are very important for improving the performance of the VRFB.

In addition to the voltage efficiency, Coulombic efficiency will also impact on cell performance. Coulombic efficiency is affected by the selectivity of the membrane that determines the rate diffusion of the vanadium ions from one half-cell to the other, leading to self-discharge. Coulombic efficiency is also affected by side reactions such as hydrogen and/or oxygen evolution during charging and air oxidation of the V^{2+} ions in the negative half-cell electrolyte. Gassing side reactions are a property of the electrode material as well as the electrolyte flow rate. Gassing an air oxidation not only reduce Coulombic Efficiency but can also decrease capacity over extended operation, requiring electrolyte rebalancing in order to restore capacity as discussed by Corcuera and Skyllas-Kazacos[144]. Coulombic efficiency is therefore dramatically affected by the properties of the membrane as well as battery design and operation.

2.7.3 Cell Components and Design Requirements

The exploded view of a single cell of the VRFB is shown in **Figure 2.8**. The basic VRFB cell is constructed from two half-cells, each containing an end plate, an insulating frame, current collectors (usually copper or brass), a graphite plate with flow channels for the electrolytes (anolyte and catholyte) flow, carbon or graphite felt (GF) of the desired thickness, and a gasket. The half-cells are separated by an ion exchange membrane that prevents mixing of the two half-cell electrolytes while allowing a transfer of hydrogen ions to complete the circuit.

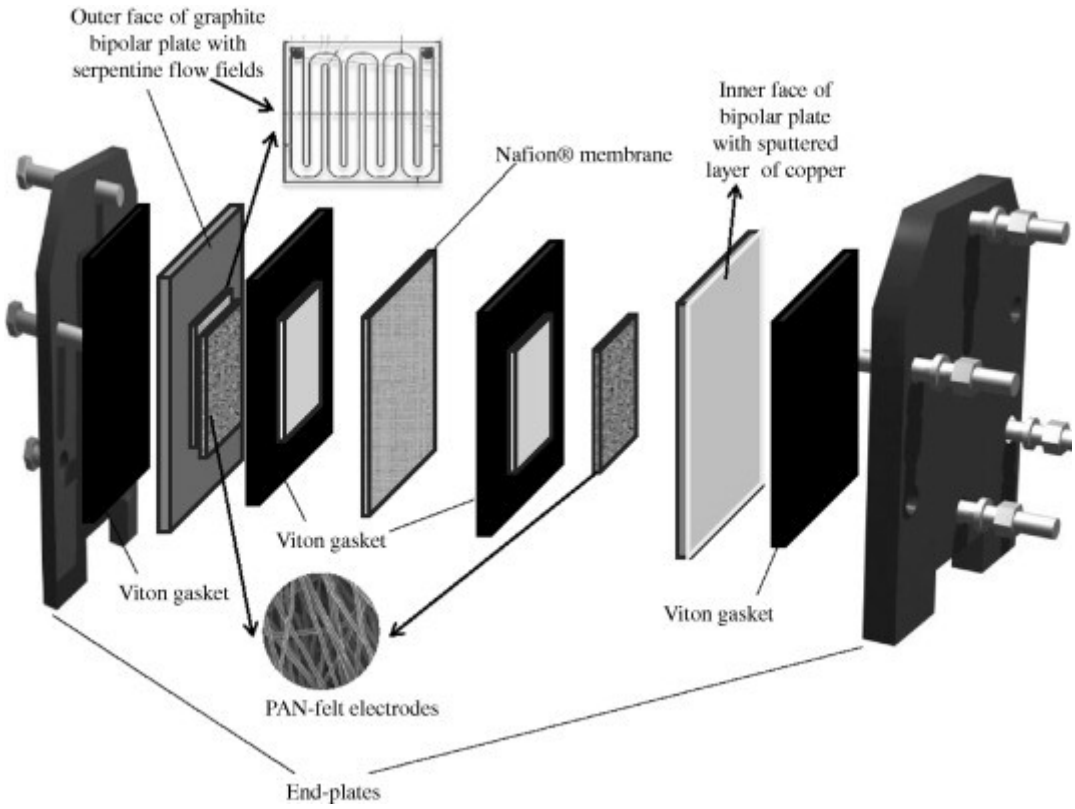

Figure 2.8. - Scheme of a VRFB single cell.

The GF provides the electroactive surface where the electrochemical reactions take place. Increasing the degree of compression will reduce the electrical resistance of the felt, but will increase pressure drop and the associated pumping energy losses through the stack. Cells are fed through a common manifold that must be designed to minimized shunt currents. Shunt currents and pumping energy are parasitic losses that must be minimized. With a good design and pump control, these can consume less than 2-3% of the total energy produced by the battery, as reported by Tang et al[145].

2.7.4 Cost analysis

Cost-effective electrochemical energy storage has the potential to dramatically change how society generates and delivers electricity. Unfortunately, present state-of-the-art technologies are too expensive for broad deployment. First is needed a reduction in manufacture costs and associated overheads, which are identified as the single largest cost-savings opportunity for today's battery-based storage options. In addition, increasing production volume and market competition will lead to lower material costs, which makes flow batteries as a promising technology platform capable of achieving the low costs required for widespread implementation. A key enabling development will be the discovery of tailored molecules that are long lived, provide large cell voltages, and have costs similar to existing commodity chemicals.

Energy storage is used to balance supply and demand on the electrical grid. The need to store energy is expected to increase as more electricity is generated from intermittent sources like wind and solar[146–149].

The economics of storing grid energy is challenging. The Department of Energy's (DOE's) Advanced Research Projects Agency-Energy (ARPA-E) set a capital cost target of $100 per kW h for 1 hour of storage for widespread adoption[150]. The DOE Office of Electricity Delivery and Energy Reliability proposed cost targets of $250 per kW h by 2015, falling to $150 per kW h in the future for a fully integrated distributed energy storage system providing 4 h of storage[150]. The target cost of the energy storage device in the 2015 integrated system was $100 per kW h. These strict targets reflect the cheap cost of electricity in the United States. While in Europe flow battery technologies, as vanadium redox flow had total installation costs in 2016 of USD 315. By 2030, the cost is expected to come down to USD 108[151] Fortunately, compared with transportation applications, batteries for grid applications can tolerate higher temperature and lower energy density; this widens the scope of possible solutions to include, for example redox flow batteries. Especially vanadium redox flow batteries as the more mature and near to commercial expansion.

Combining expressions for reactor, electrolyte, and system costs and introducing the discharge voltage efficiency, $\varepsilon_{v,d} = V_d/U$, where V_d is the discharge voltage of the reactor and U corresponds to the thermodynamically reversible or open-circuit potential, to simplify notation yields the following equation for the total system price for useable energy[152]:

$$\frac{\boldsymbol{P_0}}{\boldsymbol{E_d}} = \frac{\boldsymbol{c_a R}}{\boldsymbol{\varepsilon_{sys,d} U^2 \varepsilon_{v,d}(1-\varepsilon_{v,d}) t_d}} + \frac{\boldsymbol{1}}{\boldsymbol{\varepsilon_{sys,d} \varepsilon_{q,rt} n_e F \varepsilon_{v,d} U}}\left[\frac{\boldsymbol{s_+ M_+}}{\boldsymbol{\chi_+}}\left(\boldsymbol{c_{m,+}} + \frac{\boldsymbol{c_{m,e+}}}{\boldsymbol{S_+}}\right) + \frac{\boldsymbol{s_- M_-}}{\boldsymbol{\chi_-}}\left(\boldsymbol{c_{m,-}} + \frac{\boldsymbol{c_{m,e-}}}{\boldsymbol{S_-}}\right)\right] + \frac{\boldsymbol{c_{add}} + \boldsymbol{C_{bop}}}{\boldsymbol{t_d}} \quad \textbf{(2.23)}$$

Where P_0 is the price of the installed energy storage system in dollars, E_d is discharged energy in kW h, c_a is the reactor cost per unit area in \$ m^{-2}, c_{bop} is the cost for balance-of-plant components, including power conditioning equipment, controls, sensors, pumps, pipes, fans, filters, valves, and heat exchangers, in \$ kW^{-1}, c_{add} is the addition to the capital cost to reach the system price in \$ kW^{-1}, t_d is the discharge time of the battery in h, $c_{m,i}$ is the cost per unit mass of electrolyte species i in \$ kg^{-1}, $\varepsilon_{sys,d}$ is an efficiency that accounts for losses associated with auxiliary equipment, including power conversion, electrolyte pumps, and heat exchanger fans, during discharge. The subscripts + and − denote the positive and negative active species, and the subscripts e+ and e− refer to the positive and negative electrolytes, m_+ is the mass of positive active species required to charge the battery, M_+ is the molecular weight, s_+ is the stoichiometry of the positive active species in the energy storage reaction, n_e is the number of electrons, F is the Faraday constant, and χ is the allowable state of charge (SOC) range. Moreover, the solubility of a redox species is typically a function of oxidation state. $\varepsilon_{q,rt}$. Is the round-trip coulombic efficiency, U corresponds to the thermodynamically reversible or open-circuit potential, and R is the area-specific resistance (ASR) in Ω cm^2. The ASR includes ohmic losses in the bipolar plates and separator, as well as kinetic, ohmic, and transport losses in the electrodes. The potential intercept and the ASR generally depend on SOC.

The contribution of the reactor to the system cost is a minimum at $\varepsilon_{v,d} = 0.5$ and monotonically increases as $\varepsilon_{v,d}$ either increases or decreases according to **(2.23)**. Practically, the assumption of linear polarization will probably fail at low voltage efficiency as mass-transport effects become more important. The cost of the chemicals is a minimum at $\varepsilon_{v,d} = 1$ and increases monotonically with decreasing $\varepsilon_{v,d}$. There is a voltage efficiency that yields a minimum total price for any set of component cost and performance parameters, according to **(2.23)**. In the limit of long discharge times, the total system price approaches the chemical cost.

The system price is separated into four contributions. The reduction in each of these factors between the reported 2014 minimum price and the projected future state price is shown in **Figure 2.9**. The energy and power costs are related to materials costs, with the quantities determined by the performance of the chemistry and the cell. The balance-of-plant cost, c_{bop}, captures system complexity through purchased items such as heating and cooling equipment, state-of-charge management, power electronics, and pumps if required. The costs of the storage vessels are added to the electrolyte and active materials, because these three costs should scale together with energy. The additional contribution to price, c_{add}, captures the manufacturing cost, sales, general costs, administration costs, research and development costs, and profit quantities necessary to mark up the materials cost to a system price. The 2014 c_{add} estimates were found by subtracting the material and purchased items costs from battery prices reported in the literature, after correcting for any installation costs.

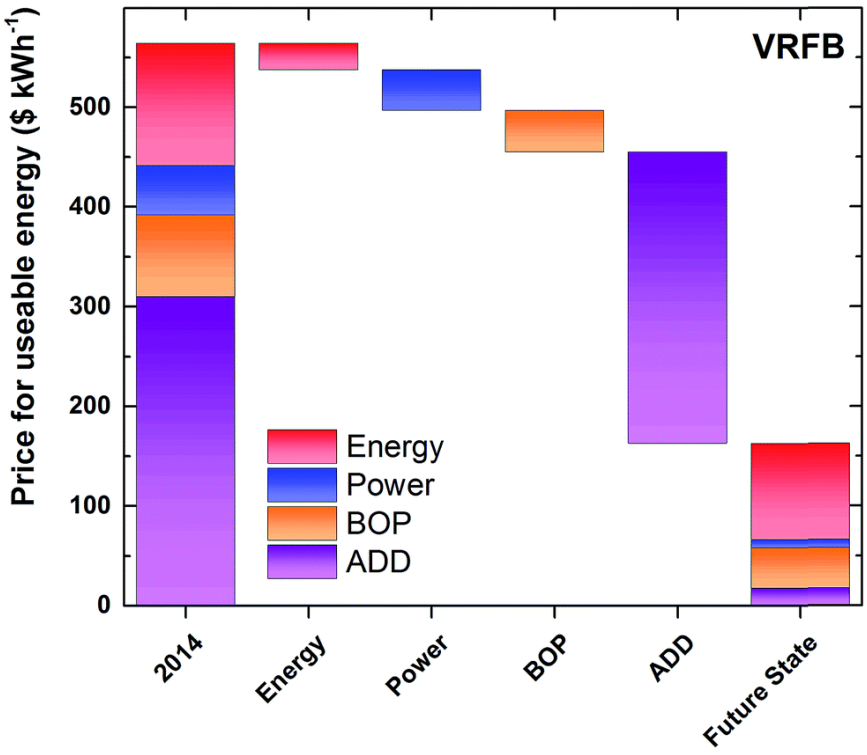

Figure 2.9. – Plot for VRFB illustrating a potential pathway to reach cost effective energy storage. Where, balance of plant (BOP) is equivalent to c_{bop} on an energy basis. The largest decrease occurs in the additional contributions to price factor (ADD) that encompasses depreciation, overhead, labor, etc[152].

The largest decrease in total system price for VRFBs is the result of smaller c_{add} values. The 10 GW h production scale considered in this analysis has the potential to enable this dramatic cost reduction[150]. The future value of c_{bop} and c_{add} are highly uncertain, but are included in an attempt to close the gap between material costs and the total equipment cost realized by the owner of the energy storage system. More importantly, these values demonstrate the dramatic lowering of price contributions that must occur to reach long-term goals. Competitive pressures, benefits from scale, and benefits from learning by doing will all be driving forces for these projected cost reductions. Whether or not the assumed values are reached depends on both the existence of a profitable energy storage market that utilizes the chemistry in question and the quality of the engineering estimates.

Table 2.1 – Performance and cost parameters required to meet cost effective energy storage.

	U_{ave} / V	**ASR / Ω cm^2**	**Equivalent weight / g (mol e−)$^{-1}$**	**Solubility mass basis / kg kg^{-1}**	**Solubility molar basis / mol L^{-1}**	**Material c_m / \$ kg^{-1}**	**Electrolyte c_e / \$ kg^{-1}**
Aqueous	1.5	0.5	150	0.05	~1–2	5	0.1

Materials-level performance and cost requirements are presented in **Table 2.1**. Electrolyte platforms would benefit from tailored molecules with low equivalent weights, fast kinetics, and cell voltages that stretch the electrolyte stability window. The active material and electrolytes must both be inexpensive. Aqueous electrolytes must be almost free. The concentration of active material targeted is 2 mol L^{-1} at least, for aqueous systems.

3 Experimental Methodology

The aim of this chapter is to give a general overview of the specific experimental methods and tools employed within the thesis dissertation, emphasizing their interest in the previous chapters. The main experimental setups shown herein are the synthetic methods with their prior and afterwards treatments, the electrochemical measurements setups and methods, as well as devices used in the process.

3.1 Felt treatments

First of all, in order to activate the carbon based, graphite felt (GF) or carbon felt (CF), electrode surface it is always pre-treated in a plasma device using oxygen atmosphere for a two steps of 10 min for each electrode face, labeled as GF/CF-HT (**Figure 3.1 i)**). Next, depending upon the process there are different synthetic methods.

Simultaneously, samples of PAN-based graphite felt (Beijing Great Wall) are thermally treated under NH_3/O_2 atmosphere (1:1) at 500ºC for 24-h using a tubular furnace. Here after, ammoxidized graphite felt ($GF_{ammoxidized}$) is used as the notation for the modified electrodes. After the treatment, the samples were cooled down under vacuum before carrying out the measurements.

3.2 Synthesis methods

Subsequently, several synthesis steps are done in order to modify the electrodes for MFRFBs. Initially, it is done a hydrothermal synthesis step introducing 1 mg/mL of graphene oxide (GO) in deionized water and then heated at 80ºC overnight (12 hours) (**Figure 3.1 ii)**). After, the electrodes are rinsed in water and dry at 60ºC. Next, a consecutive hydrothermal step introducing 1 mg/mL of p-hydroquinone in deionized water and heated at 80ºC for 10 hours (**Figure 3.1 iii)**). In parallel, another treatment is introducing the felt electrode into a hydrothermal reactor containing HNO_3 (1:1) in water miliQ (**Figure 3.1 iv)**). After, it is rinse in water and dried at 60ºC, as well as the prior described synthesis.

Furthermore, same felt after the synthesis with GO to form CF-rGO it is placed into another hydrothermal reaction in a reactor containing 2mg/mL of glycerol in water miliQ and heated at 80ºC overnight (12 hours) to follow same conditions as iii) in (**Figure 3.1v**). It is done to compare the electrodes CF-rGO/Q and CF-rGO/ROH.

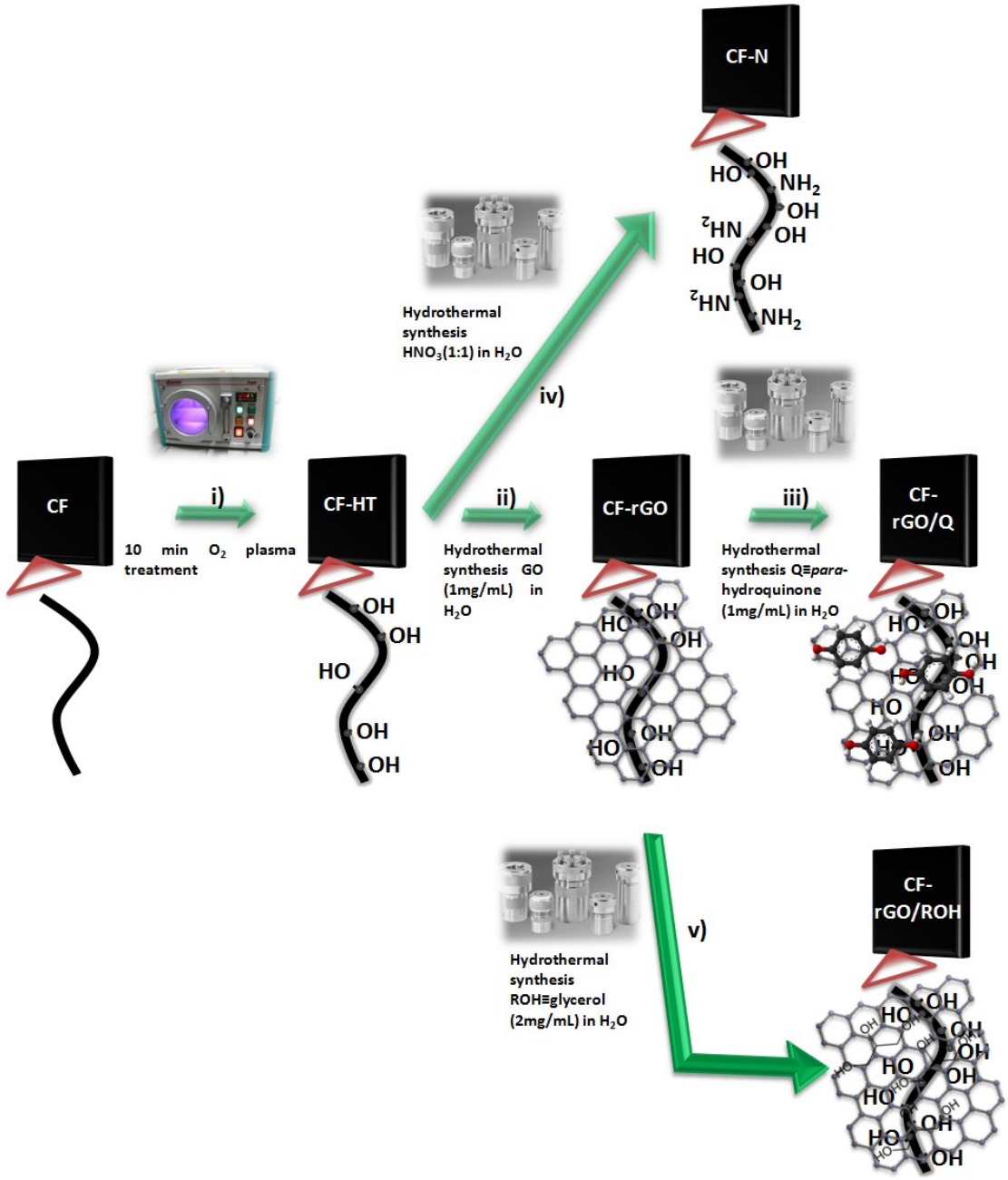

Figure 3.1. - Scheme of electrode synthesis processes over carbon felt (CF) **i)** oxygen plasma treatment. **ii)** Hydrothermal synthesis placing CF 1mg/mL in the reactor in H_2O as solvent at 80ºC for12h. **iii)** Hydrothermal synthesis to deposit p-hydroquinone over the GF-rGO material using same reaction conditions as last step. **iv)** Hydrothermal synthesis taking GF-HT and introducing in solution HNO_3:H_2O (1:1) for 12h at 80ºC. **v)** Hydrothermal synthesis taking $GF_{activated}$ or GF-HT and introducing a linear alcohol chain (ROH) as glycerol to deposit analogously to the step iii) for 12h at 80ºC.

3.2.1 TiO_2 synthesis

An initial optimization synthesis is done placing 2 pieces of 4 cm^2 graphite felt electrodes, which are previously treated for 10 min each side in an O_2 plasma chamber, inside an hydrothermal reactor containing a water-hydrochloric acid (1:1)

solution. The concentration of the precursor (titanium terc-butoxide) into the reactor for the synthesis is increased, adding 1, 2 and 5 mL. It is observed a structural variation for the electrodes, labelled as GF-TiO_2 (NPs), GF-TiO_2 (SNRs) and GF-TiO_2 (MNRs) for 1, 2 and 5 mL used as precursor respectively.

Thereafter, rutile TiO_2 nanorods have been directly grown over a plasma treated (GF-HT) commercial graphite felt (GF, 4 cm^2 and 5 mm thickness from Mersen S.A., Spain) using a hydrothermal process. The titanium precursor, 5 ml of titanium butoxide, is added into a 60 ml of 1:1 (v:v) (HCl:H_2O) solution. The obtained mixed precursor solutions and GFs were placed in a Teflon-sealed autoclave (100 ml, Parr Instrument Co.) and heated up at 100ºC. After the synthesis, a white solid precipitate was observed over the surface of GF. The as-prepared samples are cleaned by immersion in water and dried in a vacuum oven at 60ºC overnight (**Figure 3.2 i)**).

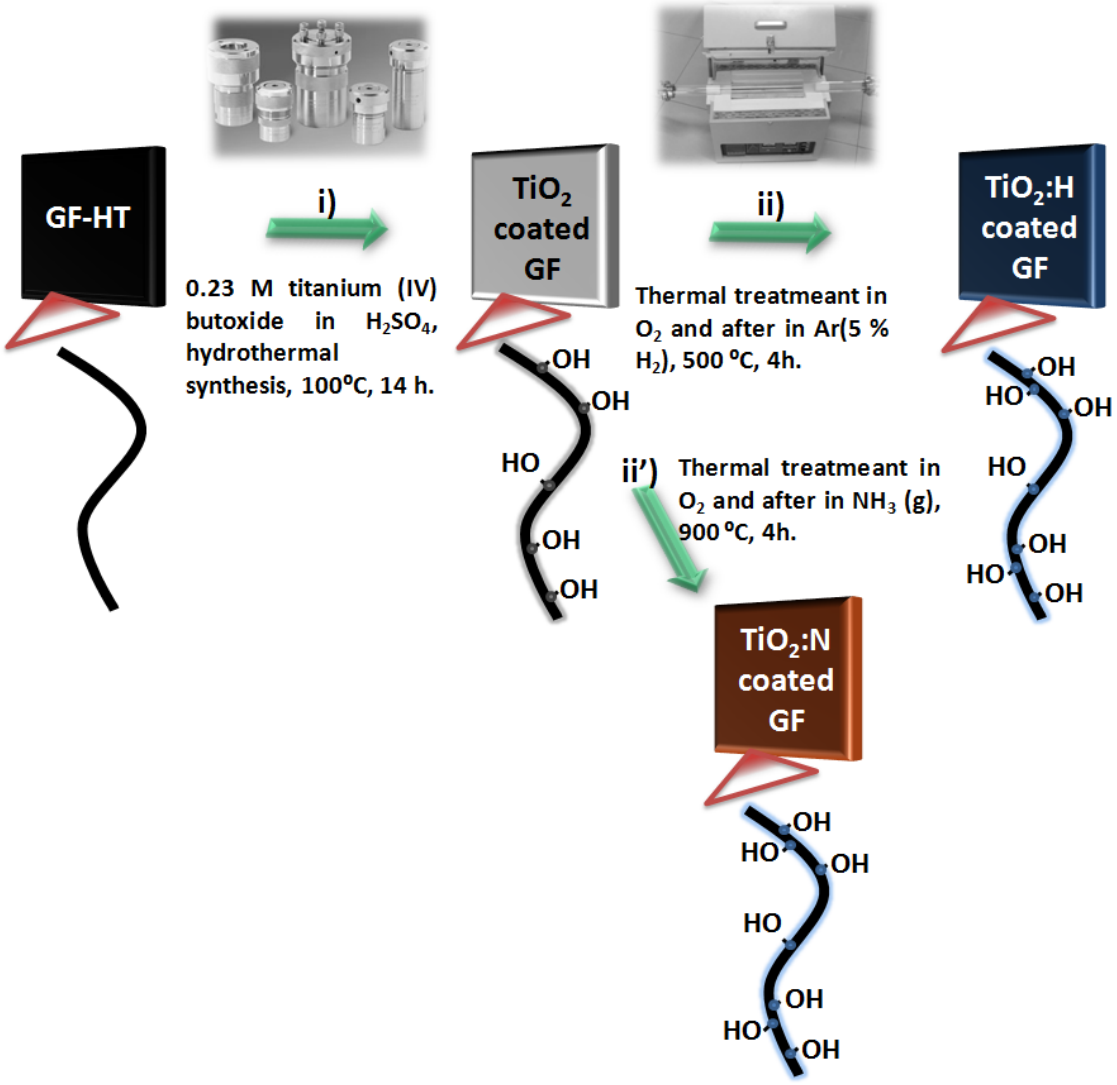

Figure 3.2. - Scheme of electrode synthesis processes over graphite felt (GF) **i)** Hydrothermal synthesis in 0.23M titanium terc-butoxide in HCl (1:1) in water at 100ºC for 14h. **ii)** Thermal treatment of GF@TiO_2 electrode initially in oxygen atmosphere and afterwards in Ar (5%H_2) at 500ºC for 4 hours each step. **ii')** Thermal treatment of GF@TiO_2

electrode initially in oxygen atmosphere and afterwards in NH_3(g) at 900ºC for 4 hours each step.

Additionally, this synthesis method does not imply toxic chemicals and is well-suited for large scale applications. The direct growth of TiO_2 nanorods avoids the use of binders to immobilize the electrocatalyst which can suffer from deactivation, while favouring the direct transfer of electrons to the electrode.

3.2.1.1 Defective TiO_2

Afterwards, the sample is annealed in oxygen atmosphere for 4 h at 500ºC in order to remove chlorine impurities. This sample is labelled as GF@TiO_2 electrode. Finally, the sample is treated in the presence of 5% hydrogen in argon atmosphere. In this case, the colour of the sample changed to blue after hydrogen thermal treatment, indicating a change in the electronic configuration of the metal oxide due to a partial reduction of it (**Figure 3.2 ii**). This new electrode was labelled as GF@TiO_2:H.

3.2.1.2 Nitrided TiO_2

Nitrided TiO_2 nanorods have been directly grown over a commercial carbon felt (CF, 4 cm^2 and 5 mm thickness from Mersen S.A., Spain) using a hydrothermal process reported above. Afterwards, TiO_2-based electrodes were nitrided by NH_3 gas at several temperatures 500, 700 and 900°C for 14 hours in order to study the reduction of the TiO_2 to TiN (**Figure 3.2 ii'**). The samples were labelled as CF@TiO_2N500, CF@TiO_2N700 and CF@TiO_2N900 electrode, respectively.

3.2.2 CeO_2 synthesis

Ceria have been directly deposit as an homogeneous 100 nm film over a plasma treated (GF-HT) commercial graphite felt (GF, 4 cm^2 and 5 mm thickness from Mersen S.A., Spain) using an Atomic Layer Deposition (ALD) technique (**Figure 3.3 i**). The prepared samples were thermally treated under reductive conditions (Ar/H_2 5% for 4h at 500°C) to allow the formation of GF@CeO_{2-x} (**Figure 3.3 ii**).

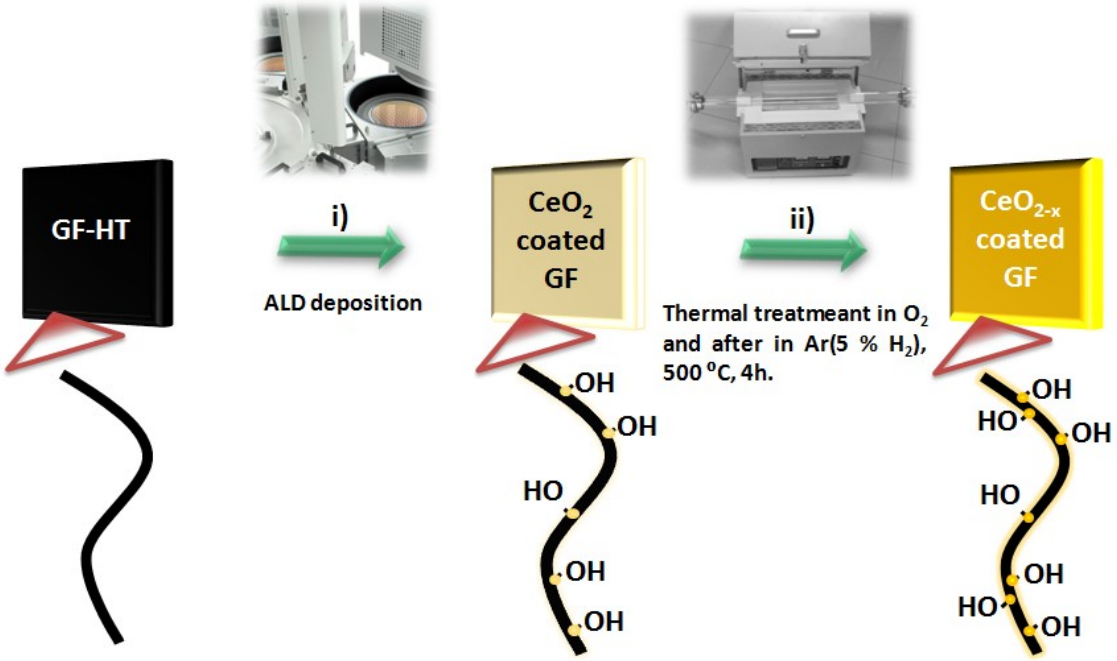

Figure 3.3. – Scheme of electrode synthesis processes over plasma treated graphite felt (GF-HT). **i)** Atomic layer deposition process for CeO_2 of 100 nm thickness. **ii)** Thermal treatment of GF@CeO_2 electrode initially in oxygen atmosphere and afterwards in Ar (5%H_2) at 500ºC for 4 hours each step.

3.3 Membrane pretreatments

The membrane used for all the experiments is Nafion 117; therefore the treatment following described is especially for this material (**Figure 3.4**). Nafion is initially cut into squares to handle it better. After, it is peeled off the thin backing layer, then dunk in water to separate the Nafion from the thick coversheet. Consequently, it is boiled at a temperature of 80ºC for 1 hour in 3% H_2O_2. Afterwards, rinsed in deionized water and boiled at 80ºC for 2 hours in H_2O. Finally, it is boiled at same temperature (80ºC) for 1 hour in 0.5M H_2SO_4 solution and rinsed several times in lightly boiling (80-90ºC) deionized water. It is always stored in deionized water.

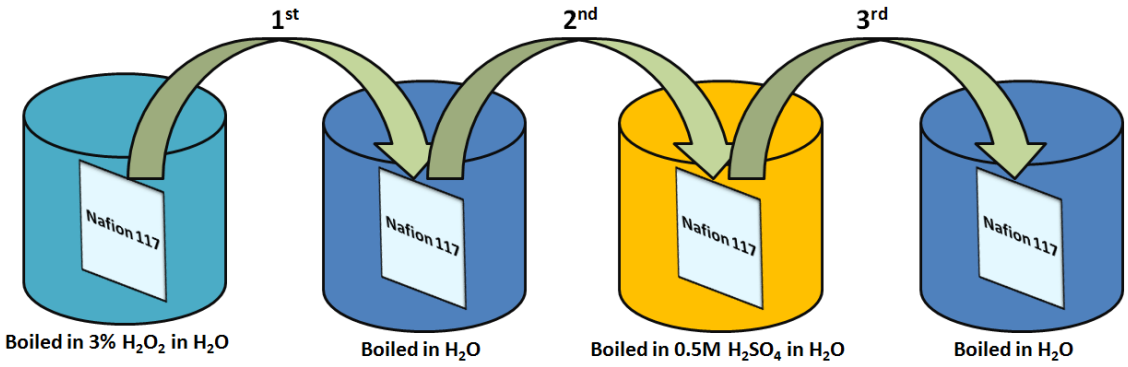

Figure 3.4. – Consecutive step processes that compose the Nafion membrane pretreatment.

3.4 Three electrode system configuration

A three-electrode glass cell is used to carry out fundamental electrochemical studies (**Figure 3.5**). As-prepared electrodes (0.25 cm^2) are used as working electrodes, platinum wire or 5 cm^2 carbon felt as counter electrode, and Hg/Hg_2SO_4 as commercial reference electrode. Nitrogen gas is used to deoxygenate the electrolyte. Electrochemical measurements are done with a Biologic® VMP-3 multi-potentiostat controlled by EC-lab® software. The hydrogen-evolution reaction of all electrodes studied is evaluated using linear sweep voltammetry (LSV) at different scan speed in 1M H_2SO_4. The electrocatalytic reaction of the all electrodes towards negative reaction in VRFB was measured by cyclic voltammetry (CV) at different scan rate in 0.05 M V^{3+} and 1 M H_2SO_4. The electrocatalytic reaction of the all electrodes towards positive reaction in VRFB was measured by cyclic voltammetry (CV) at different scan rates, from 50 to 1 mVs^{-1}, in 0.5 M VO^{2+} and 3 M H_2SO_4. Electrochemical impedance spectroscopy (EIS) spectra containing 0.05 M vanadium species in 1 M sulfuric acid (PEIS -0.26 *V* vs. SHE) was done at a frequency from 100 *mHz* to 200 *kHz*. Tafel (seen Appendix 9.1.2.3.1) measurements are done in Potentiostatic conditions in a 50% SoC V^{3+}/V^{2+} and 1 M H_2SO_4 solution. Moreover, Randles-Sevcik equation (seen Appendix equation **(9.54)**) is used to obtain the electrodes-electrolyte mass transfer tendencies.

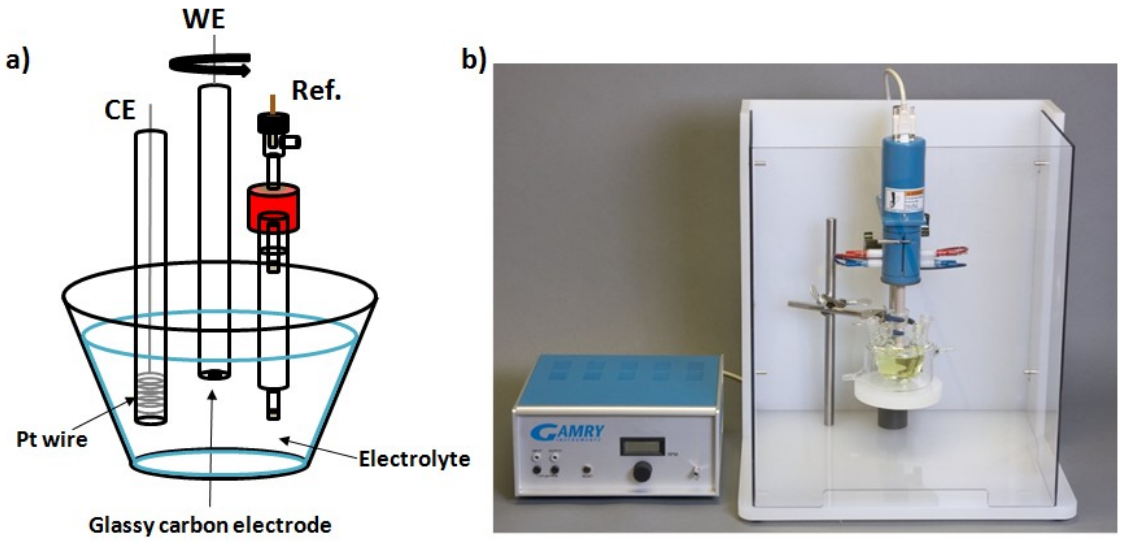

Figure 3.5. – a) Scheme of a three electrode system. **b)** Picture of the three electrode device used in our laboratory.

Analogously, for aqueous organic redox flow systems a three-electrode glass cell is used to carry out fundamental electrochemical studies (**Figure 3.5**). As-prepared electrodes (0.25 cm^2) are used as working electrodes, 5 cm^2 carbon felt as counter electrode, and Hg/Hg_2SO_4 as commercial reference

electrode. Nitrogen gas is used to deoxygenate the electrolyte. Electrochemical measurements were done with a Biologic® VMP-3 multi-potentiostat controlled by EC-lab® software. The electrocatalytic properties of the all electrodes towards positive reactions, as well as negative reactions in aqueous organic redox flow batteries were measured by cyclic voltammetry (CV) at different scan rate in 0.05 M active material and 3 M $MeSO_3H$.c Electrochemical impedance spectroscopy (EIS) spectra containing 0.05 M of quinone species in 3 M methanosulfonic acid was done at a frequency from 100 *mHz* to 200 *kHz*. Moreover, Randles-Sevcik equation is used to obtain not only the mass transfer relationship, but also the apparent constant coefficient using in both cases the same experimental conditions as CV. Last, but not least treated electrodes are studied in galvanostatic conditions using Hg/Hg_2SO_4 reference electrode and a much larger area of GF-P as a counter electrode in 0.05 M Tiron and 3 M $MeSO_3H$. into a 0.05M quinone solution in 3M methanosulfonic acid at different current densities, from 2.5 to 75 $mAcm^{-2}$, in order to study their capacity and efficiency performance towards the aqueous organic redox reactions..

3.4.1 Rotating disk set-up

A three-electrode glass cell is used to do fundamental electrochemical studies (**Figure 3.6**). Deposited Glassy Carbon (GC; 0.196 cm^2) is used as working electrodes, platinum wire as counter electrode, and Hg/Hg_2SO_4 as reference electrode. Nitrogen gas is used to deoxygenate the electrolyte. Electrochemical measurements were carried out with a Biologic® VMP-3 multi-potentiostat controlled by EC-lab® software. The electrocatalytic reaction of the all electrodes towards positive reaction in VRFB is measured by cyclic voltammetry (CV) between cut-off voltages of 1.4 and -1 V at different scan rates (50-1 mVs^{-1}) in 0.5 M VO^{2+} and 3 M H_2SO_4, in order to apply the Randles-Sevcik equation (seen Appendix equation **(9.54)**) to obtain the diffusion coefficient. Moreover, in order to get the kinetic constant values applying *Koutecký-Levick* equation (seen Appendix 9.3.1.1). It is done a linear sweep voltammetry changing the working electrode (GC) rotation speed (100-2500 rpm), between 0.3 and 1.1 V at 5 mVs^{-1} scan speed.

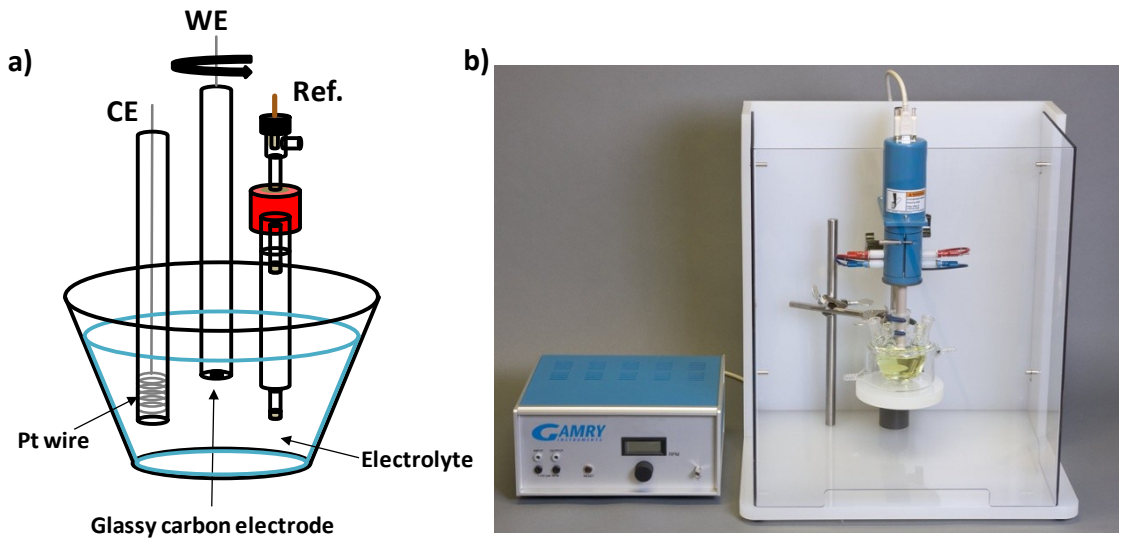

Figure 3.6. – a) Scheme of a Rotating disk electrode system. **b)** Picture of the rotating disk electrode used in our laboratory.

3.4.2 Electrode's electrical measurement

The **Figure 3.7** shows the schematic single cell assembly, which is composed of two plastic end plates, two copper current collectors in contact with the graphite current collectors and with the electrode compressed a 30% in between them. All the system is prepared to measure the electrical resistance of the electrodes synthesized in the section regarding TiO_2:H.

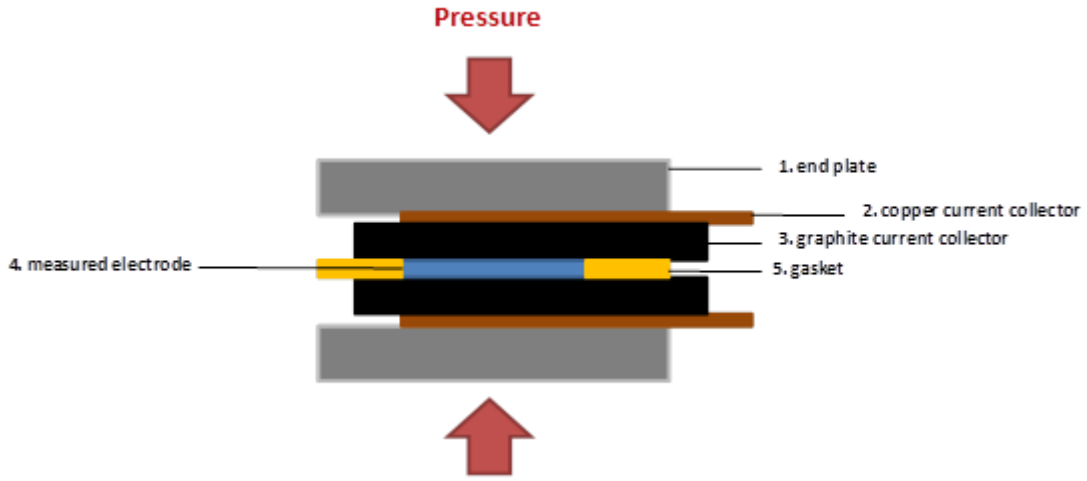

Figure 3.7. - Cell scheme employed to measure the electrode's electrical resistance.

3.5 Single cell device set-up

The electrolytes are prepared by dissolving 1, 1.6 and/or 2 M vanadium ions (Alfa Aesar) in 3 M H_2SO_4 (Aldrich, 98%) solutions. The corresponding anolytes and catholytes can be prepared through an electrochemical process. The VRFB single-cell performance was measured using an in-house designed flow cell system, which has been described in **Figure 3.8**Error! Reference source not found.. The single-cell used was assembled sandwiching the membrane Nafion® 117 (6cm × 6cm) between two pieces of working electrodes with an area of 4 cm^2, approximately compressed a 30%. Each electrode in their half-cell is placed in a groove on outer face of the graphite bipolar plates which are etched with 3 serpentines flow fields with diameter of 2 mm. The inner faces of the bipolar plate are deposited a sputtered layer of copper such as current collector. Viton® gasket is used to avoid the electrolyte leakage. Metallic aluminium end-plates are used to close the cell. In order to investigate the effect of several modifications on the carbonaceous felt, different materials have been used as negative and positive electrodes. The single-cell is connected to two glass reservoirs containing 20 mL catholytes and anolytes, respectively. The flow rate at each side is 10 mL min^{-1} and the negative reservoir was continuously purged with nitrogen to avoid any oxidation of the active species. The flow cell was charged up to 1.8 V and then discharged to 0.8 V, at different current densities, from 12.5 to 350 $mAcm^{-2}$. Even more, the single cell includes a reference "*in-house*" electrode, Ag/Ag_2SO_4. It is included in between the two porous carbon electrodes to follow the reactions on the positive and negative side independently. The performance evaluation method for the VRFB is mainly determined by the following efficiencies: 1) Coulombic efficiency (CE), the ratio of the average discharging capacity to the average charging capacity, 2) Voltage efficiency (VE), the ratio of the average discharging voltage to the average charging voltage, (3) Energy efficiency (EE), VE multiplied by CE/100. According to Faraday's law, the theoretical capacity in VRFB was calculated, for example, attaining a value of 536 mAh or 13.4 AhL^{-1} for a 1 M vanadium ions concentration, respectively. The theoretical capacity expressed in Ah L^{-1} has been calculated taking into account the total volume of the tanks (i.e. 40mL). Additionally, power test were done applying pulsed discharge current during 60 seconds also recording the potential of the cell, as well as, monitoring the potential at E_{ocv} after the mentioned pulse.

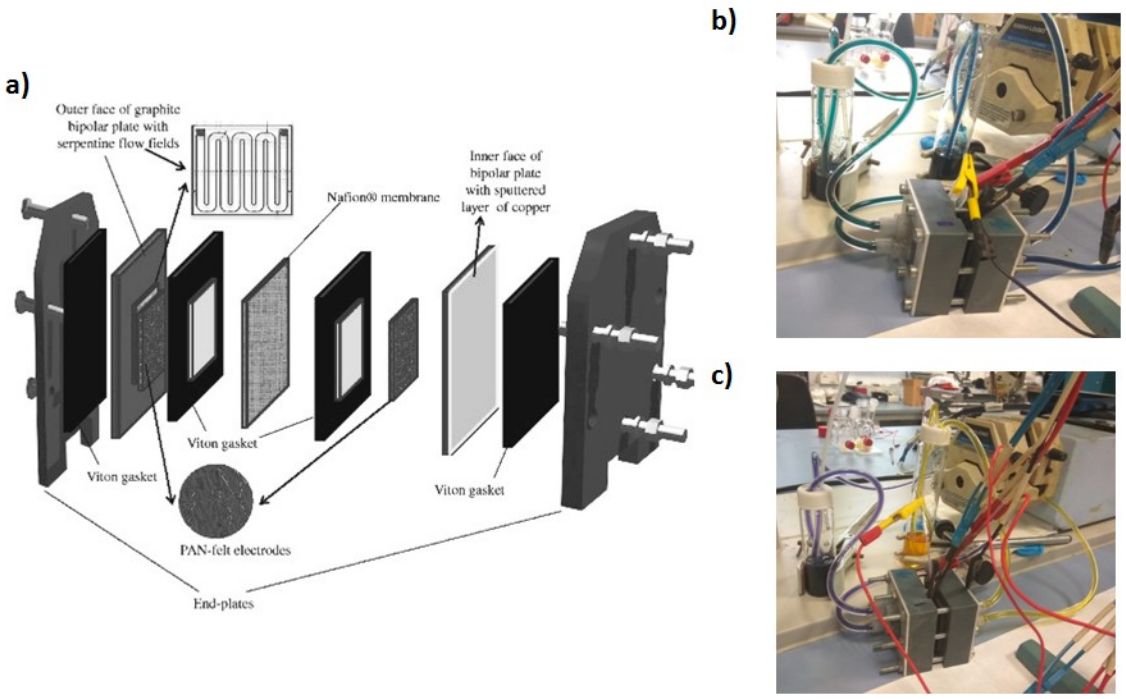

Figure 3.8. – a) Scheme of a single cell system showing each of the parts separately. **b)** Picture of the whole single cell device completely discharged. **c)** Picture of the whole single cell device completely charged.

Furthermore, in case of AORFBs the electrolytes are prepared by dissolving 0.05, 0.3 and/or 0.4 M organic active material (Alfa Aesar) in 3 M $MeSO_3H$ (Aldrich, 99%) solutions. The aqueous organic redox flow single-cell performance was measured using an *"in-house"* designed flow cell system, which has been described in **Figure 3.8**Error! Reference source not found.. The ingle-cell used is assembled sandwiching the membrane Nafion® 117 (6cm × 6cm) between two pieces of working electrodes with an area of 4 cm^2, approximately compressed a 30%. Each electrode in their half-cell was placed in a groove on outer face of the graphite bipolar plates which were etched with 3 serpentines flow fields with diameter of 2 mm. The inner faces of the bipolar plate were deposited a sputtered layer of copper such as current collector. Viton® gasket is used to avoid the electrolyte leakage. Metallic aluminium end-plates were used to close the cell. In order to investigate the effect of several modifications on the carbonaceous felt, different materials have been used as negative and positive electrodes. The single-cell was connected to two glass reservoirs containing 15 or 12.5 mL catholytes and anolytes (**Figure 3.9**), respectively. The flow rate at each side was 75 mL min^{-1} and the negative reservoir was continuously purged with nitrogen to avoid any oxidation of the active species. The flow cell was cycled to 0.8 - 1 V and then discharged to 0 V, at different current densities, 2.5 to 70-25 $mAcm^{-2}$. Even more, a reference "*in house*" electrode, Ag/Ag_2SO_4, is include in between the two porous carbon electrodes to follow the reactions on the positive and negative side independently. The performance evaluation method for Aqueous organic redox flow single cell is mainly determined by the following efficiencies: 1) Coulombic efficiency (CE), the ratio of the

average discharging capacity to the average charging capacity, 2) Voltage efficiency (VE), the ratio of the average discharging voltage to the average charging voltage, (3) Energy efficiency (EE), VE multiplied by CE/100.

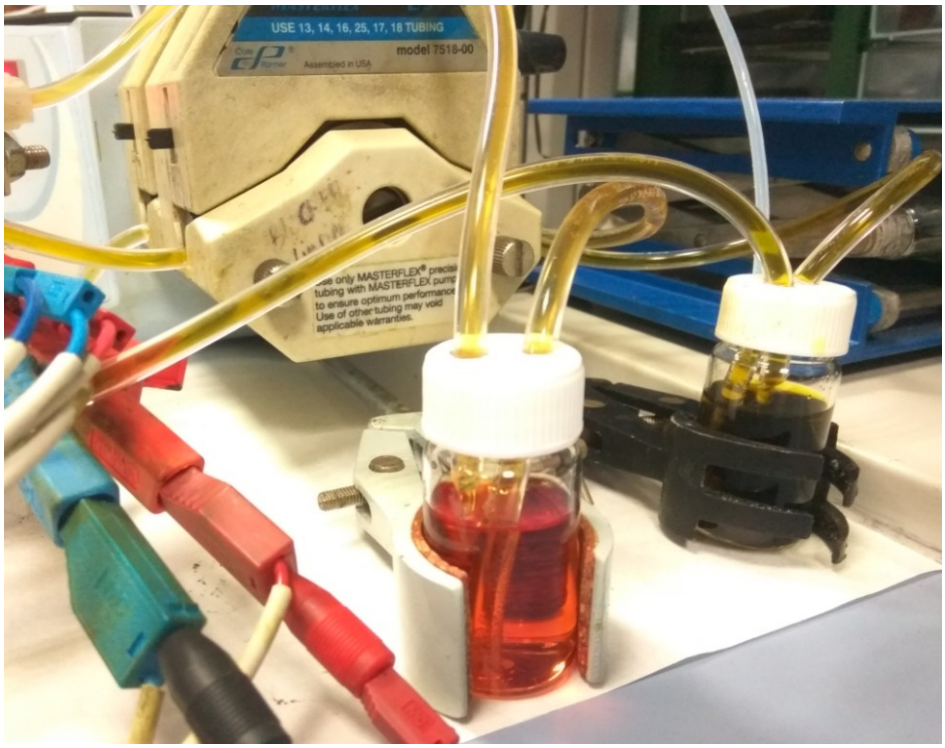

Figure 3.9. – Picture of the AORFBs reservoirs completely charged.

3.6 Characterization techniques

Along the thesis Research many techniques were used in order to obtain some information and elucidate the reason for the electrochemical experimental outcomes, especially for the electrodes implemented after the previously explained synthesis processes. The techniques are following numbered and briefly explained:

3.6.1 "In-operando" reference electrode

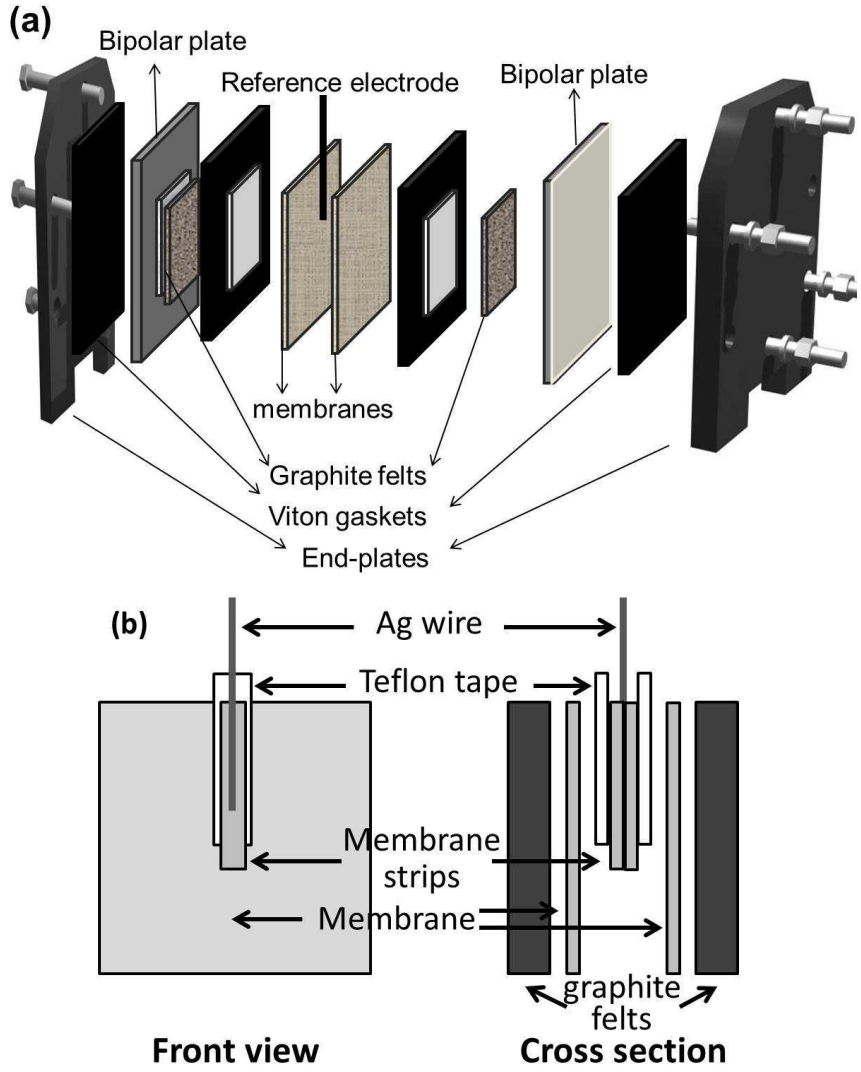

Figure 3.10. –Scheme of **a)** a filter press cell and **b)** the proposed reference electrode.

The reference electrode consisted of a silver wire, two pieces of ion-exchange membrane and two pieces of Teflon tape (**Figure 3.10b**). The silver wire was sandwiched between two rectangular pieces of membrane. Some drops of 3 M sulfuric acid were added to ensure good wettability. The stack formed by membrane/Ag wire/membrane was again sandwiched between two pieces of Teflon tape. Teflon is highly hydrophobic and, thus, it acted as physical barrier and maintained our reference electrode separated from the solution. The bottom of the membrane was not covered by the Teflon to allow ionic contact between the Ag wire and the solution. In absence of the membrane pieces, the Ag wire remains ionically insulated from the solution. The Teflon pieces are employed to prevent any possible diffusion of Ag_2SO_4 through the thin membrane (50 mm of thickness). The

reference electrode composed of Teflon/membrane/Ag wire/membrane/Teflon was inserted between the two membranes that separate the positive and negative electrodes. The rest of the cell was assembled as any filter press VRFB [153] (**Figure 3.10a**). The silver wire was slightly oxidized to obtain a thin layer of silver sulfate by applying 1 mA for 1 min in the assembled cell.

3.6.2 UV-visible spectroscopy

UV-vis spectroscopy refers to absorption spectroscopy or reflectance spectroscopy in the ultraviolet-visible spectral region. This means it uses light in the visible and adjacent ranges. The absorption or reflectance in the visible range directly affects the perceived color of the chemicals involved. In this region of the electromagnetic spectrum, atoms and molecules undergo electronic transitions from the ground state to the excited state.[154] By this technique, UV-vis Absorption for some modified electrodes have been measured in order to study their structural changes.

Figure 3.11. – Picture of the UV-visible spectrometer Perkin-Lambda 950.

3.6.3 Scanning electron microscope

The scanning electron microscope (SEM) uses a focused beam of high-energy electrons to generate a variety of signals at the surface of solid specimens. The signals that derive from electron-sample interactions reveal information about the sample including external morphology (texture), chemical composition, and crystalline structure and orientation of materials making up the sample. In most applications, data are collected over a selected area of the surface of the sample, and a 2-dimensional image is generated that displays spatial variations in these properties. Areas ranging from approximately 1 cm to 5 microns in width can be imaged in a scanning mode using conventional SEM techniques (magnification ranging from 20X to approximately 30,000X, spatial resolution of 50 to 100 nm).

By this technique, several modified electrodes deposits have been pictured in order to see their grain size, morphology and structure. The SEM is also capable of performing analyses of selected point locations on the sample; this approach is especially useful in qualitatively or semi-quantitatively determining chemical compositions (using EDS).

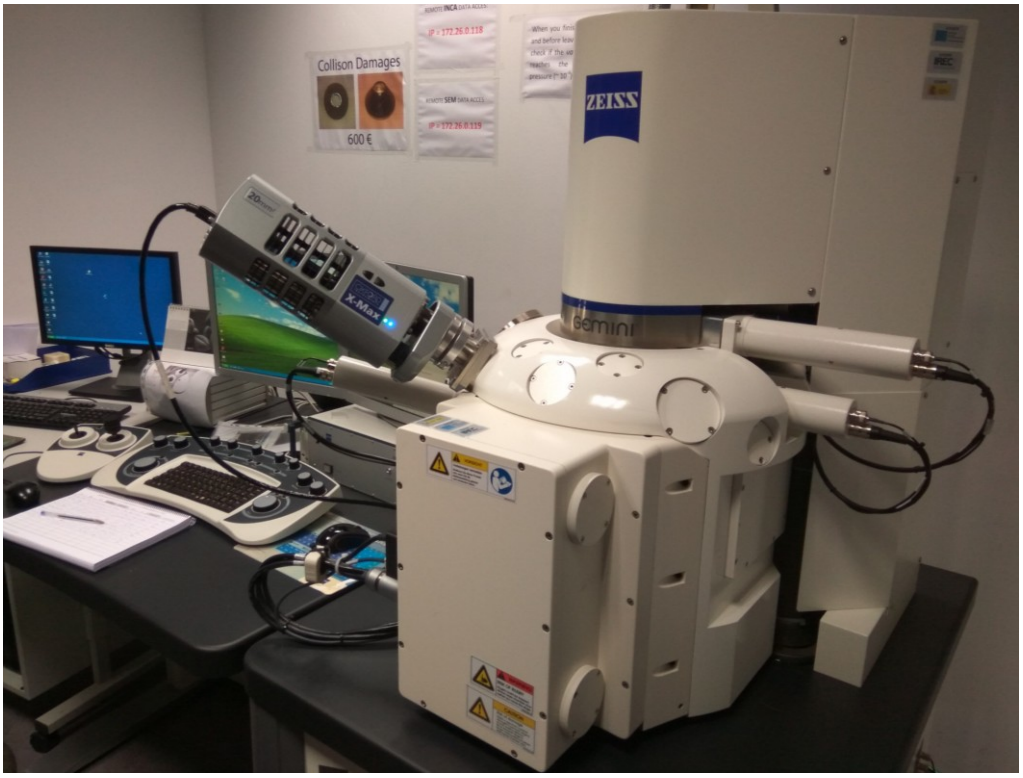

Figure 3.12. – Picture of the scanning electron microscope Zeiss Serie Auriga FESEM.

3.6.4 X-ray diffraction

X-ray diffraction (XRD) is now a common technique for the study of crystal structures and atomic spacing. X-ray diffraction is based on constructive interference of monochromatic X-rays and a crystalline sample. These X-rays are generated by a cathode ray tube, filtered to produce monochromatic radiation, collimated to concentrate, and directed toward the sample. The interaction of the incident rays with the sample produces constructive interference (and a diffracted ray) when conditions satisfy Bragg's Law ($n\lambda=2d$ sin θ). This law relates the wavelength of electromagnetic radiation to the diffraction angle and the lattice spacing in a crystalline sample. These diffracted X-rays are then detected, processed and counted. By scanning the sample through a range of 2θangles, all possible diffraction directions of the lattice should be attained due to the random orientation of the powdered material. Conversion of the diffraction peaks to d-spacing allows identification of the mineral because each mineral has a set of unique d-spacing. Typically, this is achieved by comparison of d-spacing with standard reference patterns.

All diffraction methods are based on generation of X-rays in an X-ray tube. These X-rays are directed at the sample, and the diffracted rays are collected. A key component of all diffraction is the angle between the incident and diffracted rays. Powder and single crystal diffraction vary in instrumentation beyond this.

Figure 3.13. – Picture of the X-ray diffractometer D8 Advance Bruker.

3.6.5 X-ray photoelectron spectroscopy

X-ray photoelectron spectroscopy (XPS) is a surface-sensitive quantitative spectroscopic technique that measures the elemental composition at the parts per thousand range, empirical formula, chemical state and electronic state of the elements that exist within a material. XPS spectra are obtained by irradiating a material with a beam of X-rays while simultaneously measuring the kinetic energy and number of electrons that escape from the top 0 to 10 nm of the material being analyzed. XPS requires high vacuum ($P \sim 10^{-8}$ millibar) or ultra-high vacuum (UHV; $P < 10^{-9}$ millibar) conditions, although a current area of development is ambient-pressure XPS, in which samples are analyzed at pressures of a few tens of millibar. Using this technique, surface composition of several electrodes is studied including elementary composition and most abundant functional groups.

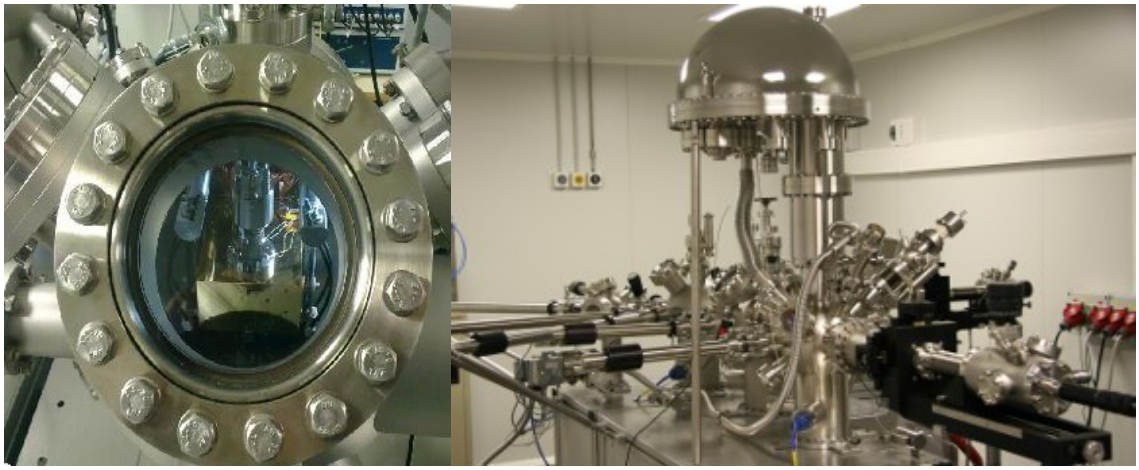

Figure 3.14. – X-ray photoelectron spectrometer SPM 150 Aarhus.

4 Vanadium Redox Flow Batteries: Architecture enhancement

In order to improve the single cell device, where the battery test are going to be done, an "*in-house*" silver-silver sulfate (Ag/Ag_2SO_4) reference electrode is introduce to follow separately the positive and negative redox reactions, and therefore know how each one of the compartment contributes to the whole cell. This allows knowing which half-cell is the limiting factor, when any modification into the battery (electrode, membrane, electrolyte or the cell itself) is done.

4.1 Reference electrode implementation into a single cell for *"in-situ"* measurements

In-depth evaluation of the electrochemical performance of all-vanadium redox flow batteries (VRFBs) under "*operando*" conditions requires the insertion of a reliable reference electrode in the battery cell (**Figure 4.1**). For that purpose, a reference electrode based on silver/silver sulfate is proposed and described for VRFBs. The relevance and feasibility of the information obtained by inserting the reference electrode is illustrated with the study of modified graphite felts as electrodes. In this case, the kinetic of the electrochemical reaction VO^{2+}/VO_2^{+} is slower than that of V^{2+}/V^{3+} at the electrode. While the slow kinetics at the positive electrode limits the voltage efficiency, the operating potential of the negative electrode, which is outside the stability widow of water, reduces the coulombic efficiency due to the hydrogen evolution reaction (HER).

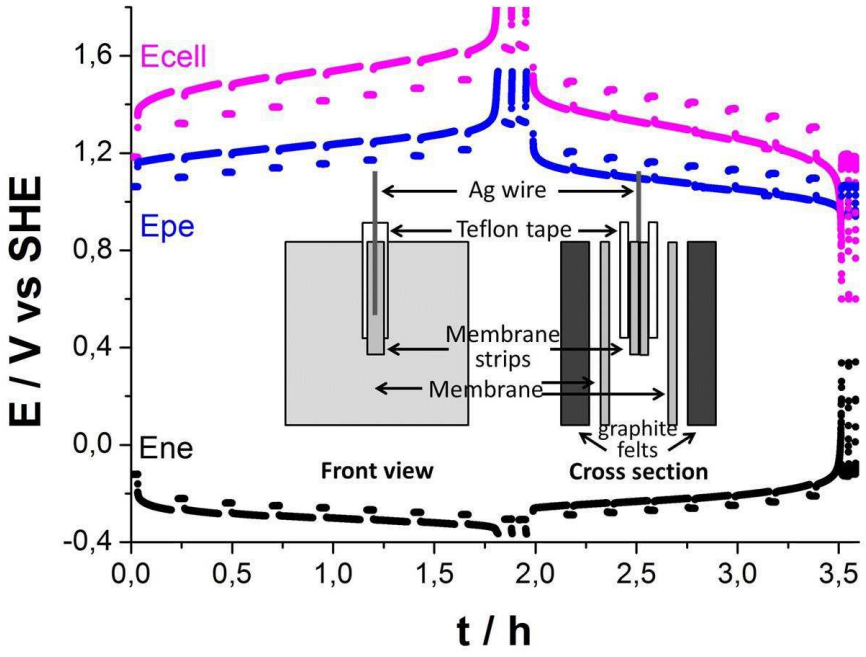

Figure 4.1. – Charge-discharge voltage plot (E_{we}, E_{ce} and E_{cell}) vs. in house Ag/Ag_2SO_4 reference electrode including OCP resting times every 20 minutes.

4.1.1 Electrochemical characterization

In-depth electrochemical evaluation of the electrodes under *operando* conditions is not trivial as it requires the insertion of a reference electrode into the filter press cell. The most widespread strategy is to characterize the electrodes by ex-situ methods in a bulky three-electrode cell prior to the full cell tests. Zawodzinski's group has shown interesting results for carbon paper electrodes by inserting a dynamic hydrogen reference electrode in a filter press cell[155–157]. Here, a reliable reference electrode for the evaluation of VRFBs *"in-operando"* condition illustrate the valuable information obtained with the exemplary case of the evaluation of the electrochemical properties of ammoxidized graphite felts, which contains both oxygenated and nitrogenated groups.

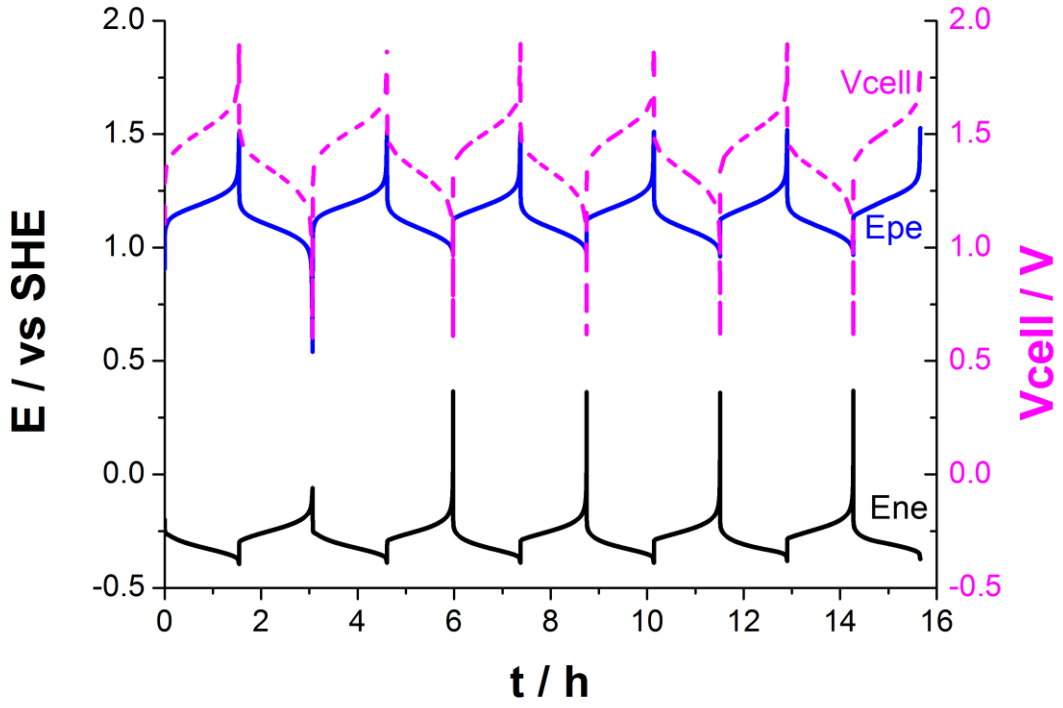

Figure 4.2. –Potential profile of VRFB upon cycling at 20 mA cm^{-2} and 30 mL min^{-1}.

Furthermore, **Figure 4.2** shows the potential profiles of several charge and discharge cycles at 20 mA cm^{-2} and 30 mL min^{-1}. The use of the reference electrode allowed the potential profiles of positive and negative electrode to be monitored separately. The limiting side (positive or negative) can be easily identified, enabling facile balancing of the two electrolytes. In this case, both electrolytes seemed quite balanced. The positive electrode forced the end of the charge while the negative electrode was responsible for the end of the discharge (except for the first cycle). This means that an irreversible reaction (hydrogen evolution) occurred simultaneously to the reduction of V^{3+} at the negative electrode during the charge. As a result, V^{3+} is not entirely reduced to V^{2+}, whereas VO^{2+} is completely oxidized to VO_2^+ forcing the end of the charge. During the discharge, there is not enough

V^{2+} to balance VO_2^+. **Figure 4.2** also reveals that the potential of the reference electrode is stable under operating conditions.

The potential of the electrodes is given by the Nernst equation **(4.1)**, where E^0 is the standard potential, R is the gas constant, T is the temperature, n is the number of involved electrons, F is the Faraday constant and a_{red} and a_{ox} are the activities of the reduced and oxidized species, respectively.

$$\mathbf{E = E^0 - \frac{RT}{nF} \ln \left[\frac{a_{red}}{a_{ox}}\right]} \quad \textbf{(4.1)}$$

The redox reaction of the couple VO^{2+}/VO_2^+ and V^{3+}/V^{2+} are described in **(2.17)** and **(2.18)**, respectively. The potential, versus standard hydrogen electrode (SHE), at the negative and positive electrode are given by **(4.2)** and **(4.3)**, respectively. It shows the potential dependence at the positive electrode (VO^{2+}/VO_2^+) on the protons activity, while the potential at the negative electrode only depend on the activities of vanadium species.

$$\mathbf{E = -0.26 - 0.059 \log \left[\frac{a_{V^{2+}}}{a_{V^{3+}}}\right]} \quad \textbf{(4.2)}$$

$$\mathbf{E = 1.0 - 0.059 \log \left[\frac{a_{VO^{2+}}}{a_{VO_2^+}}\right] + 0.118 \log a_{H^+}} \quad \textbf{(4.3)}$$

At 50% of state of charge (SoC), the potential at the negative electrode is -0.26 V vs. SHE, whereas the potential at the positive electrode is pH-dependent as mentioned. Therefore, the potential of the reference electrode can be determined at open circuit at 50% of state of charge (SoC). The observed value of V^{3+}/V^{2+} of -0.625 V (vs. our Ag/Ag_2SO_4 reference electrode) should be equal to -0.26 V (vs. HER). Inserting these values in **(4.4)**, **(4.5)** and **(4.6)** is obtained. Thus, the potential of the reference electrode is +0.365 V vs. NHE. Note that we represent all potential vs. NHE for easy comparison with other studies. The advantage of a reference electrode inserted in an all-vanadium flow battery is that the potential of the couple at the negative electrode, V^{2+}/V^{3+}, at 50% SoC can be employed as standard for the internal calibration of the reference potential. For every new reference electrode, its potential can be determined following the above described methodology, i.e. the potential of the reference electrode can be calibrated and corrected "*in-situ*". The observed potential of the positive electrode of 1.15 V (vs. HER) is slightly higher than expected due to effects of side processes such as water evaporation or oxygen evolution.

$$\mathbf{E_{ne} = E^0_{V^{2+}/V^{3+}} \text{ ; at } 50\% \text{ SoC}} \quad \textbf{(4.4)}$$

$$\mathbf{E_{ref} - 0.625 = E^{0}_{H_2/H^+} - 0.26} \quad \textbf{(4.5)}$$

$$\mathbf{E_{ref} = E^{0}_{H_2/H^+} + 0.365} \quad \textbf{(4.6)}$$

The stability of the reference electrode is further explored by monitoring the open circuit potential of an all-vanadium redox flow battery at 100% SoC. The voltage profile of the battery ($E_{positive}$ - $E_{negative}$) decreased slightly over time due to the self-discharge of the cell (**Figure 4.3a**), which is obvious by the change in color of the electrolytes. The individual potential of the positive and negative electrode (**Figure 4.3b**) revealed that the potential of the two electrodes evolved in opposite direction; the positive electrode potential slowly decreased while the negative one increased. An overlapped sinusoidal oscillation of potential is observed when magnifying the potential profile of the electrode (**Figure 4.3c**). That oscillation is the noise of the reference electrode because it occurred simultaneously in both electrodes. Therefore, the noise of the potential of the reference is ±10 mV within an interval of ca. 10 h. Because of the low frequency of the noise (10 h), this level of noise is considered to be acceptable for this application, bearing always in mind this limitation when comparing potentials obtained with 10 h difference.

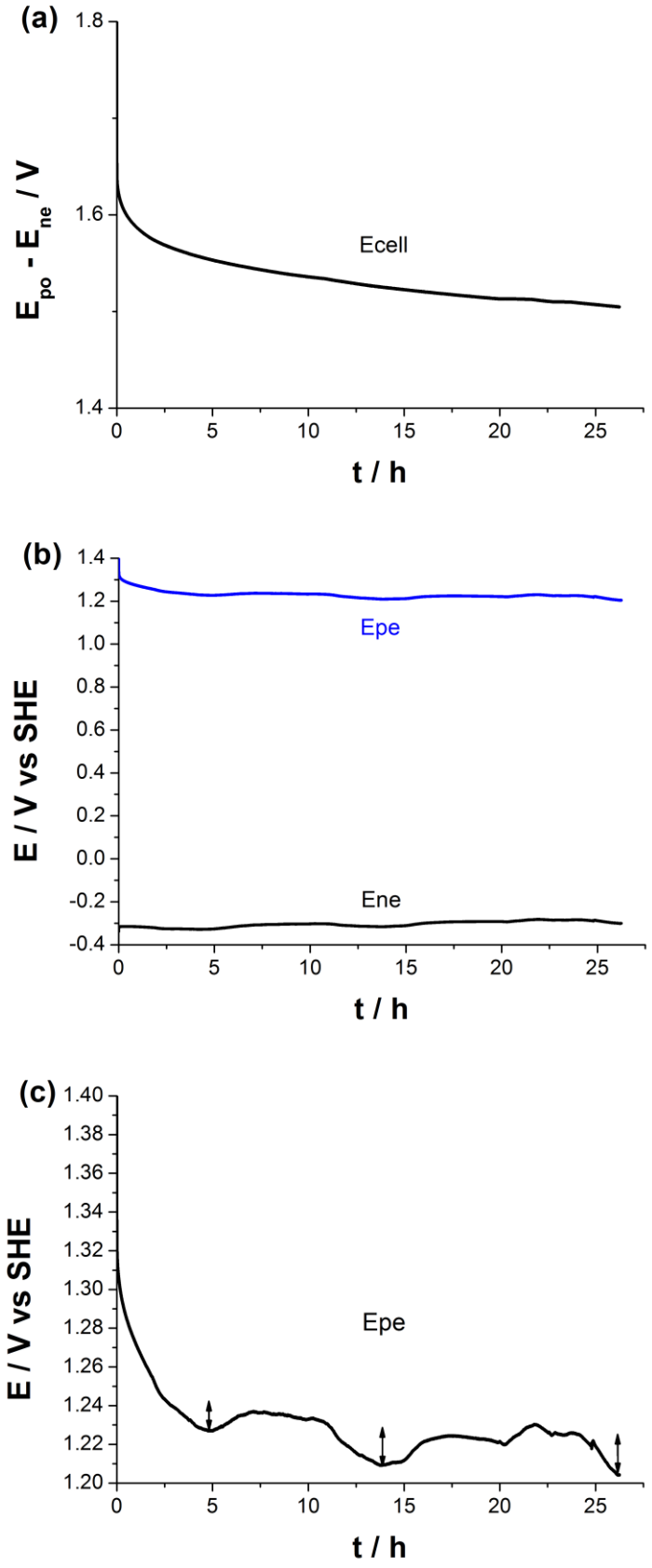

Figure 4.3. –Open circuit potential (OPC) at 100 % SoC of **a)** the battery, **b)** the positive and negative electrode and **c)** the magnification of the positive electrode.

The ionic resistance of the electrolyte between reference electrode and graphite felt was determined by electrochemical impedance spectroscopy. **Figure 4.4** shows the Nyquist plot obtained for the positive (dashed black line) and the negative electrode (solid red line) (in web version). The ionic resistance is given by the Y-interception (imaginary part = 0). A value of 0.05 and 0.04 Ohm were obtained for the positive and negative electrode, respectively. The small values of ionic resistance are due to the large geometrical area of the electrode (25 cm^2). We used these ionic resistance values to correct the current intensity in the follow-up experiments.

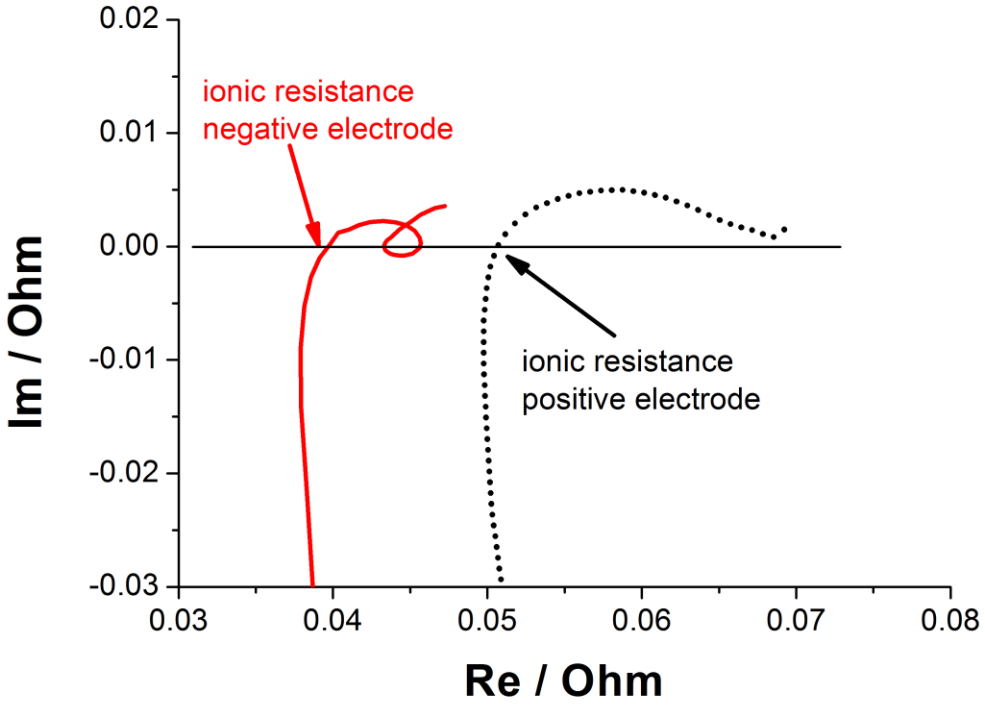

Figure 4.4. –EIS Nyquist plots of the positive (dashed black line) and negative electrode (solid red line) obtained at 50 % of SoC. The frequency range was from 100 KHz - 0.1 Hz.

4.1.2 Single cell evaluation

The kinetics of the electrochemical reactions is evaluated at the positive and negative electrode for VRFB "*in operando*" conditions to illustrate the usefulness of the reference electrode. **Figure 4.5a,** shows the voltage profiles of the cell and potential profiles the positive and the negative electrode at several current densities in a galvanostatic measurement around 50% SoC. The increasing potential with increased current is due to several factors; ionic resistance of the electrolyte, concentration overpotential and electrode kinetics overpotential. The ionic resistance of the electrolyte is corrected with the values obtained by EIS. It is also used a flow as high as 70 mL min^{-1} to minimize the concentration gradients (second factor). Thus, the higher potential for higher current density (**Figure 4.5b**) is significantly affected by the kinetic factor in this case. The potential incremented with increasing current step and it is always larger at the positive electrode. In

addition, the increasing potential with current step increases more rapidly at the positive electrode (**Figure 4.5c**). The difference in the increment of potential between the positive and negative electrode stabilized above 64 mA cm^{-2} indicating that the concentration overpotential dominates at those current densities using a flow speed of 70 mL min^{-1}. The values obtained during the charge were always lower which is more likely due to the evolution of hydrogen and oxygen.

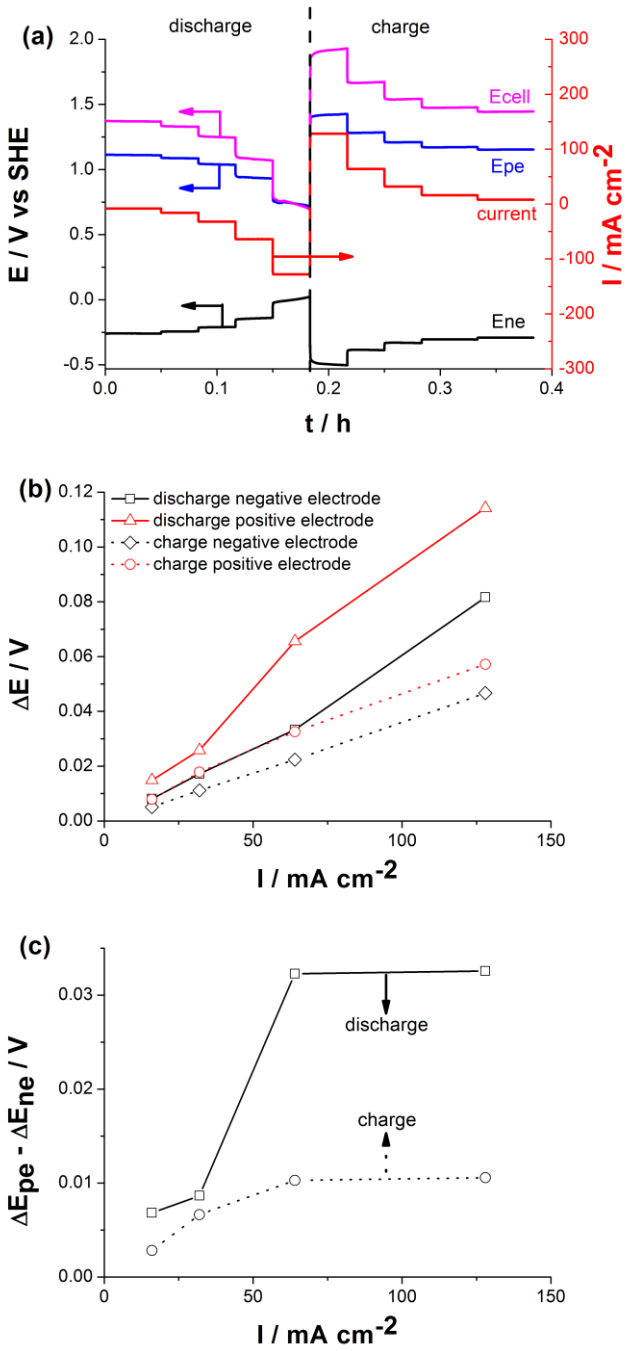

Figure 4.5. –a) Potential profile of VRFB at different current densities (8, 16, 32, 64 and 128 mA cm^{-2}), **b)** iR corrected potential increase observed for each step of current density and **c)** differences between the potential increase of the positive and negative electrode for each current step. SoC and flow were around 50 % and 70 mL min^{-1}, respectively.

Another example of electrochemical evaluation is shown in **Figure 4.6**. Using galvanostatic intermittent titration technique (GITT), the thermodynamic potentials of the positive and negative electrode can be obtained. GITT consists in a galvanostatic charge-discharge measurement during which open circuit is periodically applied. The potential recorded during the open circuit periods exclude the contribution of the ionic resistance and the concentration overpotential as well as electron transfer resistance. In addition, GITT provides values of overpotentials under "*operando*" conditions, which are represented by double arrows in **Figure 4.6a**. This information is very valuable, for example, to fit the theoretical calculation or to determine the overpotentials in the positive and negative electrode at different SoC. For ammoxidized graphite felts, case, it is also observed higher overpotentials at low SoC, although slightly lower values than the simulated ones likely due to the high flow rate used in our study. This fact indicates that there is a small contribution of the concentration on the overpotential at low SoC, even at 70 mL min^{-1} at 20 mA cm^{-2}. It is not observed an increase in overpotential at 87.5% SoC as theoretically predicted by You et al.[158]. The most likely explanation is that the actual SoC was slightly lower than the expected one due to the fast charging rate. More importantly, the overpotentials in the positive side were always significantly higher than those in the negative one, confirming the observations in the previous experiments, i.e. the slower kinetics at the positive electrode.

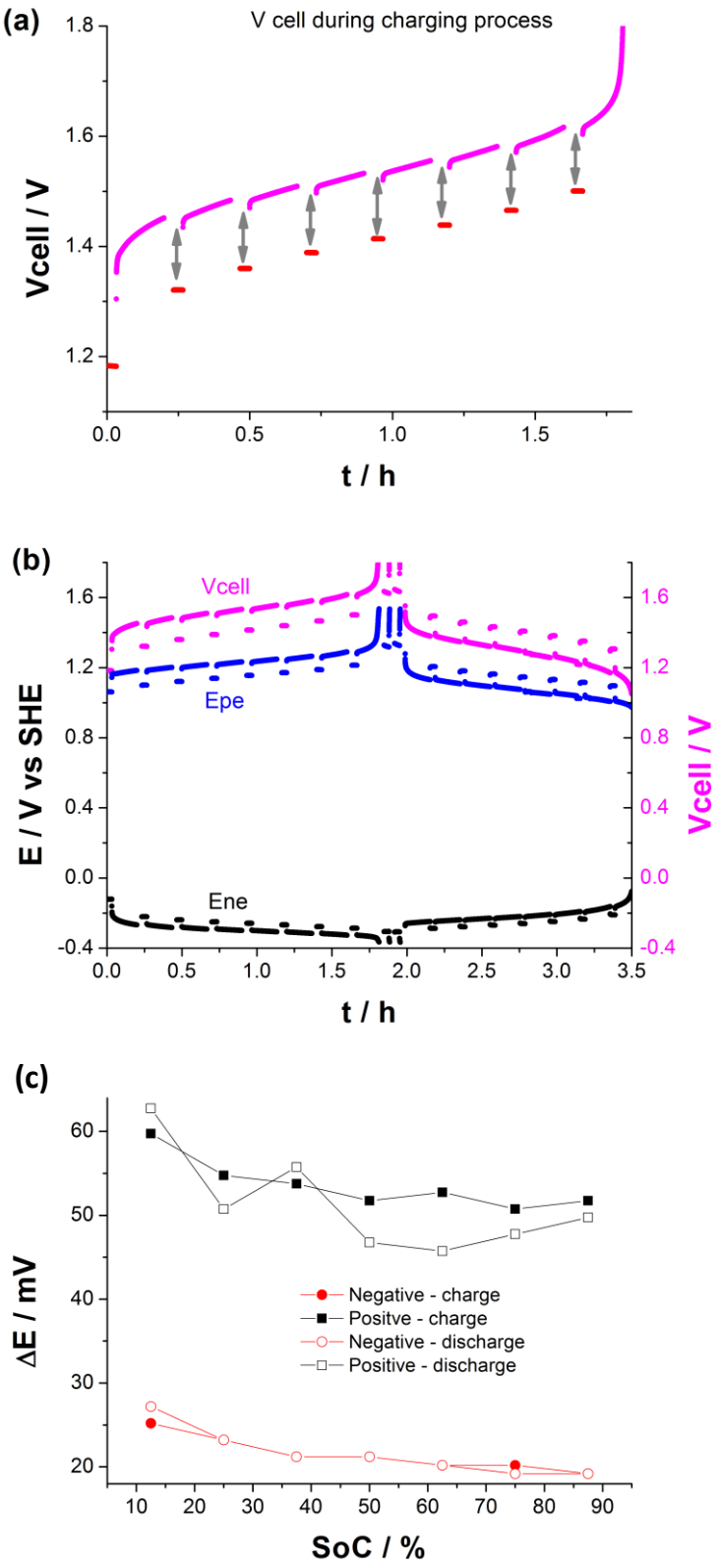

Figure 4.6. – a) Voltage profile of the battery ($E_{positive} - E_{negative}$) during charging. **b)** Voltage profiles of the battery ($E_{positive} - E_{negative}$) and potential profile of the positive electrode and negative electrode during charging and discharging. **c)** Overpotentials at different states of charge. Galvanostatic intermittent titration technique (GITT) was carried out at 20 mA cm^{-2} and 70 mL min^{-1}.

4.1.3 Conclusions

A reference electrode is proposed based on silver/silver sulfate inserted into filter press cells of VRFB. This reference electrode provides valuable information for "in-operando" conditions. For ammoxidized graphite felts, the hydrogen evolution at the negative electrode during the charge decreases the coulombic efficiency whereas the slower kinetics of the positive electrode contributes more to the decrease in voltage efficiency. The use of this reference electrode also opens new perspectives for the experimental routes allowing a fast, reliable and feasible way for proceeding the study, analysis and control for VRFBs.

5 Vanadium Redox Flow Batteries: Electrolyte Enhancements

Energy density in Vanadium Redox Flow batteries is related to the amount of vanadium able to be solved in the electrolyte, as one of the main lack of this energy storage technology companied by the operational temperature range of this technology, further research related to the solubility and stability in a broader temperature range of vanadium ions in an acidic solution has been done since the development of VRFBs.

Table 5.1 – Vanadium solubility and stability for different electrolyte conditions.

[Vanadium] / M	[H_2SO_4] / M	Stability	Temperature / ºC	additive	Ref
1.5 V(V)	3	yes	40	-	[132]
5.4 V(V)	4	months	40-60	-	[102]
4 V(IV)	3	>90 days	4	2-5wt% K_2SO_4; 3wt% sodium hexametaphosphate or 5wt% urea	[142]
3-3.5 V(V)	6M SO_4^{2-}	yes	40	-	[99]

In the past years, as **Table 5.1** summarize, there has been great effort to increase the stability of vanadium species in sulfuric acid solutions, aimed for developing high concentration, stable vanadium in a wide range of temperatures electrolytes for VRFB systems[99,102,132,142,159,160].

5.1 Thermally Stable Positive Electrolyte with a Superior Performance in All-Vanadium Redox Flow Batteries

The approach has been to include a new positive electrolyte formulation for vanadium redox flow battery (VFRB) with a significant improvement in electrochemical properties, as temperature operational range, is reported in this section. A 5KDa- poly(ethyleneimine)-based dendrites (dPEI) demonstrates enhanced performance when used as additive for positive electrolytes in VFRB[161]. Thermal stability test at 40º C shows that the dPEI additive avoids the precipitation of V(V) during 720 hours. The concentration of dPEI additive is optimized in a very low dosage of 0.6 % w/v. This cost-effective electrolyte increases the energy density up to 18 WhL^{-1}, which is an increment of 38% comparatively to the additive-free system (13 Wh L^{-1}). Moreover, the electrolyte performance in terms of

energy efficiency remains stable at 88 % over a wider operational temperature up to 60º C.

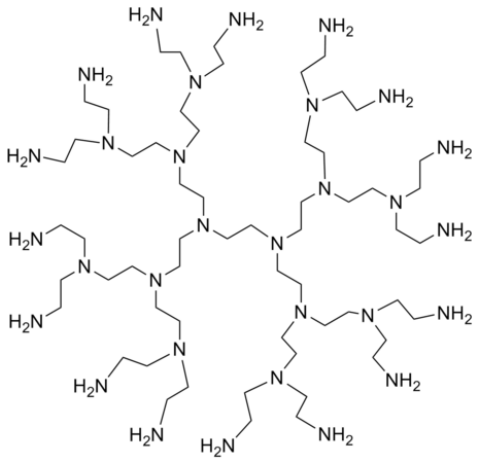

Figure 5.1. – 5 kDa poly(ethyleneimine)-based dendrites (dPEI) formula.

Besides, the effect of the new positive electrolyte formulation containing a 5KDa-poly(ethyleneimine)-based dendrite (dPEI) with a 100% functionalized -NH_2, which constitutes a cost-effective way to improve the performances in term of energy capability and thermal stability of the vanadium ions without environmental issues. **Figure 5.2** depicts the configuration of the aqueous VFRB cell with the dPEI molecule.

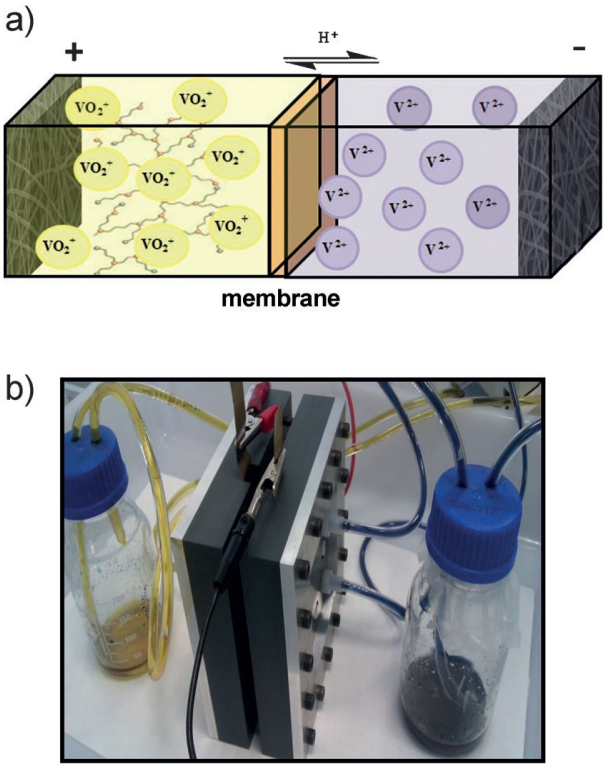

Figure 5.2. – VFRB single-cell, **a)** Schematic illustration of the cell with dPEI. **b)** VFRB experimental system.

The working principle of the aforementioned dPEI additive could be as a stabilizer by means of the formation of adduct due to interaction between the electroactive species (i.e. vanadium (V) ions) and functional groups (i.e. –NH or $–NH_2$) of the polymer at elevated temperatures. Moreover, the additive could act as a precursor of functional groups for the surface modification of carbon electrodes introducing ($–NH_2$) groups[162], which turns as a provider of active sites grafted to the electrode for electron transfer.

5.1.1 Characterization

First, to prove this hypothesis, as **Error! Reference source not found.** shows, the tability of the vanadium concentration at 40ºC for a 3M V(V) in 3M H2SO4 in presence of 0.6% w/v of dPEI. After 720 hours, the vanadium concentration remains constant at room temperature but slightly decreases to 2.7-2.8 M at 40ºC. It is a rise of 40% for the vanadium concentration in the electrolyte comparatively in absence of any additive.

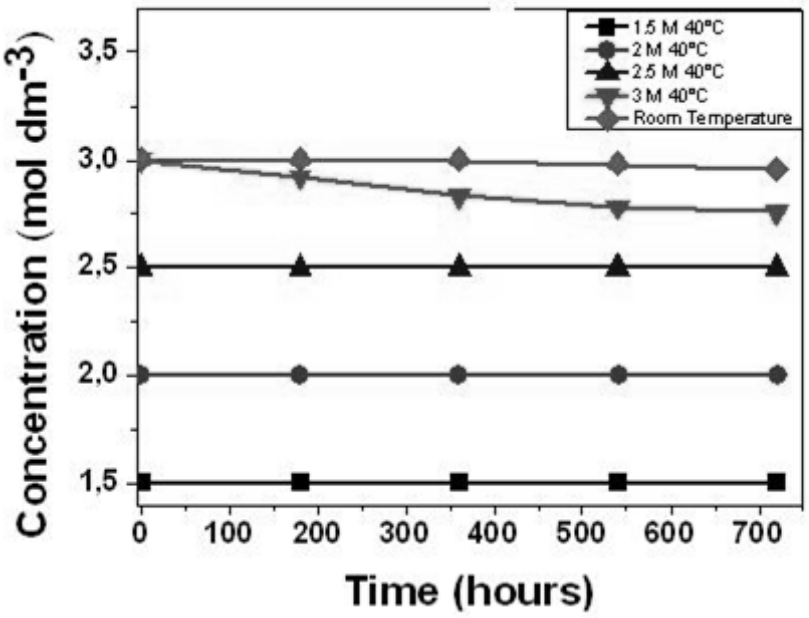

Figure 5.3.- Shows the stability of different concentrations of V(V) ions, from 1.5 to 3M, in presence of 0.6% w/v of dPEI at temperature of 40ºC.

Thereafter, the thermal stability of 1 M V(V) solutions with 0.6% additive at elevated temperatures is evaluated. Note that it is well-known that 1M V(V) precipitates after 18 hours at 40ºC [163]. Sealed samples of 1 M V(V) with additive were placed in a water bath at 40ºC during 720 hours. Samples are periodically

taken and analyzed by atomic absorption spectroscopy. The concentration of V(V) in all samples with dPEI remains unchanged (i.e. 1 M) at 40ºC. As a consequence, the improved solubility electrolyte can be achieved due to dPEI additive.

Table 5.2- Atomic concentration obtained from XPS spectra for graphite felt surface using pristine and dPEI-containing electrolyte.

Graphite electrode	Atomic concentration / %		
	C1s	N1s	O1s
before	86.8	1.0	12.2
After dPEI	77.0	1.5	21.5

To test the effect of the additive on the surface of the electrode, the commercial graphite felt (GF) is analyzed by XPS after and before charge and discharge experiment at 20 mA/cm^2 using dPEI- containing positive electrolyte. **Table 5.2** presents a comparison of atomic content (%) and **Figure 5.4** shows the XPS-spectra on the surface of both electrodes[164]. The results show that the atomic concentration of N1s and O1s are increased after the current-constant experiment using a dPEI additive, which implies the functionalization of the surface electrode. Fitting of the C1s spectrum (**Figure 5.4**) can be solved into two individual components 284 eV and 285 eV, representing graphitic carbon and carbon at graphene sheet edges due to C–H and C–N species. The Oxygen functionalities are represented by peaks at 531 eV, 532 eV and 533 eV. These are assigned to C=O groups, C–OH groups and/or C–O–C groups, and chemisorbed oxygen (COOH carboxylic groups) and/or water, respectively.

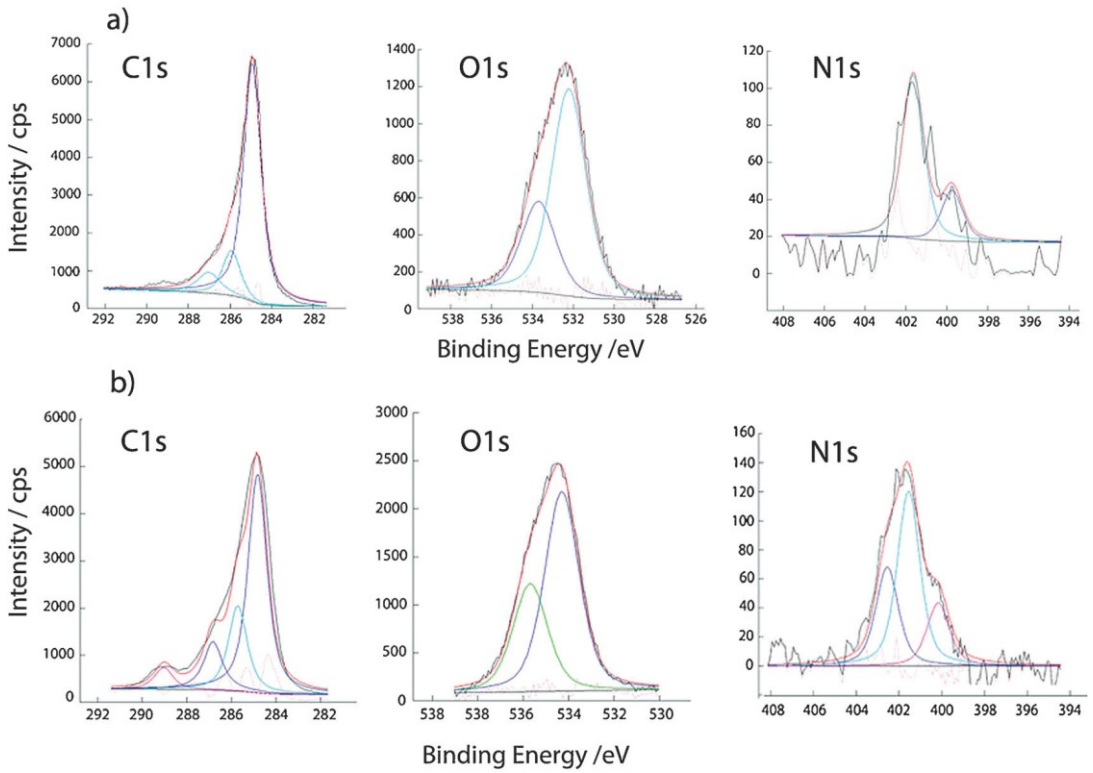

Figure 5.4. – X-ray photoelectron spectra of the commercial graphite felt before **a)** and after **b)** treatment with dPEI-containing electrolyte in a constant-current experiment at 20 mAcm^{-2}.

Considering nitrogen functionalities, the binding energies around 399 eV, 401 eV and 403 eV correspond to pyridinic, pyrrolic and graphitic or quaternary, respectively. Before treatment with dPEI-containg electrolyte, increases the contribution of C-N functionalities (i.e. 285eV in C1s spectra), also the C-O-C groups and chemisorbed oxygen (i.e. 532 and 533 eV) and an additional peak appears (i.e. 403 eV in N1s spectra) corresponding to quaternary nitrogen. As consequences, the additive introduces functional groups, (i.e. quaternary nitrogen functionalities) into surface electrode.

5.1.1.1 Electrochemical characterization

Table 5.3- Electrochemical parameters obtained from cyclic voltammetry (**Figure 5.5**).

dPEI conc. / %w/v	I_{pa} / g A^{-1}	I_{pc} / g A^{-1}	I_{pa}/I_{pc}	ΔE / V
0	4.11	3.14	1.31	0.31
0.15	4.35	3.43	1.27	0.30
0.30	5.06	3.74	1.35	0.29
0.60	6.01	4.91	1.26	0.29
1.20-2.5	5.21	4.12	1.26	0.30

Firstly, the electrochemical properties of the dPEI additive as well as their dose effect in a positive electrolyte were evaluated using graphite felt. The cyclic voltammetry (CV) is displayed in **Figure 5.5** and the related data based on CV analysis is summarized in **Table 5.3**. As it can be seen, well-defined peaks for anodic and cathodic peak associated with the V(IV)/V(V) redox couple are obtained for all electrolytes tested. Comparing the CV associated with fresh and 0.15, 0.30, and 0.60 % w/v dPEI-containing electrolytes (**Figure 5.5a**), the current density increase with the increment of the dose additive. This positive effect on the electrochemical properties towards positive reaction is due to the increment of functionalized groups introduced in the surface of the graphite felt electrode. These extra groups introduced in situ for the additive improve the electron transfer process for the oxidation and reduction process of the V(V)/V(IV) redox couple[165]. Increments up to 33% and 34% of the anodic and cathodic peak current were observed for 0.60% w/v dPEI containing electrolyte, indicating the improvement of the dPEI on the positive reaction kinetics. Moreover, the ratios of anodic peak current to cathodic peak current (Ipa/Ipc) and the peak potential separation for V(IV)/V(V) redox reaction are decreased, implying the dPEI improves the reversibility of positive reaction.

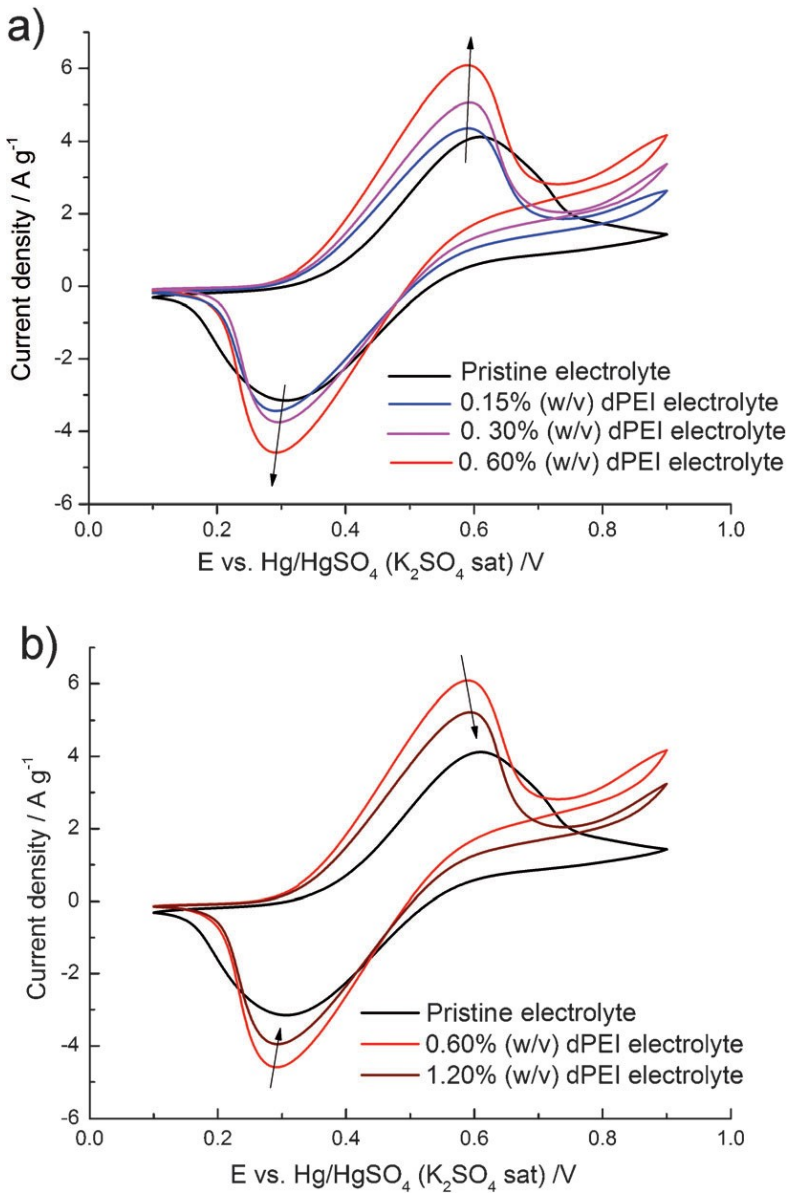

Figure 5.5. – Evaluation of electrochemical properties and dose effect of the dPEI-containing electrolytes through the VO^{2+}/VO_2^+ redox couple (scan rate 1 mVs^{-1}).

Regarding the dose effect, a higher additive concentration up to 1.2 % w/v leads to a dramatic decrease of both anodic and cathodic peaks current (i.e. 21% and 23 %, respectively). No effect had been found using a 2.5% dose of the additive in electrochemical activity. This is probably attributed to the decrease in mass transport with a higher additive dose due to an increment of viscosity of the electrolyte. Therefore, the activity of dPEI in 0.6% w/v concentration demonstrates a superior performance in term of electrocatalytic feature in comparison with fresh electrolyte.

5.1.2 Single cell performance

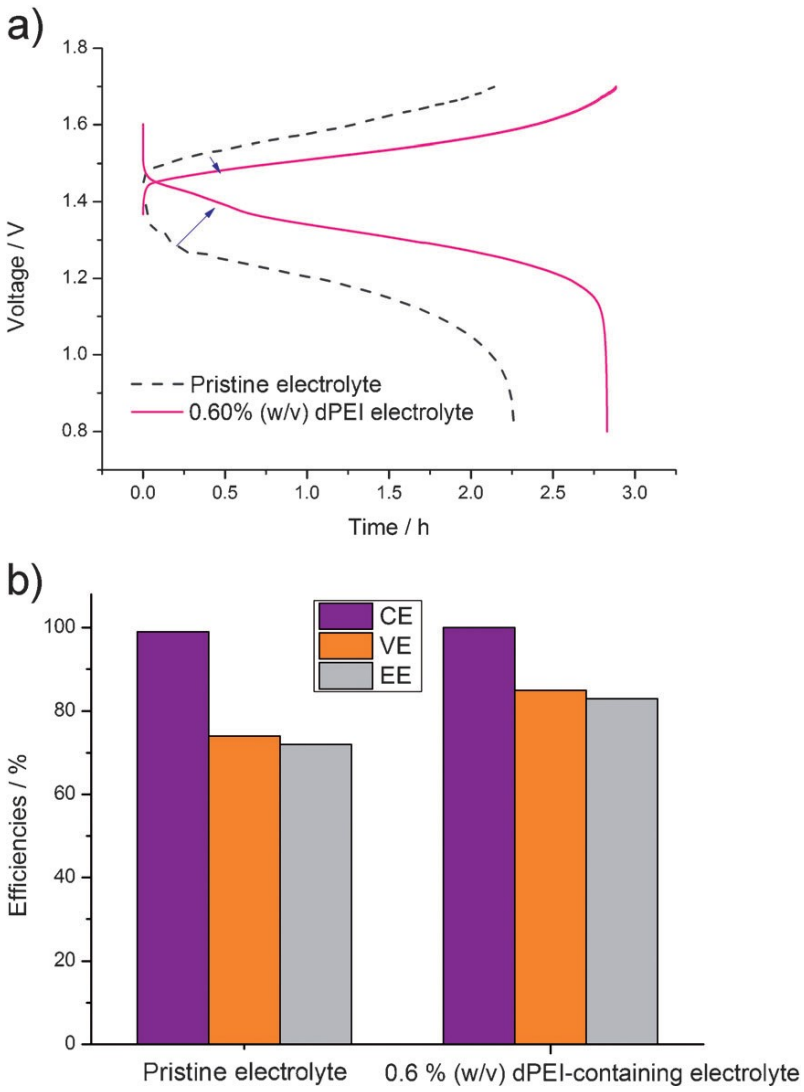

Figure 5.6. – Performance of dPEI-containing positive electrolyte in a VFB cell. **a)** charge/discharge profiles at 20 mAcm_2 and 13 mLmin_1, **b)** Efficiencies corresponding to the profiles in a). CE=coulombic efficiency, VE=voltage efficiency, EE=energy efficiency.

To ensure the potential application of a dPEI-containing positive electrolyte in large-scale batteries, a comparison with a fresh electrolyte is done in a VFRB single-cell prototype. **Figure 5.6a**, shows the charge and discharge curves for a constant-current with an operational voltage from 0.8V to 1.7 V at a current density applied of 20 mA/cm^2. The dPEI-containing electrolyte demonstrates a longer charging and discharging time than for the fresh electrolyte, leading to a superior battery capacity. For example, the discharge time obtained is increased from 2.24 h to 2.84h for a fresh electrolyte and 0.6% for a dPEI-electrolyte respectively, corresponding to discharge value of 1.12 and 1.42 Ah, which is very close to the theoretical value of 1.34 Ah. Consequently, a maximum discharging capacity is achieved using dPEI-containing electrolyte due to improvements of the

electrocatalytic activity. Note that the cell with dPEI in a positive electrolyte presents a lower charging voltage and higher discharging voltage than the fresh one. The latter is caused by the improvement of kinetics leading to a decrease in voltage losses and an increase in VE. As a consequence of the VE increased, the energy efficiency was largely improved using the 0.6% dPEI-containing positive electrolyte above 84% at a current density of 20 mA/cm^2, which is higher than that for VFRB single cell with fresh electrolyte (**Figure 5.6b**). The improvement in battery efficiency implies a better redox reversibility of the positive electrolyte, which results from the addition of dPEI electrolyte. These results are in accordance with the results of CV test.

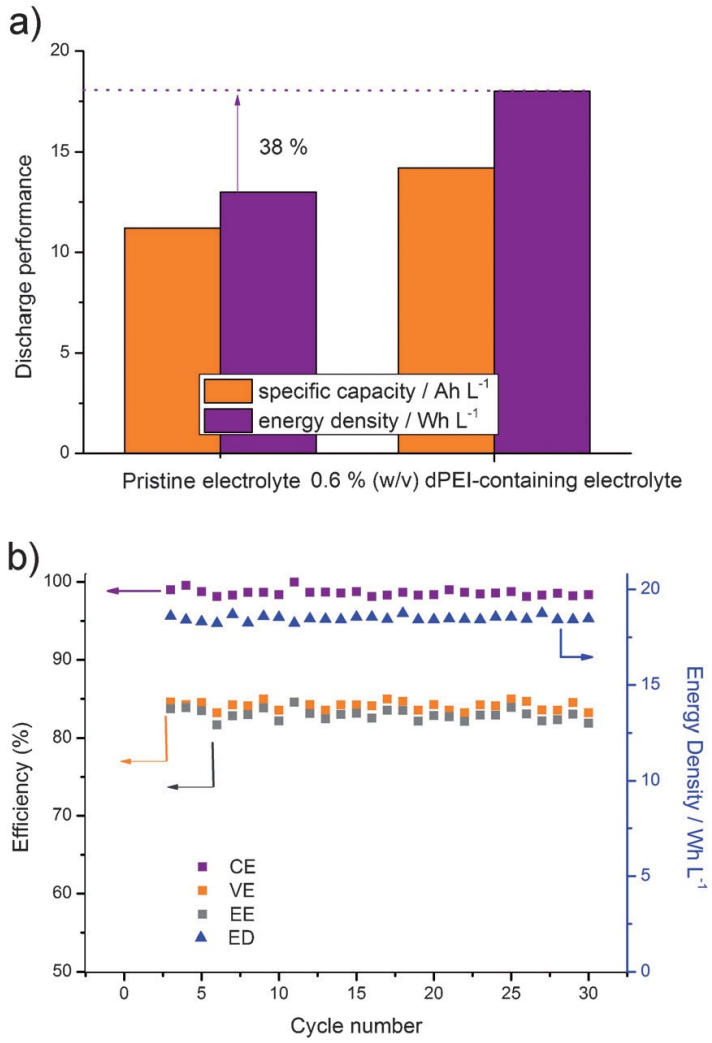

Figure 5.7. – a) Energy density and discharge capacity of the VFB single cell with pristine and dPEI-containing positive electrolyte. **b)** Cyclic performance of VFRB with 0.6%(w/v) dPEI-containing positive electrolyte at 25ºC at 20 mAcm^{-2} and 13 mLmin^{-1}.

In addition, the discharge capacity and energy density have been calculated for both electrolytes and depicted in **Figure 5.7a**. Notably, the VFRB with 0.6% dPEI-containing positive electrolytes demonstrates a superior discharge capacity (14.2

AhL^{-1}) and energy density (18 WhL^{-1}) to a fresh electrolyte; thus achieving significant improvement up to 38% in vanadium redox flow cell. Moreover, the cyclic performance of a VFRB (**Figure 5.7b**) remains constant over several cycles, demonstrating the good stability and no degradation of the additive.

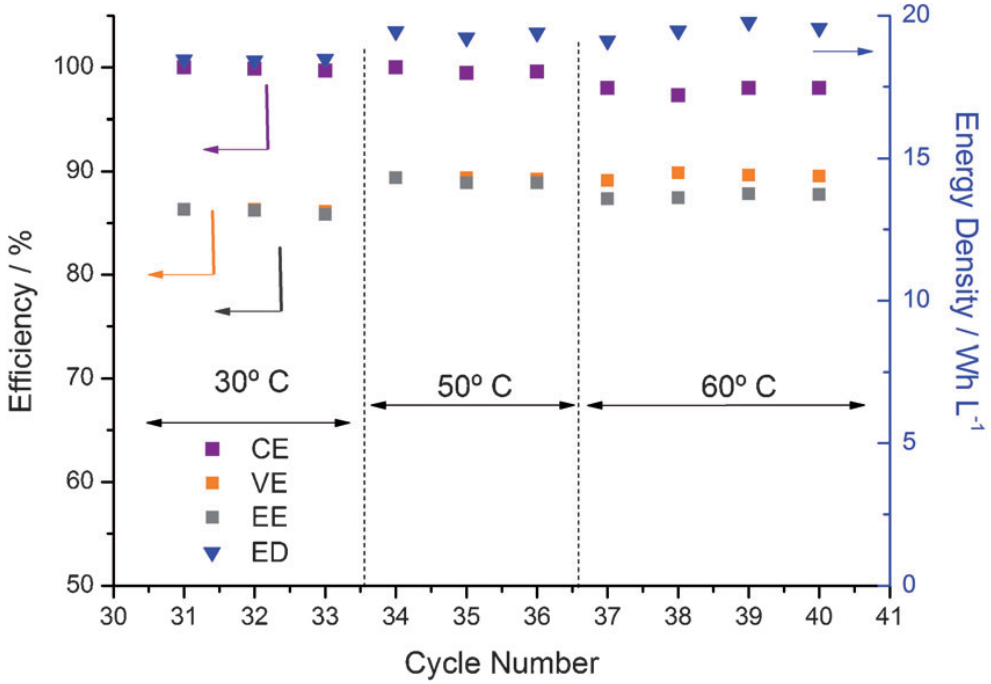

Figure 5.8. – Performance of VFRB with 0.6%(w/v) dPEI-containing positive electrolytes at 30, 50, and 60ºC.

Finally, in order to overcome the drawbacks of VRFB related to thermal stability at 60ºC, several charge and discharge experiments at 20 mA/cm^2 are done to demonstrate the outstanding performance of the dPEI-containing positive electrolyte. **Figure 5.8** gives the columbic, voltage and energy efficiency as well as energy density as a function of cycling number and temperature. Stable performance with an energy efficiency of 88% was observed during a course of 40 cycles. This is probably due to the stabilization of the V (V) ions carried out by the dPEI- containing electrolyte. The energy density at 60 º C was 19.5 W h L^{-1}. Note this value is higher than that obtained at 25º C (ca.18 WhL^{-1}). This is probably due to the water evaporation in each compartment leading to an increment of proton concentration.

5.1.3 Conclusions

In summary, a cost-effective formulation of dPEI-based positive electrolyte for VFRB was successfully demonstrated in terms of thermal stability and energy density, as 3M V(V) in 3M H_2SO_4 in presence of 0.6% w/v of dPEI at 40ºC only slightly decreases to 2.7-2.8 M. The overall performance as a single cell device is improved, as the stabilization of the V (V) ions done by the dPEI increases the energy density to 19.5 W h L^{-1} at 60ºC and the excellent electrochemical performance for 40 cycles (ca. 88 % of energy efficiency) from 30 to 60ºC of operational temperature could boost the marketability of VRFB technology.

6 Vanadium Redox Flow Batteries: Electrode Enhancements

The electrodes are the core components of the VRFB related to the power density supplied and our main focus improving this technology, which perform a very important role in providing active sites for the reaction of redox couples dissolved in the electrolytes making them a key role component on the interface electrode-electrolyte interactions (mass, charge and electron transfer). During the operation of VRFB, the energy efficiency is limited by the voltage efficiency, increasing the bottleneck effect as the current density is increased, mainly ruled by the activation and concentration polarizations, which are highly determined by the VRFB electrode. For these reasons, electrodes need to be optimized in order to reduce charge transfer resistance and increase mass transfer and kinetics towards the active species, as well as enhancing the current density it can hold. The essential requirements for the VRFB can be summarized as follows:

i) The electrode needs a highly surface functionalization, which provides the active sites for the redox reaction of the particular redox couple.

ii) The electrode must be chemically stable in highly acidic environments because the VRFB supporting electrolyte consists of strong acids.

iii) The electrode must be electrochemically stable in the operation potential window of the VRFB, avoiding side reactions.

iv) The electrode must have an excellent charge transfer reactions towards the negative (V^{3+}/V^{2+}) and positive (VO_2^+/VO^{2+}) VRFB reactions.

Much attention has been paid to enhancing the electrochemical properties of the electrode for practical use in VRFBs[36,39]. During the last 30 years, many researchers have reported valuable outcomes and know-how. By analyzing the technical progress of the VRFB, we are now able to build a foundation for providing practical guidelines for further research in this area. A variety of carbon materials, including carbon felt, graphite felt, carbon paper, graphene, and carbon nanofibers have been widely investigated as electrodes for the VRFB because they can meet the mandatory requirements discussed above.

Furthermore, a more diverse range of electrode materials was considered beyond the conventional carbon felt electrode. In 2011, around 13 articles were published, and a notable success was achieved by integrating Bi into the graphite felt electrode as the catalyst instead of precious metals or CNT. Around the same time, graphene oxide was first proposed as a new electrode material or catalyst for the VRFB. In the following year, around 16 articles were published, and in this period, remarkably cheap oxide catalysts such as Mn_3O_4 were successfully integrated on

the surface of the carbon felt electrode. The composite electrode composed of graphene and catalysts was developed and evaluated in the VRFB. In parallel, the feasibility of metal-decorated CNT, N-doped CNT, and carbon nano-walls were also examined with a view to their potential as electrodes for the VRFB.

2013 and 2014 were the most promising years in terms of the electrode research, with approximately 54 articles published. Graphene or graphene oxide (GO) were mainly investigated as an electrode or catalyst for the VRFB, and the graphite felt electrode decorated with various metal oxides (e.g. Nb_2O_5, WO_3, CeO_2, and PbO_2) showed attractive electrochemical performance. Research on the electrochemical performance of the CNT/CNF grown carbon felt electrode was also reported in this period. Moreover, it was highlighted that Bi decoration could notably improve the reactivity of the carbon felt electrode towards redox reactions of V ions. On the other hand, biomaterials were proposed as a new type of catalyst, which can be easily adopted as the electrode for the VRFB.

Accordingly, since pristine carbon materials offer a poor kinetic reversibility, they require functionalization treatments in order to guarantee highly efficient VRFB systems to operate at a large (charge/discharge) current density (> 25 mA/cm^2).Although the various explained approaches that modifies the battery's electrodes have provided some enhancement, the poor performance of the electrochemical reaction that takes place in the negative side of the battery remains a challenge, reducing efficiency and stability in VRFB systems[166,167].

$$\mathbf{2H^+ + 2e^- \leftrightarrow H_2\,, E^0 = 0\ V\ vs.\ NHE} \qquad \textbf{(6.1)}$$

Furthermore, taking into account the reduction standard potential values for VRFB negative reaction **(2.17)** compare to hydrogen-evolution reaction (HER) **(6.1)**, makes the last one thermodynamically favourable, as it has been demonstrated in **section 4.1**, **Figure 4.5c**. However, individual studies of electrochemical processes on the negative electrodes demonstrated that HER and VRFBs negative reaction occur simultaneously[168]. As a consequence, HER directly competes with V^{3+}/V^{2+} reaction in VRFB, causing imbalances, an increment in the overall cell polarization and performance losses over cycling.

Additionally, oxygen evolution reaction (OER) also could take place as a side reaction in all-vanadium redox flow batteries. However, due to the highly acidic working conditions it is not thermodynamically favoured, as well as following Le Chatelier's principles. Besides, the OER **(6.2)** potential is positively shifted related to the positive reaction in VRFBs **(2.18)**. Carbon based electrodes and also polar plates are subjected to corrosion within an oxygen evolution reaction, in order to avoid it experimentally the cut off potential should be set below 1.9 V.

$$\mathbf{2H_2O \leftrightarrow O_2 + 4H^+ + 4e^-\,, E^0 = 1.23\ V\ vs.\ NHE} \qquad \textbf{(6.2)}$$

Along this thesis, several modifications on the VRFB electrodes have been done, as improvements by different metal oxides configurations on the negative (TiO_2, TiO_2:H, TiO_2:N_x) and positive (CeO_2) electrodes, in order to enhance the reachable capacity, power density, efficiencies, operational current density and stability of the battery, which will be described in the ongoing chapter.

6.1 Electrodes developed

Recently, intensive efforts have been made to improve the state-of-the-art over the negative electrode materials for VRFB systems, as shown in **Table 6.1**. For example, Li et al.[169] achieved an excellent Energy efficiency (EE) value (ca. 78%) and Coulombic efficiency (CE) value (ca. 98%) at 150 mA/cm^2 after 4 cycles, using a low-cost Bi as electrocatalyst. The same authors[170] have proposed Niobium Oxide (V) Wolframium doped, Nb_2O_5(W), as an electrocatalyst, demonstrating outstanding performance and leading to 98.5% of CE and 78.7% of EE value at the same current density mentioned before, after more than 50 cycles. This is the best EE value ever reported in the literature. As an alternative strategy, Park et al.[171] demonstrated the successful introduction of N- and O- containing groups on a surface of a felt electrode by means of corn protein as precursor, achieving a performance up to 68.8% of EE value and 98.8% of CE value at 150 mA/cm^2 over 5 cycles. Despite the significant progress that has been made through the use of a new catalyst for high-efficiency negative electrodes in VRFB, the electrolyte-utilization ratio (i.e. specific discharge capacity and theoretical capacity ratio) is quite low, achieving up to a maximum of 64% of theoretical capacity[169]. In this regard, further improvement to reduce parasitic reactions in the negative half-cell reaction, as HER (i.e. high CE values), is still necessary, as well as a high storage capacity to guarantee high performance systems for a long cycle life. Although the study of long-term stability at several rate capabilities is rarely discussed in the literature (up to 50 cycles)[170], Haipeng Zhou et al have reached up to 200 cycles for 100 mA/cm^2 [172]. Following this behaviour we focused deeper on a high stability of our electrode applying larger current densities.

Table 6.1.- Electrochemical performance in single cell conditions comparative for different treated electrodes based on physical and chemical modifications on carbonaceous structures.

Modification or activation method	Reagent & Treatment Conditions	Parameters of VRFB single cell								Ref
		Electrode size /cm	[$VOSO_4$] / M	Max. j / mA cm^{-2}	CE / %	VE / %	EE / %	Electrolyte Utilization ratio	Cycles$_{max.}$	
Corona + H_2O_2	4 A, 15 s x 2 + 30% H_2O_2, 1 h	5 x 5	1.7	145.8	96.7	70.3	68.0	96.1	20 (32mA/cm^2)	[173]
N-doped	Corn protein-derived and	2.5 x 2.5	2	150	98.0	70.0	68.6	37.3	80	[171]

carbon	coating								(50mA/cm^2)	
Graphene nanosheet	Graphite, ball-milling, 24 h and coating	2.5 x 2.5	/	150	97.0	67.8	65.8	65.3	35 (50mA/cm^2)	174
CNF/CNT	CVD growth, 700ºC in C_2H_4	2.5 x 2.5	2	100	97.7	67.5	66.0	29.9	15 (40mA/cm^2)	175
Bi	$BiCl_3$, electro-deposited onto GF	5 x 5	2	150	97.2	80.3	78.1	63.8	50 (50mA/cm^2)	169
Mn_3O_4	1 M $(C_2H_3O_2)2Mn$ $4H_2O$, 200ºC, 12 h	/	2	40	85.4	90.2	77.0	/	20 (40mA/cm^2)	176
WO_3	$(NH_4)6W_7O_{24}$ $6H_2O$, 550ºC in N_2, 2 h	3 x3	1.5	60	95.1	81.8	78.1	62.2	50 (30mA/cm^2)	177
PbO_2	Pulse electrodeposited	3 x 4	0.5	80	99.7	78.3	78.1	82.1	30 (50mA/cm^2)	178
Nb_2O_5(W)	$NH_4[NbO(C_2O_4)(H_2O)]xH_2O$ $(NH_4)10W_{12}O_{41}$ $5H_2O$, 170ºC, 48 h	2.5 x 2.5	2	150	98.3	74.3	72.8	54.1	50 (150mA/cm^2)	170
ZrO_2	$Zr(NO_3)_4$ $5H_2O$, precipitation	5 x 5	2	200	93.7	71.9	67.4	56.0	200 (100mA/cm^2)	179
CF 20% wt TiO_2/C	Spry drying at 65^{0}C for 6h (vacuum)	5 x 5	1	20	82.4	90.1	74.2	68.6	4 (20mA/cm^2)	180
CF 20% wt TiO_2/C	Spry drying at 65^{0}C for 6h (vacuum)	5 x 5	3	200	90.0	73.0	65.4	76.1	3 (200mA/cm^2)	181
GF@TiO_2:H	Hydrothermal synthesis 100^{0}C for 14h; annealing in Ar(H2) at 500^{0}C for 4h	2 x 2	2	200	95.8	63.7	61.0	81.6	100 (150mA/cm^2) In total 140 cycles up to 350 mA/cm^2	89
GO-rGO/GF	CVD NiF/GF, immersed in GO(aq) 24h at 60ºC, immersed in HCl and reduced on Zn foil for 30min	3 x 2	0.85	100	-	-	-	-	50 (50 mA/cm^2)	
Mn3O4 NPs/CCs	MnOOH NFs electrode on CCs at 2mA/cm^2. Annealing under N_2(g) at 600ºC for 3h	2 x 2	1	400	97	73	71	94	500 (100 mA/cm^2)	
GF-Ta2O5 NPs	Hydrothermal synthesis at 240ºC for 12h	5 x 5	1.6	80	95	78	74	58	100	

GF-TiC	Hydrothermal synthesis at 180ºC for 14h. Annealing 1250ºC for 5h	5 x 4	1.6	100	-	62	61	<29	65 (80 mA/cm^2)
N- and –WO3 decorated CF	Urea hydrothermal reactor on CF at 180ºC for 12h. Hydrothemal WO3 formation at 180ºC for 3h	1.5 x 1.5	1.8	200	96	68	67	51	-
NiO NPs-GF	Deep coating in $Ni(NO_3)_2$ and dry at 60ºC. Annealing under Ar at 300ºC for 30 min	4 x 4	2	150	-	72	-	67	300 (100 mA/cm^2)
TiNb2O7-rGO	GO synthesis by Hummer's method. $TiNb_2O_7$ NPs hydrothermal 200ºC for 24h. $TiNb_2O_7$-rGO hydrothermal 75ºC for 24h. Annealing in Ar atm at 700ºC for 2h	5 x 5	1.6	160	97	74	72	70	200 (120 mA/cm^2)
CF-SnO2 NPs	Hydrothermal $SnCl_4$ at 150ºC for 4 h. Annealing under Ar at 400ºC for 3h	5 x 5	1.5	150	97	80	78	117	50 (50 mA/cm^2)

6.1.1 Titanium dioxide (TiO_2)

The electrocatalyst of the TiO_2 nanoparticles exhibits excellent results in comparison with commercial electrodes, even at high current densities. It is used in order to produce the total abatement of HER over the negative VRFB reaction, as well as, to guarantee VRFB long-term stability.

It is well-known that many metal oxides have resistance to corrosion as well as offering outstanding catalytic properties[182,183]. In this scenario, titanium dioxide (TiO_2) is an useful material for photocatalysis[184], gas sensors[185–187], Li-ion batteries[188,189], and catalysis[190,191]. In addition, TiO_2 is a great candidate which is well-suited to work at low pH with interesting electrochemical properties and stability to corrosion, especially concerning hydrogen-evolution reaction. Over the past decade, density functional theory (DFT) predictions, in conjunction with experimental efforts, have played an important role in designing electrocatalysts. For HER, the activities (in terms of exchange current density) of different catalytic surfaces can be correlated with their hydrogen-binding energy (HBE) via a volcano-type relationship, revealing that an optimal HBE would lead to the highest reaction. By contrast, some oxide-covered metals are known to be poor HER catalysts because their HBE values are too large. Therefore, it is common knowledge that TiO_2 dramatically reduces the hydrogen-evolution reaction rate by several orders of magnitudes[192–194], **Figure 6.1** visually explains the cell potential region where the hydrogen evolution takes place. Consequently, as the graphite felt is covered by

the TiO2 the HER is depleted to more negative potentials comparatively to the negative VRFBs reaction (V3+/V2+).

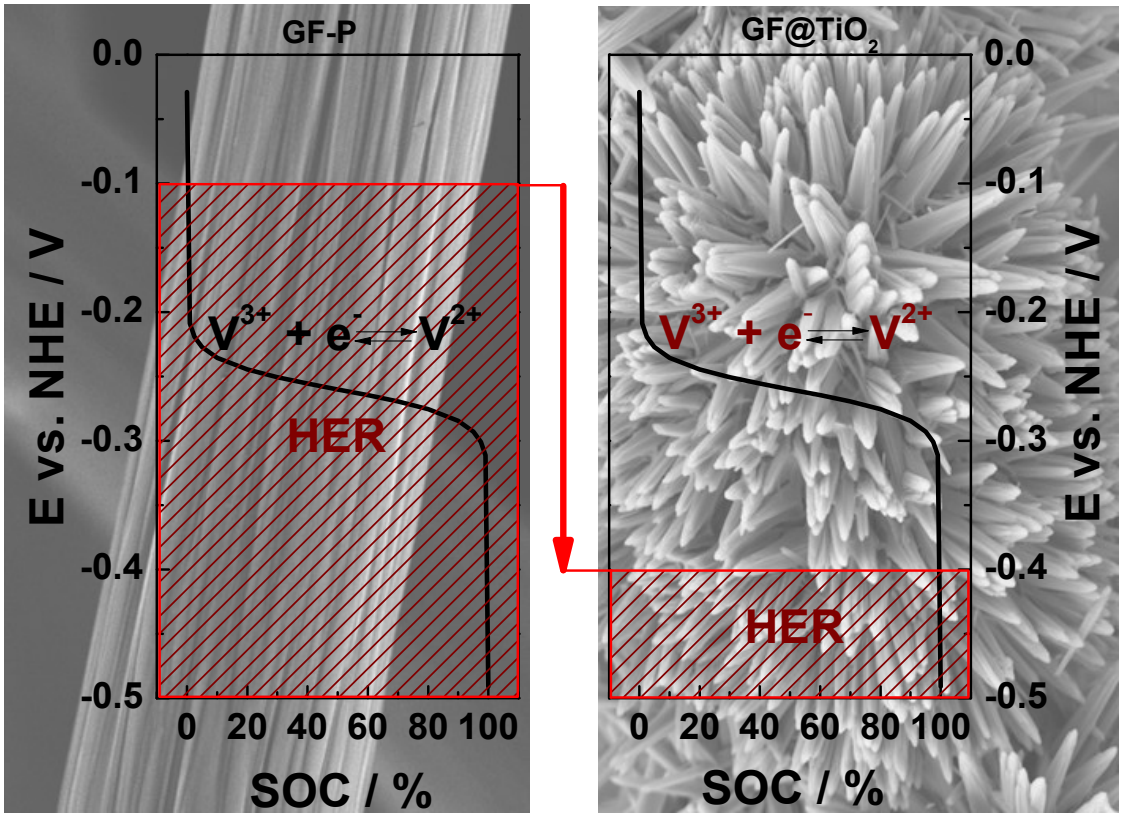

Figure 6.1. – Effect of the presence of TiO_2 over the reactions taking place in the negative compartment of the battery.

6.1.1.1 Characterization

Initially, the structural shape of the titanium dioxide deposited on the carbon fibres can be morphology characterized seeing **Figure 6.2**. Firstly, in **Figure 6.2a.** the felt fibres are just thermal treated by O_2 plasma. From **Figure 6.2b** can be observed that there are only titanium dioxide nanoparticles (NPs) to **Figure 6.2d.** obtaining a TiO_2 multi-nanorods covering the whole surface of the graphite felt (GF). Passing by an intermediate, which titanium dioxide single-nanorods decorates the surface (**Figure 6.2c**) in a different structural orientation than the multi-nanorods.

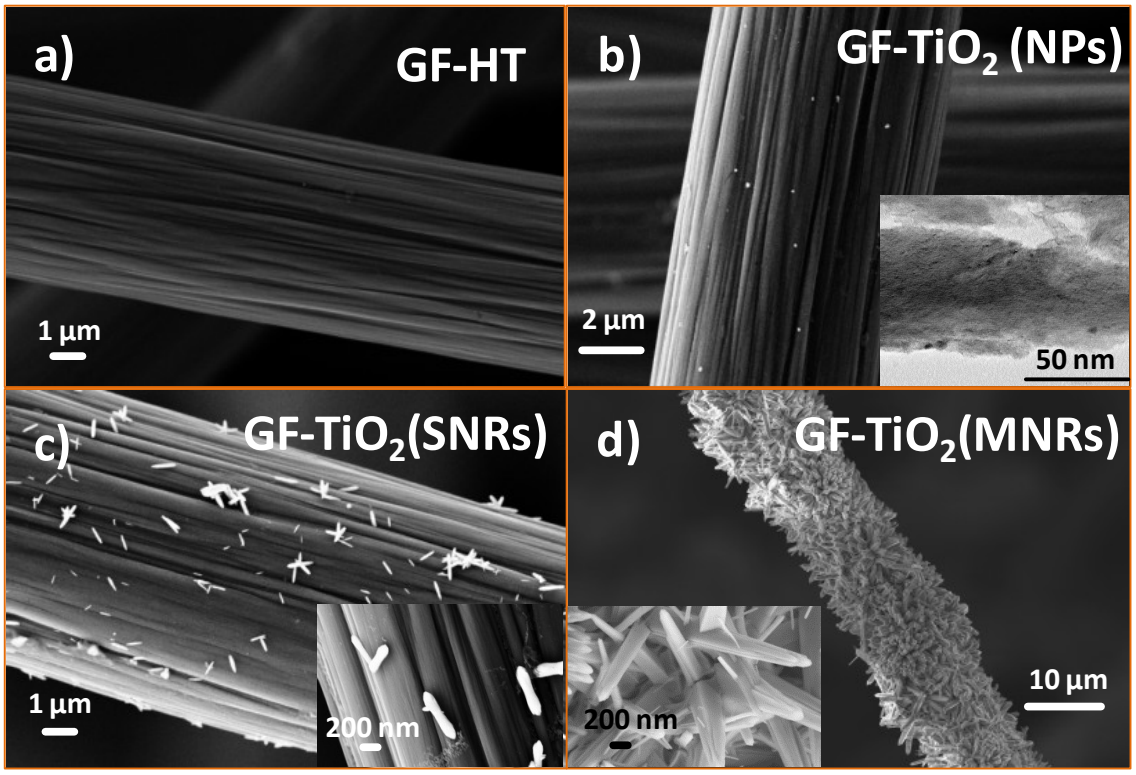

Figure 6.2. – FESEM images of different titanium dioxide morphologies decorating the surface of the graphite felt **a)** GF-HT, **b)** GF-TiO2(NPs), **c)** GF-TiO2 (SNRs) and **d)** GF-TiO2 (MNRs).It is also shown a TEM image as the caption in b).

Although the mentioned structural changes previously mentioned, there is no effective change in the XRD diffraction pattern (JCPDS no.: 21-1276) shown in **Figure 6.3**. In all cases, the peaks are related to titanium dioxide in its rutile form. It is also included the rutile unit cell, as well as, the crystallographic parameters related to it. The broad peak near 2θ = 25º and 43º in the spectrum of GF-P electrode is attributed to the crystallographic planes of (002) and (004) of the originally GF electrode. Additional diffraction peaks appears in the pattern of GF@TiO_2 electrode at 27.4º; 35.8º and 54.3º; which are consistent with the rutile TiO_2 (110), (101), and (211) crystalline planes, respectively.

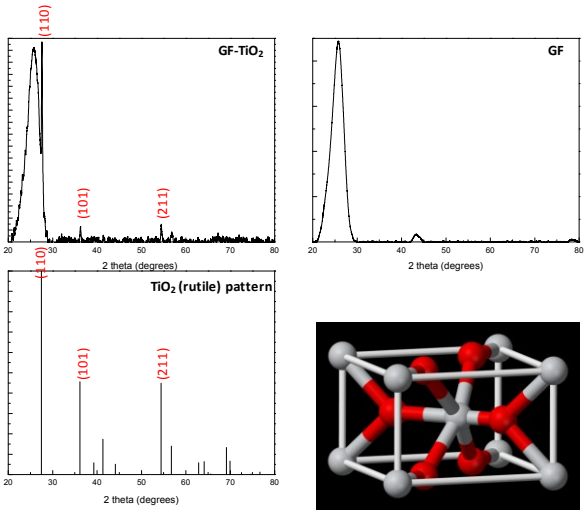

Crystallographic parameters

Crystal system:	Tetragonal
Space group:	P42/mnm
Space group number:	136
a (Å):	4,5890
b (Å):	4,5890
c (Å):	2,9540
Alpha (°):	90,0000
Beta (°):	90,0000
Gamma (°):	90,0000

Calculated density (g/cm^3): 4,26
Volume of cell (10^6 pm^3): 62,21
Z: 2,00

RIR: 3,45

Figure 6.3. – X-ray diffraction spectra of GF electrode and as-prepared GF@TiO_2.

6.1.1.1.1 Electrochemical characterization

Besides, the electrochemical characterization in a three electrode cell,of the GF-TiO_2 samples expose an inhibition of the hydrogen evolution reaction (HER) **(6.1)**, as it can be seen in **Figure 6.4b.** The maximum current value for an electrode potential at -0.9 V vs. NHE following the trend [A/g]: GF-HT [-5.8]> GF-P [-4.7]> GF-TiO_2 (SNRs) [-3.3]> GF-TiO_2 (NPs) [-2.0]> GF-TiO_2 (MNRs) [-1.2]. First, focusing on the fact that HER increases from the pristine graphite felt to the plasma treated one it is because an increase on the active surface area, which will favor kinetically HER reaction onto the carbonaceous surface. Next, there is a HER decrease when the amount of TiO_2 covering the surface increases which follows the trend: SNRs < NPs < MNRs. It is due to a large bounding energy of atomic hydrogen to rutile TiO_2 phase[182,195–197], which inhibits a posterior hydrogen formation.

Additionally, in case it is only considered the reduction standard potential for the reaction **(2.17)** (E^0 (V^{2+}/V^{3+}) = -0.26 V vs. NHE) all the samples that have titanium dioxide on its surface posses a neglected tendency towards the reaction of hydrogen evolution.

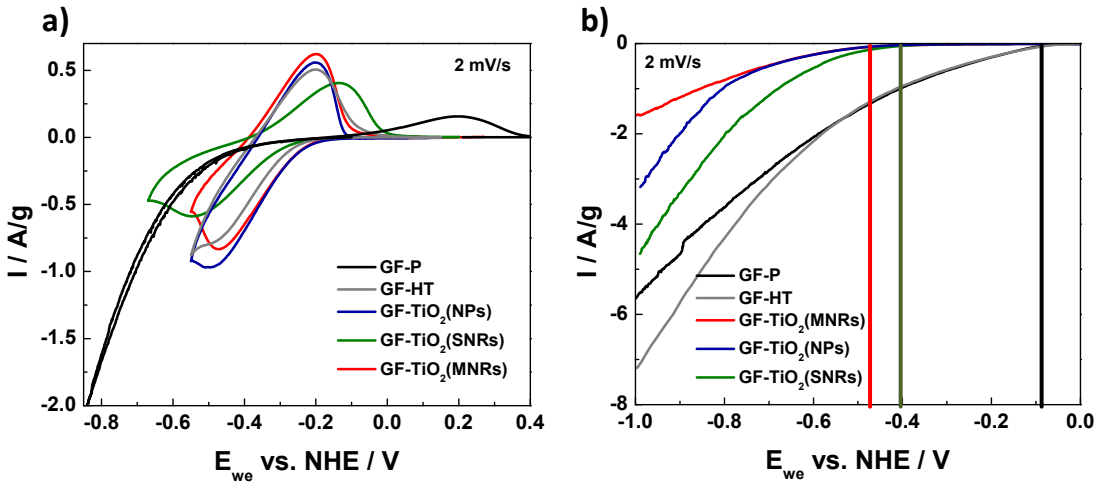

Figure 6.4. –. a) Cyclic voltammetry (CV) on the 5th cycle for different electrode synthesized at a 2 mV/s scan rate, in 0.05 M V^{3+} and 1 M H_2SO_4 solution as electrolyte **b)** Linear Sweep Voltammetry (LSV) 5th cycle for different electrode samples done at 2 mV/s scan rate, in 1 M H_2SO_4 solution as electrolyte. In both cases, the system was continuously purged with a nitrogen flow.

Furthermore, **Figure 6.4a.** reveals the electrochemical characterization towards the negative side VRFB reaction. The values obtained from **Table 6.2** indicate a reversibility increasing from the initial value for GF-HT electrode, which shows competition of the negative side redox reaction (V^{3+}/V^{2+}) and the hydrogen evolution reaction (HER). Afterwards, the activity towards the negative reaction, more especifically V^{3+} reduction to V^{2+}, is reduced among cycling and therefore the HER is favored (**Figure 6.5**). Following, GF-TiO_2 (NPs) displays a better reversibility towards vanadium reaction (lower value of ΔE and I_{red}/I_{ox} ratio closer to 1) comparatively to GF-HT, as the functional groups of TiO_2 catalyze the V^{3+}/V^{2+} reaction. However, this functional groups of the titanium dioxide are reduced through continuous cycling, as **Figure 6.5** shows. When the amount of initial precursor is increased in order to avoid the rapidly reduction of these functional groups, it is found the formation of SNRs on the surface that extend the ΔE in spite the fact that the ratio of reduced/oxidized intensity is enlarged. Finally, GF-TiO_2 (MNRs) has the best electrochemical performance among the entire samples tested in this series of experiments. Moreover, the functional groups that catalyze the vanadium negative redox reactions are stable among ciclic voltammetry cycling, as seeing in **Figure 6.5**.

Table 6.2. – Electrochemical parameters of cyclic voltammetry from **Figure 6.4a**.

Compound	E_{ox} / V	E_{red} / V	ΔE / V	I_{red}/I_{ox}
GF –HT	-0.201	-0.497	0.296	0.54
GF-TiO_2(NPs)	-0.200	-0.495	0.293	0.64
GF-TiO_2(SNRs)	-0.137	-0.544	0.407	0.76
GF-TiO_2(MNRs)	-0.200	-0.472	0.272	0.79

In brief, when it is done stability test of the electrodes through the negative half-cell reaction (**Figure 6.5**), it suggests that TiO_2 MNRs is the modified preferred electrocatalyst, which not only shows better performance in terms of reversibility and selectivity towards the negative half-cell reaction, but also superior stability. The electrochemical values follow the trend: TiO_2 MNRs (ΔE=0.27 V; I_{red}/I_{ox} = 0.8) > TiO_2 SNRs (ΔE=0.41 V; I_{red}/I_{ox} = 0.76) > TiO_2 NPs (ΔE=0.29 V; I_{red}/I_{ox} = 0.64).

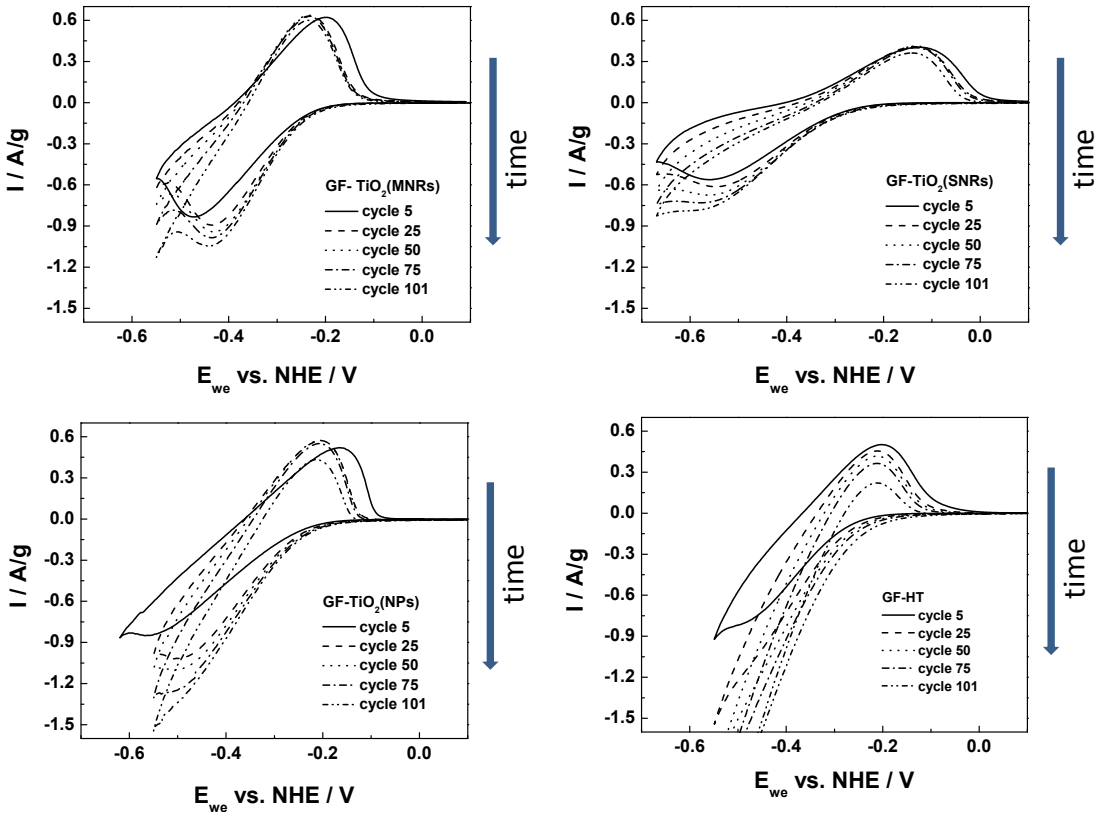

Figure 6.5. – Cyclic Voltammetry at 2 mV/s scan rate for different TiO_2 structures deposited on Graphite felt, as electrodes, showed for time spaced cycles from the 1st to the 101st cycle. The electrolyte solutions is composed by 0.05 M V^{3+} and 1 M H_2SO_4 which was continuously purged with a Nitrogen.

Equally important, the charge transfer reaction between the electrode and the electrolyte, towards the negative reaction for VRFBs, is measured using an electrochemical impedance spectroscopy at a fixed potential of -0.26 V vs. NHE (**Figure 6.6**). By these means, the charge transfer resistance values obtained are: GF-HT (79.9 Ohms) > GF-P (44.8 Ohms) > GF-TiO_2 SNRs (31.6 Ohms) > GF-TiO_2 NPs (31.1 Ohms) > GF-TiO_2 MNRs (21.2 Ohms). It evidences the facility enhanced charge transfer in case of the modified carbon electrode (GF) with a multi-nanorods layer. In case it is partially decorated with SNRs or NPs, the resistance is very similar, but slightly lower for the NPs which evidence the better charge transfer between the electrolyte and the carbon material through the titanium dioxide.

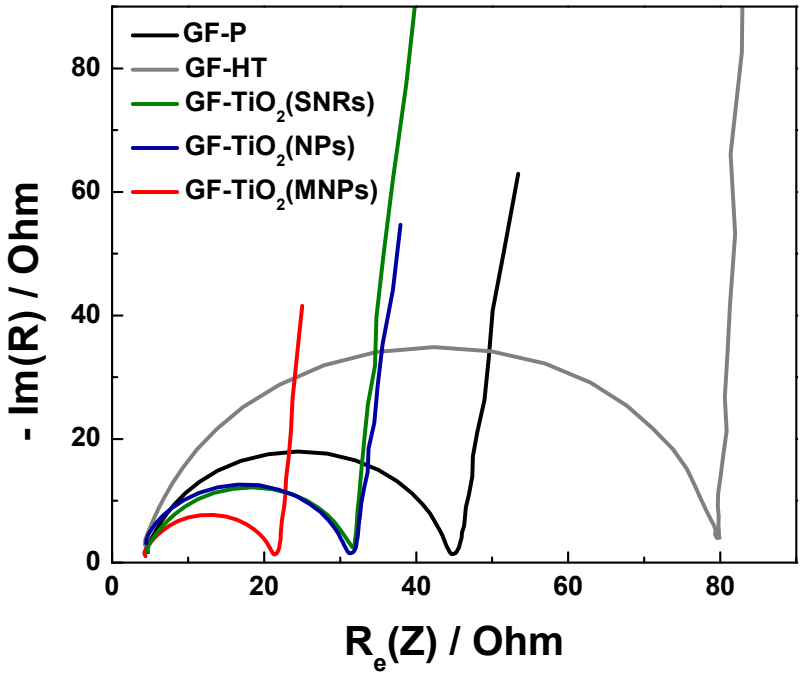

Figure 6.6. –. Potentiostatic electrochemical impedance spectroscopy (PIES) has been done for different electrodes in a 0.05 M V^{3+} at 50% SoC and 1 M H_2SO4 solution. It was purged continuously with nitrogen gas. The potential used was -0.26 V vs. NHE.

6.1.1.2 Single cell performance

Furthermore, to evaluate the feasibility of the battery using these modified electrodes, galvanostatic single cell experiments were done in a 1 M vanadium ions and 3 M H_2SO_4 electrolyte solution with these electrodes used as negative electrodes while GF-HT were used on the positive electrode, reaching 50 mA/cm^2 as maximum current density. The specific capacity increases as the decoration on the negative electrode of titanium dioxide structure goes from NPs to SNRs, finishing in MNRs as top value (**Figure 6.7a**). Following the trend (Ah/L): GF-P (8.6) < GF-HT (9.9) < GF-TiO_2 SNRs (11.6) > GF-TiO_2 NPs (13.0) > GF-TiO_2 MNRs (13.8) at 25 mA/cm^2. Although these are evidences of the increasing selective active groups towards V^{3+}/V^{2+} redox reaction, reaching to more electroactive vanadium electrolyte, the semiconductor nature of TiO_2 increases the overvoltage in GF-TiO_2(MNRs) when the fibers are completely covered by it (higher current polarization).

Besides, the trendy selectivity towards vanadium negative reaction is confirmed by the Coulombic efficiency values for the modified titanium dioxide different electrodes (**Figure 6.7b**). Therefore GF-TiO_2(MNRs) has the largest value obtaining around 99% CE, while GF-TiO_2(NPs) get a little bit less close to 98% and GF-TiO_2(SNRs) as expected give the lowest value among the titanium dioxide samples with 96%. As shown in **Figure 6.7b**, these values are for 50 mA/cm^2 current

density applied. However, the voltage efficiency values show another fact which is the reduction to 82% for GF-TiO_2(MNRs), from 93 and 92% for GF-TiO_2(NPs) and GF-TiO_2(SNRs) respectively. This decreasing is, as it is previously said, due to the semiconductor properties titanium dioxide. Therefore, as titanium dioxide thickness is increased the electrode polarization also increases. As the voltage efficiency works as limiting factor, the energy efficiency follows the same tendency with close percentage values: GF-TiO_2 NPs (91%) > GF-TiO_2 SNRs (89%) > GF-TiO_2 MNRs (80%). As a consequence of that overvoltage polarization, further treatments are done in the following section.

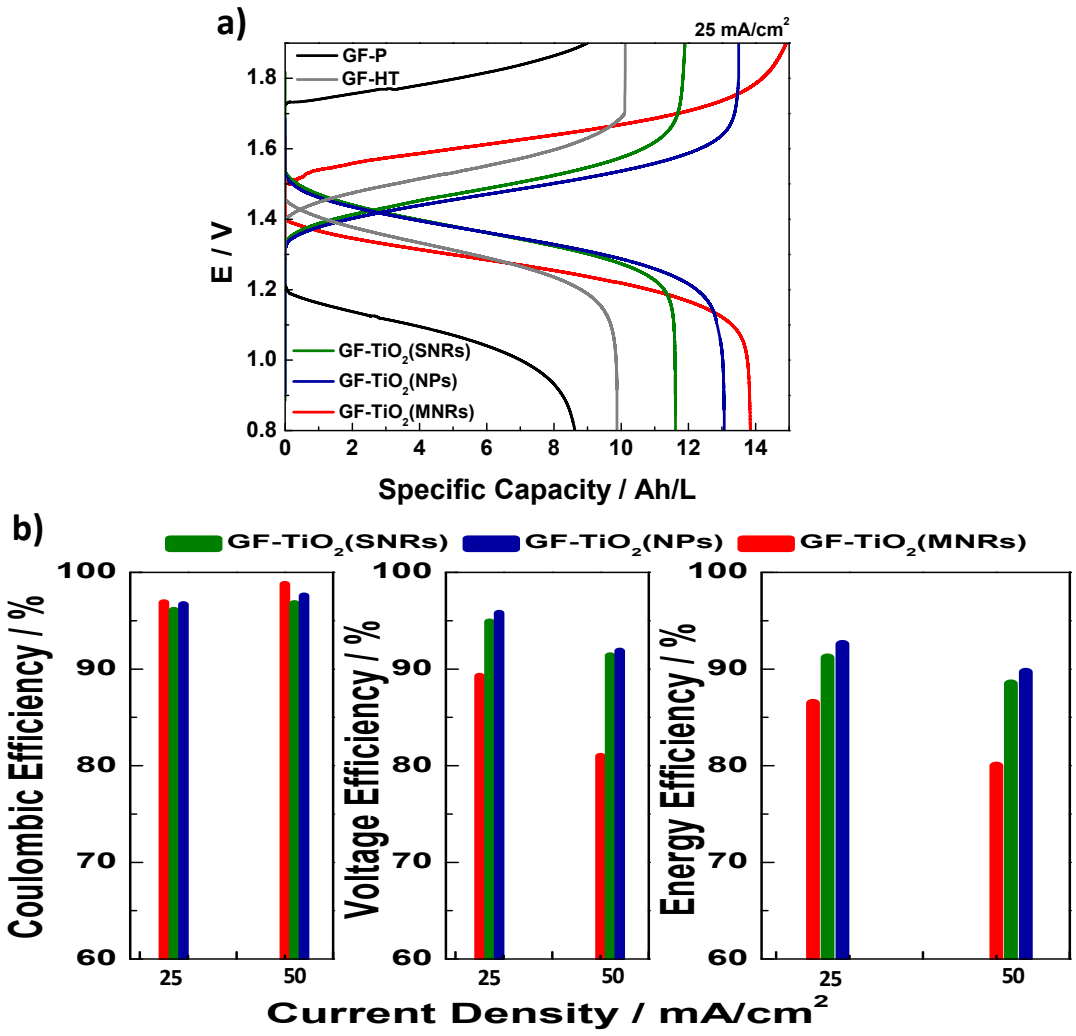

Figure 6.7. – a) Charge-discharge voltage plot profiles for GF-P, GF-HT, GF-TiO_2(SNRs), GF-TiO_2(NPs) and GF-TiO_2(MNRs) at 25 mA/cm^2 as current density applied **b)** Coulombic, Voltage and Energy Efficiencies for GF-TiO_2(SNRs), GF-TiO_2(NPs) and GF-TiO_2(MNRs) at two different current densities 25 and 50 mA/cm^2.

6.1.2 Reduced titanium dioxide (TiO_2-H)

The improved effects caused by hydrogen heat-treatments lead to an enhancement of the electrochemical effectiveness in the charge transfer from TiO_2 layer to the electrolyte, as the previous section was lacking off. It is due to the introduction of several defects in the crystal structure. More importantly, the complete depletion of HER on the negative electrode of the battery remains (**Figure 6.8**). Moreover, the long-term stability is studied at several rates capabilities for, alternatively, 1 M or 2 M vanadium concentrations as electrolyte in order to observe the effect caused by an increase to the electrolyte concentration to the thermodynamically stable limit.

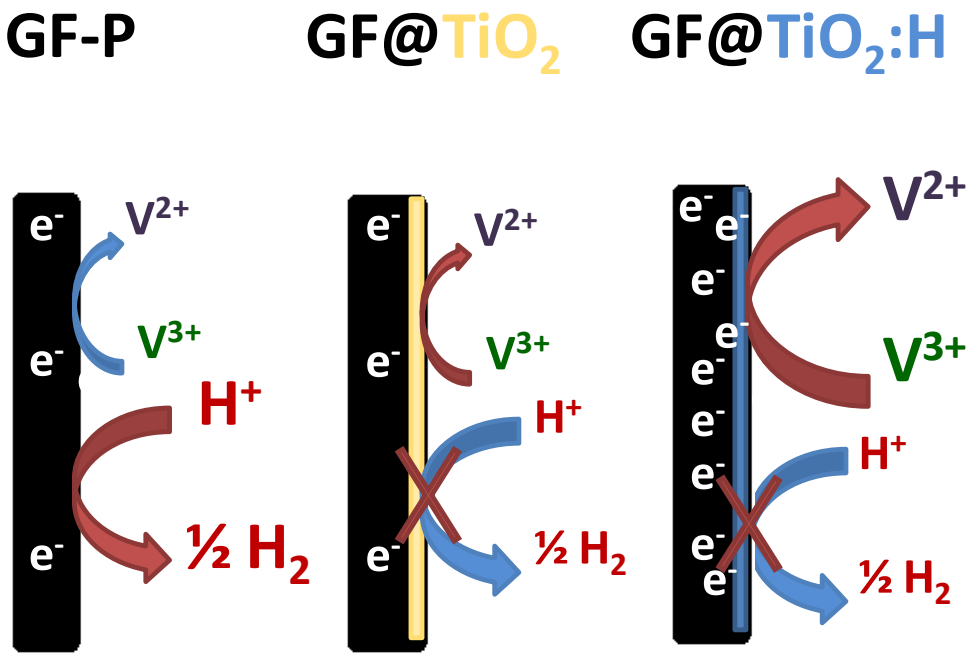

Figure 6.8. – Scheme of the processes involved for the different electrodes of this section.

Hydrogen treated TiO_2 as electrocatalyst has been demonstrated for high performance all-vanadium redox flow batteries (VRFB) as a simple and eco-friendly strategy, boosting the obtainable battery's capacity. GF@TiO_2:H electrode performs an abrupt inhibition of the hydrogen-evolution reaction (HER), which is a critical barrier for operating at high rate for long-term cycling in VRFB. Significant improvements in charge-discharge and electron transfer processes towards V^{3+}/V^{2+} reaction is achieved on the surface of reduced TiO_2, as a consequence of the formation of oxygen-vacancies in the lattice structure and oxygen-functional groups. Key performance indicators of VRFB, which have been increased in terms of high capability rates and electrolyte-utilization ratio achieved (82% at 200 mA/cm^2). Additionally, high Coulombic efficiency (up to 96th cycle~100%, after >97%) is obtained, demonstrating the feasibility of achieving long-term stability.

6.1.2.1 Characterization

As described in **Figure 6.8**, this work is aimed to introduce TiO_2:H groups as promoter for V^{3+}/V^{2+} redox reaction, attributed to abundant oxygen-containing groups as well as rutile oxygen vacancies formation[198]. **Figure 6.9** exhibits the field emission scanning electron microscopy (FE-SEM) images of the graphite felt pristine (GF-P), thermal-treated graphite felt in absence of titanate precursor (GF-HT) and TiO_2-based GFs. Typically the GF-P shows a smooth carbon fibers morphology and porous electrodes (**Figure 6.9.a**). The surface of the GF@HT electrode (**Figure 6.9.b**) is cleaner than those of the bare one. This phenomenon can be caused by the weak reaction between HCl and graphite felt removing the surface contaminants and forming a more hydrophilic area. A dense TiO_2 coverage was obtained (**Figure 6.9.c**) with a thickness layer about 1.3 microns on the GF fiber after the hydrothermal process, electrode named GF@TiO_2. Higher magnification (**Figure 6.9.d**) corroborated the compact structure of the coated layer, which are further composed of several structures with "flower-like" morphologies, which are further composed by primary high density of nanorods with thickness lower than 250 nm. An increasing agglomeration of the nanorods has been observed after hydrogen-treated GF@TiO_2 electrode, named GF@TiO_2:H (**Figure 6.9.d**). Figure S1 shows that all fibers in GF-P electrode have been covered by homogeneous shell of TiO_2:H, maintaining their "flower-like" morphology after long-term stability studies.

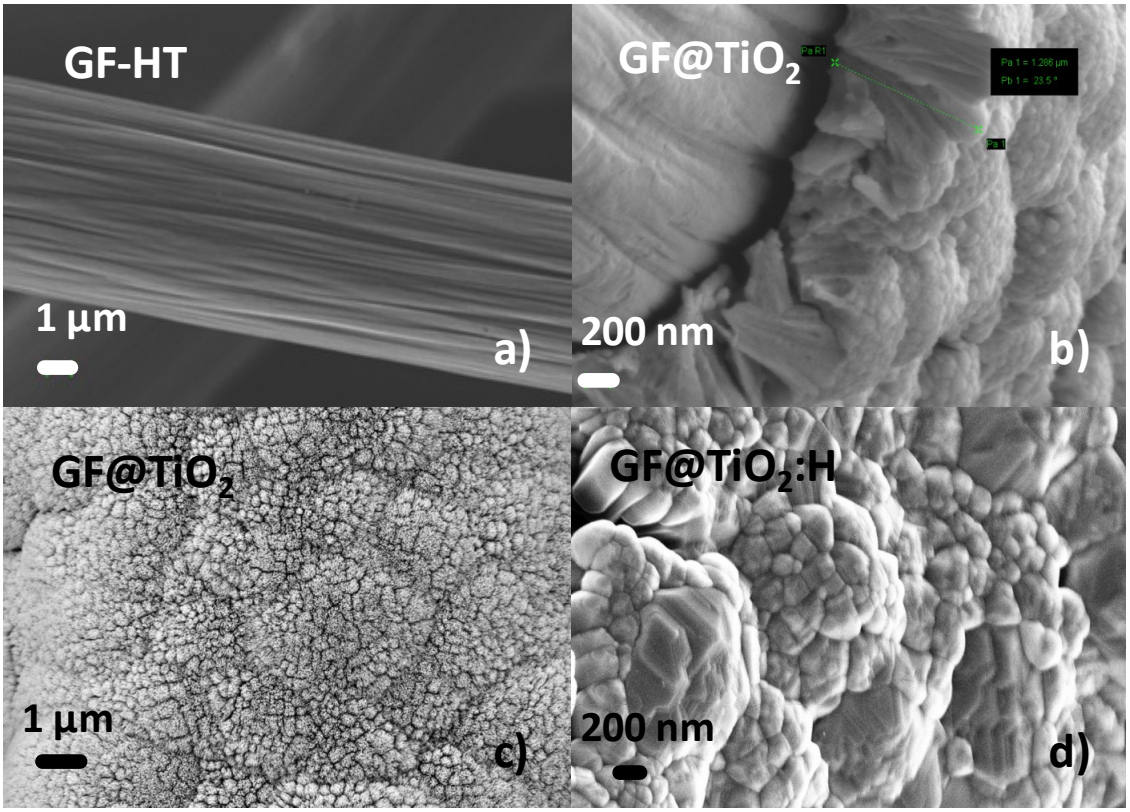

Figure 6.9. - FE-SEM images of the **a)** core graphite GF-HT; **b)** core/shell structure showing a cross section of the TiO_2 coating layer; **c)** morphology details of the coating layer of the GF@TiO_2 electrode; **d)** coating layer of the GF@TiO_2:H electrode.

X-ray diffraction pattern of GF-P, GF@TiO_2 and GF@TiO_2:H electrodes are given in **Figure 6.10.a**. The broad peak near 2θ = 25º and 43º in the spectrum of GF-P electrode is attributed to the crystallographic planes of (002) and (004) of the originally GF electrode. By comparing the XRD patterns of all GF electrodes, it can be found that the XRD patterns originally from GF show a strong decrease in diffraction intensity after TiO_2 coating. Additional diffraction peaks were appearing in the pattern of GF@TiO_2 electrode at 27.4º; 35.8º and 54.3º; which are consistent with the rutile TiO_2 (110), (101), and (211) crystalline planes, respectively. All peaks are in line with the standard pattern (JCPDS no.: 21-1276). After hydrogen treatment, the obtained GF@TiO_2:H displayed the same XRD patterns, indicating that no phase transition occurred in the reduction process.

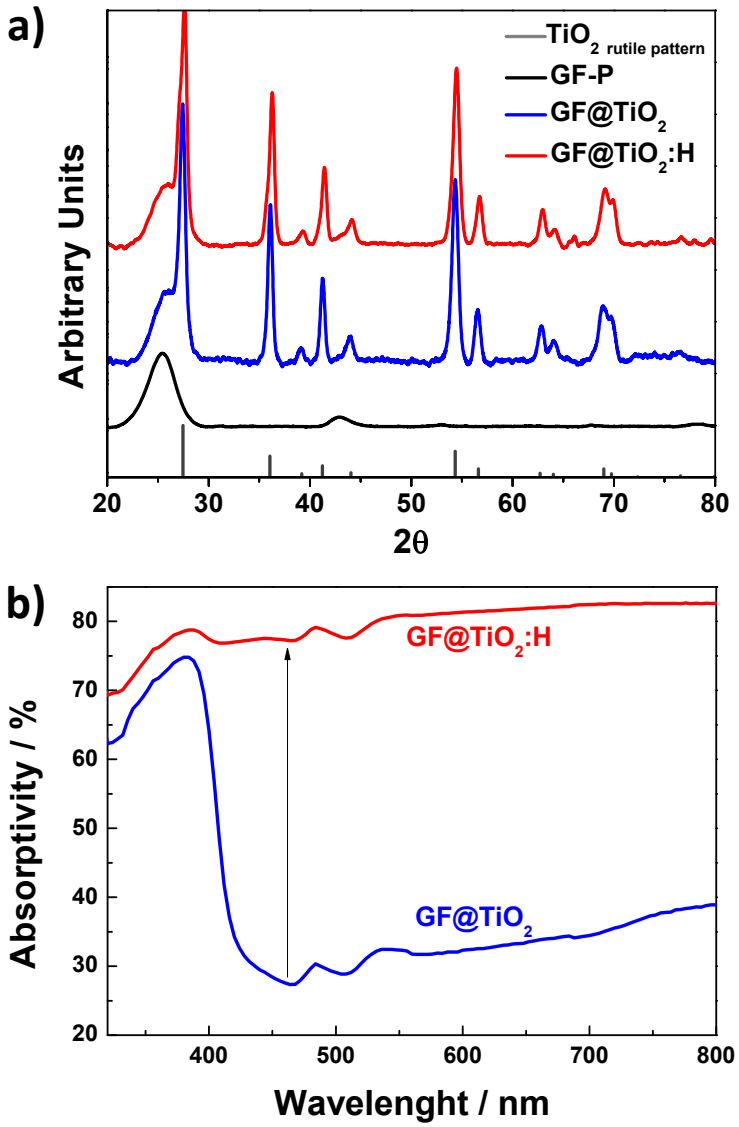

Figure 6.10. - **a)** X-ray diffraction spectra of GF electrode and as-prepared GF@TiO_2 and GF@TiO_2:H electrodes; **b)** UV-visible absorption spectra.

TiO_2 nanorods after hydrogen thermal treatment displayed a color change from white (GF@TiO_2) to blue. This suggested that GF@TiO_2:H electrode has an optical response in the visible range extending its absorption from UV into 800 nm (**Figure 6.10b**) in contrast to GF@TiO_2 electrode, which only presents absorption in the UV region (< 400 nm). This expansion in the absorption from the UV to visible spectra could be attributed to oxygen vacancies formation in the titanium dioxide structure (bands at 441 and 486 nm), responsible for the changes in the electronic distribution, and therefore, the blue colour[190,199]. These defects, clearly evidenced by UV/vis absorption spectra above 500 nm, could play an important role in the electrocatalytic properties towards negative reaction in VRFB.

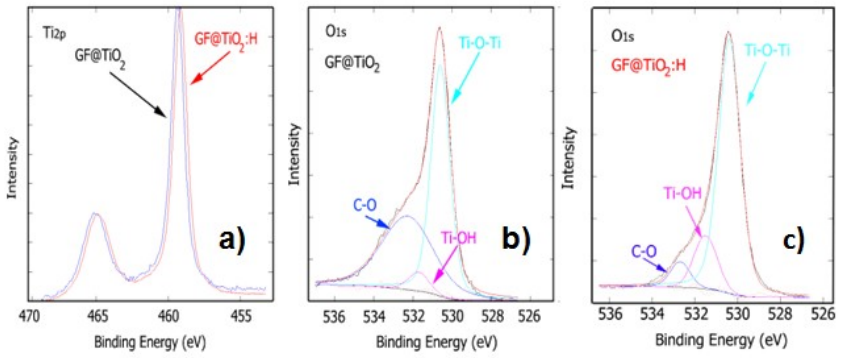

Figure 6.11. - **a)** XPS Ti 2p core level spectra of the GF@TiO_2 and GF@TiO_2:H electrodes; **b)** XPS O1s core level spectra of GF@TiO_2 and **c)** GF@TiO_2:H electrode.

Furthermore, we examine the change of surface chemical bonding of TiO_2 induced by hydrogen thermal treatment. It was performed an X-ray photoelectron spectroscopy (XPS) measurement on both samples, i.e. GF@TiO_2 and GF@TiO_2:H electrodes (**Figure 6.11.a**). The positions of the peaks were calibrated to the graphite peak at 284.3 eV. Although both TiO_2 nanorods displayed typical Ti 2p core-level XPS spectra with Ti^{4+} characteristics (strong Ti $2p_{3/2}$ peak at binding energy ~459.0 eV and Ti $2p_{½}$ at 464.8 eV), GF@TiO_2:H electrode displayed these peaks negatively shifted, which evidences a closer Fermi level to the conduction band. Therefore, it confirms a higher electron-donor density (enhanced conductivity)[200], coherent with the UV-vis information previously mentioned. However, no presence of Ti^{+3} have been determined from XPS spectra. The O 1s core-level XPS spectra of the GF@TiO_2 and GF@TiO_2:H electrodes can be convoluted in three different peaks revealing chemical structure differences between the involved materials. First, one at 530.6 eV attributed to Ti-O-Ti species. Second, another peak at 531.7 eV related to Ti-OH groups. Last, a broad band centred at 532.3 eV related to oxygen bonding to carbon on the surface

of graphite felt. From the fitting (**Figure 6.11.b** and **Figure 6.11.c**), can be seen that the bonding Ti-OH/Ti-O-Ti ratio significantly increases almost 150%, from 8.1 in the GF@TiO_2 electrode to 19.6 in case of GF@TiO_2:H. Additionally, it was observed a factor six diminution of the C-O bonding signal in the hydrogenated sample. All evidences mentioned confirm a partial reduction due to titanium dioxide oxygen deficiency as well as hydrogen absorption over the oxygen atoms linked to the Ti.

6.1.2.1.1 Electrochemical characterization

Studying the electrochemical characterization of the used electrodes, It was measured the surface resistance of them using a single cell. From the I-V representation it can be obtained an initial value of 49.5 mOhm/cm^2 for GF-P, which is increased when we covered with a TiO_2 shell (185.2 mOhm/cm^2) due to the semiconductor nature of the material. Accordingly with the XPS data treatment, the partial reduction of the shell to generate TiO_2:H enhances the conductivity which is exposing as a diminution in the surface resistance (26.8 mOhm/cm^2) below the initial value of pristine GF. These values are coherent with the electrochemical impedance spectroscopy (EIS) for the V^{3+}/V^{2+} redox reaction happening on the electrode, showing the same behaviour (**Figure 6.12**).

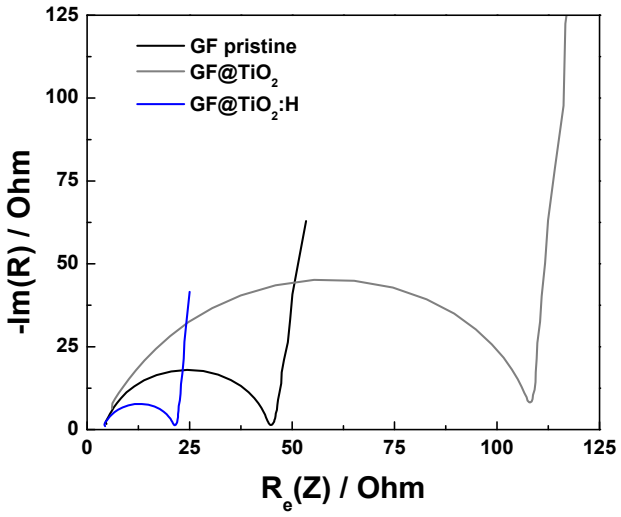

Figure 6.12. - Cell scheme employed to measure the electrode's electrical resistance.

In order to experimentally verify the inhibition of the hydrogen-evolution reaction of the as-prepared electrodes, it was conducted linear sweep voltammetry (LSV) measurements using sulphuric acid media without vanadium electroactive ions (1M H_2SO_4). The current intensity obtained from these analyses corresponds to HER

(6.1). As it can be seen in **Figure 6.13.a**, there is a relevant modification in the HER caused by the presence of the TiO_2 coating layer onto the graphite felt, while the GF-P electrode shows a maximum value of current-to-weight ratio up to 5.5 Ag^{-1}, GF@TiO_2 and GF@TiO_2:H electrodes present 0.6 and 0.2 Ag^{-1}, respectively. The lower onset potential value showed in **Figure 6.13.b** also clearly evidences the poor HER that takes place on the TiO_2 nanorods. In case of GF-P electrode, the onset potential was -0.1 V vs. NHE, while this potential was shifted to more negative values, up to -0.6 V vs. NHE for TiO_2-based electrode. The most striking feature is that the HER contribution is very important using GF-P as negative electrode in VRFB at the V^{3+}/V^{2+} redox potential, (ca. -0.26 V vs. NHE), indicating the competition between both reaction.

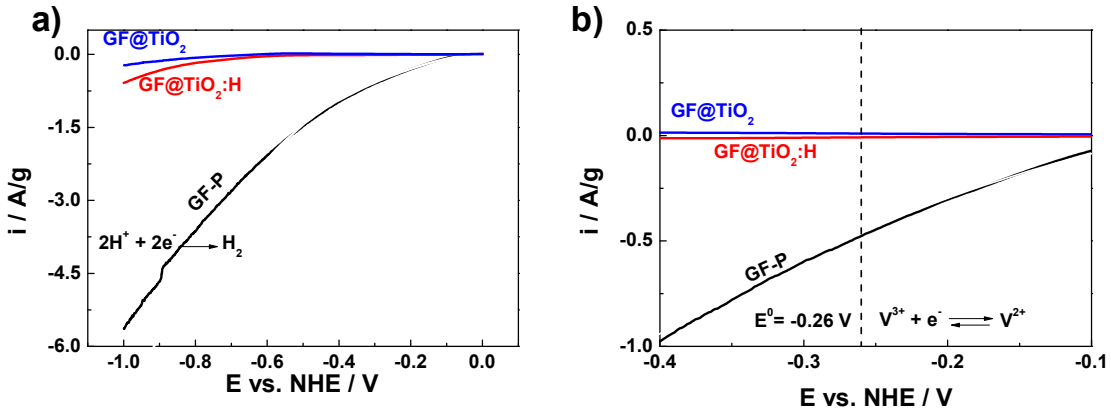

Figure 6.13. -. **a)** Linear sweep voltammetry (LSV) of pristine graphite felt, GF@TiO_2 and GF@TiO_2:H electrodes using a 1M sulphuric media with potential window of 0 to -1V; **b)** Hydrogen-evolution reaction at E^0= -0.26 V obtained from figure a) at the standard reduction potential value for negative reaction. Scan rate: 2 mV/s.

Nevertheless, the hydrogen-evolution reaction is totally absent using GF@TiO_2 or GF@TiO_2:H electrodes at this potential, guarantying a superior performance. These results can be thermodynamically explained by a largely negative Gibbs free-energy of the intermediate hydride state (ΔGH^*), indicating a highly energetic adsorption of the atomic hydrogen on TiO_2-site. From volcano-type relationship (**Figure 6.14a**), the hydrogen-binding energy (HBE) of the intermediate hydride state is obtained, ca. 70 kcal mol^{-1}. This HBE value is large, leading to a slow desorption in successive steps and in consequence, reducing the hydrogen-evolution rate (j_o). The optimal value of ΔGH^* should be zero (i.e. $\Delta G^{Pt}{}_H{}^* \sim 0.09$ eV), corresponding to the highest hydrogen-evolution rate; for instance, in the case of well-known highly efficient platinum catalyst (see the schematic representation of free-energy diagram for TiO_2 and Pt electrocatalyst in **Figure 6.14b**).

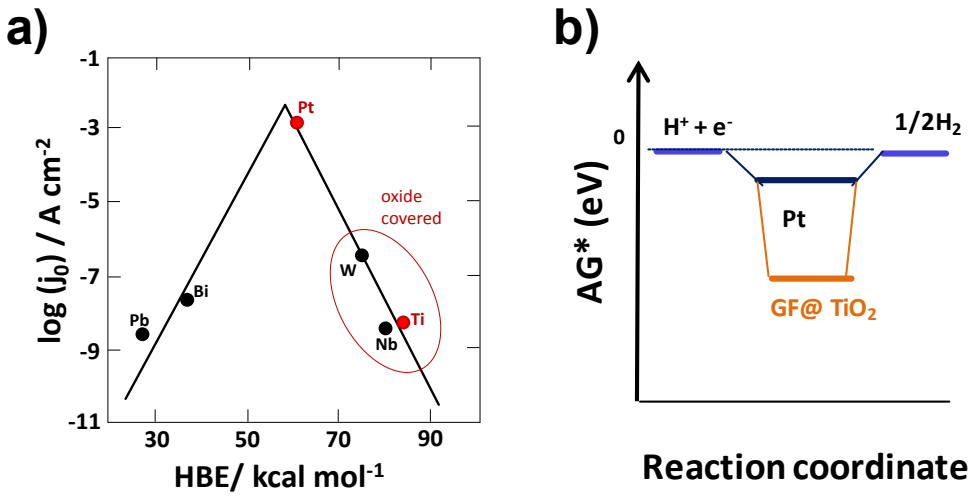

Figure 6.14. - **a)** Volcano-plot where HBE is the hydrogen-binding energy and j_o denotes the exchange current density[193]; **b)** schematic representation of free-energy diagram of intermediate hydride state.

Thereafter, the electrocatalytic reaction of TiO_2 nanorods materials towards the negative reaction of the VRFB was investigated and compared to raw GF-P electrode. **Figure 6.15a** shows cyclic voltammetry experiments (CVs) for all materials under study. To evaluate the performance, we analysed several parameters from CVs, described as follow: the peak-to-peak potential separation (ΔV), the ratio of oxidation and reduction peak current (I_{pa}/I_{pc}), and the redox onset potential. Significant differences between all samples can be observed, for example, the GF-P electrode does not display an anodic peak, but a poor cathodic peak can be appreciated (i.e. low current density peak). The irreversibility behaviour is ascribed to the high contribution of hydrogen-evolution reaction occurring on GF-P and GF-HT electrodes. This effect on the thermal treatment has been evaluated upon the negative reaction in VRFB, showing absence not only of the anodic peak, but also de cathodic (**Figure 6.16**). On the contrary, well-defined peaks for both oxidation and reduction processes were obtained using the GF@TiO_2 and GF@TiO_2:H electrodes, indicating the positive effect of the TiO_2 coating. Comparing both electrodes, the most pronounced peaks appeared using GF@TiO_2:H electrode. It is obtained current-to-weight ratio values of 0.4 and 0.6 Ag^{-1} for the cathodic, 0.268 and 0.670 Ag^{-1} for the anodic peak considering GF@TiO_2 and GF@TiO_2:H electrodes respectively. Consequently, the ratio of the redox peak current (I_{pa}/I_{pc}) value obtained for GF@TiO_2 electrode is 0.67 and 0.96 for GF@TiO_2:H, near to the ideal value, which is the unity for one electrode transfer process. Moreover, the onset potential is significantly reduced from GF@TiO_2:H electrode was around 15mV higher than that of GF@TiO_2 electrode, as shown in **Figure 6.15b**. Additionally, the potential peak separation for GF@TiO_2 electrode (ΔV= 273 mV) is approximately 50mV larger than in case of GF@TiO_2:H electrode (ΔV= 225 mV), indicating higher reversibility over the last one.

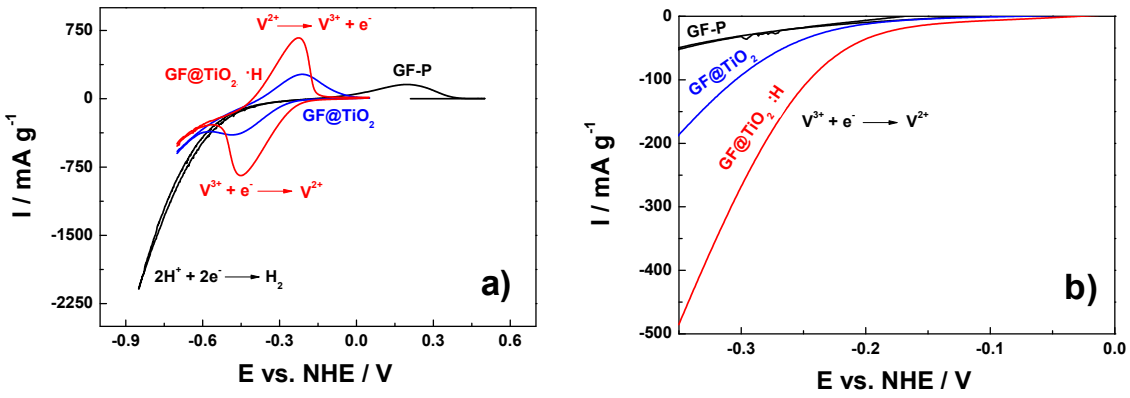

Figure 6.15. - a) cyclic voltammetry performed for negative half-cell using the as-prepared electrodes in 0.05 M V^{3+} and 1M H_2SO_4. Scan rate: 2 mV/s. **b)** Onset potential obtained from figure a).

The origin of the improved electrochemical behaviour can be caused by an increment in electrical donor properties as a consequence of oxygen-vacancies generation in the lattice of the TiO_2 after hydrogen treatment. These oxygen-vacancies are known to be electron donors, determining the surface and electronic properties of TiO_2[201,202], which improve the charge transport in TiO_2 as well as the electron transfer at the interface. To demonstrate the enhancement of the electronic properties, the resistance of the electrodes was measured, increasing in the following order: $GF@TiO_2$<GF-P<$GF@TiO_2$, indicating smaller polarization for $GF@TiO_2$:H electrodes in VRFB operation. Indeed, electrochemical impedance spectroscopy measurement of $GF@TiO_2$ and $GF@TiO_2$:H electrodes showed that the charge-transfer resistance of $GF@TiO_2$:H for V^{3+}/V^{2+} reaction is markedly smaller than the $GF@TiO_2$ electrode (**Figure 6.12**). Therefore, the enhancement of the electrocatalytic properties in combination with the low hydrogen evolution reaction of the $GF@TiO_2$:H electrode demonstrates a superior performance.

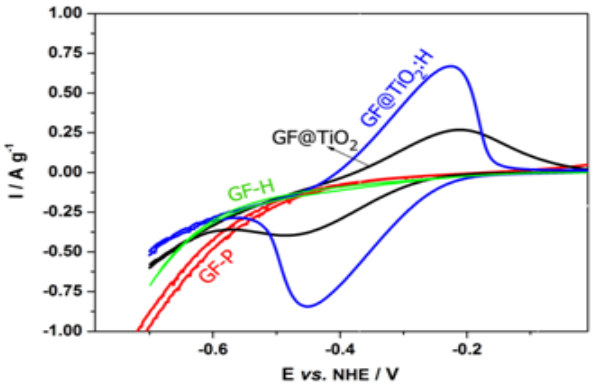

Figure 6.16. - Cyclic voltammetry of the all electrodes prepared in this work (GF-P, GF-HT, $GF@TiO_2$ and $GF@TiO_2$:H) in a 0.05M V^{3+} in 1M H_2SO_4 solution.

6.1.2.2 Single cell performance

Consequently, to ensure the potential application of TiO_2 nanorods electrodes such as a negative electrode in large-scale VRFB batteries, a flow-type single cell was assembled using a GF-P as a positive electrode, their performance was compared to pristine GF negative electrode using 1M electrolyte concentration. **Figure 6.17a**, shows a comparison of the voltage profiles developed by all electrodes between 0.8 and 1.8 V at low charge/discharge current densities (ca. 25 mA/cm^2). The GF@TiO_2:H electrode clearly yields the best performance of all. Comparing the GF-P and TiO_2-based electrodes, a significant increase in discharge capacity can be observed in the following order (the discharge capacity value obtained in Ah/L is given in parenthesis): GF-P (8.6) < GF@TiO_2 (11) < GF@TiO_2 (12.5). These results lead to 93% and 82% of the electrolyte-utilization ratio (theoretical capacity value is ca. 13.4 AhL^{-1}), using GF@TiO_2:H and GF@TiO_2 electrode, respectively. However, it is obtained near 64% of electrolyte-utilization ratio using a GF-P electrode. Additionally, a dramatically over-potential drop was detected using TiO_2 nanorods decorating the GF during the charge and discharge processes at low current. An abrupt IR drop (overvoltage drop when the current was reversed from charge to discharge) was observed in the following order (in parenthesis the value of IR calculated from the **Figure 6.17a**): GF-P (0.46 V) > GF-TiO_2 (0.28 V) ~ GF@TiO_{2-x}:H (0.27 V). These findings are consistent with the efficiency values (Figure 8b). At the same charge/discharge rate (i.e. 25mA/cm^2), the VE value increased up to ~ 90% using GF@TiO_2 and GF@TiO_{2-x}:H electrodes, in comparison to 61% using a GF-P electrode. The same trends occur with EE values and reach up to ~90% and 58% using GF@TiO_2/GF@TiO_2:H and GF-P electrode, respectively. Additionally, the CE for GF@TiO_2 and GF@TiO_2:H electrodes is ~99%, whereas for GF-P electrode the CE is. 95%. The origin of the enhanced performance can be ascribed to the total abatement of the HER carried out by the TiO_2-based graphite felt electrodes in comparison with commercial GF-P electrodes.

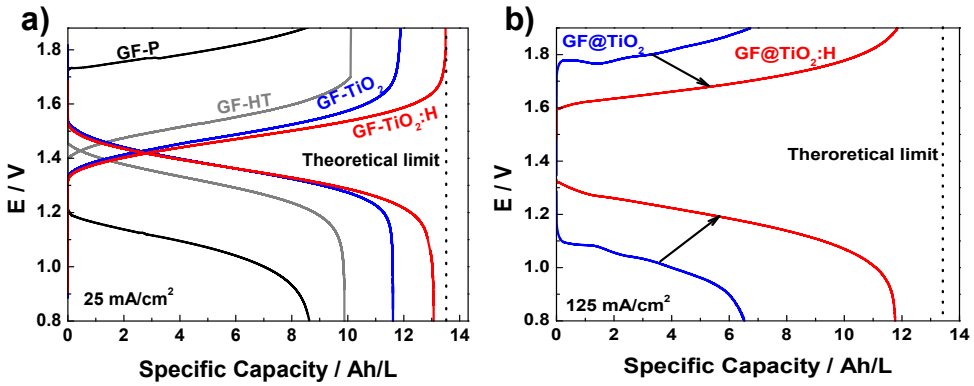

Figure 6.17. - **a)** Galvanostatic full cell charge/discharge profile for GF-P (black line), GF-HT (grey line), GF@TiO_2 (blue line) and GF@TiO_2:H (red line) at 25 mA/cm^2 using 1 M vanadium concentration in 3M H_2SO_4 as electrolyte. **b)** Galvanostatic charge/discharge profile for GF@TiO_2 (blue line) and GF@TiO_2:H (red line) at 125 mA/cm^2 using 1 M vanadium concentration in 3M H_2SO_4 as electrolyte.

In fact, the enhanced performance in VRFB for GF@TiO_{2-x}:H electrode was significantly evidenced at highest charge/discharge rate (**Figure 6.17b**), where HER has a major contribution. The most remarkable feature was the loss of electrolyte-utilization ratio of VRFB using GF@TiO_2 electrode when increasing the charge/discharge rate up to 125mA/cm^2, achieving ~7 Ah/L of specific capacity, while GF@TiO_2:H presents a value close to 12 Ah/L. It is attributed to large polarization and high over-potentials working at such high currents for a semiconductor material, limiting their rate capability. As a result, poor specific overall efficiencies were obtained (i.e. EE is 55.6% value for TiO_2, while the reduced electrode achieve a 70.7%). The GF@TiO_2:H electrode presents higher electrical properties and fast electron transfer causing low polarization and an increment in the operating current density range up to high current densities, see **Figure 6.18**. Comparatively for 1M of active electrolyte it was run for several cycles increasing the applied current density from 12.5 to 125 mA/cm^2 for GF@TiO_2, where it is obtained an optimum value of 80% electrolyte utilization at 50 mA/cm^2. It gives us a value close to 12 Ah/L. Same case-scenario for the reduced electrode obtaining an optimum (same values as mentioned before) at 150 mA/cm^2.

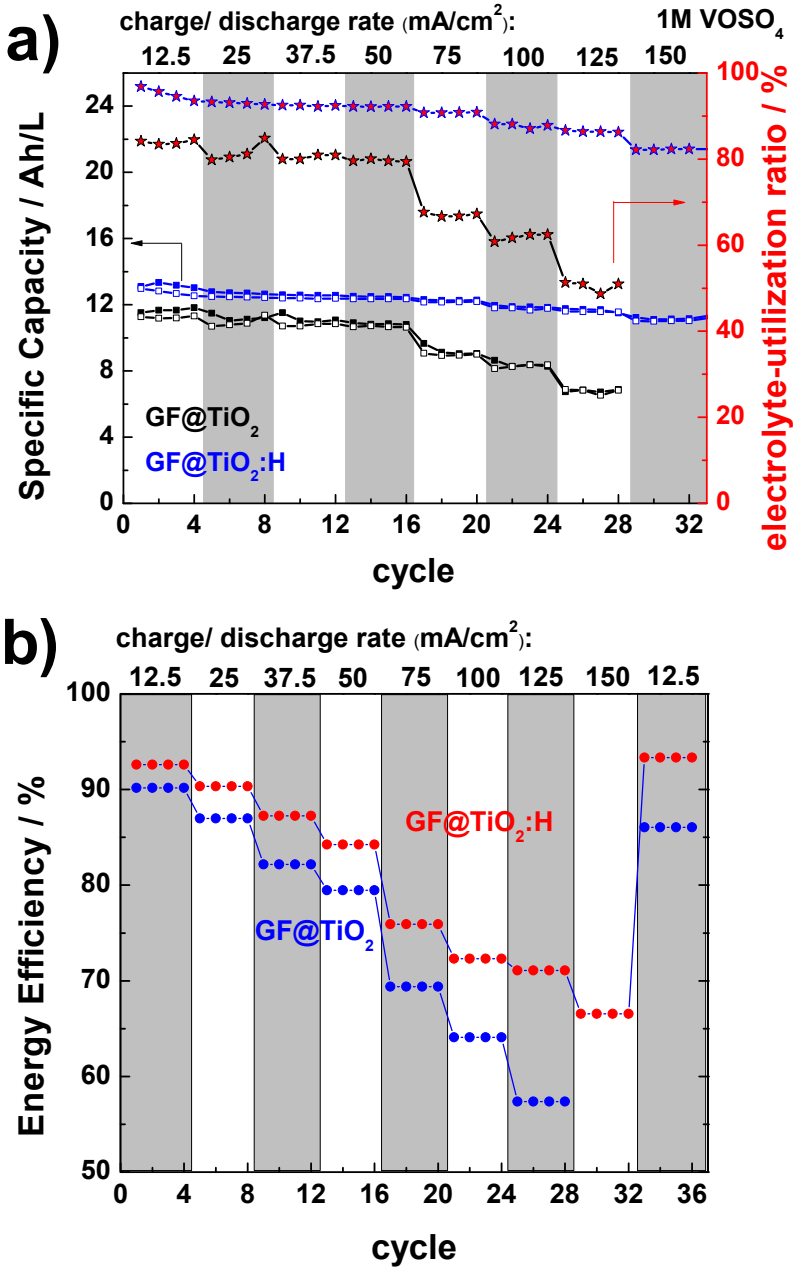

Figure 6.18. - a) Full cell specific capacity and electrolyte-utilization ratio depencency with the current density applied (from 12.5 to 150 mA/cm^2) on GF@TiO_2 and GF@TiO_2:H as electrodes, for 1M vanadium concentration and 3M H_2SO_4 as electrolyte; **b)** Full cell EE dependency with the applied current density (from 12.5 to 150 mA/cm^2) of GF@TiO_2 and GF@TiO_2:H as electrodes, for 1M vanadium concentration and 3M H_2SO_4 as electrolyte.

Then, it is performed a long cycling test at 1M $VOSO_4$ at the optimum mentioned value for GF@TiO_2:H electrode, 150 mA/cm^2 (**Figure 6.19**). Notably, the performance in terms of specific capacity discharged and EE of GF@TiO_2:H electrode remained almost unchanged, exhibiting excellent long-term stability after 100 cycles. The GF@TiO_2:H electrode showed an energy efficiency of 71.2 % at 125mA/cm^2 and 66.1 % at a rate of 150mA/cm^2; in both cases the specific capacity is maintained at a value ca. 11 Ah/L. After high current

polarization, 150mA/cm^2, a remarkable recovery to the initial values, shown in **Figure 6.18b**, to low current density (i.e 12.5mA/cm^2) was observed.

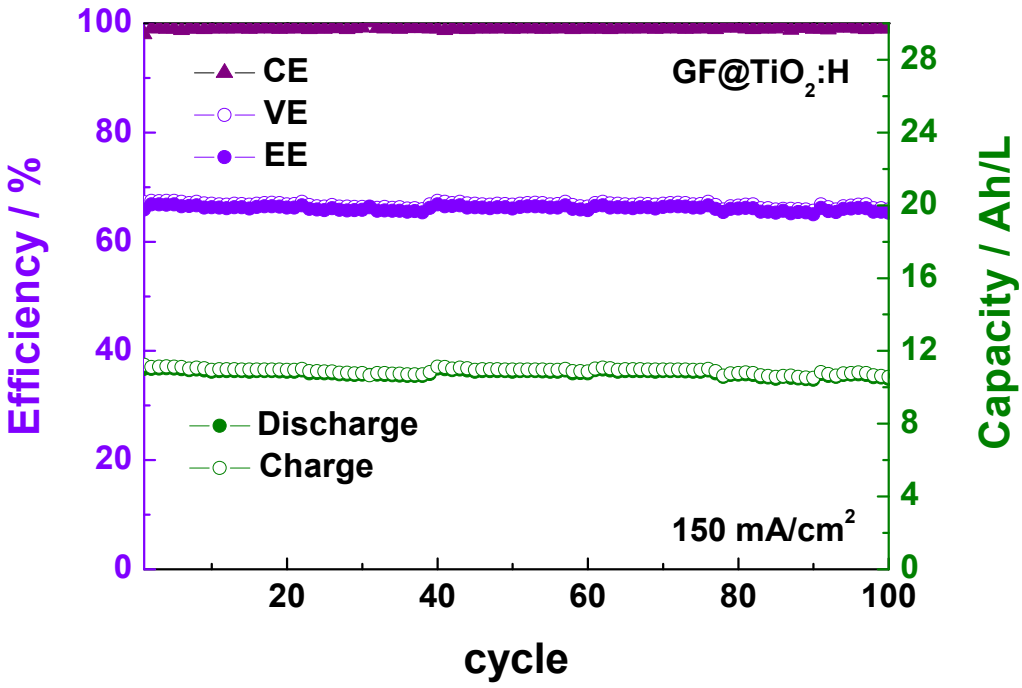

Figure 6.19. - Long-term cycling of the GF@TiO_2:H electrode in a single cell for 1M $VOSO_4$ and 3M H_2SO_4.

Thereafter, it is cycled the same prototype of the VRFB with a higher concentration of vanadium ion (2 M $VOSO_4$) and same acidic conditions (3 M H_2SO_4) are evaluated at high current density, in order to improve the amount of active material in the same volume, being capable of duplicate the energy per volume. Obtaining an electrolyte-utilization ratio of 81%, 62%, and 40% related to 200, 250, and 300 mA/cm^2, respectively. In spite of the larger polarization due to the increased active ion concentration, these outstanding performances (**Figure 6.20**) (i.e. 300 mA/cm^2), show an excellent result in terms of specific capacity and CE vales. Comparatively with the results obtained by Tseng et al (2014) at 200 mA/cm^2, the CE attains values up to 90% at 3rd cycle. However, the CE value VRFB using GF@TiO_2:H electrode remain constant during cycling to reach values up to 96%, indicating that GF@TiO_2:H electrode, guarantee working without capacity fading (absence of side reactions) at high current densities for concentrated electrolytes in $VOSO_4$. The maximum reached current density for stable cycling is 350 mA/cm^2. However, the values obtained are poor (41% VE, 98% CE, 40% EE and 4.4 Ah/L).

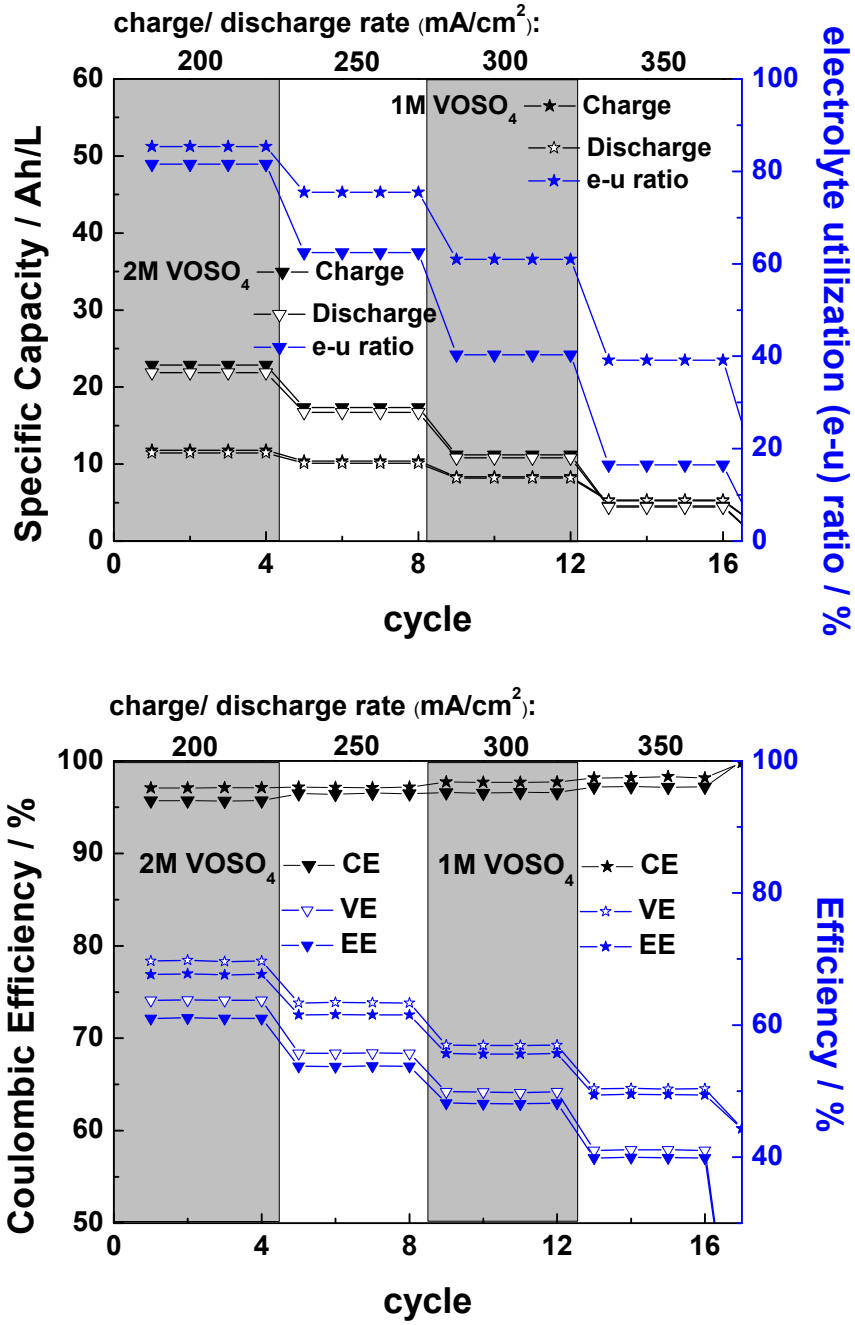

Figure 6.20. - On the top, full cell specific capacity and electrolyte utilitation ratio dependency with the current density applied (from 200 to 350 mA/cm^2) on GF@TiO_2:H for 1 and 2M vanadium concentration in 3M H_2SO_4 as electrolyte. Above, CE, VE and EE dependecy with the current density applied (from 200 to 350 mA/cm^2) for GF@TiO_2:H for 1 and 2M vanadium concentration in 3M H_2SO_4 as electrolyte.

Additionally, EE values of 61% at 200 mA/cm^2 are obtained much closed to the maximum EE value obtained by Tseng et al (i.e. 65.4%). Besides, the previous experiments at 2M are compared with 1 M electrolyte in order to evaluate the performance of GF@TiO_2:H electrode at high current density. In this case, we obtain a specific capacity value, Ah/L (in parenthesis is given the electrolyte-utilization ratio in %) of: 11.77 (88); 10.33 (77); 8.4 (63) and

12.6 (94) at 150, 200, 300 and 25 mA/cm^2. The efficiencies values remain constant, achieving CE~96% for charge/discharge rates applied and EE values attain up to 67.5% at 200 mA/cm^2. It is clearly observed an efficiency decrease related to the concentration as it is expected due to an increasing polarization of the ionic species solvated.3

Finally, based on all the presented results, the mechanistic interpretation is proposed for all electrodes used (**Figure 6.21**). Firstly, V^{3+} ions interact with the hydroxyl groups on the graphite felt surface, generating O-V bonds, which extract a proton to the solution. Consequently an electron is donated to the V^{3+} reducing it to V^{2+} and breaking the previously formed bond (O-V) and taking the proton again from the solution. In this case, this redox reaction competes with the hydrogen evolution reaction as the protons are easily adsorbed to the C surface to form an H-H bond and lastly be desorbed. The last reaction is kinetically more favourable causing imbalance and low performance, for which we look for a catalyst to inhibit HER and enhance the V^{3+}/V^{2+} redox reaction. Secondly, after the coverage with TiO_2 there are two conditions that favour the V^{3+} reduction: i) Increase of –OH groups due to the presence of titanium dioxide itself that promote the number of active sites for the reaction to happen, enhancing the electron charge transfer at the interface electrode/vanadium. ii) Highly stable proton absorption over the Ti-O bond inhibiting side reaction as HER. However, large electrode polarization is dominant at high rate capability leading to a limited specific capacity and a modest electrolyte-utilization ratio. Thirdly, the partially reduced sample (TiO_2:H) favours the V^{3+}/V^{2+} due to an increment in electron mobility as an increasing hydroxyl active sites are present on the surface, and therefore, more vanadium ions are capable of react simultaneously.

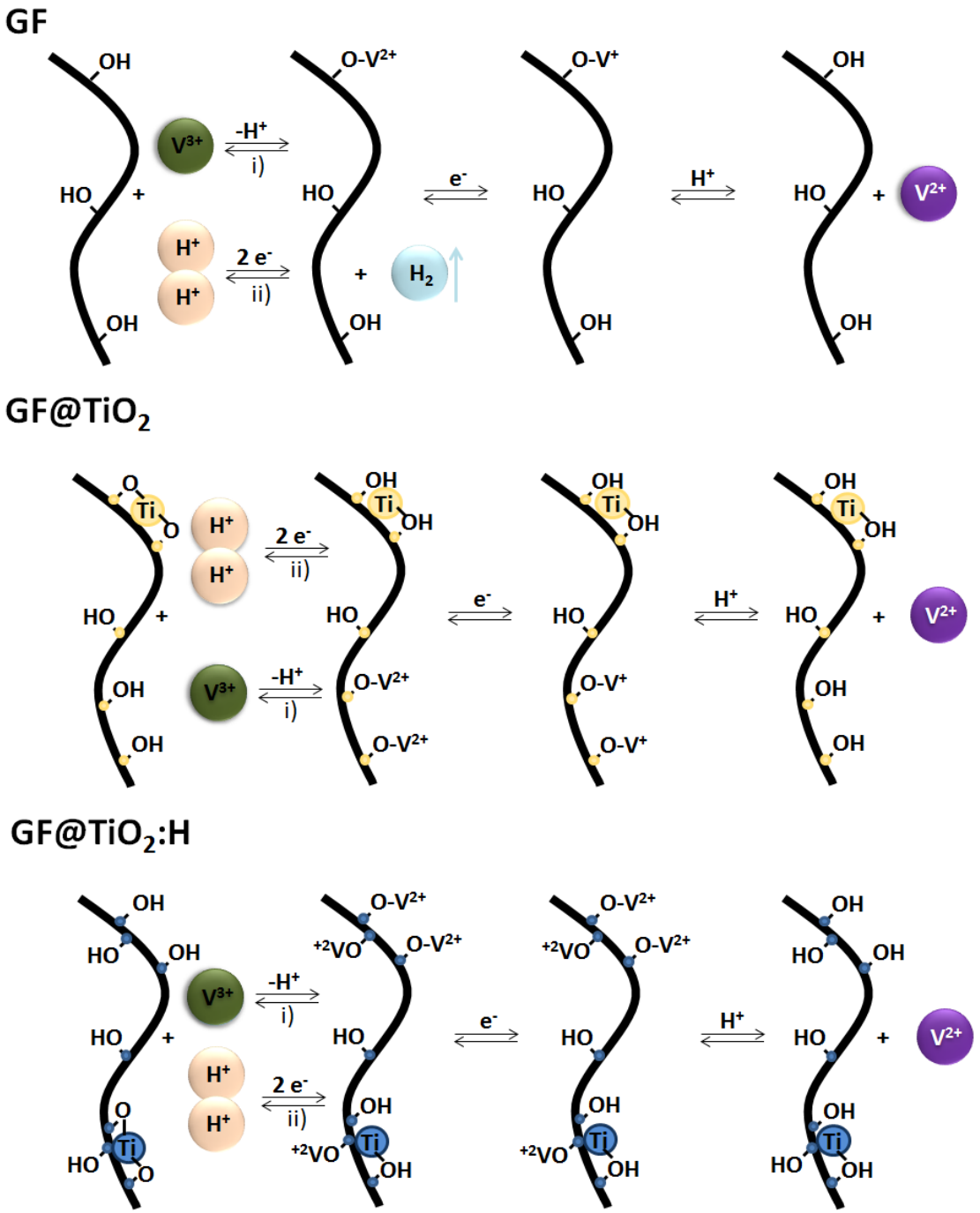

Figure 6.21. - Mechanism proposed for VRFB's negative reaction using GF, GF@TiO_2 and GF@TiO_2:H as electrodes.

In brief, TiO_2:H based graphite felt electrode, as a low-cost, efficient and novel electrocatalyst towards the negative reaction was demonstrated to enhance the electrochemical performance in all-vanadium redox flow battery, especially at high charge/discharge rates. GF@TiO_2:H electrodes showed greatly improved electrochemical properties (i.e. fast electron charge process) in combination with a better selectivity to V^{3+}/V^{2+} reaction, inhibiting hydrogen-evolution reaction. Furthermore, the electronic donor properties

are increased, comparatively with pristine and thermal treated, as a consequence of the oxygen-vacancies formation in the structure of titanium dioxide. A specific discharge capacity of around 11 Ah/L with a 66.1% of energy efficiency was observed after 100 cycles of charge/discharge at high current densities rates up to 150mA/cm^2. In addition, significantly improved the electrolyte-utilization ratio to 87% was achieved using 1 M in vanadium solution. Afterwards, the performance of 2 M vanadium ion concentrations has been evaluated at high current density up to 300 mA/cm^2 during 140-cycles, showing the great durability of the battery. Particularly, at 200 mA/cm^2 the CE value was > 96%, electrolyte-utilization ratio was 80%, with a specific capacity of 22 Ah/L, demonstrating the total suppression of HER and long term stability of VRFB. These results (**Table 6.3**) suggest that the TiO_2:H based graphite felt is a powerful electrocatalyst for high-performance VRFB application.

Table 6.3- Efficiency and electrolyte utilization ratio as a function of several variables as electrode, electrolyte concentration and current density applied.

Negative electrode	cycle /number	Electrolyte concentration / M	Current density / mAcm^{-2}	Electrolyte-utilization ratio / %	CE / %	VE / %	EE/ %
GF-P	1	1	25	64	95.0	61.0	58.0
GF@TiO_2	1	1	25	82	98.8	90.0	89.0
GF@TiO_2:H	1	1	25	93	98.9	91.0	90.0
GF@TiO_2:H	120	2	25	100	96.4	94.0	90.6
GF@TiO_2	28	1	125	48	96.3	57.7	55.6
GF@TiO_2:H	28	1	125	86	99.1	71.9	71.2
GF@TiO_2:H	96	1	150	83	99.3	66.6	66.1
GF@TiO_2:H	101	2	200	80	96.0	64.0	61.4
GF@TiO_2:H	124	1	200	77	97.0	69.0	67.6
GF@TiO_2:H	130	1	300	63	97.5	56.7	55.5
GF@TiO_2:H	104	2	250	60	96.0	55.6	53.6
GF@TiO_2:H	109	2	300	40	96.7	49.5	47.8
GF@TiO_2:H	140	1	25	94	92.0	95.0	87.7

6.1.3 Nitrided titanium dioxide (TiO_2-N)

In this section, an enhanced catalyst applied to all-vanadium redox flow batteries (VRFBs) has been developed. It is made of a structural porous carbon felt covered by TiO_2 rutile phase, which is nitrided using ammonia annealing at high-temperature (900^oC). Consequently, a synergetic effect of N- and O-functionalization over carbon felt (CF) and partially formed TiN (metallic conductor) phase onto the TiO_2 decorating electrode's structure shows an outstanding charge and mass transfer over the electrode-electrolyte interface. In this case, carbon felt (CF) is used instead of graphite felt (GF) as a raw material due to the lower graphitization grade of CF, which will help having a larger initial surface functionalization and reducing synthesis cost. However, CF has a lower conductivity and heavier weight comparatively to GF. Moreover, this material (CF@TiO_2:N) has

not only improved in terms of catalysis towards the V^{3+}/V^{2+} redox reaction (k_0= 1.6 x 10^{-3} cm s^{-1}), but also inhibited the hydrogen evolution reaction (HER), which is one of the main causes of imbalances that lead to battery failure. This has allowed us to achieve an impressive high-power peak output value up to 700 *mW cm*$^{-2}$ (**Figure 6.22**), as well as work at high current density in galvanostatic conditions (i.e. 150 *mA cm*$^{-2}$), exhibiting low ohmic losses (overpotential) and great redox reversibility of the device for a conventional single cell. It allows our system to reach a superior Energy Efficiency (71%). An inexpensive, earth abundant, environmentally friendly and scalable synthesis method to boost VRFBs technology based on nitrided CF@TiO_2 is presented, being able to overcome certain constrains, and therefore to achieve high energy and power density working conditions.

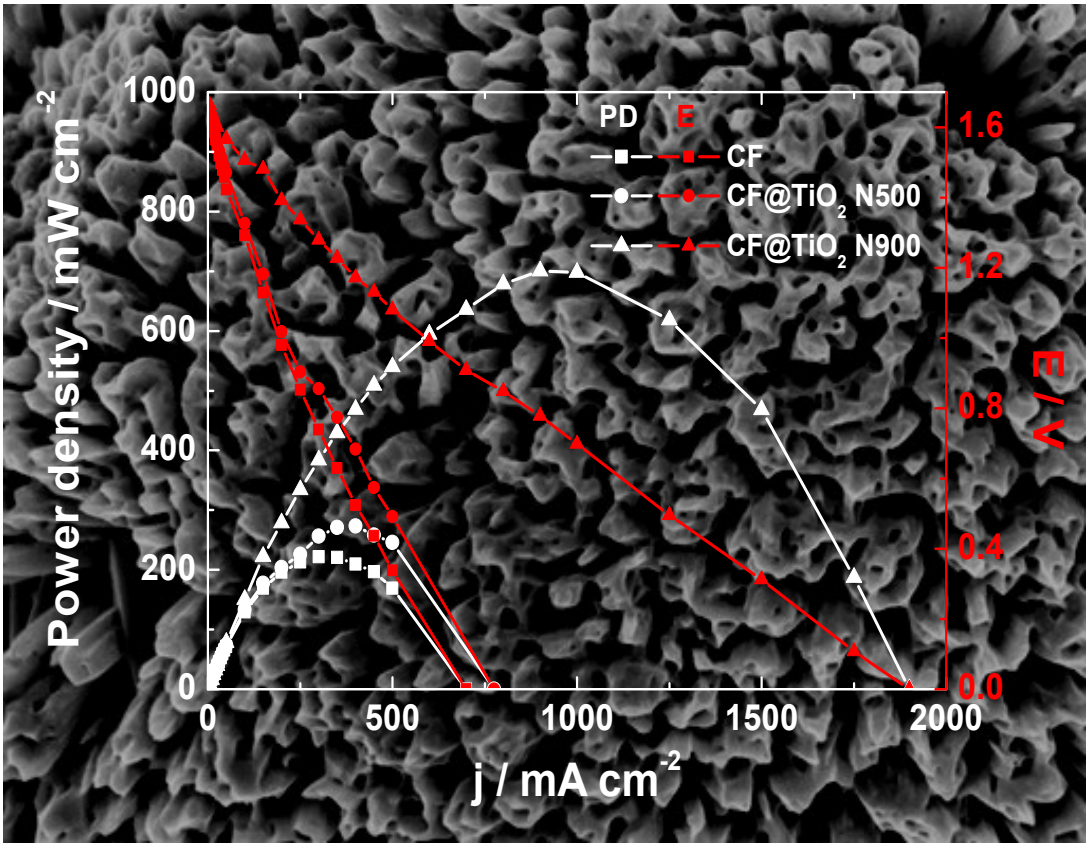

Figure 6.22. - Scheme of the power rate for the different electrodes involved in this section. The picture behind shows the GF@TiO_2:N after cycling.

Therefore, using free-standing TiN nanowires synthesized by a two-step process, in which TiO_2 nanowires are first grown onto the surface of graphite felt via a seed-assisted hydrothermal method and then partially converted to TiN through nitride reaction, synergistically coupled with the functionalization (O- and N-groups) done at the surface of the carbon felts making the electrode even more enhanced towards V^{2+}/V^{3+} redox reaction. An energy efficiency values above 70% have been obtained at high current densities, of up to 300 *mA cm*$^{-2}$. In addition, the electrodes exhibit good stability and high capacity retention during the cycle tests. This excellent performance is

explained by assuming that there is a first step of the overall reaction that involves an ion exchange process between V^{3+} ions transported from the bulk of the electrolyte and the hydrogen atoms located at the Ti-N-O-H and Ti-N-H surface bonds. In this way, V^{3+} ions can be adsorbed easily on the Ti-N and Ti-N-O bonds. In a second step, electron transfer takes place, facilitated by Ti-N and Ti-N-O bonds acting as an electron donor. In the final step, the reduction reaction is completed by an ion-exchange between the V^{2+} formed on the electrode surface and the protons in the electrolyte. During the discharge process, a similar oxidation reaction in the opposite direction occurs. Unlike our previous article[89] based on carbon felt electrodes covered by TiO_2, here the outstanding electrical conductivity of TiN provides an explanation for the better battery performance of the electrode due to improved electron transport and transfer.

.Furthermore, nitrogen-doped carbon samples have been widely investigated for electrochemical applications[203], especially for the oxygen reduction reaction in fuel cells, concluding that the facilitated adsorption of oxygen allowed by the presence of nitrogen improves the electrocatalytic activity of carbon materials[204–207]. Moreover, the formation of C-OH, C=O, and C-O functionalities has also been shown to enhance cell performance[208]. The formation of O functional groups increases the standard heterogeneous electron transfer rate for V^{3+}/V^{2+}, from 3.2x 10^{-7} to 1 x 10^{-3} *cm* s^{-1}, one of the highest values ever reported[209]. Moreover, the introduction of N surface functional groups has also been shown to help decreasing the fraction of the current directed towards H_2 evolution[89]. Among the four main types of nitrogen groups, the quaternary or graphitic-N has been found to be the more stable in the acidic environment[208]. However, pyrrolic-N has been proposed to be the most electrochemically active nitrogen site for enhancing the catalytic activity in these nitrogen-modified carbon-based electrode materials for VRFB[210].

6.1.3.1 Characterization

6.1.3.1.1 Structural characterization

The morphological structures of the as-prepared electrode are characterized by FE-SEM. TiO_2 nanowire coverage directly growth into the surface of carbon felt with a rod morphology by hydrothermal process (**Figure 6.23a**). Some changes can be appreciated after the NH_3 thermal treatment, which forms local agglomerations of TiO_2-nanorods in the case of the CF@TiO_2 N500 sample (**Figure 6.23b**), due to the reductive conditions of the ammonia gas[211]. In the case of higher annealing temperatures, the rods become more compact and decrease their length (**Figure 6.23c** and **d**) with a well-dispersed rods decoration over the carbon felt surface after NH_3 treatment.

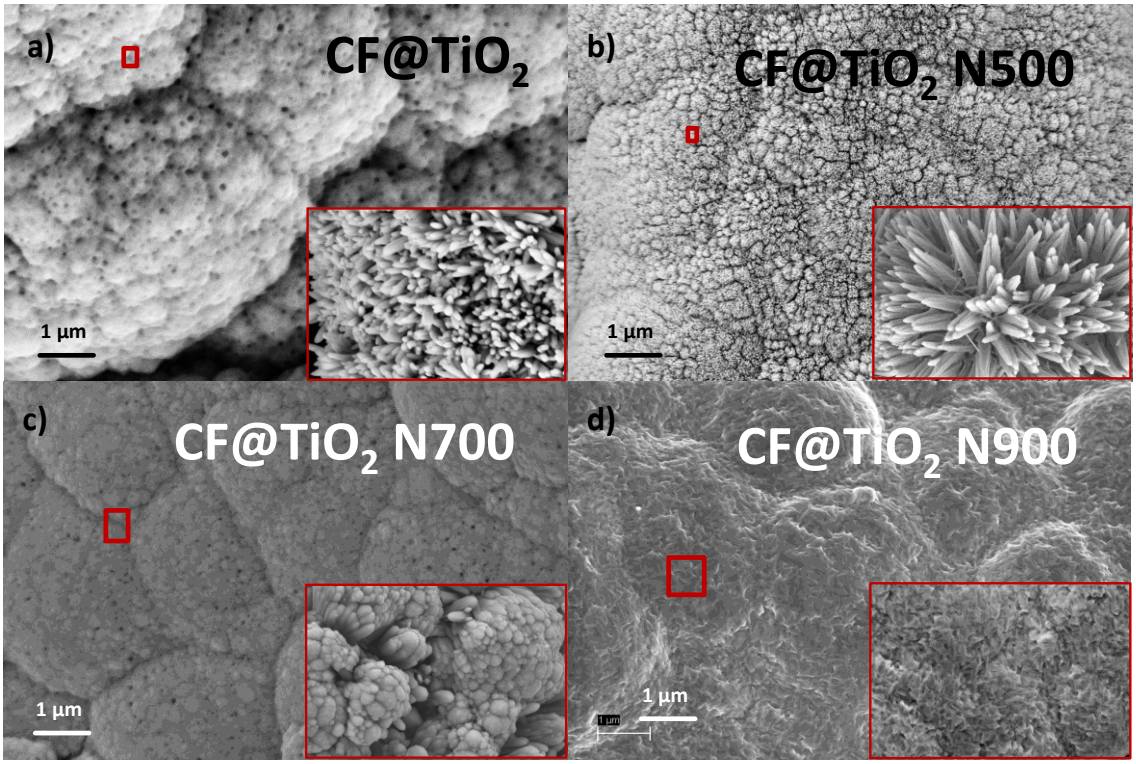

Figure 6.23. - FE-SEM images of the: a) CF@TiO2; b) CF@TiO2 N500; c) CF@TiO2 N700 d) CF@TiO2 N900.

Subsequently, the XRD spectra of the samples annealed at different temperatures (**Figure 6.24c**) shows an initial rutile (TiO_2) structure of the deposit over carbon felt with the diffraction peaks at 27.4, 35.8, and 54.38 θ, consistent with the rutile TiO_2 (110), (101), and (211) crystalline planes, respectively. All peaks are in line with the standard pattern (JCPDS no.:21-1276). After the NH_3-treatment at 900ºC, three diffraction peaks appear at 61.8; 42.7 and, 37.2 2θ, which correspond to the (111), (200) and (220) planes of the cubic TiN phase (JCPDS: 65-0714). Below 900ºC as a temperature annealing, it can only be observed a broad peak due to the nitride process at 42.7 corresponding to (210) for the rutile phase.

Therefore, a more detailed analysis **(Figure 6.24b)** of the diffraction peaks associated with the rutile phase shows a distortion of the peak profile produced by the incorporation of nitrogen into the interstitial sites of rutile phase.

i) First at all, the rutile peaks show an asymmetrical shape indicated by the area patterned with a sparse green square, as **Figure 6.24b** shows around 36º. It corraborates that nitride process due to the chemical interaction at the surface level is breaking TiO_2 bonds producing a lattice weakness generating defects and vacancies and giving rise to a damaged outermost TiO_2 layer, which justifies the asymmetrical shape of the peaks as the damaged area contributes essentially with larger interatomic distances, i.e. to the left area of the peaks[212]. The optical absorption capability of these defects with localized energy state in the bandgap of the material explains the color change revealed in the optical absorption spectra (**Figure 6.24a**).

ii) Secondly, the TiO_2 rutile structure remains even after the appearance of a cubic TiN phase around 900 °C pointing out that only a TiN formation. However, the position of the XRD pattern of the rutile peaks shift towards higher 2θ values as the temperature is increased from 500 to 900ºC, i.e. from 27,58º to 27,71º showing that rutile has undergone a nitrogen doping over titanium dioxide nanorods as temperature is increased achieving strain values (Δd/d) around +1%, where "d" is the inter-planar spacing. The crystalline domain size from these XRD spectra considering Debye-Scherer formula is around 50 *nm*.

iii) Thirdly, as the nitrided treatment reaches 900ºC, there is an overall modification of the sample structure. The broad peaks presented in the green area, observed in **Figure 6.24b,** disappears pointing out that stoichiometry of TiO_2 is recovered and TiN phase formed. Therefore, it is plausible to assume that TiN is localized at the outermost zone of the remain unaffected TiO_2, exactly where TiN stress phase formation can be relaxed. For this phase, the crystalline domain from the Debye-Scherer formula is around around 30 *nm*. Additionally, the XRD of CF@TiO_2N500 and CF@TiO_2N700 does not show any peak realated to TiN. In consequence, at this stage, TiN phase is not yet seggregated from the TiO_2 and Nitrogen is only present inside of the TiO_2 lattice such as the peak deformation corraborates. It is also worth consider such high temperatures could also functionalize the carbon felt surface.

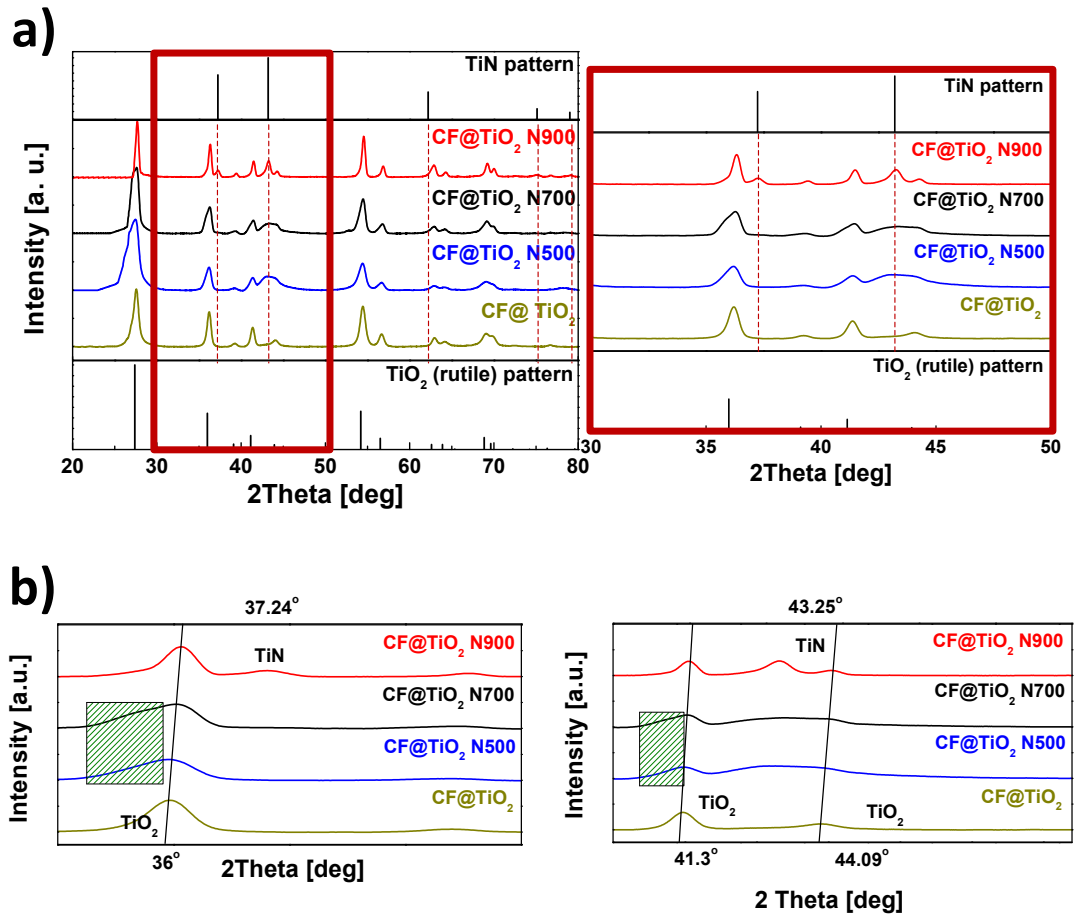

Figure 6.24. -. - a) X-ray diffractogram of $CF@TiO_2$, $CF@TiO_2$ N500, $CF@TiO_2$ N700 and $CF@TiO_2$ N900 electrodes, showing chacteristic TiN (top) and TiO_2 (rutile, bottom) patterns. **b)** Detailed analysis of the XRD peaks showing the asymmetrical shape due to the nitrided process as well as the appeareance of the new TiN phase at 900ºC.

6.1.3.1.2 Chemical Characterization

XPS spectra analysis shows the surface effects of the nitride process. The influence of nitrogen incorporation on the state of titanium was probed through the Ti2p spectra (**Figure 6.25**). Significant differences can be distinguished for the $CF@TiO_2$ N900 sample, it can be seen that 3 doublets are needed to fit the titanium signal corresponding to the different expected bonds Ti-O (458.5 eV), Ti-N-O (456.8 eV) and Ti-N (455.9 eV) in a relative percentage of 50%, 29% and 21%, respectively. Comparatively the typical TiO_2 doublet related to titanium (IV) at 458.5 e eV is seen in $CF@TiO_2$ and $CF@TiO_2$ N500, with a small additional doublet contribution from Ti (III) in the lattice structure in case of $CF@TiO_2$ N500 at 458.9 eV.

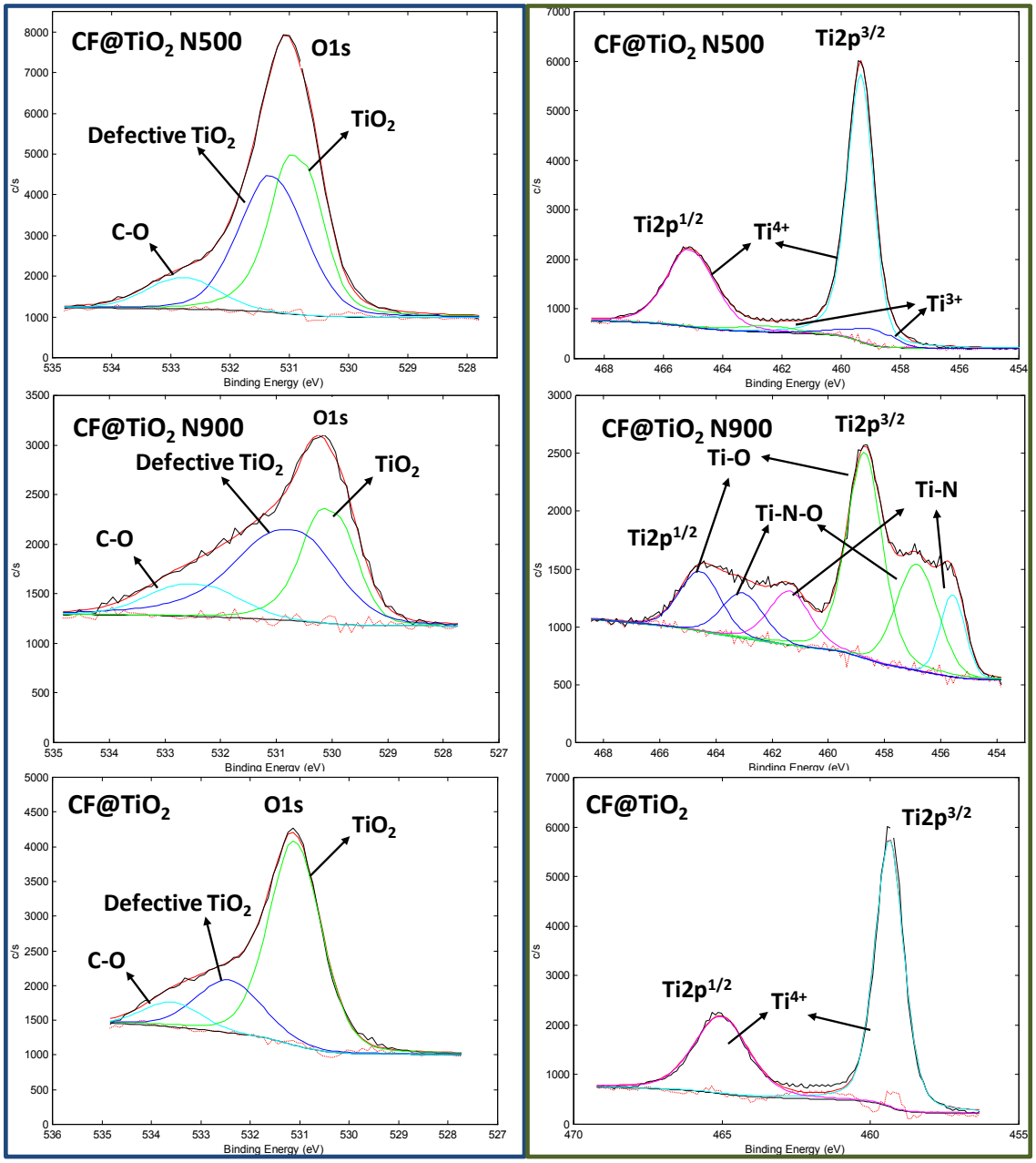

Figure 6.25 - O1s and Ti2p XPS spectra for CF@TiO_2, CF@TiO_2 N500 and CF@TiO_2 N900.

Furthermore, the O1s spectra in **Figure 6.25** shows an increasing surface defect formation over the metal oxide lattice by oxygen deficient groups, Ti-O (dark blue peaks) at 531.5 eV, following the relative area percentage: CF@TiO_2 (22%) < CF@TiO_2 N500 (45%) < CF@TiO_2 N900 (51%). There is also the existence of small contributions related to different oxygen bonds over the carbon surface centered at higher energy values (533 eV) (light blue peaks). Oxygen XPS band for CF@N900 (**Figure 6.26**) gives evidence for the oxygen groups formed on the carbon felt surface, as three deconvolution peaks related to C=O (rel. 2%) at 530.8 eV, C-O (rel. 69%) at 532.1 eV and C-O-H (rel. 29%) at 534.2 eV

Hence, bearing in mind that XPS signal is accurate for a few nanometers thickness (about 10 *nm*)[213,214], the crystalline domain determined from the XRD spectra the surface of CF@TiO_2 N900 electrode could be described as a TiO_2 surface with numerous zones of TiN (21%) surrounded by Ti-O-N transition areas between TiN and TiO_2 at surface level (29%).

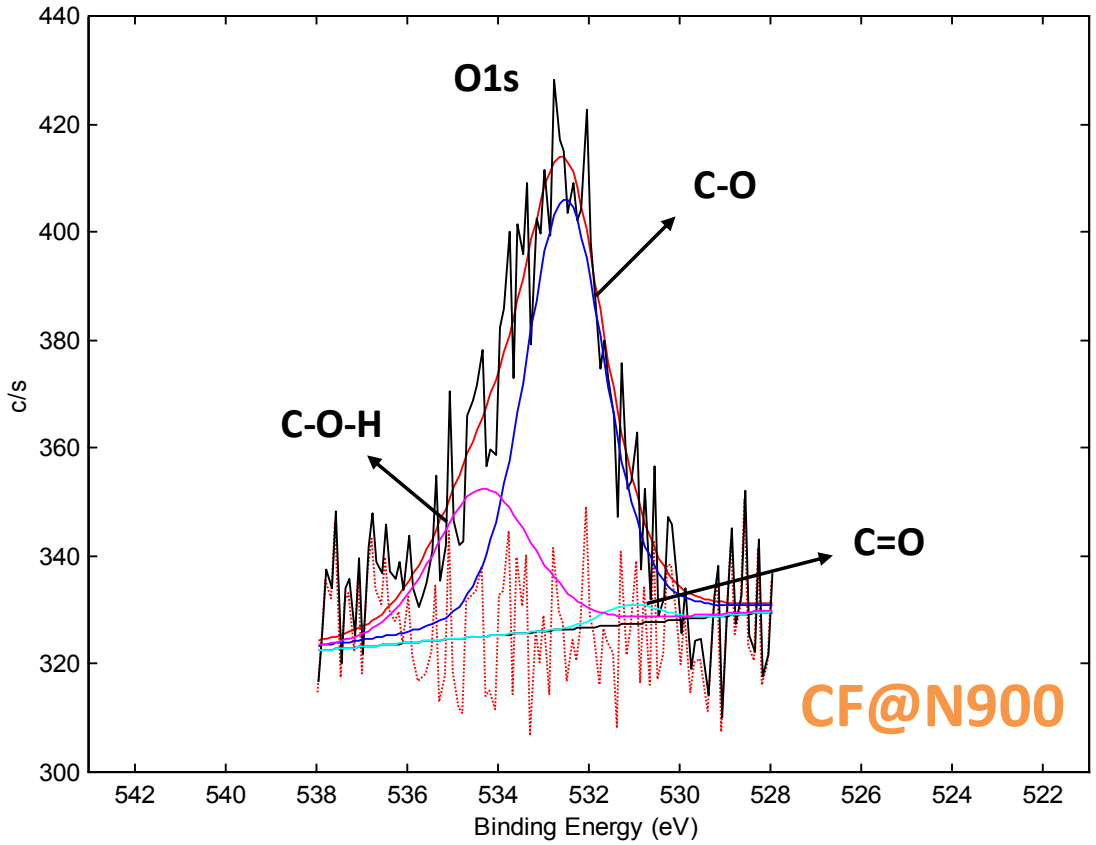

Figure 6.26 - XPS O1s band spectra for the sample CF@N900.

It is confirmed by the N1s XPS band spectra (**Figure 6.27**) that CF@TiO_2 N900 shows as main contributions the N-Ti (4% at.) bonding at 396 eV, as well as Ti-N-O (4% at.) at 398 eV, both centered at 396.1eV. Moreover, there is a 2% contribution of the spectra coming from pyridinic, pyrrolic and graphitic nitrogen groups formed at the carbon felt surface uncovered , which are centered at 400.2 eV. A 55% corresponds to pyridinic-N (399.7 eV), 31% to pyrrolic-N (400.3 eV) and 13% to graphitic-N (401.3 eV). The nitrogen functionalization is confirmed for CF@ N900, as the deconvolution of the high resolution N1s spectra reveals the presence of the peaks related to: pyridine-N (399.7 eV), pyrrole-N (400.3 eV) and graphitic-N (401.3 eV).

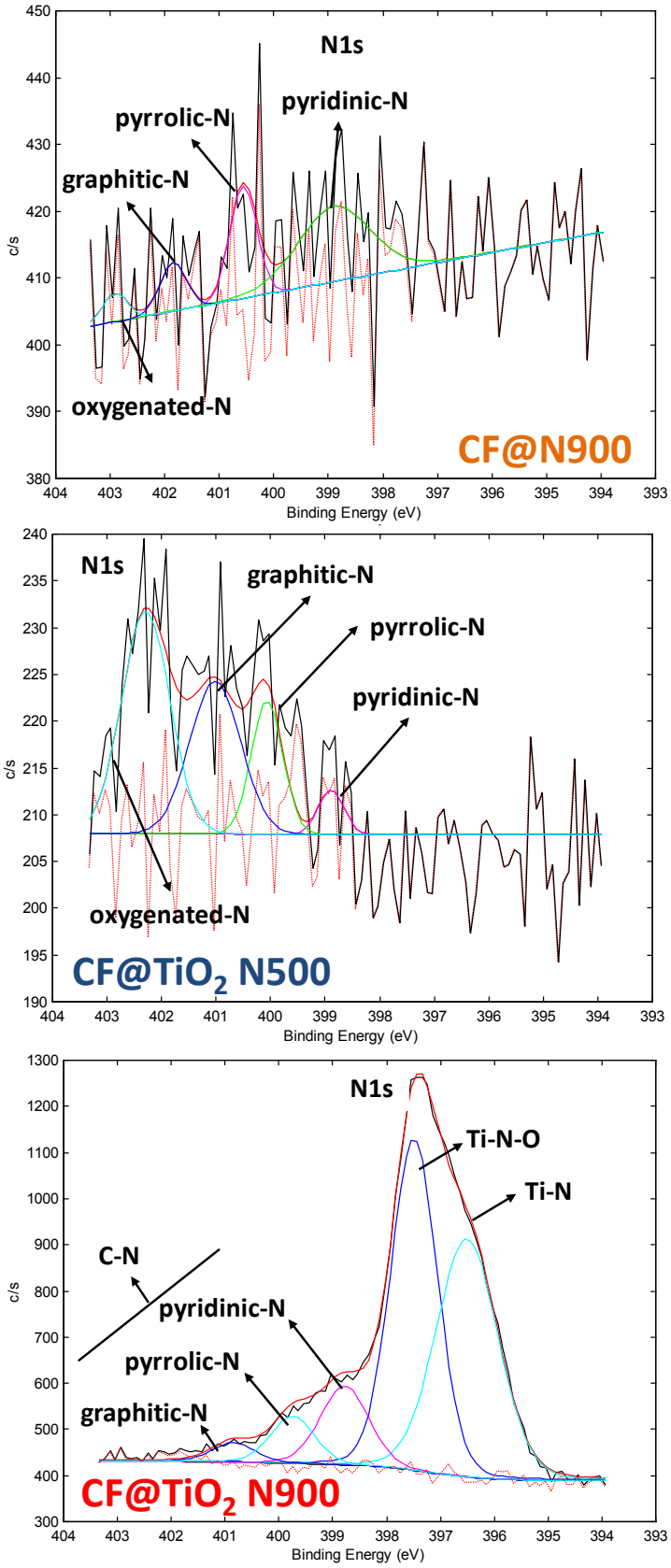

Figure 6.27 - XPS N1s band spectra for the samples CF@N900, CF@TiO_2N500 and CF@TiO_2 N900.

Besides, the NH_3-tratment remarkably modifies the surface chemical states and, consequently, the optical properties of the TiO_2. For example, the color of the rutile's deposit, which is completely white in the case of the initial TiO_2 sample (**Figure 6.28a**) and it turns bluish on the deposit after NH_3-treatment at 500*ºC* (**Figure 6.28b**), due to defect formation on the rutile[215,216] caused by the reducing effects produced by the presence of ammonia. The annealed sample at 700*ºC* (**Figure 6.28c**) is changed to black due to a deeper defect formation. Finally, the case of 900*ºC* (**Figure 6.28d**) turns to a brown color as a result of the titanium nitride (TiN) formation. The following reactions explain the annealing processes that the electrodes are subjected to in presence of ammonia when reaching certain temperature[217]:

$$2NH_3 \longleftrightarrow N_2 + 3H_2 \quad \textbf{(6.3)}$$

$$TiO_2 + H_2 \longleftrightarrow TiO + H_2O \quad \textbf{(6.4)}$$

$$TiO + NH_3 \longleftrightarrow TiN + H_3O^+ \quad \textbf{(6.5)}$$

$$TiO_2 + NH_3 \longleftrightarrow TiON + H_3O^+ \quad \textbf{(6.6)}$$

$$2TiO + N_2 \longleftrightarrow 2TiON \quad \textbf{(6.7)}$$

Initially, when ammonia gas is heated it is decomposed to hydrogen and nitrogen gas **(6.3)**. Hydrogen partially reduces the titanium dioxide phase to titanium monoxide **(6.4)** which in the presence of the acidic electrolyte will form the oxyhydroxide. However, in order to produce titanium nitride, the heating temperature should reach at least 800*ºC*. Below that temperature reaction **(6.5)** does not take place, therefore TiN is not formed. Intermediate reactions **(6.6)** and **(6.7)** takes place from 700ºC to form the oxynitride phase[218].

In order to confirm these findings the UV-vis spectra, shown in **Figure 6.28e**, is done for the as-prepared electrodes. Considering the CF@TiO_2 electrode as the initial spectra, there is broad absorbance decay, from 400 to 850 nm wavelength, corresponding with the visible and Near-IR region. It increases to maximum absorbance when the sample is annealed in ammonia at 500ºC. When annealed at 700ºC, the absorbance is lowered around 5% relative to the CF@TiO_2 N500 sample, from 400 to around 700 nm. Finally, the absorption after nitride formation appears to be stronger in the visible range (400-550 nm) for the sample annealed at 900ºC in presence of ammonia (CF@TiO_2 N900). Afterwards has a linear decreasing absorbance, from 550 to 850 nm, as the color of our electrode's deposit turns from black to dark brown[219,220].

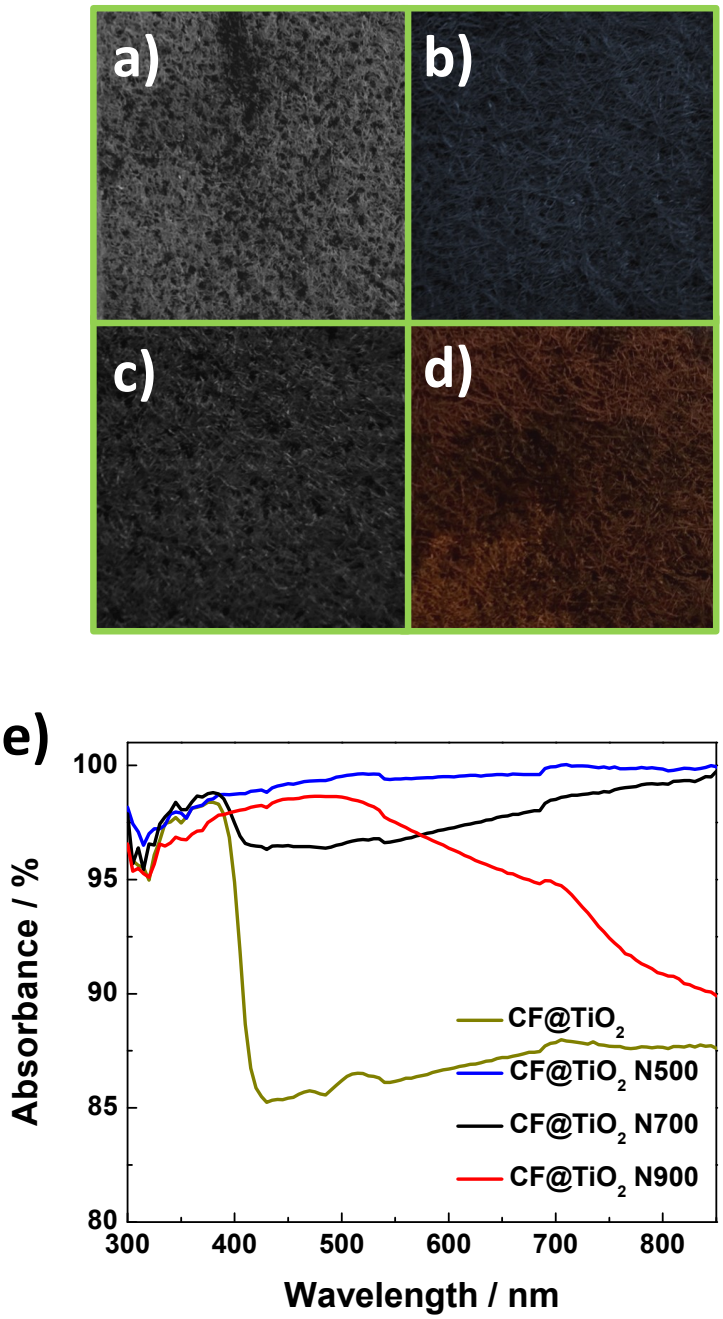

Figure 6.28 - Images, taken from Carl-Zeiss optical lens, of the electrodes after their respectively treatment: **a)** CF@TiO_2; **b)** CF@TiO_2 N500; **c)** CF@TiO_2 N700 **d)** CF@TiO_2 N900 **e)** UV-vis Absorption spectra for CF@TiO_2, CF@TiO_2 N500, CF@TiO_2 N700 and CF@TiO_2 N900.

6.1.3.1.3 Electrochemical characterization

After study the chemical modification of the different electrodes, cyclic voltammetry (CV) was done as electrochemical analysis towards V^{2+}/V^{3+} redox reaction (**Table 6.4**). Several electrochemical observations can be made from the CV (**Figure 6.29a**). It is clearly evidenced the poor electrocatalytic activity of the CF towards

the negative reaction in VRFB, as large differential peak potential corresponding to the V^{3+}/V^{2+} redox reaction is observed. This irreversibility is due to CF electrode promotes the HER over the V^{3+}/V^{2+} redox reaction. TiO_2 electrocatalyst over the surface of the CF electrode displayed oxidation and reduction peaks and therefore HER is largely avoided, but no these peaks are no symmetrical and the obtained current density values are the lowest for all modified electrodes tested. Further differences can be observed, when compare CF@TiO_2 N500 and CF@TiO_2 N900 electrodes:

1) The highest current densities for both processes, oxidation and reduction, is displayed by CF@TiO_2 N900 electrode (i.e. I_{ox}= 24.01 mA/cm^2 and I_{red}= -27.67 mA/cm^2), which evidences the greater electrochemical conversion of the active species on its surface due to a larger electrochemical active surface area towards the V^{3+}/V^{2+} redox reaction.

2) The peak-to-peak potential separation (ΔE) and the ratio of the reduction peak and the oxidation peak current (I_{red}/I_{ox}) provide information about the reversibility of the redox process. For one-electron transfer reaction, the values for a reversible redox reaction are ΔE = 0.059 V and I_{red}/I_{ox} = 1 at 298 K. A Slight difference of the ΔE values between both electrodes, CF@TiO_2 N500 and CF@TiO_2 N900, can be observed 0.24 and 0.22 V respectively. However, a significant increase from 0.60 to 0.87 for I_{red}/I_{ox} can be observed, showing a higher symmetry for CF@TiO_2 N900 electrode towards the reaction. Thus, in terms of electrochemical reversibility, the CF@TiO_2 N900 electrode presents better features, achieving values for a quasi-reversible reaction towards V^{2+}/V^{3+}.

Table 6.4 – Electrochemical values obtained from the cyclic voltammetry plots.

Sample	E_{ox} / *V*	E_{red} / *V*	ΔE / *V*	I_{ox} / *mAcm*$^{-2}$	I_{red} / *mAcm*$^{-2}$	I_{red}/I_{ox}
CF	**-0.066**	**-0.625**	**0.69**	**9.21**	**-13.98**	**0.66**
CF@TiO_2	**-0.228**	**-0.469**	**0.24**	**3.67**	**-6.84**	**0.54**
CF@TiO_2 N500	**-0.233**	**-0.468**	**0.24**	**5.28**	**-8.77**	**0.60**
CF@TiO_2 N900	**-0.232**	**-0.456**	**0.22**	**24.01**	**-27.67**	**0.87**
CF@N900	**-0.230**	**-0.463**	**0.23**	**15.95**	**-20.56**	**0.78**

Additionally, in order to elucidate the electrochemical influence of the nitrided process onto TiO_2 layer, as well as on the carbon felt, samples without TiO_2 layer have also been prepared and analyzed, labeled as CF@N900. As observed in **Table 6.4**, the main differences between these two electrodes is the lower current density, from 33% for reduction to 25% for oxidation reactions, slightly smaller ΔE (0.23 V) and reduced I_{red}/I_{ox} (0.78) displayed by CF@N900 comparatively to $CF@TiO_2$ N900 electrode. It points out the positive benefit of the proposed technological route to enhance the VRFB negative redox reaction. Accordingly, the experimental data have shown a synergetic effect between the nitrided process effect over the CF and on TiO_2 structure, coupling the better electron transfer towards V^{3+}/V^{2+} redox reaction due to functionalization over the carbon electrode's surface and over the TiN nanocatalyst formed.

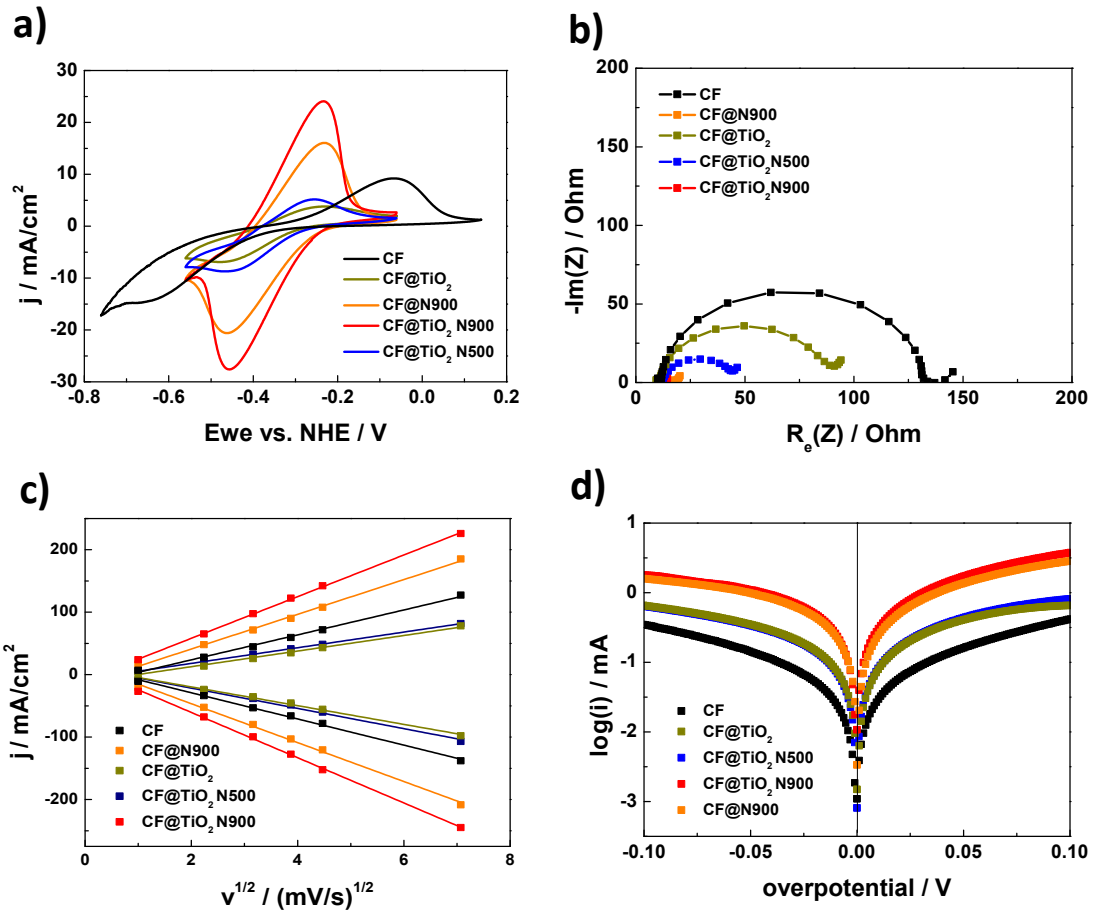

Figure 6.29 – a) Cyclic Voltammetry of the electrodes in 0.05 M $V^{3+}$and 1 M H_2SO_4 solution. The voltage was scanned negatively from E_{ocv} at 50% SoC (V^{3+}/V^{2+}) at a scan rate of 1 $mV\ s^{-1}$, to -0.56 *V* vs. SHE and after reversing the direction to an oxidative potential up to -0.06 *V* vs. SHE. **b)** Potentiostatic Electrochemical Impedance Spectroscopy (PEIS) done at -0.26 V vs. SHE. **c)** Randles-Sevcik plot of *j* vs. $v^{1/2}$. **d)** Tafel plot log *i* vs. *η* (overpontential) for the different electrodes used in a 0.05 M 50% SoC V^{2+}/V^{3+} in 1 M H_2SO_4 solution.

The change in the electrochemical behavior of the prepared electrodes is a crucial characteristic to consider, for that purpose electrochemical impedance spectroscopy (PEIS) was done for all the electrodes at -0.26 V vs. SHE. Nyquist plots (**Figure**

6.29b) of all electrodes studied resembled a semi-circle at high frequency region and a sloped line at the low frequency region ascribed to charge transfer process and the diffusion process, respectively. The data were fitted using Randles equivalent circuit (**Figure 6.29b** onset). The following elements can be ascribed to the fitting: i) the R_s element represents the ohmic resistant, combining the electrolyte resistance, connection resistance, and the electrode resistance; ii) CPE-1 has a Faradic component (Y_1), which is a double layer capacitance (C_{dl}) of the interface between the electrode and the electrolyte, and a no-Faradic component (n_1), iii) charge transfer resistance (R_{ct}), and iv) CPE-2 has a Faradic component (Y_2), which represents the diffusion capacitance in pores of the electrodes, and a no-Faradic component (n_2). The data parameters obtained are listed in **Table 6.5** with an error less than 10%.

Table 6.5 – Parameters obtained from the Nyquits fitting plots with the equivalent circuit model of **Figure 6.29b**.

Sample	R_s / Ohm	CPE-1		R_{ct} / Ohm	CPE-2	
		Y_1 (C_{dl})	n_1		Y_2	n_2
CF@TiO_2	10.4	0.004451	0.92136	80.5	0.77467	0.81453
CF@TiO_2 N500	11.7	0.020095	0.89663	34.4	1.589	0.91352
CF@TiO_2 N900	12.3	0.084218	0.76553	1.25	2.781	0.6693
CF@N900	13.9	0.034198	0.61148	4.79	1.83	0.75279
CF	11.4	0.000322	0.97239	122	0.96348	0.58562

Consequently, CF@TiO_2 N900 sample has an electrochemical charge transfer resistance undeniable low compare to other electrodes, 1.25 *Ohm*, which is more than three times better compared to CF@N900 electrode. There is a great variation in the charge transfer resistance of the CF@TiO_2 sample compared to the nitrided electrodes. This process highly improves the charge transfers between the negative electrode and the vanadium ions, especially for CF@TiO_2 N900, when TiN phase is formed, as well as nitrogen groups functionalization over the carbon felt, as XPS previously shown (Figure S4). It makes CF@TiO_2 N900 as the best electrode synthesized in this study, reducing the charge transfer resistance almost two orders of magnitude compared to CF@TiO_2[221]. It is also worth considering CF@N900, which performed the second best, helped by the N and O-groups over the carbonaceous surface, showing an R_{ct} of 4.79 *Ohm*. Moreover, C_{dl} values are found to follow the same trend as the R_{ct}, obtaining the larger value for CF@TiO_2 N900 (8.4×10^{-2} F) electrode due to higher amount of the active sites available for the reaction, which also agrees well with the CV analysis.

Besides, in cyclic voltammetry, the peak current, i_p, depends not only on the concentration and diffusion properties of the electroactive species but also on the scan rate, as described by the Randles-Sevcik equation:

$$i_p = 0.4463nFAC\left(\frac{nF\nu D}{RT}\right)^{1/2}$$

Where i_p is the current maximum in amps, n is the number of electrons transferred in the redox event (usually 1), A is the electrode area in [cm^2], F is the Faraday constant in [C mol^{-1}], D is the diffusion coefficient in [cm^2/s], C is the concentration in [mol/cm^3], v is the scan rate in [V/s], R is the gas constant in [J K^{-1} mol^{-1}] and T is the temperature in [K]. When a linear behavior is observed between the scan rate and the peak current for the redox couple V^{3+}/V^{2+}, the reaction is diffusion controlled. Prior to use this equation it is worth mention it is applied just as a qualitative approximation because it applies to reversible reactions and planar electrodes while the studied electrodes are porous and quasi-reversible reactions. In order to estimate the mass transfer the Randles-Sevcik equation is used [222]. The equation's plot (**Figure 6.29c**) gives us a relationship where the slope is directly related to the associated mass transfer, which follows the trend: CF@TiO_2 N900 > CF@N900 > CF > CF@TiO_2 N500 > CF@TiO_2. These values evidence the higher mass transfer on the CF@TiO_2 N900 electrode towards the negative reaction, which is directly a consequence of a larger active area of the vanadium ions over the electrode and therefore being less diffusive limited. Moreover, the close value of CF@N900 to CF@TiO_2 N900 also evidences a facilitated mass transfer due to larger active area on the electrode's surface.

The Tafel equation was applied in order to confirm the catalytic properties of the different carbon felt modified electrodes (**Figure 6.29d**), which was mathematically treated and their values disclosed in **Table 6.6**. As seen, the exchange current density follows the trend (*mA*): CF@TiO_2 N900 (9.58 x 10^{-1}) > CF@N900 (6.87 x 10^{-1}) > CF@TiO_2 N500 (3.51 x 10^{-1}) > CF@TiO_2 (2.38 x 10^{-1}) > CF (6.6 x 10^{-2}). It is directly related to the equilibrium exchange current on the electrode towards the negative VRFB reaction. Therefore, our synthesized material at high temperature (900^oC) shows a superior electron exchange current with the electrolyte towards the redox reaction (V^{3+}/V^{2+}), which implies good catalytic behavior of highly nitrided electrodes. The heterogeneous rate constant was also determined, see **Table 6.6**, obtaining 1.6 $\times 10^{-3}$ cm s^{-1} for CF@TiO_2 N900 electrode one order of magnitude larger than CF@TiO_2 N500 electrode (5.8 x 10^{-4} cm s^{-1}). CF@TiO_2 N900 rate constant value is among the best values in the literature[223].

Table 6.6 – Exchange current density (i_0) values and heterogeneous kinetic rate constant obtained from the Tafel plot in 0.05 M V^{3+} in 1 M H_2SO_4 at 50% SoC (V^{2+}/V^{3+}) for the electrodes CF, CF@TiO_2 and CF@TiO_2 N500, CF@TiO_2 N900 and CF@N900.

Electrode	I_0 / mA	k^0 /cm s^{-1}
CF	0.066	1.1×10^{-4}
CF@TiO_2	0.238	3.9×10^{-4}
CF@TiO_2 N500	0.351	5.8×10^{-4}
CF@TiO_2 N900	0.958	1.6×10^{-3}
CF@N900	0.687	1.1×10^{-3}

Since the lower contribution of the parasitic reactions must be settled in order to assess a high Coulombic efficiency, as well as long lifespan of the electrodes performance, CV are performed in absence of any vanadium ion to study the HER on the surface of the different studied electrodes (**Figure 6.30**). The maximum current density values for the as prepared electrodes towards HER increases in the following order (mA cm^{-2}): CF@TiO_2 (89) < CF@TiO_2 N900 (150) < CF@TiO_2 N500 (180) << CF@N900 (248) < CF (258). Compared to CF, it is obvious the large inhibition of hydrogen evolution presented on the felt covered by titanium dioxide as rutile phase, shifting the onset potential of HER, from -0.024 to -0.49 *V* vs. SHE[224]. The nitrided samples, CF@TiO_2 N500 and CF@TiO_2 N900, also inhibited the HER compared to the carbon felt, though not as strongly as before the nitride treatment, -0.15 and -0.30 *V* vs. SHE onset potential for annealing at 500 and 900*ºC*, respectively. In spite of the inhibition of HER produced on its surface it is not as powerful as in the case of pure titanium dioxide, due to the presence of fewer oxygen C-O centers, as shown by XPS for TiO_2 and CF@TiO_2 N500 [89]. Moreover, CF@TiO_2 N900 has a more negative onset potential compared to CF@TiO_2 N500 as the activation energy towards HER is comparatively larger. Last but not less important, CF@N900 increases the kinetics towards HER, in spite the fact that postpones the onset potential compared to CF. This result related to CF@N900 hydrogen evolution reaction demonstrates the usefulness of TiO_2 presence to inhibit H_2 formation. Thus, CF@N900 is not studied into a single cell.

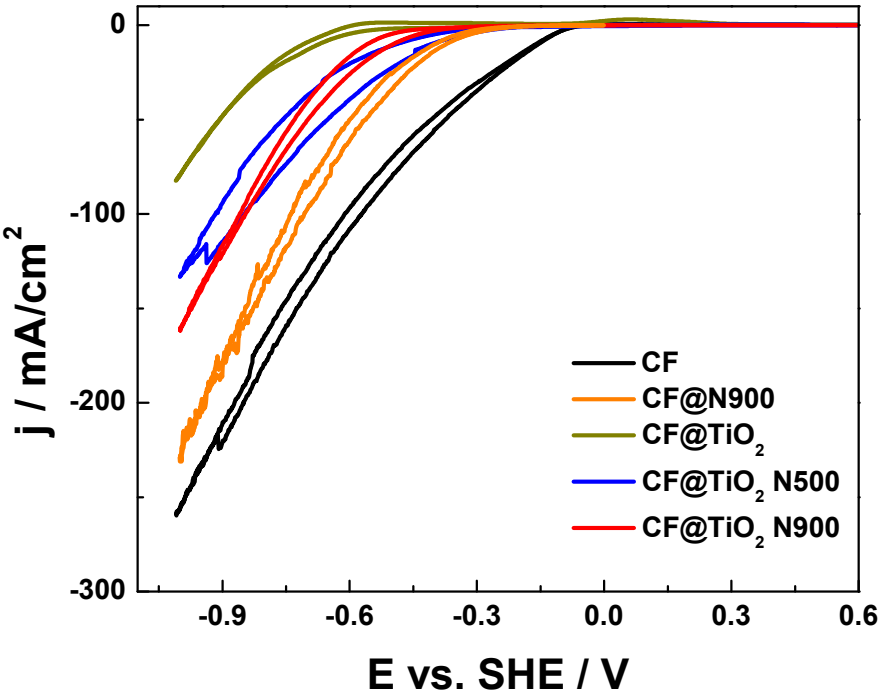

Figure 6.30 – Cyclic voltammetry (CV) of carbon felt, CF@TiO_2 and CF@TiO_2 N500 and N900 electrodes using a 1M sulphuric media at 2 *mV* s^{-1}, with potential window of 0.6 to -1 *V* vs. SHE.

6.1.3.2 Single cell performance

Finally, in order to assess the performance of the modified electrodes in a single cell, the carbon felt electrode incorporated with the nitrided titanium dioxide catalyst is used as the negative electrode in all-vanadium redox flow battery, while for all the experiments treated carbon felt (CF-HT) was used as positive electrode. **Figure 6.31** shows several battery cycles at different current densities, from 25 to 150 *mA* cm^{-2}, in order to observe the effect on the capacity. It can be said that our carbon felt capacity drops dramatically from 12.6 *Ah* L^{-1} at 25 *mA* cm^{-2} current density to 3.3 *Ah* L^{-1} at 100 *mA* cm^{-2}. However, it recovers at least partially its capacity when it is returned to the initial current density applied (10.9 *Ah* L^{-1}). On the contrary, the nitrided TiO_2 electrode retains the majority of their charge capacity from 13.1 and 13.6 *Ah* L^{-1} at 25 *mA* cm^{-2} to 9.8 and 10.1 *Ah* L^{-1} at 150 *mA* cm^{-2}. This outstanding performance is a consequence of the synergetic catalytic effect of the oxygen and nitrogen sites on the carbon nitrided CF@TiO_2 over the adsorption, redox reaction and later desorption of V^{2+}/V^{3+} redox pair [203,225].

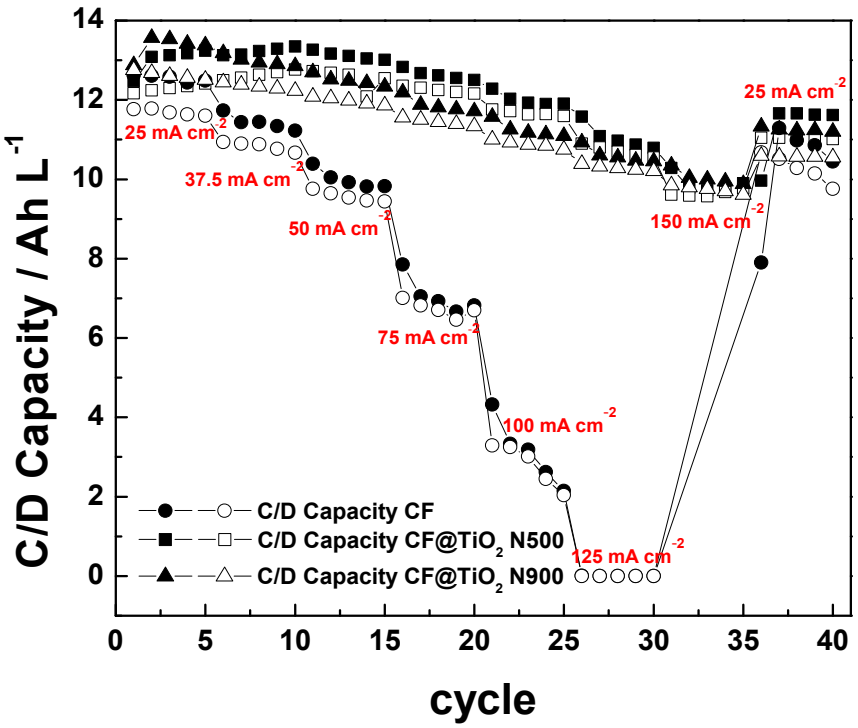

Figure 6.31 – Battery's capacity as a function of the current density for different modified electrode used as, CF, CF@TiO_2 N500 and CF@TiO_2 N900

Furthermore, the sample treated at 500*ºC* displays low voltage losses over the charge and discharge if we compare with CF. However, still higher than the nitrided one at 900*ºC*. One of the main reasons for this is the formation of TiN coupled with the nitrogen and oxygen group formation on the carbon felt, which allows a reduced charge transfer resistance. As a consequence of this, during the charge-discharge at 150 *mA* cm^{-2}, the ohmic drop decreases, from CF@TiO_2 N500 to CF@TiO_2 N900 by 104 *mV* and 56 *mV* for charge and discharge respectively (**Figure 6.32**). As all components remained constant between tests, any differences on the system are due to the negative electrode. Therefore, the surface properties of the electrodes have a critical influence not only over the redox reaction kinetics, as previously shown, but also its ohmic resistance.

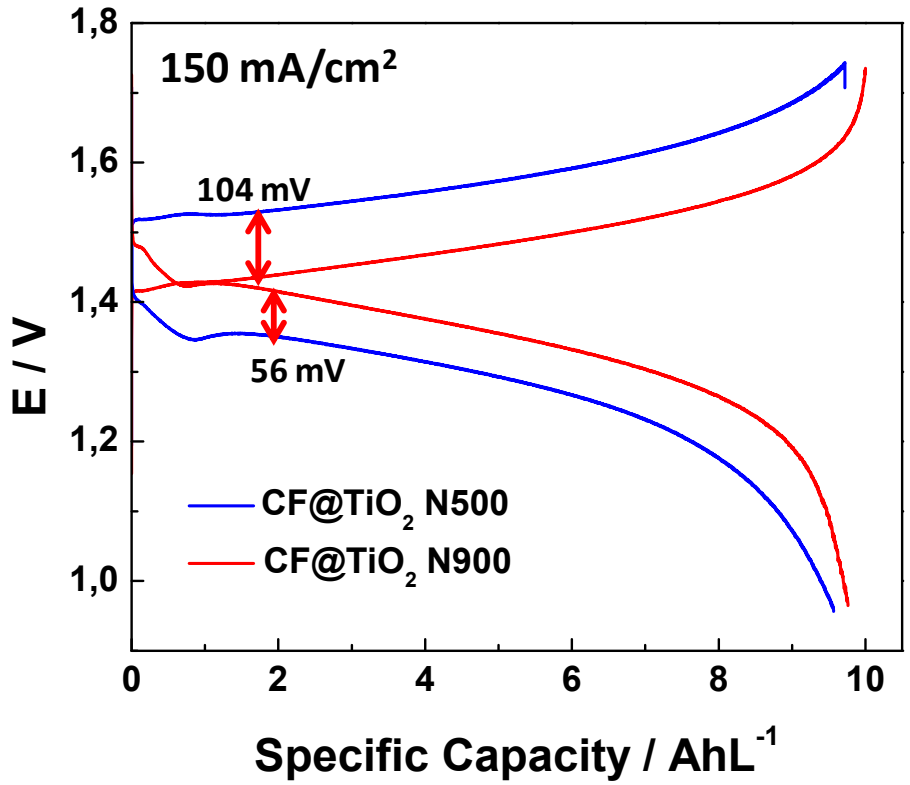

Figure 6.32 – Comparative between voltage profiles for CF@TiO_2 N500 and CF@TiO_2 N900 for current density applied of 150 *mA* cm^{-2}.

Subsequently, **Figure 6.33a and b** presents the Coulombic, Voltage and Energy efficiency for the electrodes CF, CF@TiO_2 N500 and CF@TiO_2 N900 respectively, as we cycle with current densities from 25 to 150 *mA* cm^{-2}. The sample annealed at 900*ºC* shows smaller losses as the current density is increased, and therefore a higher efficiency. A maximum energy efficiency of 86.5% is seen at the lowest current density (25 mA cm^{-2}), dropping to 71% at 150 *mA* cm^{-2}. These values are lower compared to the state of the art in the literature[226] as a consequence of different single cell set-up design and conditions. Nevertheless, for the same experimental conditions it is clear that the coating of nitride TiO_2 on the surface of the graphite felts has a drastic improvement on performance of the battery compared to CF. Similarly, the decrease in energy efficiency for CF@TiO_2 N500 is markedly less than for the CF, where the efficiency decays abruptly when the current density applied increases. Especially up to 100 *mA* cm^{-2}, where the value collapses due to large overpotential, as seen in **Figure 6.34d**.

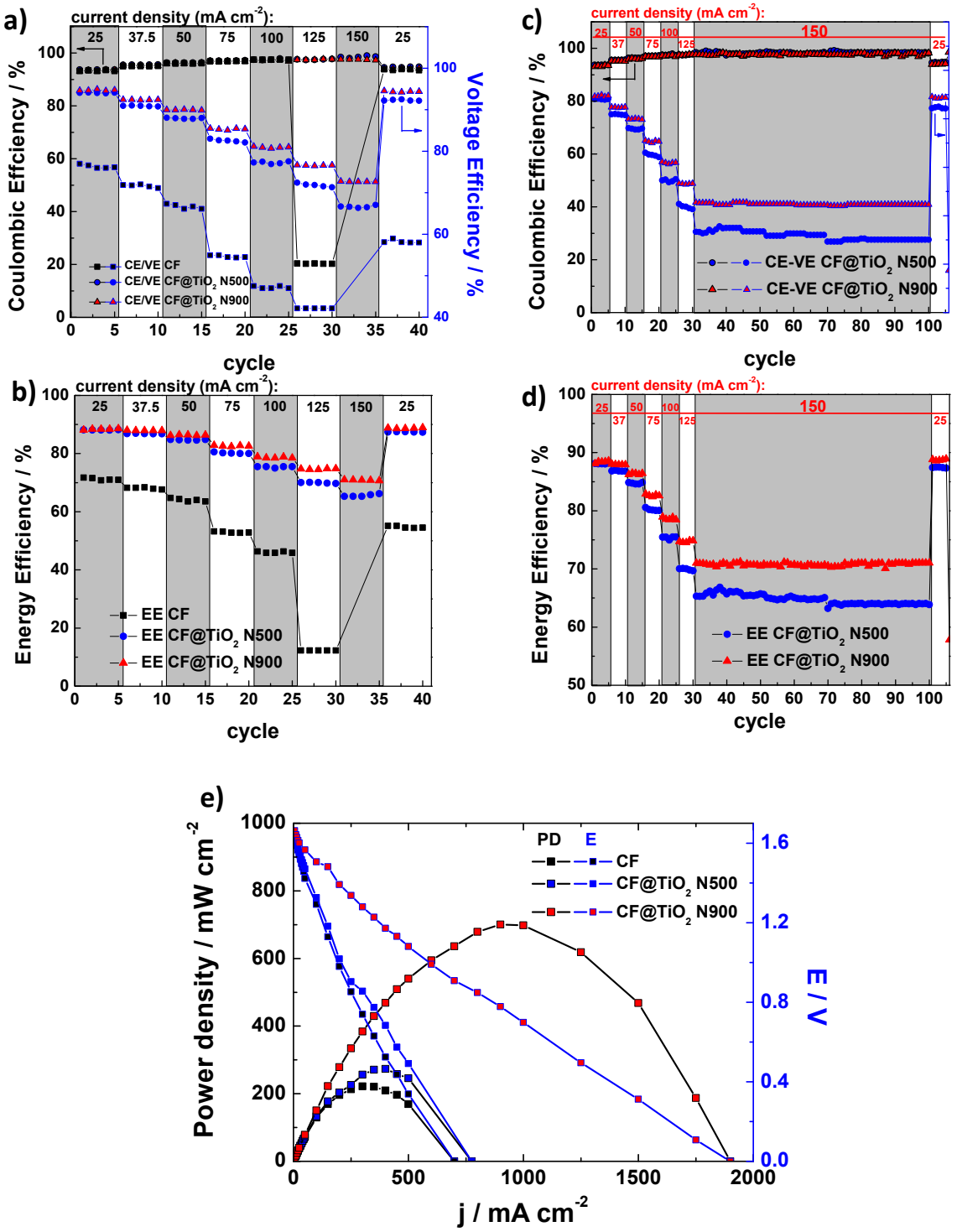

Figure 6.33 – a) CE and VE **b)** EE dependency with the applied current density (from 12.5 to 150 *mA cm*$^{-2}$) of CF, CF@TiO_2 N500 and CF@TiO_2 N900 as electrodes, for 1M of initial vanadium ions and 3 M H_2SO_4 as electrolyte. Single cell long-term cycling of the CF@TiO_2 N500 and N900 electrodes for 1M vanadium ions and 3 M H_2SO_4. **c)** Coulombic Efficiency (CE) and Voltage Efficiency (VE) ; **d)** Energy Efficiency (EE). **e)** Power density plot vs. current density for the electrodes CF, CF@TiO_2 N500 and CF@TiO_2 N900.

The Voltage efficiency, which is the ratio of charge and discharge voltage, follows the same trend as the Energy efficiency, a consequence of being the limiting factor of the battery performance. The Coulombic efficiency, the difference between charge and discharge capacity, shows similar values for all samples (**Figure 6.35**), above 95% for all current densities. The exception being for carbon felt above current density 100 *mA* cm^{-2}, due to an enormous overpotential that causes a Coulombic efficiency drop to approximately a 20%. As HER increase, the overpotential does increase as well, which is confirmed in **Figure 6.34d**, causing critical imbalances between charge and discharge process that ultimately makes the system to fail when CF is used as negative electrode. Moreover, **Figure 6.34d** shows the Voltage profiles between 0.8 and 1.8 *V* for carbon felt, CF@TiO_2 nitride at 500*ºC* and 900*ºC*, applying increasing current densities. It is obvious the larger ohmic drop for CF than nitrided electrodes, especially low ohmic drop is observed for CF@TiO_2 N900 capable of a lower polarization when high currents are applied. Considering the different charge-discharge profiles, it is clear the logarithmic tendency of the overpotential when increasing the current density, seen in **Figure 6.34d**.

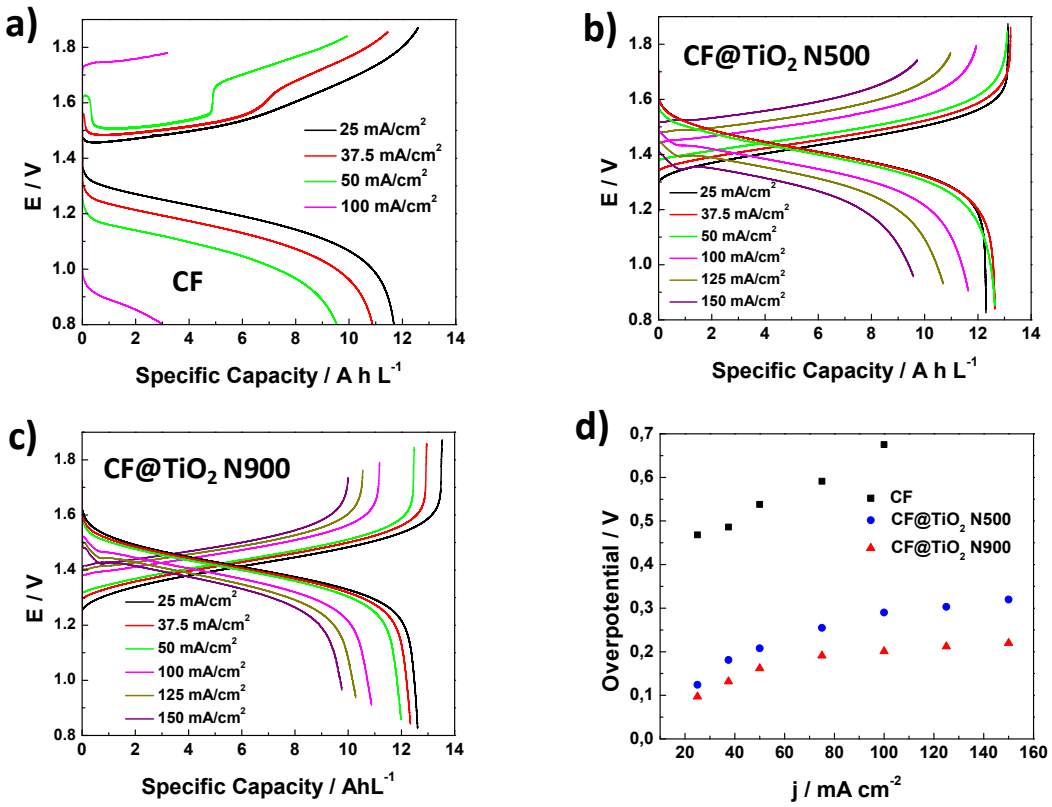

Figure 6.34 – Charge-discharge voltage profiles between 1.8 and 0.8 *V* at different current densities (25 to 150 *mA* cm^{-2}) for **a)** CF, **b)** CF@TiO_2 N500 and **c)** CF@TiO_2 N900. **d)** Overvoltage during charge period comparatively to E_{ocv}.

Thus, the nitrided catalysts annealed at 500 and 900ºC exhibited a stable cycling performance above 100 cycles at different current densities with more than 50 cycles at high-current (150 *mA* cm^{-2}). Nitrided CF@TiO_2 displays an initial Energy efficiency of 88.9% and 87.2%, for 900 and 500ºC annealing temperature, respectively. After 100 cycles, which is the largest stability published up to date for these materials, corresponding to 2-3 weeks of cycling, the enhancement of CF@TiO_2 N900 achieved a stable cycling energy efficiency of 71.2% at 150 *mA* cm^{-2} compared to 63.9% energy efficiency in case of CF@TiO_2 N500. Therefore, the electrode improvement can be observed especially at high current densities due to the significantly reduced polarization by increased redox active sites towards vanadium ions for the fast charge and mass transfer, which is consistent with all the electrochemical data previously shown. Following cycling at increased current densities, the system was returned to a charge-discharge rate of 25 *mA* cm^{-2}, in order to evaluate the catalyst stability (**Figure 6.33c and d**). Remarkably, the initial energy efficiency was recovered after cycling at high current densities, indicating an electrochemical and chemical robustness of nitrided CF@TiO_2 catalyst in concentrated acidic and high current conditions. Moreover, Coulombic efficiency and Voltage efficiency values were the highest for CF@TiO_2 N900 samples. Nitrided CF@TiO_2 catalyst was shown to exceptionally enhance the electrochemical performance of the VRFB system. In fact, CF@TiO_2 N900 induces a fast charge transfer and vanadium ion adsorption, resulting in a high rate capability at 150 *mA* cm^{-2} and excellent capacity retention. This outstanding performance is a consequence of the synergetic catalytic effect of the oxygen and nitrogen sites on the nitrided carbon felt and TiO_2 over the adsorption, redox reaction and later desorption of V^{2+}/V^{3+} redox pair [203,225].

In fact, the observed improved performance in the electrode's mass and charge transfer, low ohmic resistance, as well as, limiting current density enables CF@TiO_2 N900 material to reach a superior power density, which is coherent with the electrode reaching a superior current values in the CV, previously shown in **Figure 6.29a**. The value of power density obtained, 700 *mW* cm^{-2}, is two and a half times higher than when annealed at 500°C and three times more than carbon felt electrode. The shape of the polarization curves (**Figure 6.33e**) show that the maximum current density supply by the device is increased by two effects: i) a low ohmic drop as the current density is increased and ii) faster vanadium mass transfer, allowing larger amounts of vanadium to be polarized over the electrode surface as the power density increases. The voltage decay is much smoother in CF@TiO_2 N900 electrode. It reaches a greater maximum power, while the other samples show abrupt voltage decay and significantly lower maximum power density. Therefore, the modified carbon felts (CF@TiO_2 N900) have enhanced the electrochemical performance of the negative electrode in all-vanadium redox flow batteries and, more importantly, the power density, which is usually insufficient in flow batteries technology.

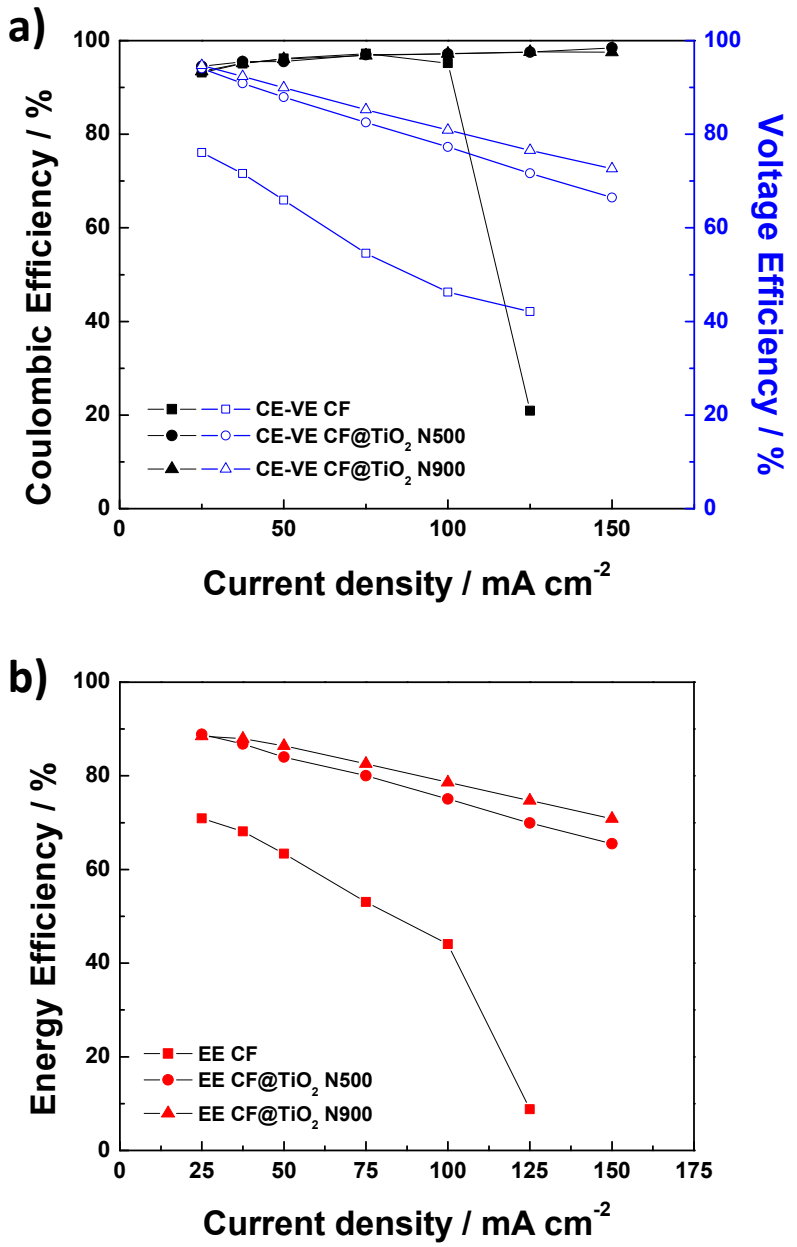

Figure 6.35 – Average efficiencies (CE, VE and EE) as a function of the current density applied for different electrodes in galvanostatic single cell conditions.

6.1.3.3 Mechanism proposed

Based on previous research[227] and implementing the presented results, the mechanism proposed for the electrodes used is shown in **Figure 6.36a and b**. Firstly on CF, V^{3+} ions are adsorbed over the oxygen groups, -OH and C-O, on the carbon felt surface, generating O-V bonds, which breaks a O-H bond in the case where it is adsorbed on the hydroxyl group and releases a proton to the solution. Consequently, an electron is donated to the V^{3+} reducing it to V^{2+} and breaking the previously formed bond (O-V) and taking the proton

again from the solution to re-form the hydroxyl groups. In this case, this redox reaction competes with the hydrogen evolution reaction as the protons are easily adsorbed to the C surface to form an H-H bond and subsequently desorbed as H_2. The former reaction is kinetically more favourable, causing electrolyte imbalance and low performance. The inhibition of the HER is therefore an important factor in catalyst performance, as well as the enhancement of the V^{3+}/V^{2+} redox reaction.

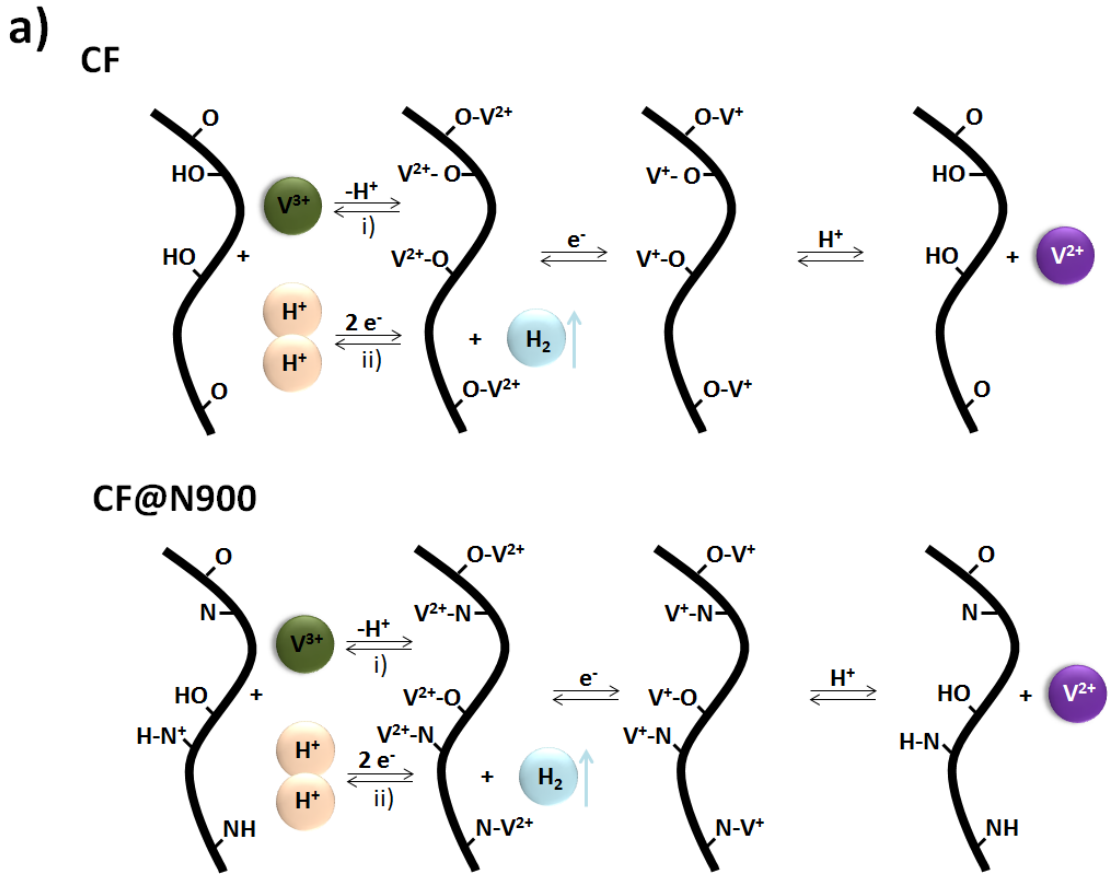

Secondly, on CF@N900, V^{3+} ions are adsorbed over the oxygen (-OH and C-O) and nitrogen (pyridinic, pyrrolic and graphitic-N) groups on the carbon felt surface, generating O-V and N-V bonds, which breaks a O-H, N-H, $^{+}$N-H bond in the case where it is adsorbed on the hydroxyl, pyrrolic or graphitic group, respectively, releasing a proton to the solution. Consequently, an electron is donated to the V^{3+} reducing it to V^{2+} and breaking the previously formed bond and taking the proton again from the solution. This redox reaction also competes with the hydrogen evolution reaction for the same reasons as with the[228].

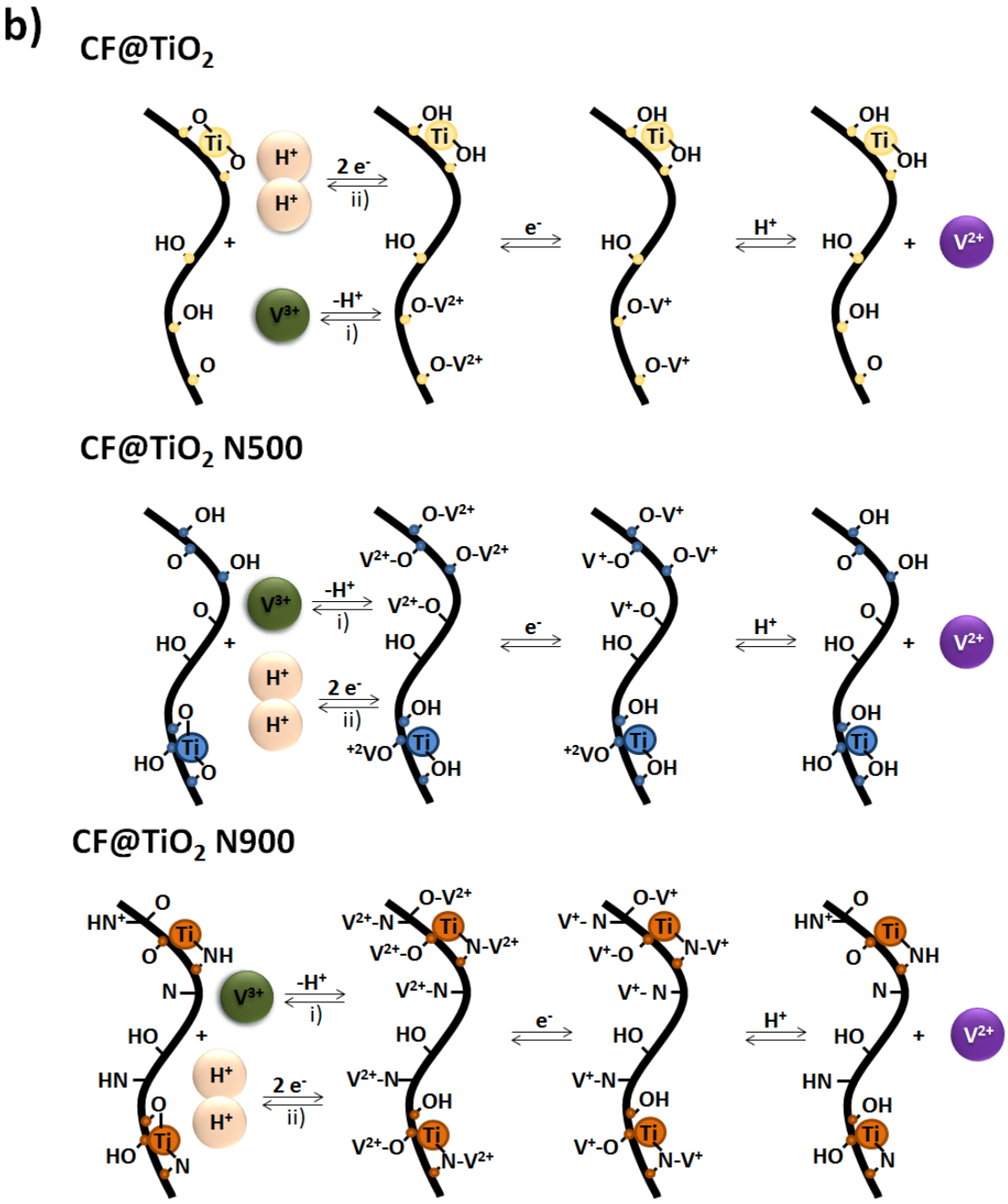

Figure 6.36 – a) Mechanism interpretation, based on published results[227], for the negative reaction of VRFBs using CF and CF@N900 electrodes. **b)** Mechanism interpretation, based on published results[227], for the negative reaction of VRFBs using CF@TiO_2, and nitrided CF@TiO_2 as electrodes.

Thirdly, after the TiO_2 is deposited there are two conditions that favour the V^{3+} reduction: i) Increase of –OH groups and less importantly –O groups, as XPS data shows, due to the presence of titanium dioxide itself that promote the number of active sites per area for the reaction to happen, enhancing the electron charge transfer at the electrode/vanadium interface. ii) Highly stable proton absorption over the Ti-O bond inhibiting the HER side reaction. However, large electrode polarization is dominant at high rate capability

leading to a limited specific capacity and a modest electrolyte-utilization ratio (SoC).

Consequently, the partially reduced sample (CF@TiO_2 N500) favours the V^{3+}/V^{2+} due to a reduced charge transfer resistance as an increased number of oxygen active sites (-OH and -O), especially hydroxyl groups, are present on the surface (**Figure 6.25**), and therefore, more vanadium ions are capable of reaction simultaneously.

Finally, for the sample where TiN is partially formed (CF@TiO_2 N900) there are two conditions that favour the V^{3+} reduction[229]: i) Increase of –N groups on the carbon felt and over the TiO_2 surface forming TiN, due to the nitride process that promotes the number of active sites, enhancing the electron charge transfer at the interface electrode/vanadium. ii) Increase of oxygen groups, especially hydroxyl electroactive sites (-OH) over the electrode surface, for which electron charge transfer is facilitated by the nitrogen groups, most favoured by pyrrolic-N[230,231].

6.1.4 Cerium oxide (CeO_2)

In this section is studied the demonstration of ALD Ceria deposit over commercial Graphite Felt and its function as catalyst for the positive VRFB redox reaction (VO^{2+}/VO_2^+) by itself (GF@CeO_2) , as well as, after heat treatment under reductive atmosphere (GF@CeO_{2-x}) for high performance all-vanadium redox flow batteries (VRFB) as a simple and eco-friendly strategy, well-suited for large-scale applications (**Figure 6.37**). Analogously to the previous section, where Hydrogen-treated rutile TiO_2 shell in a graphite felt core (GF@TiO_2:H) is used as negative enhanced electrode[89]. It is done to further improve the device, similarly to the negative reaction enhancement by this method, showen in previous section, the positive reaction is improved using a better electrode as the positive compartment would be now the limiting factor in the overall cell performance. Moreover, significant improvements in charge and electron transfer processes towards VO^{2+}/VO_2^+ redox reaction is achieved using GF@CeO_{2-x} electrodes due to the enhancement of CeO_2 charge and electron transfer after hydrogen annealing. It is a consequence of the formation of oxygen vacancies in the lattice structure, similarly as the case of hydrogen treated TiO_2. We have achieved a good quality performance for VRFB not only in terms of high capability rates (250 $mAcm^{-2}$) but also the capacity retention achieved (60% at 200 $mAcm^{-2}$). Additionally, high coulombic efficiency (CE, 98%) and attonishing stability, over 100 cycles at 200 mA/cm^2, demonstrating the feasibility of achieving an outstanding long-term stability, using 1.5 M Vanadium ions in 3 M H_2SO_4.

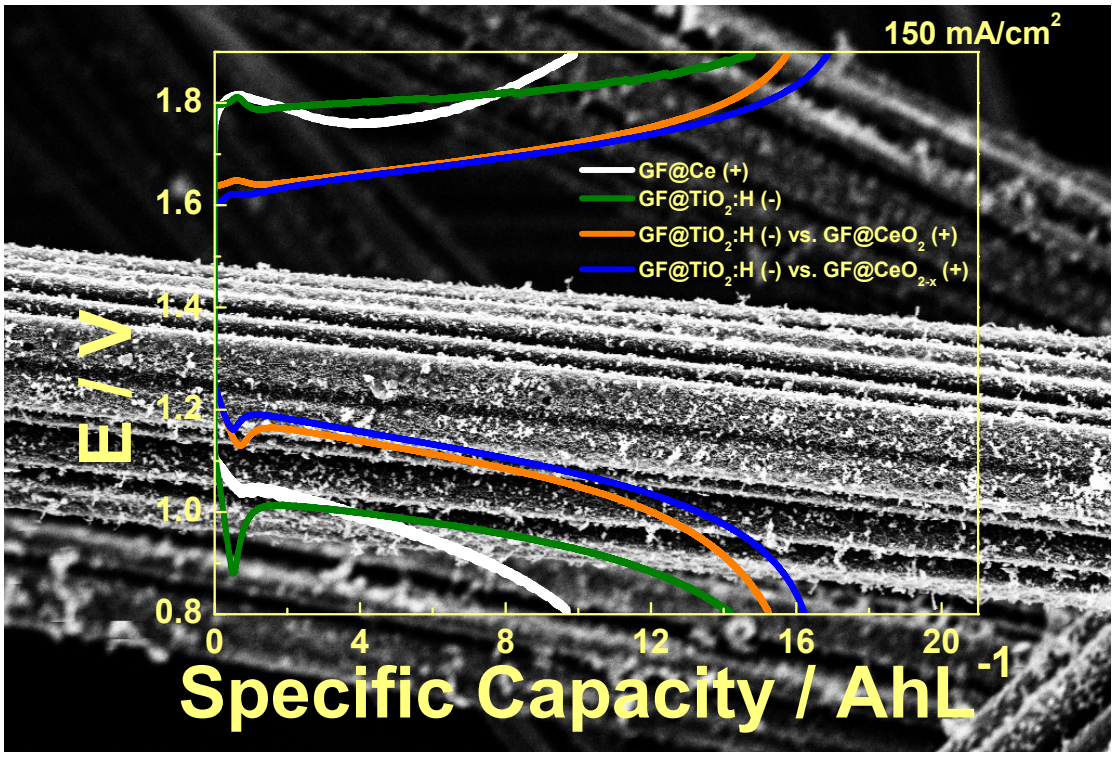

Figure 6.37. – Scheme of the charge-discharge displayed plots for the different electrodes involved in this section in an electrolyte solution of 1.5 M vanadium ions and 3 M H_2SO_4 at a current density of 150 mA/cm^2. The picture behind shows the GF@CeO_{2-x} ALD deposited.

Furthermore, the slower kinetics of the VRFB positive reaction **(2.18)** as it is a more complex reaction comparatively to the one electron transfer for the negative VRFBs reaction. Accompanied by the side reactions in the positive half-cell, diminishes the overall battery performance due to a kinetic overpotential that lowers the voltage efficiency of the battery as well as the capacity. For that purpose Ceria is deposited over the positive electrode material, which is a cheap well-known material, in addition to its standard potential and faster kinetics in acidic solution, E^0 = 1.72 V, acts avoiding Oxygen Evolution Reaction (OER) during the battery cycling by shifting OER to larger potentials. Moreover, CeO_2 and specially, CeO_{2-x}, also enhance the electrocatalytic properties among cycling as a consequence of the electro active oxygen groups, formed on the electrode's surface.

6.1.4.1 Characterization

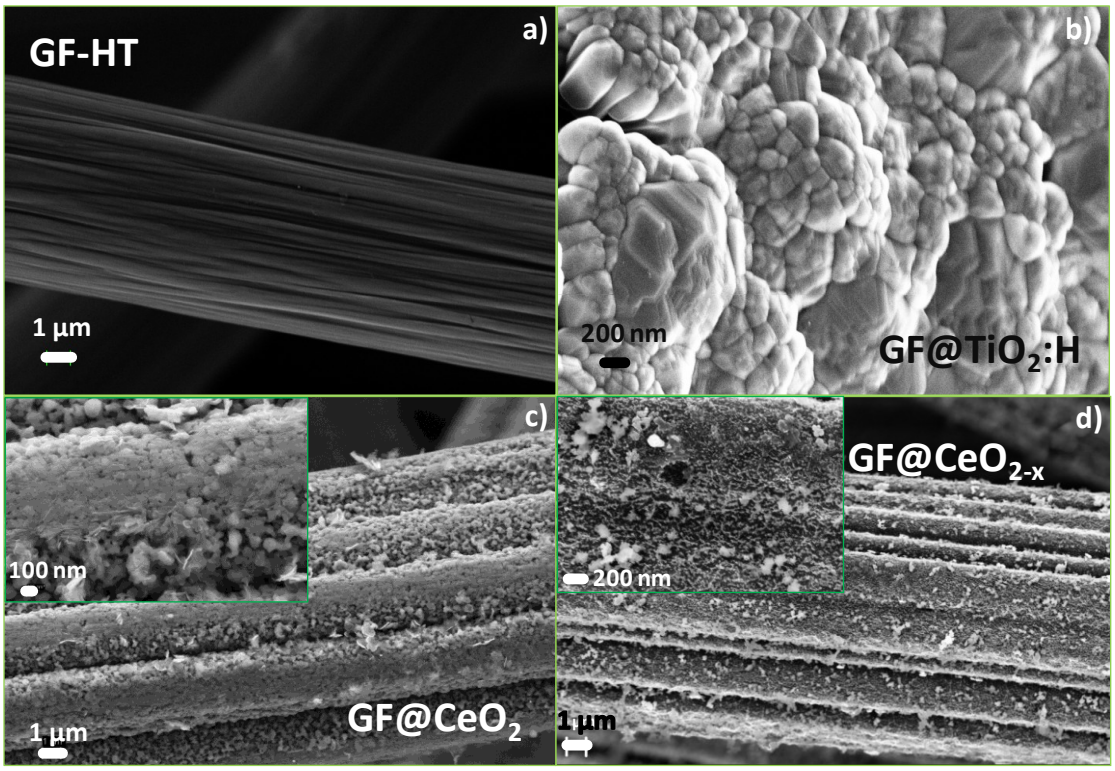

Figure 6.38. – FE-SEM images of the **a)** core graphite GF-HT; **b)** morphology details of the coating layer of the GF@TiO_2 electrode; **c)** coating layer of the GF@CeO_2 electrode; **d)** coating layer of the GF@CeO_{2-x} electrode.

As it can be seen, **Figure 6.38** exhibits the field emission scanning electron microscopy (FE-SEM) images of the TiO_2 and CeO_2 based GFs. Typically the GF shows a smooth morphology but a slightly porous surface. A nanorods crystal structure has been observed in GF@TiO_2:H (**Figure 6.38b**). **Figure 6.38c and d** show that GF has been covered by a homogeneous ALD deposit of CeO_2 maintaining the original GF surface morphology and increasing the roughness in case of the reduced one compared to the non-reduced. It also can be seen on the **Figure 6.39** the completely coverage on the GF by CeO_2 using the ALD technique.

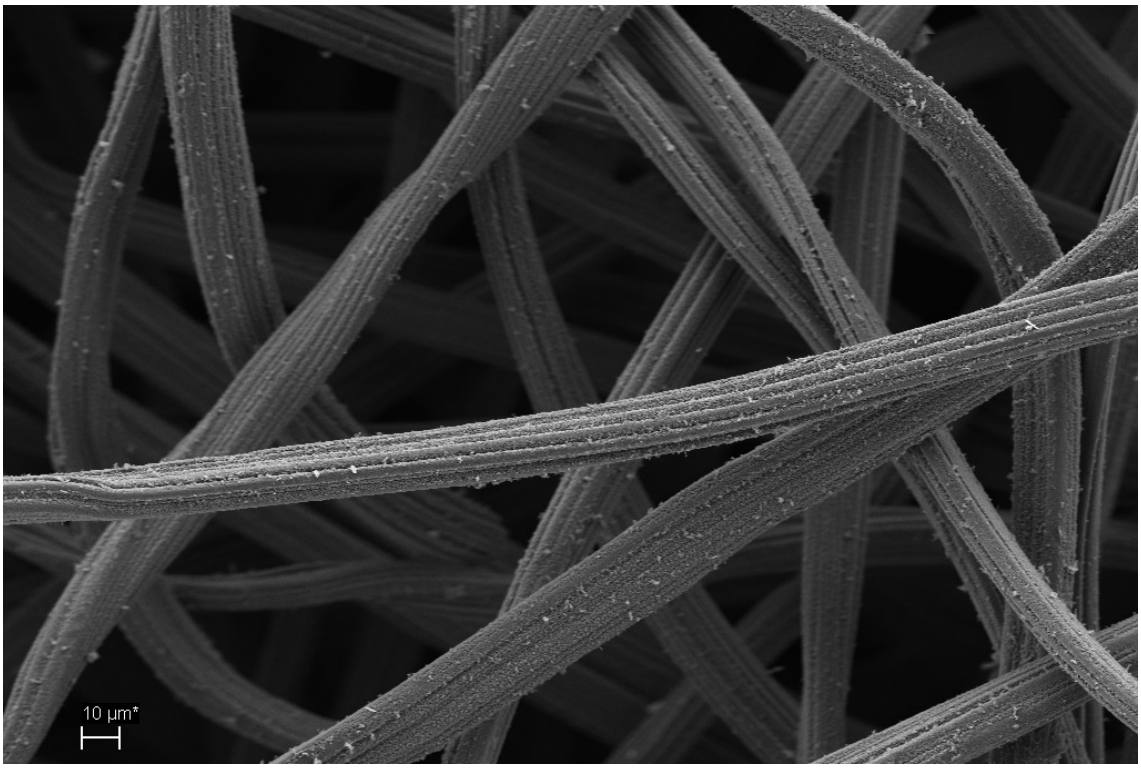

Figure 6.39. – FE-SEM Image of the ALD deposit of GF@CeO_2.

X-ray diffraction pattern of GF, GF@CeO_2 and GF@CeO_2:H electrodes are given in **Figure 6.40**. The broad peak near 2θ = 25 and 43^0 in the spectrum of GF-P electrode is attributed to the crystallographic planes of (002) and (004) of the original GF electrode. Additionally, diffraction peaks appeared in the pattern of GF@CeO_2 electrode at 28.5^0; 33.0^0, 47.5^0 and 56.3º (**Figure 6.40**); which are consistent with the Ceria (CeO_2) (111), (200), (220) and (311) crystalline planes, respectively. All peaks are in line with the standard pattern (JCPDS no.: 01-081-0792). After the treatment under reductive conditions, the obtained GF@CeO_{2-x} displayed different XRD patterns at 26.3º, 43.9º and 55.7º, indicating that a phase transition to CeO_{2-x} occurred in the reduction process. In spite the fact that the most intense peak is hindered under the broad peak related to GF, it can be observed on the two subsequently peaks on a low intensity marked by an asterisk. It also can be observed peaks related to CeO_2, which implies a partial reduction of the ceria structure by and oxygen deficiency presence on the lattice structure.

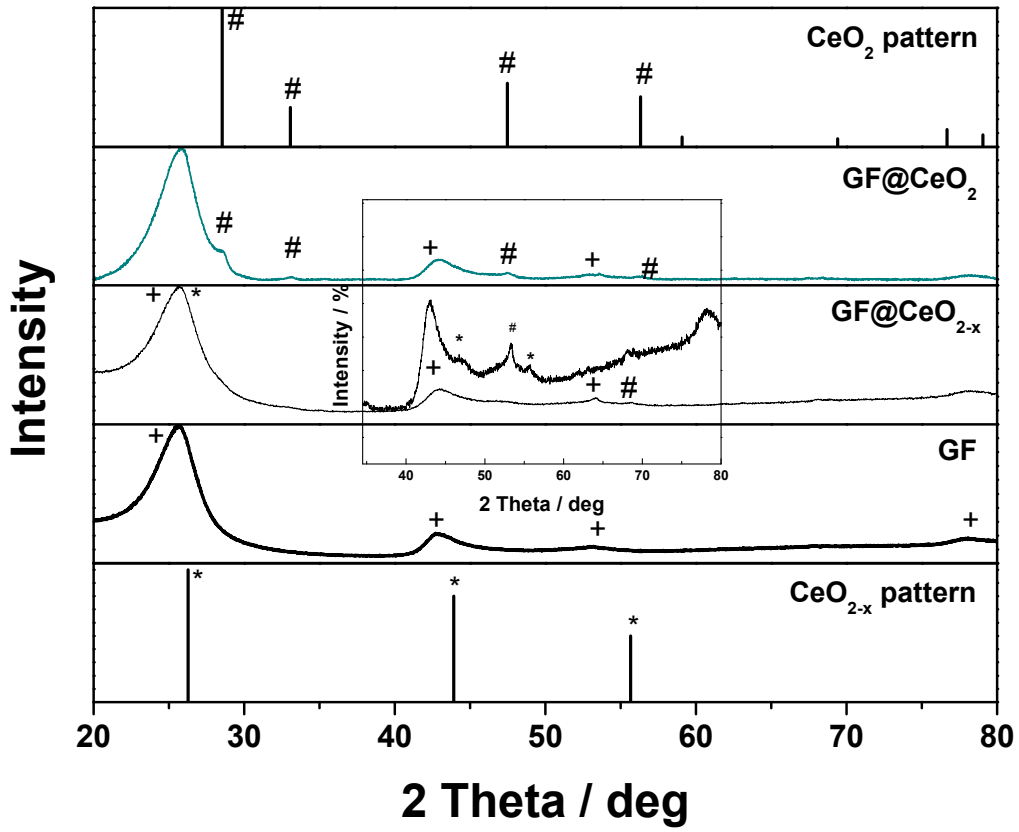

Figure 6.40. – X-ray diffraction spectra of GF-HT electrode and as-prepared GF@CeO_2 and GF@CeO_{2-x} electrodes.

6.1.4.1.1 Electrochemical characterization

Additionally, in order to experimentally verify the electrochemical characterization of the cerium-based catalysts, are performed several experiments in a three electrode cell. For that purpose, a drop cast deposit of the cerium materials is done over a glassy carbon (GC) electrode in case of the positive electrode catalyst, while the negative catalysts has been broadly explained in previous sections, where the electrocatalytic reaction of TiO_2 nanorods materials towards the negative reaction of the VRFB was investigated. **Figure 6.41** shows cyclic voltammetry experiments (CVs) for the ceria materials under study over the GC. To evaluate the electrocatalytic performance, we analysed several parameters from CVs, described as follow: the peak-to-peak potential separation (ΔV), the ratio of oxidation and reduction peak current (I_{pa}/I_{pc}), and the redox onset potential. Significant differences between all samples can be observed. For example, the GF electrode displays a cathodic peak due to VO^{2+}/VO_2^+ oxidation as well as surface oxidation of the felt and oxygen evolution reaction, but a smaller anodic peak can be appreciated (i.e. lower current density peak). This behaviour is ascribed to the difficult on the VO_2^+ reduction over the carbon surface[225,232,233].

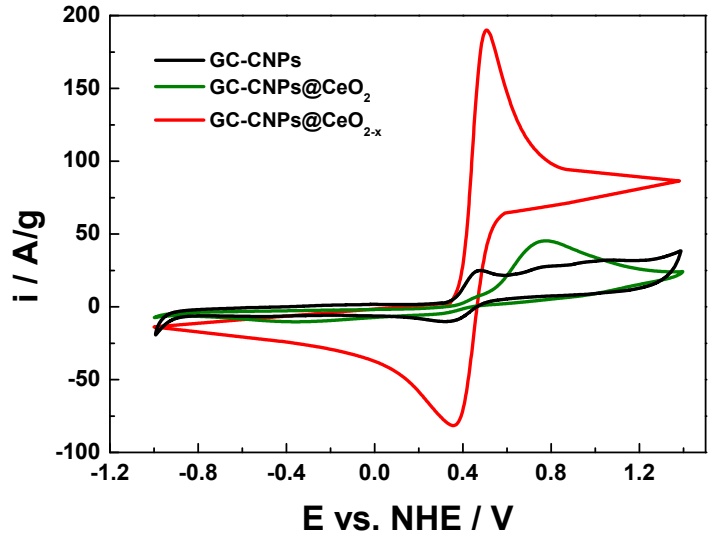

Figure 6.41. – Cycled Voltammetry performed using the as-prepared electrodes deposit over GC electrodes in 0.5 M VO^{2+} and 1M H_2SO_4. Scan rate: 10 mVs^{-1}.

On the contrary, enhanced oxidation processes are obtained using the CeO_2 and CeO_{2-x} NPs, indicating the positive effect of the CeO_2 coating and the doped improvement as oxygen vacancies are generated. Comparing both electrodes, the most pronounced peaks appeared using CeO_{2-x}. For example, in case of the cathodic peak current-to-weight ratio values of 45 and 190 Ag^{-1} were obtained for CeO_2 and CeO_{2-x}, respectively. The same trends were observed for the anodic peak, 10 and 81 Ag^{-1} for CeO_2 and CeO_{2-x} electrodes, respectively. Consequently, the ratio of the redox peak current (I_{pa}/I_{pc}) value obtained for CeO_2 electrode was 0.17 and for CeO_{2-x} electrode 0.72, closer to their ideal value unity for one electrode transfer process (**Table 6.7**). Moreover, the potential peak separation carried out by CeO_2 (ΔV= 290 mV) is larger than that of CeO_{2-x} (ΔV= 140 mV), indicating higher reversibility for the second cited. The origin of the improved electrochemical behaviour can be caused by an increment of charge and electron transfer properties, as oxygen-vacancies are induced in the lattice of the CeO_2 after thermal treatment in reductive atmosphere, which is analogous to the behaviour of other metal oxides[89].

These oxygen-vacancies are known to be electron donors, determining the surface and electronic properties of CeO_2, which improves the charge transport in CeO_2 as well as the electron transfer at the interface[42]. Indeed, electrochemical impedance spectroscopy measurement of GF@CeO_2 and GF@CeO_{2-x} electrodes showed that the charge-transfer resistance of GF@CeO_{2-x} for VO^{2+}/VO_2^+ reaction is remarkably smaller than the GF@CeO_2 electrode (**Figure 6.42**).

Table 6.7- Performances displayed for all electrodes studied in three electrode voltammetry for positive electrodes: oxidation, reduction and differential potential (E_{ox}, E_{red}, ΔE, mAg^{-1}); oxidation and reduction intensity (I_{ox}, I_{red}, mA) and intensity ratio (I_{red}/I_{ox}).

Sample	E_{ox} / V	E_{red} / V	ΔE / V	I_{ox} / mA	I_{red} / mA	I_{red}/I_{ox}
GC-CNPs	1.124	0.9694	0.15	0.795	0.165	0.21
GC-CNPs@CeO_2	1.214	0.9265	0.29	0.4311	0.07489	0.17
GC-CNPs@CeO_{2-x}	1.163	1.025	0.14	0.7137	0.5153	0.72

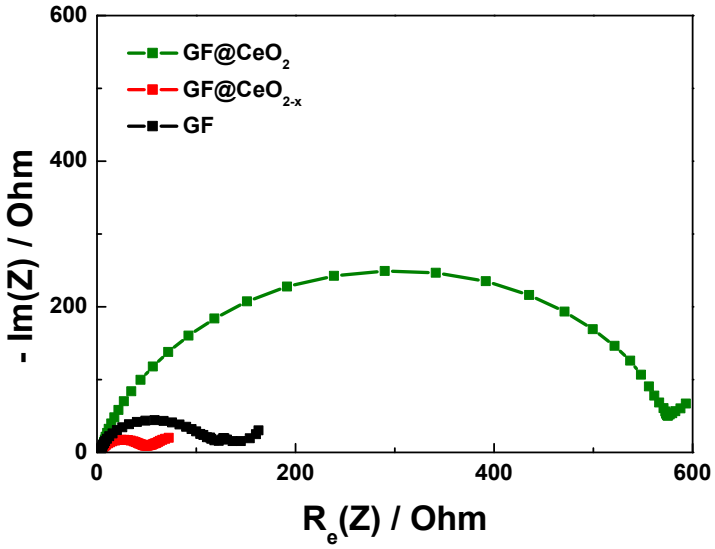

Figure 6.42. - Electrochemical impedance spectroscopy (EIS) has been done in a three-conventional electrode (0.25 cm^2) using GF, GF@CeO_2 and GF@CeO_{2-x} as working electrode and Hg/Hg_2SO_4 and platinum wire such as reference electrode and counter electrode, respectively. Electrolyte solution was 0.05 M V^{3+} in a 3 M H_2SO_4. EIS measurements were performed at open circuit potential (i.e. -0,33V vs. NHE) of 5 mV amplitude in the frequency range of 0.1-200 kHz at room temperature.

Besides, as we observed in the CV after the vanadium oxidation peak there is an oxygen evolution reaction that does not happen in presence of the Ceria (**Figure 6.41**). It is a consequence of the standard redox potential of cerium, as metal oxide, in between the VO^{2+}/VO_2^+ reaction and the OER, shifting the OER initial point at higher values. Therefore, the enhancement of the electrocatalytic properties in combination with the low oxygen-evolution reaction of the GF@CeO_{2-x} electrode demonstrates a superior performance on the positive electrode.

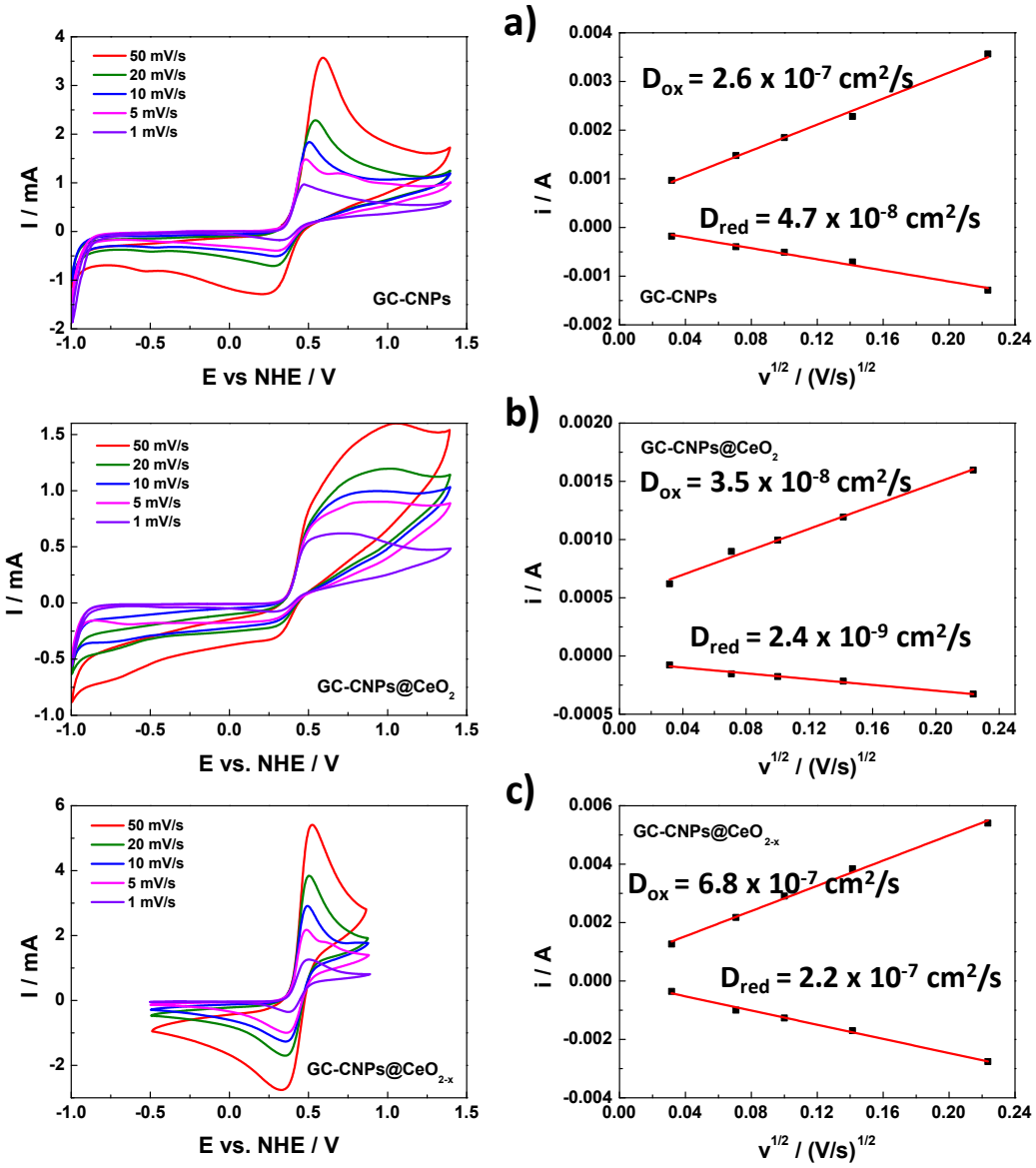

Figure 6.43. – On the left, cyclic voltammetry at several scan rates for Randles-Sevcik calculations in order to obtain Diffusion coeficient in 0.5 M $VOSO_4$ 1 M H_2SO_4 solution. **a)** carbon nanoparticles deposit over glassy carbon (GC-CNPs) **b)** GC-CNPs@CeO_2 **c)** GC-CNPs@CeO_{2-x}. On the right, Randles-Sevcik plots and Difusion constant done over GC in 3 electrode cell as positive electrode for: **a)** GC-CNPs, **b)** GC-CNPs@CeO_2, **c)** GC-CNPs@CeO_{2-x}.

Furthermore, Randles-Sevcik (**Figure 6.43**) and rotating disk electrode (**Figure 6.44**) experiments are done for the positive catalysts, CNPs@CeO_2 and CNPs@CeO_{2-x}, depositing some nanoparticles on top of a glassy carbon electrode (GC). This manner it is possible to obtain the Diffusion coefficient for the redox reaction of VO^{2+}/VO_2^+ on the surface of the different electrodes, showing one order of magnitude in the electrode diffusion enhancement in the oxidation while two in the reduction process between the CeO_{2-x} and CeO_2 catalysts. The best diffusion values correspond to $6.8x10^{-7}$ and $2.2x10^{-7}$ cm^2/s for the oxidation and reduction process, respectively. Moreover, it is obtained the kinetic constant for the oxidation of V^{4+} to V^{5+} measuring the

mentioned reaction in absent of diffusion limitations using a rotating disk electrode for this purpose. Here, it can be observed an increasing value from GF (3 x10^{-5} m/s) < GF@CeO_2 (2 x10^{-5} m/s) < GF@CeO_{2-x} (4 x10^{-5} m/s). Therefore the partially reduced ceria NPs are capable of a faster kinetic constant, improving the electrochemical performance towards the positive VRFBs redox reaction.

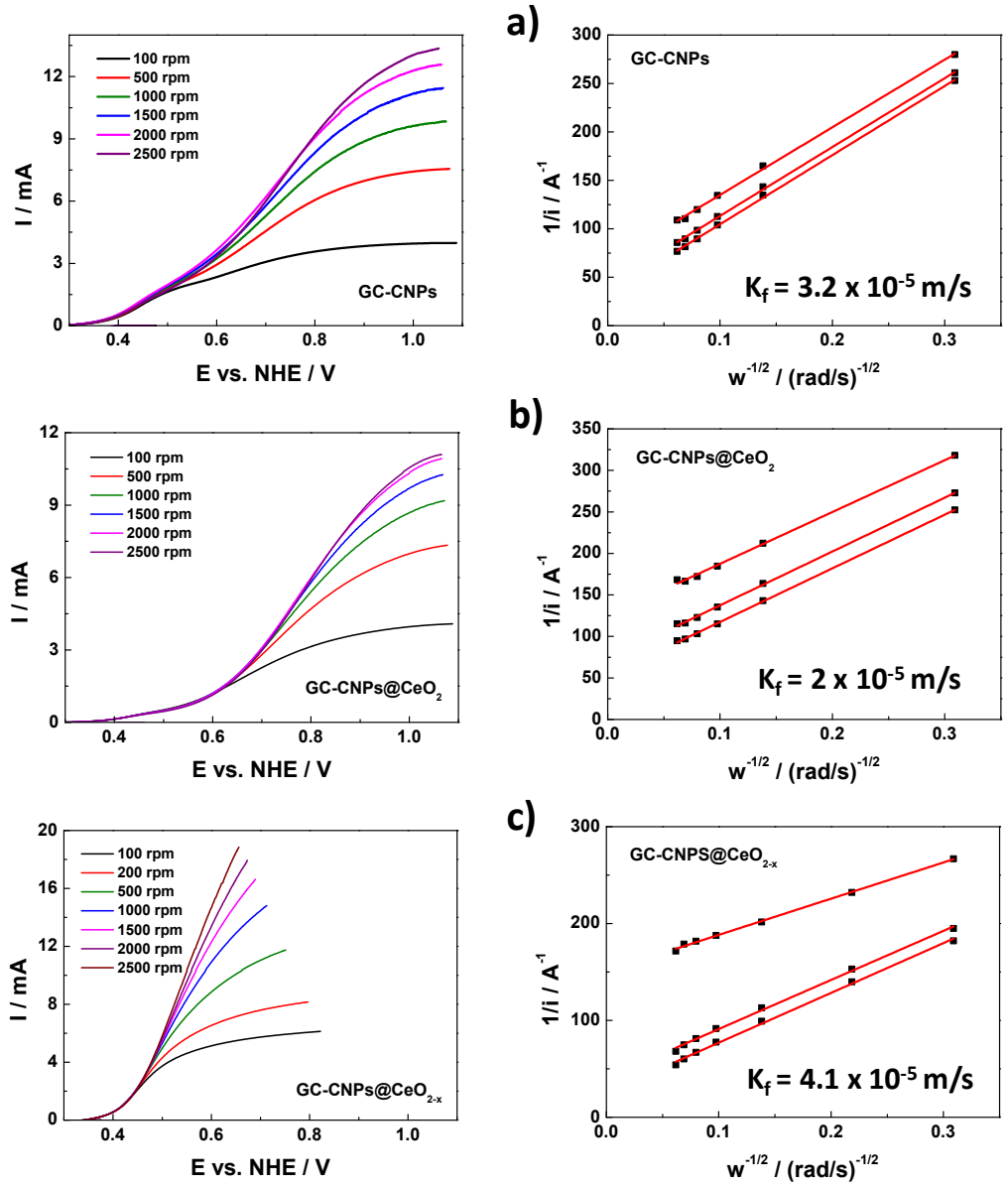

Figure 6.44. – On the left, rotating disk electrode experiments on several sample deposit onto glassy carbon in 0.5 M $VOSO_4$ 1M H_2SO_4 solution. **a)** GC-CNPs **b)** GC-CNPs@CeO_2 **c)** GC-CNPs@CeO_{2-x}. On the right, rotating disk electrode plot for several sample deposit onto glassy carbon as positive electrode to obtain the kinetic constant for: **a)** GC-CNPs, **b)** GC-CNPs@CeO_2 and **c)** GC-CNPs@CeO_{2-x}.

6.1.4.2 Single cell performance

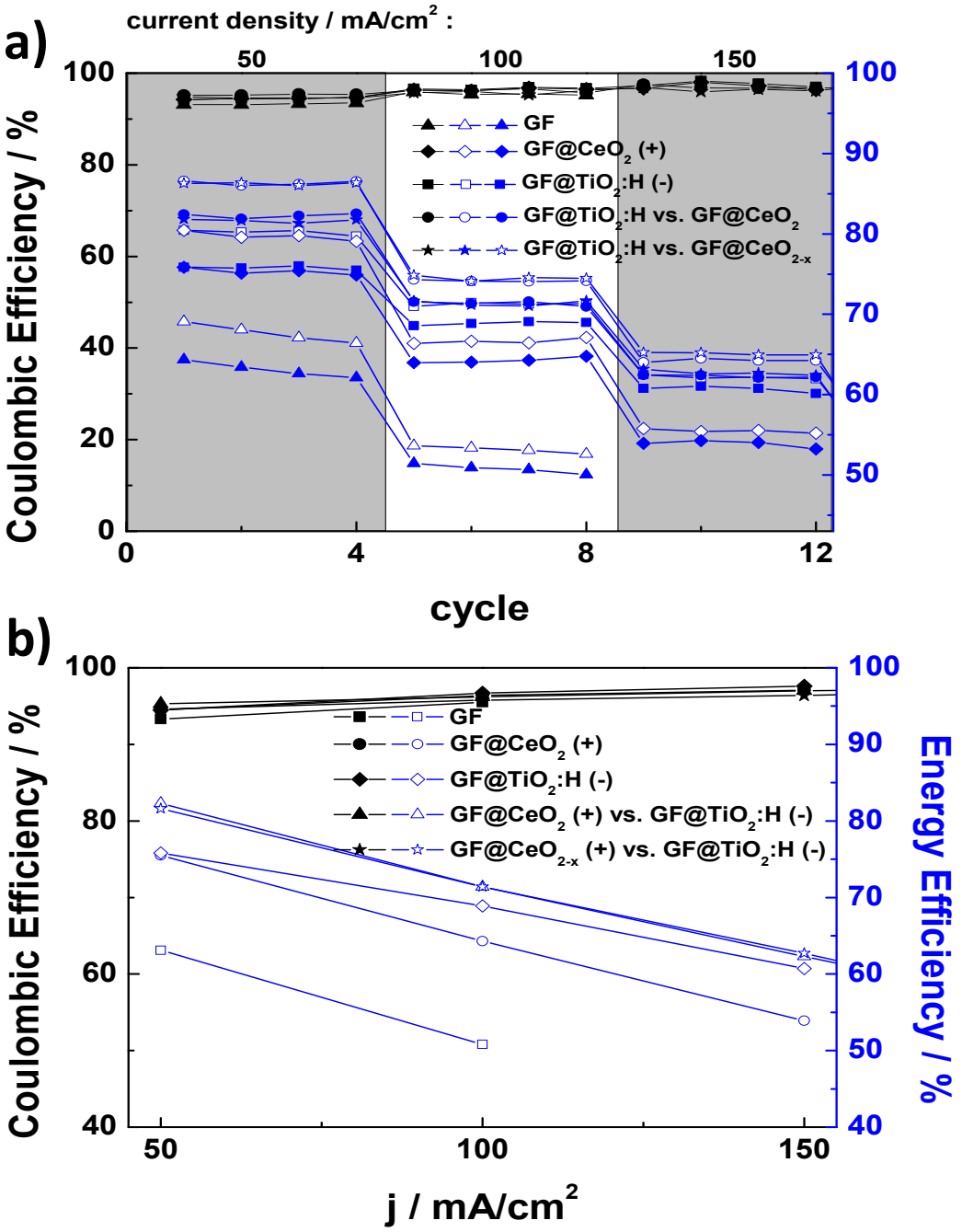

Figure 6.45. – a) Coulombic and voltage efficiencies amog cycling for increasing current densities applied, from 50 to 150 mAcm^{-2}, using different electrodes for the single cell. **b)** Coulombic and energy efficiencies relationship as incresing current densities applied, from 50 to 150 mAcm^{-2}, using different electrodes for the single cell. All the galvanostatic charge-discharge cycles are done in 1.5 M vanadium ions and 3 M H_2SO_4.

Finally, in order to ensure the potential application of ALD CeO_2 electrodes as positive electrode in large-scale VRFB batteries, a flow-type single cell is assembled using a GF@TiO_2:H as negative electrode. Its performance is compared to GF electrode using 1.5 M electrolyte concentration. **Figure 6.45a,** shows a comparison of the Efficiencies developed by a combination of different electrodes (GF or GF@TiO_2:H as negative electrodes and GF, GF@CeO_2 and GF@CeO_{2-x} as positive electrodes). For that purpose, the cell is operated at different values of current density, from 50 to 250 mA/cm^2. However, these values could not be achieved by all of them due to high polarization of the electrodes over the cut off value. In case of GF is only possible to apply up to 100 mA/cm^2, while 150 mA/cm^2 for GF on the negative and GF@CeO_2 on the positive, as well as for GF on the positive and GF@TiO_2:H on the negative due to a reduction of the overvoltage polarization of the cell. The relation between current and Efficiency for the different samples can be seen in **Figure 6.45b**. In case of the Coulombic efficiency (CE), it can be clearly notice a slightly increasing value as the current density is incremented and always above 95% CE. This tendency is a consequence of a decrease of the time that could be taking place ionic cross over and also side reactions (hydrogen evolution and/or oxygen evolution reaction). If we focus into the energy efficiency (EE) values, it is obvious a moderate descendant percentage as the current density increases. It is less pronounce when the electrodes are GF@TiO_2:H on the negative side, while using GF@CeO_2 on the positive. Even less current can be applied to the pre-treated pristine electrodes (GF), 100 mA/cm^2 as maximum. In order to compare, all the modified electrodes it can be seen in **Table 6.8**. The efficiency enhancement of them follows the order: GF@CeO_{2-x} (+) vs. GF@TiO_2:H (-) > GF@CeO_2 (+) vs. GF@TiO_2:H (-) > GF (+) vs. GF@TiO_2:H (-) > GF@CeO_2 (+) vs. GF (-) >> GF (+) vs. GF (-).

Table 6.8- Performances displayed for all electrodes studied in this work: current density applied (*j*, $mAcm^{-2}$); Coulombic efficiency (CE, %); voltage efficiency (VE, %) and energy efficiency (EE, %).

Sample	j / mA/cm^2	CE / %	VE / %	EE / %
GF(+) vs. GF(-)	**100**	**95.5**	**53.2**	**50.8**
GF@CeO_2(+) vs GF(-)	**100**	**96.4**	**66.6**	**64.3**
GF@TiO_2:H(-) vs. GF(+)	**100**	**96.7**	**71.3**	**68.9**
GF@TiO_2:H(-) vs. GF@CeO_2(+)	**100**	**96.2**	**74.2**	**71.4**
GF@TiO_2:H(-) vs. GF@CeO_{2-x}(+)	**100**	**95.8**	**74.5**	**71.4**
GF@CeO_2(+) vs GF(-)	**150**	**97.1**	**55.5**	**53.9**
GF@TiO_2:H(-) vs. GF@CeO_2(+)	**150**	**97.6**	**62.2**	**60.7**
GF@TiO_2:H(-) vs. GF@CeO_2(+)	**150**	**97**	**64.2**	**62.3**
GF@TiO_2:H(-) vs. GF@CeO_{2-x}(+)	**150**	**96.4**	**65.1**	**62.7**

In addition, it is analyzed the capacity retention on each one of the electrodes likewise the previously commented efficiencies. Seeing **Figure 6.46a**, all the electrodes get retention above 80% electrolyte utilization ratio at 50 mA/cm^2 of current density. However, as we increase it, the capacity retention decays. It is the case of GF, giving values below 50% at 100 mA/cm^2. The same issue happens for GF@CeO_2(+) vs. GF(-) at 150 mA/cm^2, but not in case of GF(+) vs. GF@TiO_2:H holding a 60% retention at the same current density. Although the best performance at 150 mA/cm^2 it is shown when our battery is enhanced in the positive side by a Ceria shell reduced and a reduced Rutile in the negative around a Graphite Felt core (80% capacity retention), they faded to a 60% electrolyte utilization ratio when 200 mA/cm^2 is applied.

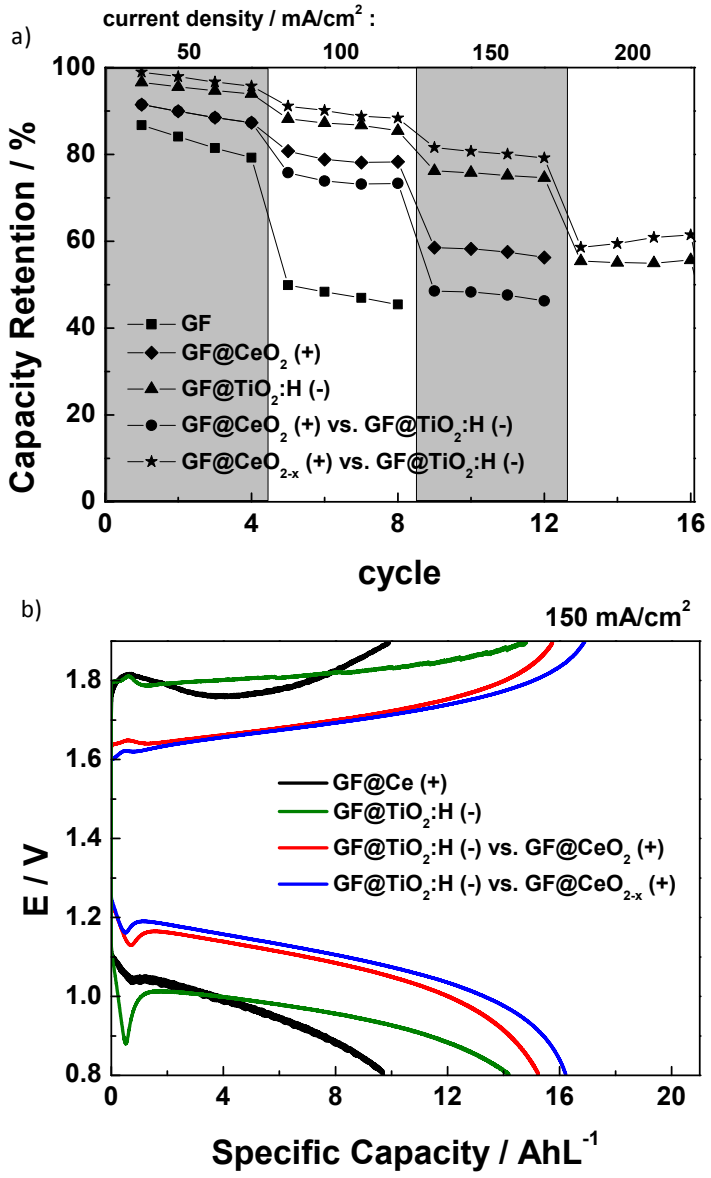

Figure 6.46. – a) Current density dependence with capacity retention of over cycles. **b)** Voltage profile correlating charge/discharge process performed at 150 mAcm^{-2} using an electrlyte of 1.5 M vanadium ions in 3M H_2SO_4.

In order to compare the different charge and discharge profiles using a variety of electrodes, it has to be at a highest 150 mA/cm^2 current density (**Figure 6.46b**). First, the Ceria electrode in the positive side of the cell while using only GF on the negative shows (9.6 AhL^{-1}) a pronounce slope, especially during charge, that evidence the highly abundant hydrogen evolution reaction taking place, which generates an overpotential while charging due to large electrode surface not in contact with the electrolyte. Secondly, in the opposite case using GF as positive electrode and GF@TiO_2:H as negative one (14.1 AhL^{-1}). The charge and discharge profiles reduce their slope, which means a side reaction inhibition as the case of the hydrogen evolution reaction (HER). Also catalysis over the reaction as the initial potential is substantially reduced, and therefore the kinetics are increased. Comparatively the oxygen evolution that occurs in this case is significantly much lower that the hydrogen evolution of the previous case. Finally, while using GF@TiO_2:H(-) on the negative side of the cell and the reduced (16.2 AhL^{-1}) and non-reduced (15.2 AhL^{-1}) Ceria shell over the GF, our profiles are slightly better in terms of capacity reached as a consequence of a more abundant active sites (-OH groups) on the negative and positive electrodes, following the proposed mechanism[227] (**Figure 6.47**). In case the capacity values are compared to the literature, an 80% of the theoretical capacity is achieved which value is above recent publications[234,235]. Bayeh et al. with TiNb2O7-rGO electrodes obtained a 70% for similar current densities, and also Yun et al. with GF-NiO NPs just reached a 67% of the theoretical capacity. It can be also observed in case of the Ceria sample reduced comparatively with the non-reduced, that the first one cited presents oxygen vacancies in the metal oxide structure and as a result increases the active –OH sites.

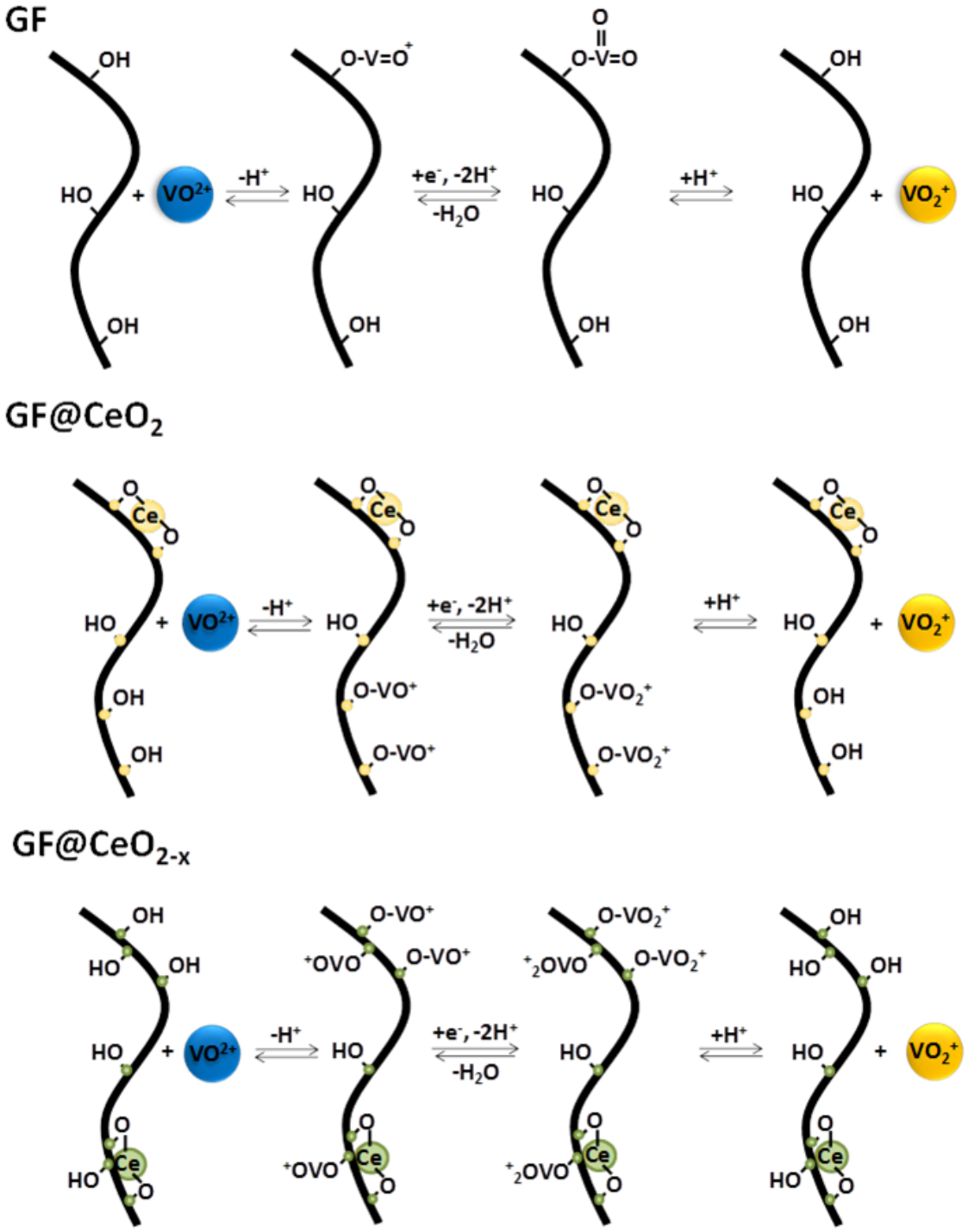

Figure 6.47. – Schematic mechanism proposed for positive reaction of VRFBs over different electrodes.

Furthermore, it is the reason not only the capacity due to catalytic improvement, but also in terms of voltage efficiency (defects enhance the conductivity of this semiconductor). The above explained tendency is kept at other current densities.

Thus, we wanted to verify the low self-discharge of the cell in static conditions and how the different electrodes behave. For that purpose, it was measured the OCV of the cell during 18 hours after charging at low current density (25 mA/cm^2). Looking at the **Figure 6.48,** we can elucidate when both electrodes are enhanced not only preserve better its potential during this period, but also has an initial greater value of open circuit voltage. It is followed by only one improved electrode, positive electrode covered by CeO_2. Both shows better stability than the case of pristine electrodes, where the OCP decays rapidly. It is an evidence of the really low self-discharge of this kind of technology.

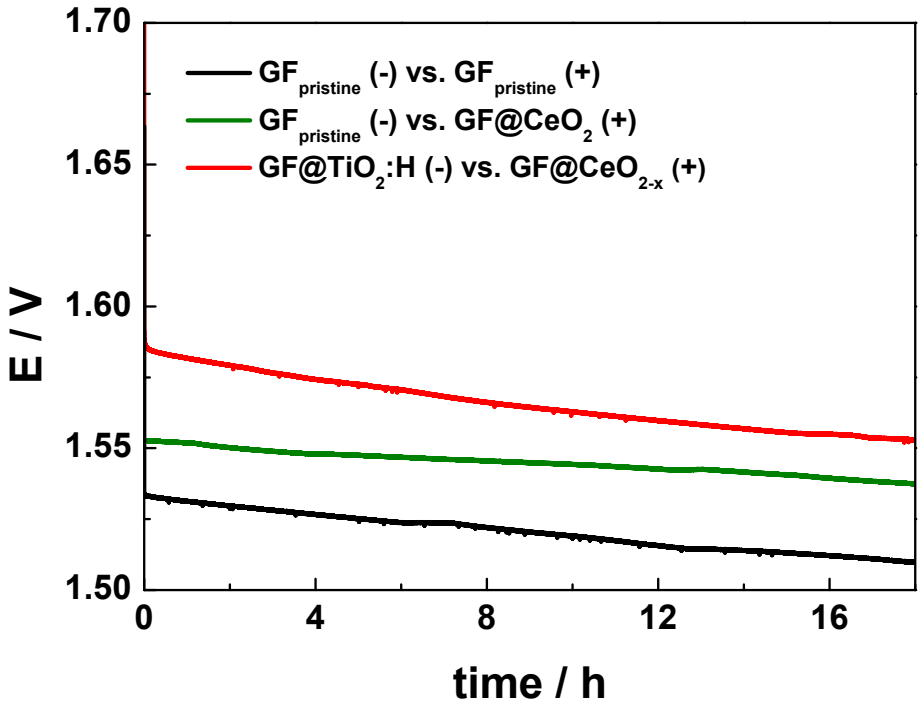

Figure 6.48. – Self-discharge process from a totally charged battery through time for different electrodes.

Afterwards, it is done a long term stability for the electrodes that shows a better performance, in particular the case of GF@TiO_2:H (-) vs. GF@CeO_{2-x} (+). We have cycled for 100 times at 200mA/cm^2 obtaining a 52% EE and 98.5% CE as well as an initial capacity of 12 AhL^{-1}, which degenerates until a 76% of the initial capacity. After this 100 cycles our cell is capable of last over other 60 cycles at 150 mA/cm^2 before experiment a capacity fading (below 62% of the initial capacity, from 13 to 8 AhL^{-1}) as we observe in the **Figure 6.49**. The EE and CE remains over these cycles around 58 and 98 % respectively. These electrodes enhance our battery performance allowing going up to 150 cycles easily without degradation, because of the reasons mentioned before our battery could be an advantageous choice for commercial application.

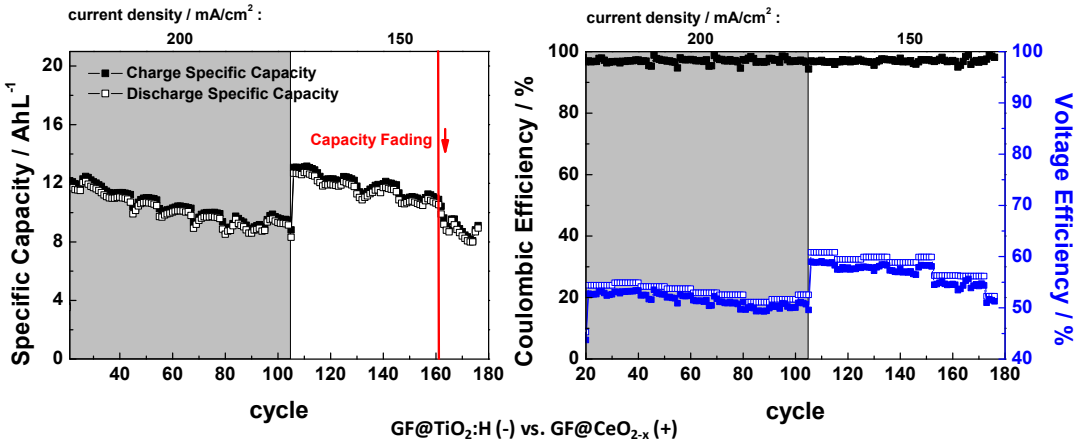

Figure 6.49. – Long-term stability of the GF@TiO_2:H (-) vs. GF@CeO_{2-x} electrodes. **a)** specific capacity over cycling at 200 and 150 mA/cm^2. **b)** Voltage and Coulombic Efficiencies over cycling at the same current density.

6.2 Conclusions

Along the experimental work done, it has been accomplished much obtaining the following conclusion points that summarize this chapter about electrodes modifications for all-vanadium redox flow batteries:

1. Titanium dioxide especially in its rutile (110) phase acts as a powerful electrocatalyst towards the VRFBs negative half-cell reaction. Increasing the active groups on the electrode surface and decreasing the side reactions taking place (HER). However, when the TiO_2 thickness increases above certain limit the semiconductor properties enlarge the charge transfer resistance towards the vanadium negative redox reaction due to an ohmic drop. In spite that fact, kinetically the reaction towards V^{3+}/V^{2+} is faster when the graphite felt is completely covered by the nanorods (GF-TiO_2(MNRs)). In order to improve the electrodes performance, it would be relevant to improve the conductivity when the fibers are completely covered by titanium dioxide nanorods in its rutile phase.

2. TiO_2:H based graphite felt electrode, as a low-cost, efficient and novel electrocatalyst towards the negative reaction was demonstrated to enhance the electrochemical performance in all-vanadium redox flow battery, especially at high charge/discharge rates. GF@TiO_2:H electrodes showed greatly improved electrochemical properties (i.e. fast electron charge process) in combination with a better selectivity to V^{3+}/V^{2+} reaction, inhibiting hydrogen-evolution reaction. Furthermore, the electronic donor properties were increased, comparatively with pristine and thermal treated, as a consequence of the oxygen-

vacancies formation in the structure of titanium dioxide. A specific discharge capacity of around 11 Ah/L with a 66.1% of energy efficiency was observed after 100 cycles of charge/discharge at high current densities rates up to 150mA/cm^2. In addition, significantly improved the electrolyte-utilization ratio to 87% was achieved using 1 M in vanadium solution. Afterwards, the performance of 2 M vanadium ion concentrations has been evaluated at high current density as well, (300 mA/cm^2) during 140-cycles, showing the great durability of the battery especially when reached 200 mA/cm^2. The CE value was > 96%; electrolyte-utilization ratio was 80%, with a specific capacity of 22 Ah/L, demonstrating the total suppression of HER and long term stability of VRFB. These results (**Table 6.3**) suggest that the TiO_2:H based graphite felt is a powerful electrocatalyst for high-performance VRFB application.

3. The partially reduced sample (TiO_2:N) favours the V^{3+}/V^{2+} due to a reduction of the charge transfer resistance as an increasing active sites are present on the surface, and therefore, more vanadium ions are capable of react simultaneously. TiN is formed over the TiO_2 decorating the carbon felt, consequently two conditions favour the V^{3+} reduction: i) The increase of O and N groups due to the presence of the catalyst formed (TiN-TiO_2) itself that promote the number of active sites for the reaction to happen, enhancing the electron charge transfer at the interface electrode/vanadium. ii) The increase of O and N groups due to the presence of them over the carbon felt structure. All these qualities have allowed us to achieve a high-power output of the cell up to 1500 mW/cm^2 (**Figure 6.22**), as well as work at high current density (150 mA/cm^2) with low ohmic losses and high redox reversibility. It allows our system to be able to obtain great energy efficiency (71%). We firmly believe this is a highly promising material in order to obtain a VRFB capable of give a strong energy momentum, from which this types of battery possess an undeniable lack. It could be a future perspective focus on the implementation of this enhanced electrode in a cell where other components of the battery has been improved, as the membrane and/or the electrolyte, and therefore obtain not yet reported values capable of compete with lithium technology.

4. Hydrogen treated TiO_2-based couple with defective Ceria-based graphite felt electrodes for negative and positive cell are an excellent option as low-cost, efficient and novel electrocatalysts that enhance the electrochemical performance in vanadium redox flow battery, especially at high charge/discharge rates. GF@TiO_2:H electrodes showed greatly improved electrochemical properties (i.e. low charge transfer resistance) in combination with the inhibition of hydrogen-evolution reaction. GF@CeO_{2-x} exhibits an improved kinetic over the positive reaction, as well as, delay the oxygen evolution due to its standard potential. Moreover, the electronic donor properties were

enhanced as a consequence of the oxygen-vacancies generation in the GF@TiO_2:H and GF@CeO_{2-x} electrodes, in case we compare to heat treated and thermally annealed in argon atmosphere. A specific discharge capacity around 10 AhL^{-1} with a 50% of energy efficiency was observed after more than 100 cycles of charge/discharge at high current densities rates up to 200$mAcm^{-2}$. The battery was capable of several docents more of cycles at high current (150 mA/cm^2) before reaching the capacity fading. In addition, it has been significantly improved the electrolyte-utilization ratio to 80% using 1.5 M in vanadium solution at 150 mA/cm^2. Additionally, at 200 mA cm^{-2}, the CE value was > 97%, electrolyte-utilization ratio was 60%, with a specific capacity of 12.3 AhL^{-1}, demonstrating the highly suppression of HER, OER, ion species cross-over and long term stability of VRFB. These results are presented in the literature for the first time, suggesting that the combination of these two electrodes can be powerful electrocatalysts for high-performance VRFB application.

6.3 Vanadium redox flow batteries perspective.

Given the current trend towards reducing greenhouse emissions and increasing the outbreak of renewable energy sources, along with demands of high-quality power and implementation of smart grids, there appears to be a general agreement on the need for stationary energy storages (EESs) in the electrical grid. The demand for it has rapidly changed the worldwide landscape of energy system research, which "recently" brought the RFB technology into the spotlight. Deemed suitable for large-scale energy storage, the unique mechanism of RFBs does offer tremendous research opportunities, although current fundamental research is clearly outpaced by industrial prototype development. Concrete and comprehensive research is therefore urgently needed in this field on, but not limited to, the topics of complex charge transfer and redox reaction kinetics on the electrode surface, transport in membranes, and fluid mechanics through the electrode. The growing interest and worldwide research and development (R&D) activities suggests a bright outlook for developing improved RFB technologies for the future electric grid[236].

Other important factors that should be considered in constructing a plan for future research on high power density VRFB systems are: i) how to promote uniformity and reduce the cost for integrating oxygen groups on the surface of electrodes, ii) how to develop catalysts with a large specific surface area and good electrical conductivity, iii) how to optimize the correlation between the flow rate and the electrochemical response of the electrode, iv) optimal cell and stack design to ensure uniformity electrolyte flow distribution to avoid "dead zones" in the electrode that can lead to gassing side reactions during charging, v) development of low-cost carbon bipolar substrates with good corrosion resistance during over-charge to ensure long cycle life[227].

When evaluating or developing new high performance electrode materials, therefore, appropriate analytical methods are needed that can evaluate both the electrochemical and the hydraulic properties of the material. In the RFB, there is a

flow of electrolyte through the electrodes; therefore its electrochemical responses will be highly dependent on the electrode structure/morphology, as will the pressure drop and pumping energy losses, which are almost always ignored when reporting energy efficiencies[145].

There are a variety of promising pathways for substantial improvements in the performance and cost of RFB systems. Although improvements in cell performance have been recently demonstrated on multiple types of conventional RFB chemistries, it appears likely than the next-generation of RFB systems will be composed of significantly different materials than those being used today. A primary focus for R&D should be on pathways that enable lower costs, both the use of inherently lower-cost materials, as well as materials that can enable significantly higher energy densities (Wh/L) and/or power densities (W/m^2). Some of the different technology-advancement opportunities mentioned in the previous chapter (Introduction) are complementary, which could potentially facilitate the pace of development. For example, it is likely that the next-generation of RFB chemistries shall use larger active-species molecules, as we will expose in the next chapter, which can facilitate the development of simple porous membranes with acceptable ionic selectivity. Additionally, advancements can be facilitated by improved understanding of RFB fundamentals (i.e. redox kinetics and impact of carbon surface species, multi-component transport of various ions and water in membranes in equilibrium with RFB chemistries, etc.)[237].

Since extensive testing of different materials, components, and cell design over a broad range of conditions is time consuming and costly, mathematic modeling and simulation would be efficient ways to systematically reduce the number of tests and provide valuable insights into the reaction environment at the cell or stack levels. Although research groups have begun to develop mathematical models that simulate over-potentials and gassing side reactions in the RFB[238,239], only small-scale cell and electrode dimensions have been considered to date. The effect of flow-rate on cell efficiency and pumping energy losses has been modeled for kW-scale stacks by Tang et al.[145], more effort is needed to develop mathematic models for full-scale electrodes and cells that consider the mass, heat and charge transfer, electrolyte flow rate and velocity as well as electrolyte flow distribution for the development of high performance RFBs.

Finally, one of most important technical issues is how to secure the long-term durability of RFBs. In addition to its corrosion resistance during overcharge at the positive electrode, the chemical and mechanical stability of the bipolar carbon substrate materials must also be considered, while the development of improved methods to reduce contact resistance between the bipolar plate and current collectors.

To increase the value of electrode research and development for RFB, an in-depth and more considered research effort that includes all aspects of the electrode material selection and cell design along with the effects of the flowing electrolyte on overall battery performance should therefore be addressed.

7 Organic Redox Flow Batteries

7.1 Current trend in Redox Flow Batteries

Despite the fact that the systems described previously were already proposed several decades ago, they are still the subject of current research. A lot of interesting technologies have been reported over the last few months[240,241]. These systems show several inconvenient related to the vanadium abundance, the cost of it, as well as the geopolitical impact caused by its mining. As a consequence, the implementation of organic redox active species is a first step in order to avoid these disadvantages. However, as conventional inorganic redox flow batteries they also have several drawbacks, which limits their commercial success. Once the solubility and stability of these molecules is improved, the development of RFBs based on inexpensive and sustainable redox active organic materials can overcome their commercial limitations.

7.2 Rise of the organic active materials

When the term "organic" or "all-organic" in association with redox flow batteries it is referred only to the redox active materials used and not to the solvent or the supporting electrolyte, which can be an aqueous or organic solvent capable of solve the organic redox active material. **Figure 7.1** shows a scheme of an organic redox flow battery system.

Intensive research on the use of RFBs as flexible and scalable energy storage systems came to the conclusion that future RFB systems, irrespective of their use for domestic or large-scale application, have to utilize noncorrosive, safe, and especially low-cost charge-storage materials[242,243]. In the last decade the first steps were taken by the utilization of organic additives such as complexing agents[244,245], followed by metal-ligand complexes with organic ligands as charge storage materials[124,246], and subsequently to flow batteries with an inorganic and an organic active material[66,247]. In recent years, organic/halogen[248,249], and all-organic RFBs were developed[1,250]. Organic compounds offer the potential to overcome several metal-related problems and may lead to sophisticated high-performing RFBs for tomorrow's electricity grids, due to its earth abundance and low cost, as well as fast kinetics. For that purpose, new organic redox-active charge storage materials have to be discovered and investigated for application in RFBs. These materials need to be low-molar-mass compounds or redox-active polymers, with a molar mass < 1000 g/mol and ≤ 2 redox-active units per molecule, both with well-defined electrochemical properties. Selected examples are summarized in **Figure 7.2**. These systems have inherent advantages, as small molecules are used, little or no synthetic effort, potential high solubility, and good diffusion coefficients, whereas polymers offer the prospect of using more cost-efficient and robust separators compared to ion-selective membranes.

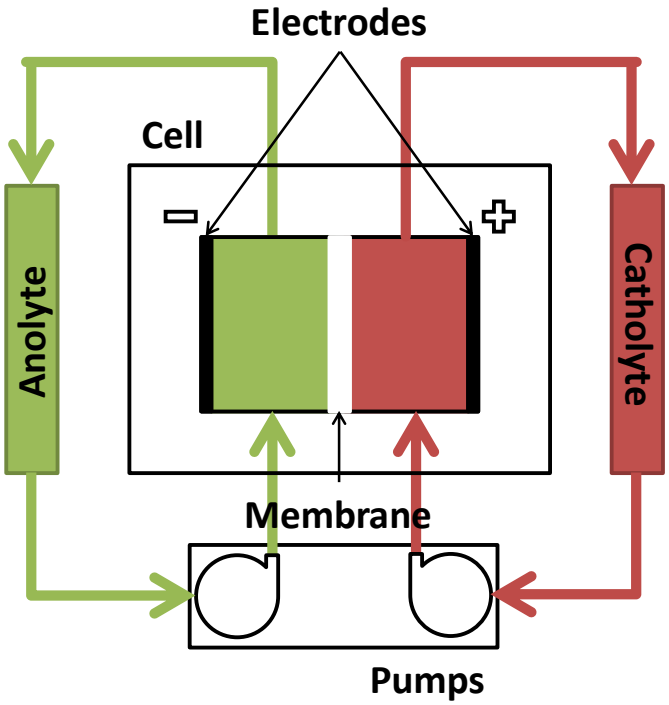

Figure 7.1 - Schematic of Organic Redox Flow Battery (ORFB).

The development of a so-called all-organic equivalent to VRFB with a bipolar redox-active material is of high interest, because this material would be able to undergo oxidation, as well as reduction reactions and could, therefore, be applied as both the cathode and anode active material. This feature would reduce the synthesis effort of the whole process and potentially overcome the problem of cross-contamination, since a slow mixing of the electrolytes would only lead to a reduced Coulombic efficiency but not to a continuously decreasing charge/discharge capacity[251], as the same molecule can be either reduced or oxidized. Organic molecules are also abundant, tunable by synthetic pathways and an improved kinetic with the possibility of having two-electron transfer process (as happens to quinones)[1,2]. Such a battery has the potential to meet the demanding cost, durability, eco-friendliness, and sustainability requirements for grid-scale electrical energy storage.

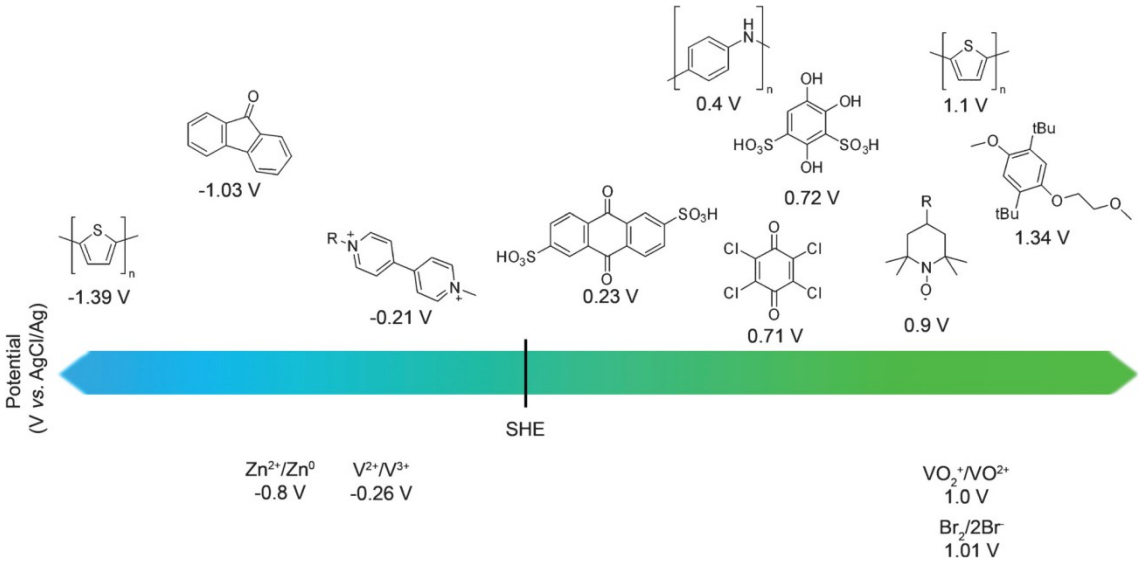

Figure 7.2 –. Schematic overview of selected organic/inorganic active materials and their redox potentials[240]; recalculated to a SHE reference if measured against another reference electrode. Conversion factors: SHE to AgCl/Ag=+0.197 V, SHE to SCE=+0.241 V, SHE=Fc^+/Fc=+0.750 V[252]; NHE: normal hydrogen electrode, SCE: standard calomel electrode, Fc: ferrocene[247,249,261,253–260].

7.3 Quinones as electroactive molecules

In case of quinones as active material possess a charge capacity in the range of 200–490 Ah/kg, and cost about $5–10/kg or $10–20/kWh, leaving ample scope for achieving the US Department of Energy's target of $100/kWh for the entire battery system. As a consequence of the successful perspective of quinones, they could work as organic redox-active material, especially anthraquinones, working as anode material[262].

In a preliminary study, conducting cyclic voltammetry measurements to investigate the electrochemical properties of anthraquinone in buffered and unbuffered aqueous solution at different pH values were done[263]. In these studies, quinoidic structures revealed promising properties for charge-storage applications in flow batteries. The solubility could be ensured by suitable substituent, and the redox potential can be adjusted in the same manner.

An alkaline quinone flow battery by using commercially available 2,6-dihydroxyantraquinone (2,6-DHAQ, **Figure 7.3**) and ferrocyanide/ferricyanide [264]. This system represents an improvement over the organic/halogen aqueous RFB [2]**Error! Reference source not found.**. The ferricyanide/ferricyanide replaced the angerous $Br_2/2Br^-$ redox couple. In contrast to this, ferricyanide/ferricyanide has a low toxicity and is non-volatile. The authors claimed on the basis of these characteristics that the reported RFB can be used as a cost-efficient, nontoxic, nonflammable, and sage energy-storage system. However, the strongly alkaline electrolyte is also highly corrosive (pH 14; 1M KOH).

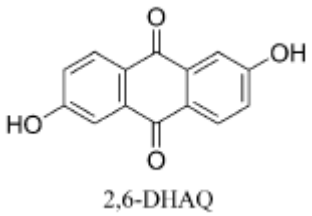

Figure 7.3 - Schematic representation of the chemical structure of 2,6-dihydroxyanthraquinone (2,6-DHAQ).

The introduction of electron-donating hydroxyl groups in the 2,6-DHAQ reduce the reduction potential and increase the battery voltage[2,264]. Moreover, the hydroxyl groups of the quinone, shown in **Figure 7.3**, are deprotonated in alkaline solution, which improves the solubility up to 0.6 M in 1 M KOH solution at room temperature. The reduction potential is independent of the pH value above pH 12. Hence, the reversibility of the redox displayed a rapid kinetic rate constant and two one-electron reductions separated by 60 mV.

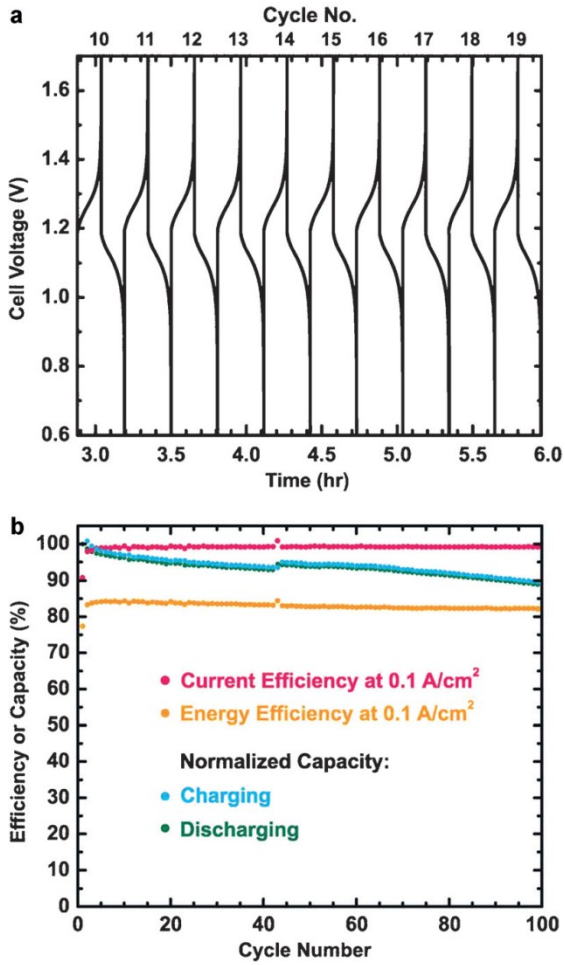

Figure 7.4 – Top. Galvanostatic charge-discharge plots for a single cell using 0.5 M 2,6-DHAQK2 in 1 M KOH and 0.4 M K4Fe(CN)6 in 1 M KOH as anolyte and catholyte, respectively. **Bottom**. Energy, charge and discharge efficiencies during 100 cycles for a single cell using 0.5 M 2,6-DHAQK2 in 1 M KOH and 0.4 M K4Fe(CN)6 in 1 M KOH as anolyte and catholyte, respectively.

The electrochemical performance was investigated in a flow cell containing a Nafion 212 membrane, 0.5 M dipotassium 2,6-dihydroxyanthraquinone (2,6-DHAQK$_2$) in 1 M KOH solution as the anolyte, and 0.4 M potassium ferrocyanide ($K_4Fe(CN)_6$) in 1 M KOH solution as the catholyte. This performance correlates to an energy density of 6.8 Wh/L. A constant current density of 100 mA/cm^2 was applied, and 100 charge/discharge cycles with a current efficiency above 99% and steady energy efficiency of 84% were measured (**Figure 7.4**) [264].

In 2014, Yang et al. reported the first aqueous organic Redox Flow Battery (AORFB). They used a water soluble 1,2-benzoquinone-3,5-disulfonic acid (BQDS) as the organic cathode active material and anthraquinone-2-sulfonic acid (AQS) **(7.1)** as well as anthraquinone-2,6-disulfonic acid as the organic anode active material.[1]

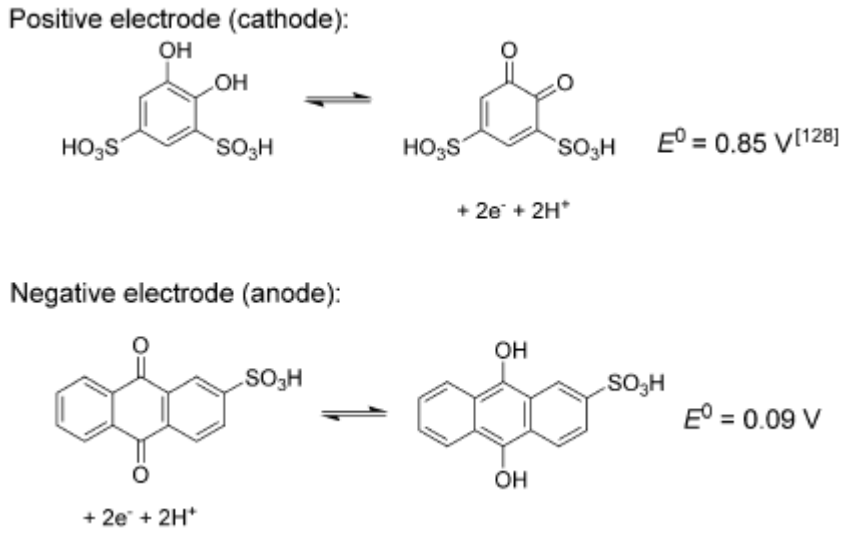

(7.1)

The authors developed a redox-flow cell with a membrane electrode assembly, which was fabricated from coated carbon paper electrodes and a Nafion 117 membrane. The flow cell contained 0.2 M BQDS and 0.2 M AQS in 1 M H_2SO_4 as the catholyte and anolyte, respectively. The electrolytes had a calculated energy density of 1.25 Wh/L. A charge/discharge experiment was done over 12 cycles at a current density of 10 mA/cm^2, obtaining values of capacity retention close to 90%.[1] Limiting factors of these organic materials are their moderate solubility in aqueous media and the observed mass transport of the reactants. These factors and the non-optimized battery setup lead to a restriction of the possible current density. The reported system can be seen as an improvement compared to the AQDS/bromide RFB in terms of safety, as the toxic bromine catholyte is replaced by BQDS. However, the capacity and the electrical performance are significantly inferior.

Zhang et al. reported an aqueous RFB with the already known water-soluble 1,2-benzoquinone-2,5-disulfonic acid (BQDS) as the catholyte and an inexpensive

anthraquinone derivative, 3,4.dihydroxy-9,10-anthraquinone-2-sulfonic acid (ARS), as the anolyte **(7.2)**.[1,265]

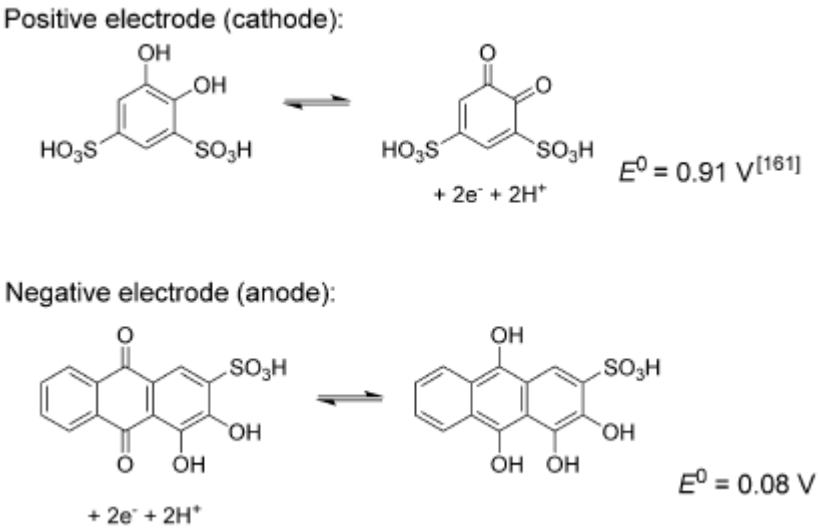

(7.2)

Both charge-storage materials are commercially available. Electrochemical researching showed that ARS exhibits a two-electron redox process and that the redox reactions of both molecules are highly reversible. The used laboratory flow cell comprised copper plates as current collectors and a Nafion 212 proton-exchange membrane. Charge/discharge measurements with 0.05 M BQDS and 0.05 M ARS in 1 M H_2SO_4 as the catholyte and anolyte, respectively, were performed with various current densities of 20, 30 and 60 mA/cm^2 to investigate the cell performance. Three cycles with an average discharge capacity of 90 mAh, calculated discharge capacity retention around 98%, as well as a Coulombic efficiency of 99% were achieved. The maximal power density of 10,6 mW/cm^2 was accomplished at 80% SOC at a current density of 60 mA/cm^2.[265]

The authors obtained good Coulombic efficiencies through fast charging and slow discharging cycling, but the not optimized flow-cell setup lead to a voltage loss. Moreover, the observed energy density of 0.4 Wh/L and the current density is limited by the restricted solubility of the used redox active molecules, especially ARS.

Considering all the concepts shown above, the target is the use of quinones molecules as the most promising candidates, especially as anode material, for the battery concept as they present a good reversibility, moderate solubility and higher electron density, as two electrons are involve in the redox process.

In the AORFBs studied, two different aqueous solutions of soluble organic redox substances such as quinones are circulated through the electrodes. The appropriate organic redox couples for the positive and negative electrodes are 1,2-benzoquinone-2,5-disulfonic acid as catholyte and disodium anthraquinone-2 7-disulfonate as anolyte, both solvated in a methanosulfonic acid solution. It is expected that an aqueous cell is capable of obtain a voltage as high as 1.0 V. The

goal is enhance the solubility of the active species, which the state of the art lacks about. Moreover, the efficiencies and stability of the device while cycling is also an important issue to consider, for that purpose, modified electrodes with the addition of oxygen and nitrogen groups on their surface by several methods have been implemented in the battery.

7.3.1 Selection criteria for electrolyte

While oxidation-reduction properties of organic compounds such as quinones have been known by electrochemists for many years, a preliminary understanding of its electrode reaction mechanism in acidic aqueous solutions is developed.

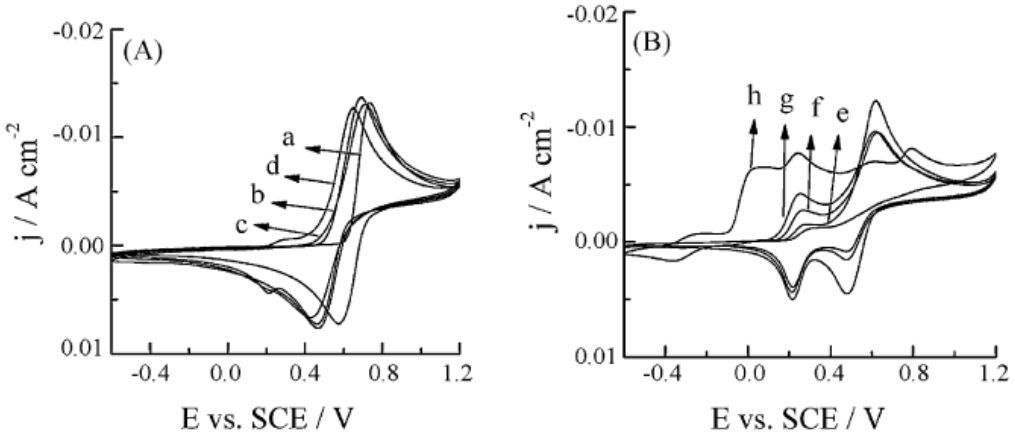

Figure 7.5 - Cyclic voltammograms for 0.05 M Tiron in 1 M KCl solutions of pH a) 0; b) 2; C)4; d)6; e)7; f)8; g)10; h) 12 at a graphite electrode, scan rate: 50 mVs^{-1}.

The structures of some catechol (quinones) derivatives are affected greatly by the pH of aqueous solutions, thereby exhibiting different electrochemical behaviors with varying the pH. As a derivative of catechol, the electrochemical behavior of tiron may be pH dependent, as seen in eq. **(7.3)**. Therefore, this section firstly deals with the influence of pH on the voltammetric behavior of tiron to make sure the suitable pH range of solutions for the use of tiron in RFBs as an active material, (**Figure 7.5A**) shows the influence of pH on the cyclic voltammograms of 0.05 M tiron at a graphite electrode in 1M KCl aqueous solution for different pH. As seen in **Figure 7.5**, the profile of I vs. E curves is almost the same in solutions with pH lower than 4. And, only one oxidation peak (E_{pa} = 0.74 V) and a corresponding reduction peak (E_{pc} = 0.58 V) are obtained. However, with the increase of pH, the oxidation peak potential shifts toward a less positive value. Also, the peak current is somewhat reduced. When the pH of solutions reaches 4, an additional much smaller oxidation peak and a corresponding reduction peak appear at around 0.25 and 0.20V vs. SCE, respectively. From **Figure 7.5B**, it is found that when the pH changes progressively from 4 to 12, the responding currents of the new coupled peaks increase gradually. In contrast, the peak current at the high potential

decreases continuously. When the pH is up to 12, multi-oxidation peaks appear on the voltammograms without the corresponding reduction peaks. This indicates that the oxidation products of tiron are difficult to be reduced in strongly alkaline solutions of pH up to 12. It is manifested by the above cycle voltammograms that in acidic solutions of pH lower than 4, the electrode reaction of tiron is simple with a relatively high potential, which is favorable for the application of tiron in RFBs. The proposed charge-discharge processes of the tiron redox reaction can be described as follows:

Positive:

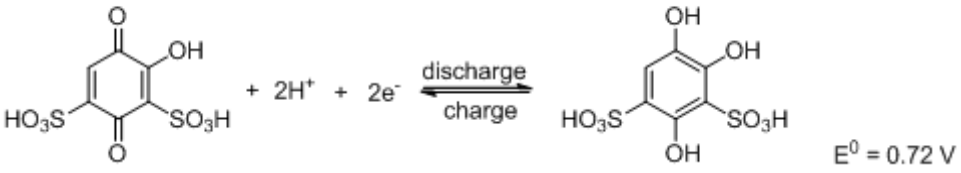

(7.3)

Hence, following the pH study described above, we decided to use acidic electrolyte solutions in order to facilitate the quinones redox reaction. Moreover, selecting an appropriate acidic solution for benzoquinones derivates (p-hydroxybenzene, o-hydroxybenzene or disodium 4,5-dihydroxy-1,3-benzenedisulfonate) as catholyte and anthraquinone derivates as anolyte (anthraquinone 2,7-disulfonate) (**Figure 7.6a**). Initially, it is done a cyclic voltammetry for different solvents (**Figure 7.6b**) at low scan speed, 1mV/s, therefore study the reversibility parameters in several conditions for p-hydroxybenzene, which are shown in **Table 7.1**. Moreover, PEIS measurements (**Figure 7.6c**) show a lower charge transfer and also minor electrical resistance when using acid solvents (3 M H_2SO_4 and 3 M $MeSO_3H$) not mixed with ethanol.

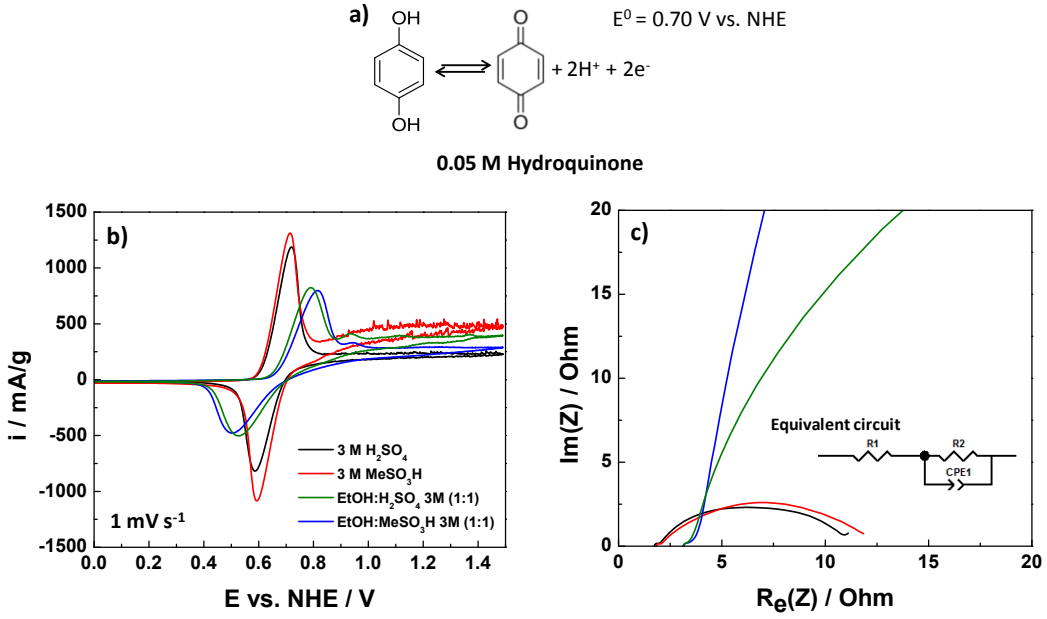

Figure 7.6. - a) p-benzoquinone redox reaction showing the standard potential. **b)** Cyclic voltammetry done for 0.05 M p-benzoquinone reaction showed in a) using different solvents (3 M H_2SO_4, 3 M $MeSO_3H$, EtOH:3 M H_2SO_4 (1:1) and EtOH:3 M $MeSO_3H$ (1:1)) at 1mV/s. **c)** PEIS at 0.7 V vs. NHE in the same conditions as b) for carbon felt as working electrode. It also shows the equivalent circuit for the system.

Furthermore, taking a closer look to the electrochemical parameters values it is obvious the greater reversibility when using methanosulfonic acid as solvent not only in terms of difference between oxidation and reduction potentials, but also the charge ratio between reduction and oxidation. Showing the lower value and closest to 1, respectively. Although the mixed solution EtOH:$MeSO_3H$ (1:1) has an initial satisfying reduction/oxidation ratio (0.90), it has the larger differential between reduction-oxidation potential. In consequence, the initial strategy to enhance the organic active material's solubility by adding a polar protic solvent with a lower dielectric constant than water and more suitable to dissolve quinone molecules was not profitable. Therefore, methanosulfonic acid will be used as solvent for the electrolyte containing quinone redox pairs.

Table 7.1.- Cyclic voltammetry electrochemical parameters from **Figure 7.6b**.

p-hydroquinone	E_{ox}/ V	E_{red}/ V	ΔE/ V	I_{ox}/ mAg^{-1}	I_{red}/ mAg^{-1}	I_{red}/I_{ox}
3M H_2SO_4	0.729	0.597	0.132	1516	-1146	0.76
3M $MeSO_3H$	0.724	0.603	0.121	1520	-1477	0.97
EtOH:H_2SO_4 3M (1:1)	0.794	0.538	0.256	1127	-1317	0.86
EtOH:$MeSO_3H$ 3M (1:1)	0.822	0.514	0.308	1391	-1543	0.90

On the other hand, looking into **Table 7.2** it can be seen how the solubility increases as the solvents become less polar. It reaches a maximum for the p-dihydroxybenzene when mixed ethanol with the acid, sulfuric or methanosulfonic. However, methanosulfonic acid by itself is capable to solve larger amount of quinone as the methyl group helps to stabilize better the quinone structure. Taking into account the values obtained from the electrochemical parameters in **Table 7.1**, for the orto- form of the dihydroxibenzene has only been considered the two acids for solubility measurements. Outstandingly, o-dihydroxibenzene reaches 3 M when using methanosulfonic acid as solvent which give an interesting initial point for an organic aqueous battery with a ground breaking quantity of active material, capable of make this technology commercially feasible.

Table 7.2. - Solubility of two different benzoquinones, as standard active molecules, in several solvents.

Active molecule	Solvent	Max. Solubility / M
p-dihydroxybenzene	H_2SO_4 3 M	0.2
	$MeSO_3H$ 3M	0.5
	Acetonitrile	1.2
	EtOH:H_2SO_4 3M (1:1)	2.2
	EtOH:$MeSO_3H$ (1:1)	2.6
o-dihydroxybenzene	$MeSO_3H$ 3M	0.8
	H_2SO_4 3 M	3.0
3,4-dihydroxybenzoic acid (+)	H_2SO_4 3M	< 0.58

	$MeSO_3H$ 3M	<0.4 M
	KOH 3M	2 M
	DMSO	5 M
	MeCN	< 0.35 M
	Na_2SO_4	< 0.3 M
1,4-dihydroxyanthraquinone (-)	H_2SO_4 3M	< 0.18 M
	$MeSO_3H$ 3M	< 0.18 M
	KOH 3M	< 0.20 M
	DMSO	0.18 M
1,8-dichloroanthraquinone (-)	H_2SO_4 3M	< 0.05 M
	$MeSO_3H$ 3M	< 0.06 M
	KOH 3M	< 0.09 M
	DMSO	0.1 M
1,8-dinitroanthraquinone (-)	H_2SO_4 3M	< 0.05 M
	$MeSO_3H$ 3M	< 0.05 M
	KOH 3M	< 0.05 M
	DMSO	0.12 M
Sodium anthraquinone-2-sulfonate (-)	H_2SO_4 3M	< 0.09 M
	$MeSO_3H$ 3M	< 0.11 M
	KOH 3M	< 0.09 M
	DMSO	0.8 M
2,4-dihydroxybenzoquinone (+)	H_2SO_4 3M	< 0.09 M
	$MeSO_3H$ 3M	< 0.85 M
	KOH 3M	0.4 M
	DMSO	0.95 M
Tiron (+)	H_2SO_4 3M	0.58 M
	$MeSO_3H$ 3M	0.57 M
	KOH 3M	> 1 M
	DMSO	0.78 M

Thus, the redox reaction for o-benzoquinone and its standard potential is shown in **Figure 7.7a**. However, when it was done cyclic voltammetry experiments in acidic conditions, using sulfuric acid or methanosulfonic at 1 mV/s (**Figure 7.7b**), it is clear a larger oxidation process compare to the reduction. It is an evidence of the low reversibility of this redox process, which can be confirmed with the reduction/oxidation ratio, in **Table 7.3**, for both acids is below 0.3. Moreover, PEIS measurements (**Figure 7.7c**) show a slightly lower charge transfer for the case of sulfuric acid as solvent compare to methanosulfonic acid, but the amount of charge related to oxidation and reduction is larger in case of methanosulfonic with a better ratio reduction/oxidation value and higher solubility. Finally, in spite of the potential difference between oxidation and reduction processes the value when using H_2SO_4 is narrower in 112 mV, our initial focus as solvent will be $MeSO_3H$ due to the excellent solubility of the *orto*- form as cathode material and higher solubility of the *para*- form as well.

Table 7.3.- Cyclic voltammetry electrochemical parameters from **Figure 7.7b**.

o-hydroquinone	E_{ox} / V	E_{red} / V	ΔE / V	I_{ox} / mAg^{-1}	I_{red} / mAg^{-1}	I_{red}/I_{ox}
3M H_2SO_4	0.784	0.528	0.256	407	-57.12	0.14
3M $MeSO_3H$	0.870	0.502	0.368	1595	-388.3	0.24

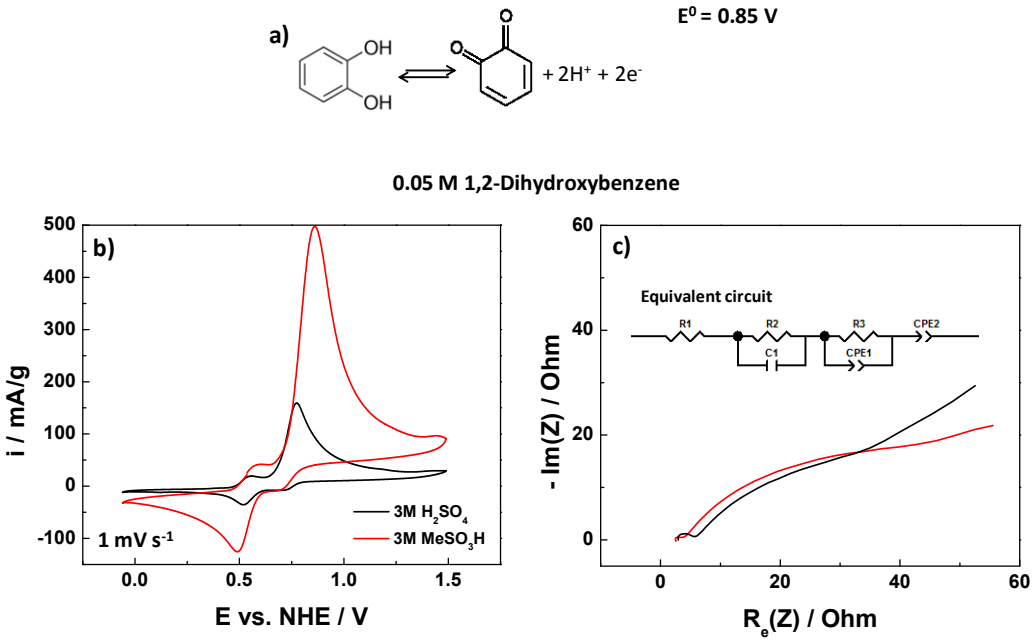

Figure 7.7. - a) o-benzoquinone redox reaction showing the standard potential. **b)** Cyclic voltammetry done for 0.05 M o-benzoquinone reaction showed in a) using different solvents (H_2SO_4 and $MeSO_3H$) at 1mV/s. **c)** PEIS at 0.7 V vs. NHE in the same conditions as b) for graphite felt as working electrode. It also shows the equivalent circuit for the system.

Additionally, as it is shown in **Figure 7.8**, not only the overall current density associated to the oxidation/reduction processes of the p-benzoquinone compare to the o-benzoquinone molecule is larger, but also the ratio oxidation/reduction. This is probably caused by an irreversible oxidation of the *orto*- form.

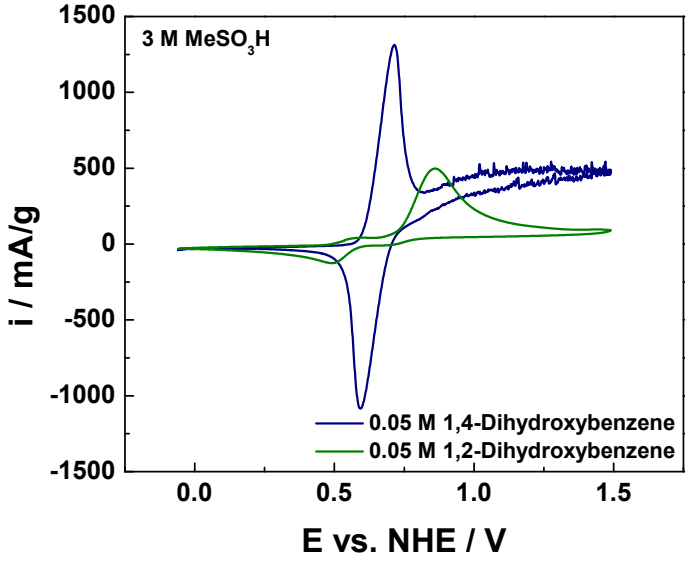

Figure 7.8. - Cyclic voltammetry comparative between the *para*- and *orto*- forms of the simplest benzoquinones (dihydroxybenzene).

Therefore, further screening over a variety of quinone derivate molecules is done to evaluate their solubility among various types of solvents (**Table 7.2**) in order to improve the solubility of p-benzoquinone with similar reversibility and intensity, as well as select an optimum redox molecule for the anolyte, more specifically, 9,10-anthraquinone-2,7-disulphonic acid (AQDS), extremely rapid and reversible two-electron two-proton reduction. This quinone/hydroquinone is implemented in an aqueous flow battery with inexpensive carbon electrodes. They are also natural products which have been extracted for millennia from common sources such as rhubarb. Moreover, it could be a renewable source for future anthraquinone-based electrolyte solution.

Knowing the principal basis of an efficient rechargeable redox flow battery is the rapid kinetics of charge-transfer at the positive and negative electrodes. Many organic redox couples, especially from the quinone family, undergo rapid proton-coupled electron transfer without the need for dissociating high energy bonds. Consequently, these redox couples have relatively high rate constants for the charge-transfer process (10^{-3} to 10^{-4} cm s^{-1}), which is 2 to 3 orders of magnitude higher than commercial vanadium redox system[266,267]. Typically organic redox couples generate a battery voltage close to 1 V.

The values of diffusion coefficients are about an order of magnitude smaller in aqueous solution than in non-aqueous solvents such as acetonitrile[268]. In aqueous solutions, the observed extent of decrease in the values of diffusion coefficients with increase in molecular mass is about 6 x 10^{-9} cm^2 s^{-1} per unit of molecular mass. This coefficient is an order of magnitude lower than that observed in acetonitrile. Thus, besides the effect of molecular mass, the molecular diameter resulting from the salvation and the interaction of ionic groups with water through

hydrogen bonding has a significant effect on the diffusion coefficient values in aqueous solutions.

This type of aqueous organic flow battery opens a new area of research for realizing inexpensive and robust electrochemical systems for large-scale energy storage. It is shown that no precious metal catalyst is needed because these redox couples undergo fast proton-coupled electron transfer.

7.3.2 Cathodic electroactive species

In this section we are going to focus on disodium 4,5-dihydroxy-1,3-benzenedisulfonate, also known as Tiron, as the cathode active material used in acidic electrolyte conditions (methanosulfonic acid environment). It is one of the quinones with a higher redox standard potential showing larger solubility in aqueous conditions. In order to improve the electrode-electrolyte's active material interaction (charge transfer and kinetics), several electrode treatments have been done.

7.3.2.1 Electrodes enhancement

Initially, the commercial pristine carbon felt electrode (CF) is subjected to a plasma treatment in oxygen atmosphere, with the purpose of increase its active surface area, as well as hydrophilicity, as the oxygen groups are boost[269]. Afterwards, two different pathways are followed. Firstly, a hydrothermal process in nitric acid conditions [61,270]. Secondly, a similar hydrothermal process, but this time, it is used graphene oxide (GO), synthesized by Hummel's method, to decrease the charge transfer resistance as due to the great graphene conductivity. This treatment is followed by another in the same conditions but introducing a quinone molecule, p-benzoquinone, as a new active site interacting between the carbon substrate (CF-rGO) and the quinone (disodium 4,5-dihydroxy-1,3-benzenedisulfonate) active material solved in the electrolyte (**Figure 7.9**). These different treatments over the positive electrode are done to know, which performs better towards the studied redox reaction and optimize it.

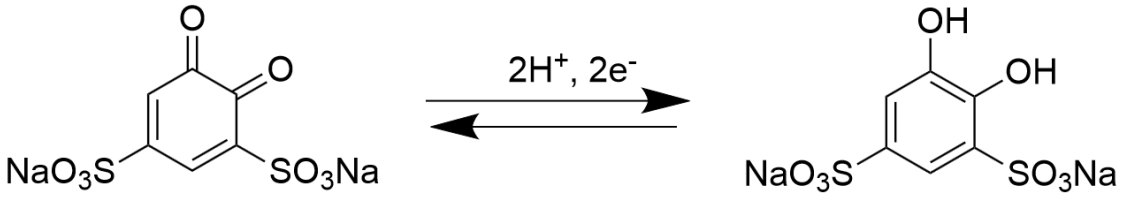

Figure 7.9. - Redox reaction of disodium 4,5-dihydroxy-1,3-benzenedisulfonateor, also known as Tiron, which implies two protons and two electrons.

7.3.2.1.1 Characterization

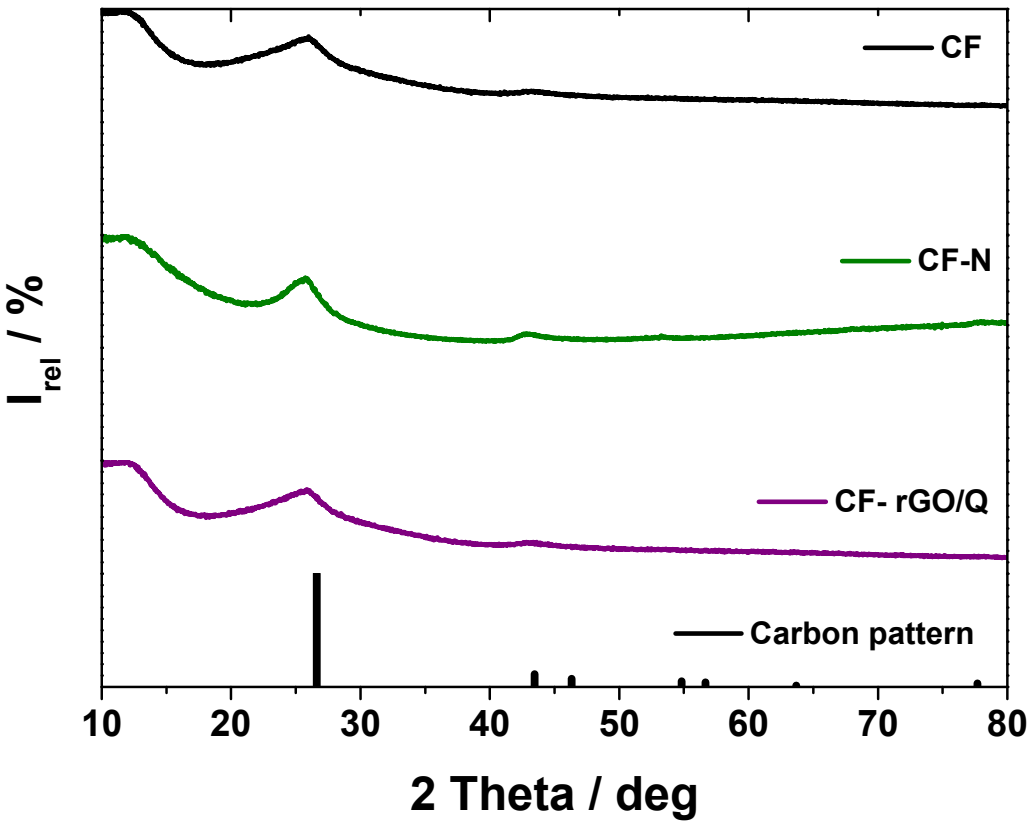

Figure 7.10.- XRD spectra for the samples GF, GF-N and GF-rGO/Q compared with the graphite pattern.

Besides, the material synthesis is characterized by several methods, the XRD diffractogram (**Figure 7.10**) showed two main peaks around 12º and 26.4, which correspond to the G and D bands related to carbon structures[271]. Also there is a hardly noticeable peak at 44.4º correspond to (101). There is not an appreciable difference in the XRD peaks between the various electrodes, as all of them are hydrocarbon based materials, and therefore other specialized techniques are more appropriate. SEM images of the various electrodes companied by its EDX elementary composition, **Figure 7.11a**, show an initial pristine electrode with less than 1% in weight of oxygen, as well as a smooth surface. When the felt is treated by oxygen plasma, it content increases moderately above 5% in weight. It also evidences an increased surface roughness as it can be seen in **Figure 7.11b**. Moreover, the CF into the acidic (HNO_3) hydrothermal treatment gives a surface functional groups reduction, decreasing the oxygen content to 1%, while passivating on the micro structure as can be appreciate in the SEM (**Figure 7.11c**). Lastly, the case that includes graphene oxide and the quinone on the felt structure gives twice as high oxygen content as the pristine or plasma activated ones and 10 times higher than the acid treated. The **Figure 7.11d** offers a vision of the graphene flake coating the CF, the presence of the quinone groups cannot be

detected by this technique. For that reason, XPS measurements are done in order to study the electrodes surface composition.

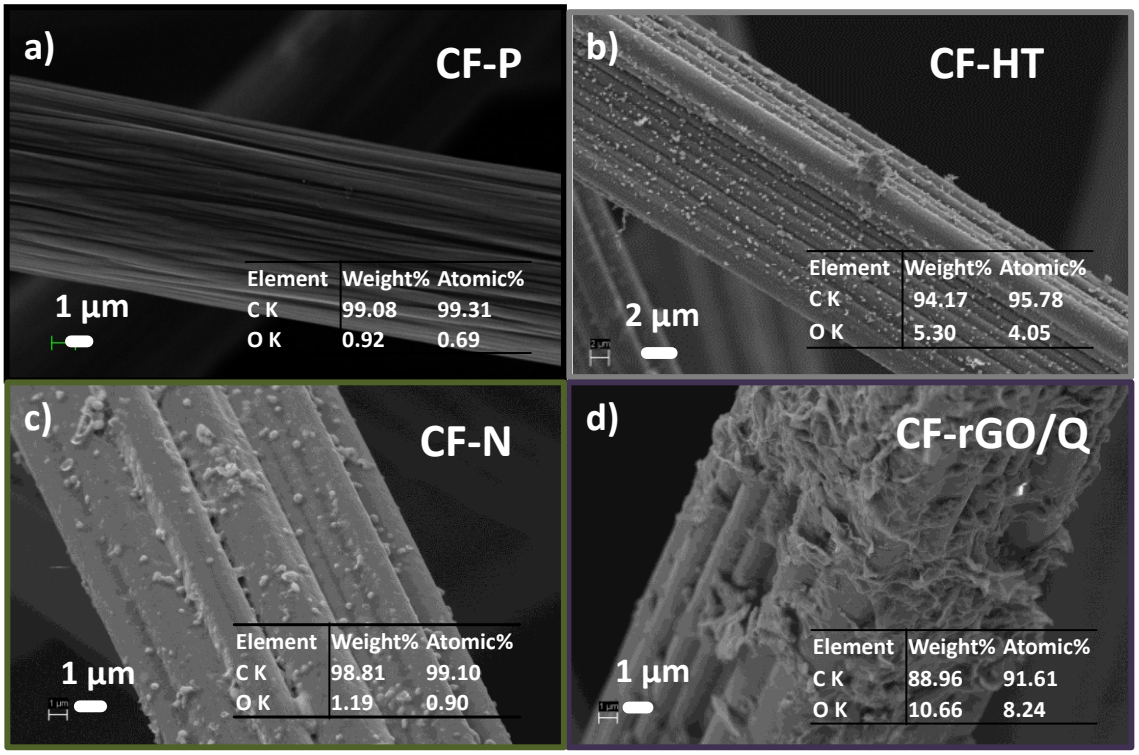

Figure 7.11. - SEM images for several electrodes **a)** CF-P. **b)** CF-HT. **c)** CF-N **d)** CF-rGO/Q.

Additionally, XPS spectra analysis (**Figure 7.12**) is done in order to study the surface effects of the different functionalization processes done on the carbonaceous electrodes (CF).

Firstly, considering the C1s XPS deconvolution peaks for the treated electrodes (**Figure 7.12**), CF-N has a carbon overall larger contribution with a 95 % at, from which the majority comes from unsaturated carbon (C=C, 284.8 eV) with a 39 %at. In case of CF-HT this C1s contribution is reduced to a 73% at. Moreover, this carbon contribution is further reduced for CF-rGO/Q with just a 67% at, which has almost equally intensity coming from saturated (C-C - 285.5 eV, 21% at) and unsaturated (C=C, 20 % at) carbon.

Furthermore, the O1s XPS spectra in **Figure 7.12** show overall oxygen content about 30% at in case of the CF-rGO/Q electrode. This content is reduced to 24% at for the CF-HT electrode, which content is being further diminished for CF-N electrode. Now, studying the main deconvolution contributions to the overall oxygen content it can be observed that C-O groups (533.2 eV) has a larger content on the CF-rGO/Q surface with a 12% at, while CF-HT and CF-N only has a 6% at and 1% at, respectively. On the contrary C=O groups (532.1 eV) on the electrode surface has greater content for CF-HT with a 12 % at, which is lowered to a 9% at

in case of CF-rGO/Q and further decreased for CF-N with a 2 % at, as seen in **Figure 7.13**. Therefore, bearing in mind these facts seems clear that the rGO/Q contribution increases the quantity of C-O groups, while decreasing the C=O groups are comparatively to GF-HT electrode, which is an evidence of the Quinone's oxygen groups are bonded to the carbon felt surface by these C=O groups. Moreover, the hydrothermal treatment in presence of nitric acid (GF-N) increases the relative contribution of acid groups (O-C=O, 531.3 eV) to the overall oxygen signal, due to a larger oxidation of the oxygen groups existing on the carbonaceous surface[61,272]

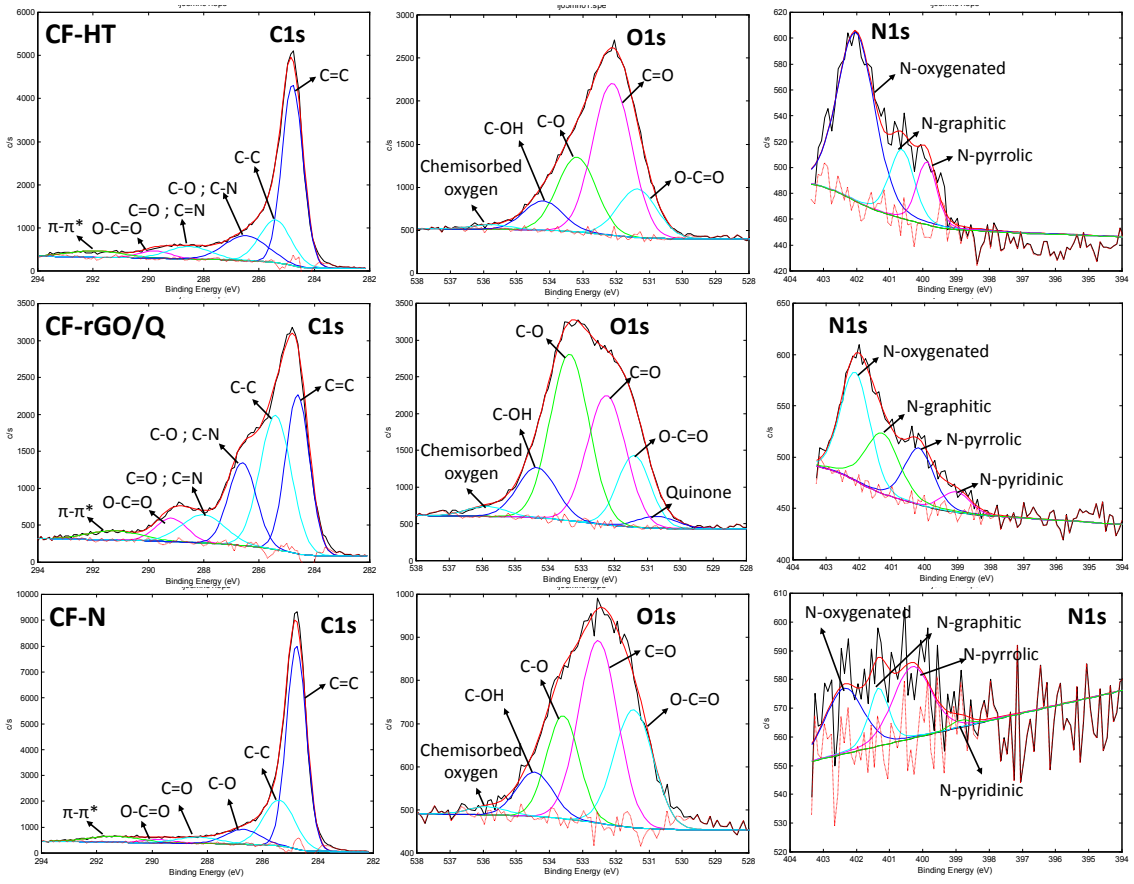

Figure 7.12.- XPS deconvoluted spectra of C1s, O1s and N1s for the electrodes GF-HT, GF-rGO/Q and GF-N.

Additionally, the N1s XPS spectra (**Figure 7.12**) has an overall nitrogen content of 3.1 % at for CF-HT coming from the commercial synthetic procedure, slightly reduced for CF-rGO/Q to 2.6 % at and almost absence for CF-N with a 0.4 % at due to the oxidative synthesis conditions. As **Figure 7.13** shows, the principal contribution to nitrogen comes from oxygenated-N (402 eV) with a 2% at for CF-HT, which is reduced to a 1% at for CF-rGO/Q. There are also minor contributions coming from graphitic-N (401.3 eV) and pyrrolic-N (400.1 eV) for both electrodes, CF-HT and CF-rGO/Q. Moreover, CF-rGO/Q has a small contribution from pyridinic-N (399 eV).

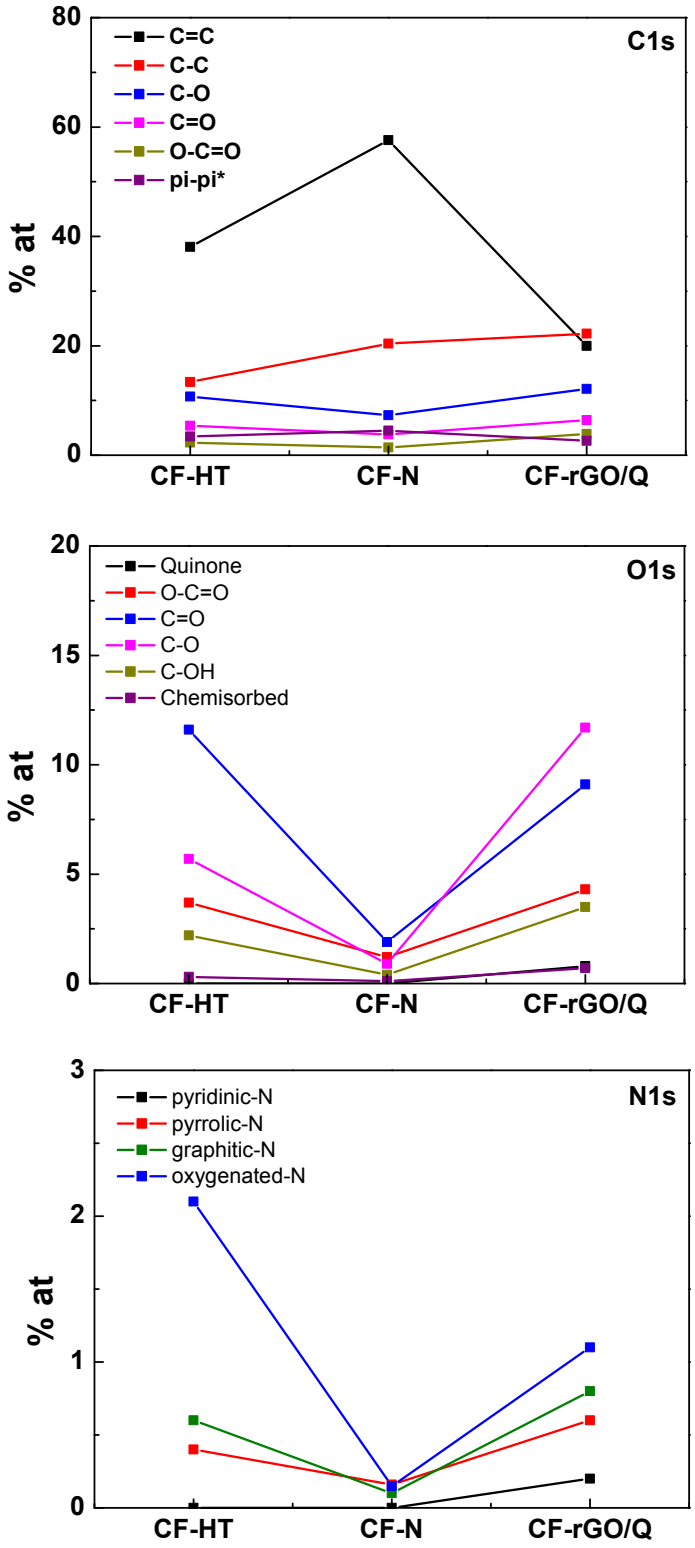

Figure 7.13. - Table chart showing the specific different groups content, from the top to the bottom, of C, O and N in atomic percentage.

Besides, considering the differences on the atomic surface content between the studied electrodes, as seen in **Figure 7.14**, there is a similar tendency for the N/C and N/O ratio, following: CF-HT > CF-rGO/Q > CF-N with. In case of N/C ratio the values are 0.042, 0.039 and 0.004, respectively. Moreover, when compare N/O ratio the values obtained are 0.13, 0.086 and 0.008, respectively. This evidences the larger proportion N groups on the carbon surface comparatively to carbon and oxygen for the CF-HT electrode..

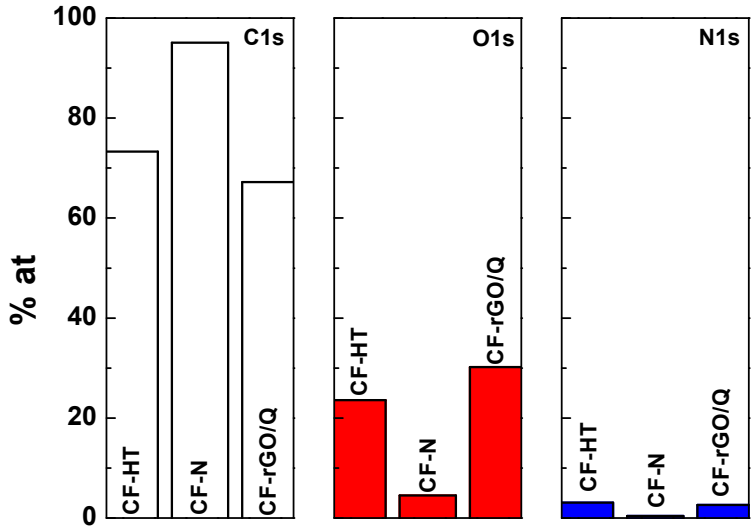

Figure 7.14. - Overall table chart showing the content of C, O and N in atomic percentage.

7.3.2.1.2 Electrochemical characterization

Initially, cyclic voltammetry (**Figure 7.15**) is done for the electrodes, CF-HT, CF-N and CF-rGO/Q, giving two redox peaks, quasi-reversible, where in principle the larger one corresponds to the two electrons involve on the quinone redox reaction (Reaction 1), which outcome is a reduction/oxidation ratio similar for all, 0.86, but a difference in the differential of potential between reduction and oxidation. This is minor in case of CF-HT electrode, placing from minor to major as follow: CF-HT (0.4) < CF-rGO/Q (0.6) < CF-N (0.7), seen in **Table 7.4**. This improvement is due to the larger nitrogen content, as well as the C=O groups which are more electroactive towards the Tiron molecule.

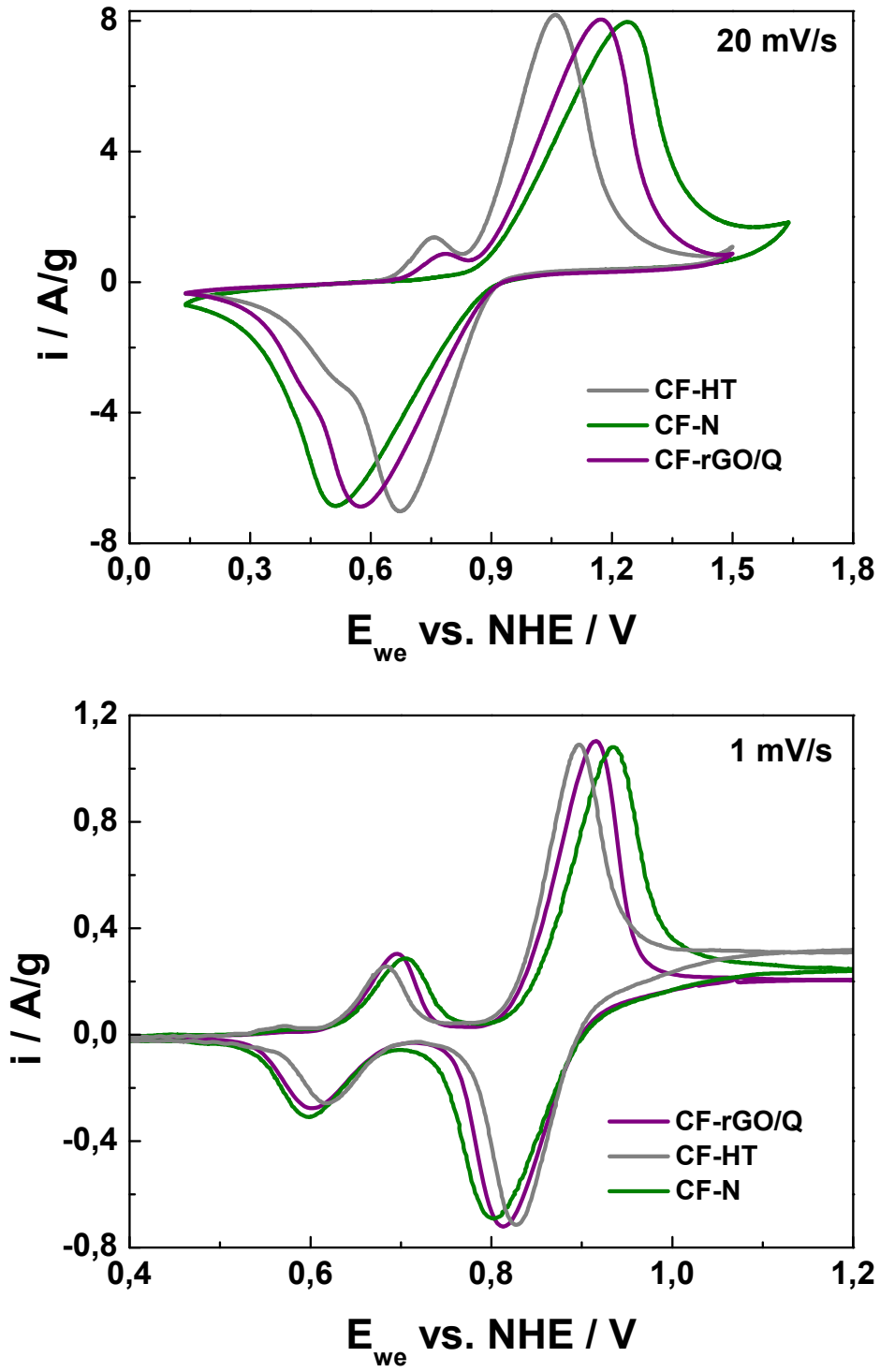

Figure 7.15.- Top cyclic voltammetry done for the electrodes CF-HT, CF-N and CF-rGO/Q as working electrodes of a 3 electrodes system with CF as counter electrode and Hg/Hg_2SO_4 as reference in a 0.05M Tiron 3 M $MeSO_3H$ solution run at a scan speed of 20 mV/s. **Bottom** cyclic voltammetry in the same conditions as described above at a scan speed of 1 mV/s.

Table 7.4.- Electrochemical values of Reaction 1 obtained from the cyclic voltammetry showed on the **Top** of **Figure 7.15** for the initial cycle.

Electrode	E_{ox} /V	E_{red} /V	ΔE / V	I_{ox} / mAg^{-1}	I_{red} / mAg^{-1}	I_{red}/I_{ox}
CF-rGO/Q	1.17	0.57	0.60	8039	-6880	0.86
CF-HT	1.06	0.67	0.39	8182	-7024	0.86
CF-N	1.24	0.51	0.73	7976	-6862	0.86

On the other hand, the minor redox peak (Reaction 2) (initially thought to be a non-reversible side reaction process (**Figure 7.16**)[273]) cannot be evaluated at a scan rate of 20 mV/s, as they overlap with the other redox process. In case the scan speed is diminished to 1 mV/s, **Figure 7.15**, it can be observed the reversibility of the Tiron redox reaction, which continues the same tendency as Reaction 1. However, not only the values for the different electrodes are much closer, almost even. In this case the side redox reaction can be studied separately. Moreover, it also follows the same trend, although reduction/oxidation ratio changes for the different electrodes as: CF-N (1.08) > CF-HT (1.01) < CF-rGO/Q (0.914), the differential of potential between reduction and oxidation follows (mV): CF-HT (67) < CF-rGO/Q (94) < CF-N (107), seen in **Table 7.5**. Therefore, considering all the three electrode's electrochemical results, CF-HT has a better electrochemical performance towards reactions 1 and 2 in terms of reversibility comparatively to the other electrodes studied. It s due to the presence of nitrogen groups facilitating the redox reaction, as well as the C=O groups which are more active towards tiron redox reaction.

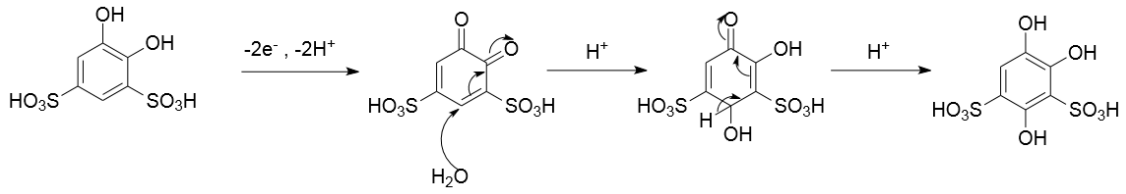

Figure 7.16. - Michael addition of water as plausible side reaction mechanism of Tiron, while oxidizing and reducing.

Table 7.5.- Electrochemical values of Reaction 2 obtained from the cyclic voltammetry showed on the **Bottom** of **Figure 7.15**.

Electrode	E_{ox} /V	E_{red} /V	ΔE / mV	I_{ox} / mAg^{-1}	I_{red} / mAg^{-1}	I_{red}/I_{ox}
CF-rGO/Q	0.696	0.602	94	3030	-2771	0.914
CF-HT	0.684	0.617	67	2548	-2574	1.01
CF-N	0.705	0.598	107	2869	-3092	1.08

Furthermore, the electrochemical analyses for several cyclic voltammetries have been done at different scan rates (20 to 1 mV/s) to apply Randles-Sevcik equation (**Figure 7.17**). It has been always considered as an approximation due to the non-flat surface of the working electrodes used, obtaining the plot of *i* vs. $v^{1/2}$. As seen in **Figure 7.17d**, the slope values for the Ox_1/Red_1, as well as Ox_2/Red_2 are related to the mass transfer in the interface electrode-electrolyte for the reactions 1 and 2. It follows the trend: CF-HT > CF-rGO/Q > CF-N. These tendencies are most probably caused due to a larger electrochemical active surface area formed by N and O groups stable on the electrode's surface, which favors Tiron (benzoquinone) electrode-electrolyte diffusion involved on the main reaction and secondary reaction. It is also noteworthy that reaction 1 has a mass transfer 10 times faster compared to the reaction 2, and as a consequence it is harder to saturate the surface towards this reaction.

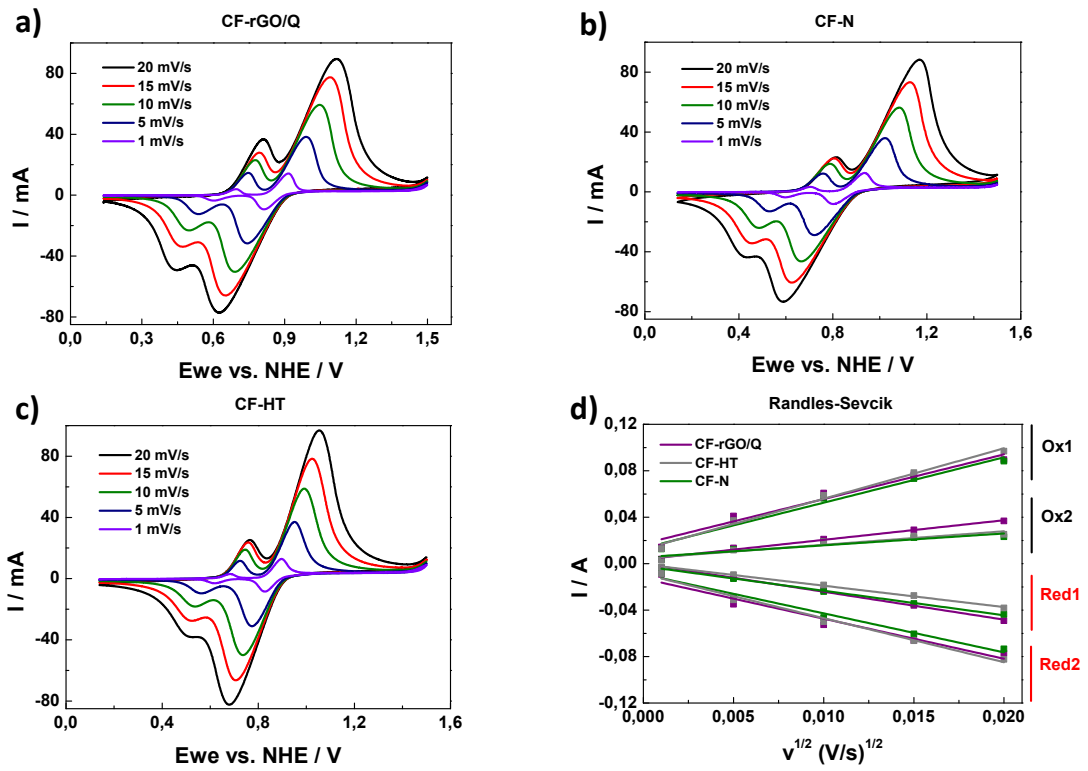

Figure 7.17.- Cyclic voltammetry of a 3 electrodes system with CF as counter electrode and Hg/Hg_2SO_4 as reference in a 0.05M Tiron 3 M $MeSO_3H$ solution run at different scan speed (20 to 1 mV/s). **a)** CF-HT. **b)** CF-rGO/Q. **c)** CF-N. **d)** Randles-Sevcik plot obtained from a) b) and c) which shows the increased mass transfer over the electrode as the slope increases.

Hence, electrochemical impedance spectroscopy done at a constant potential of 0.63 V vs. NHE highlights the previous results. GF-HT electrode's charge transfer resistance towards Tiron reaction decreases (**Figure 7.18**), as the nitrogen and oxygen content increases, especially C=O and oxygenated-N as XPS characterization suggests (**Figure 7.13**). The charge transfer resistance values increases, as the N/C and N/O ratio drops. The values follow (ohm): CF-HT (12.8) < CF-rGO/Q (25.1) < CF-N (27.9), as seen in **Table 7.6**.

Table 7.6.- Charge transfer resistance and knee frequency values for the electrodes CF-HT, CF-N and CF-rGO/Q towards Tiron redox reaction.

Electrode	R_{ct} / Ohm	f_{knee} / Hz
CF-HT	12.8	0.22796
CF-rGO/Q	25.1	0.1
CF-N	27.9	0.048

Afterwards, it is plotted $1/R_{ct}$ vs. f_{knee} in order to obtain a relationship. It shows the same tendency as well, presenting a linear relationship between the conductivity of the electrodes and the frequency at which the charge transfer occurs. This evidences that the larger the frequency at which the charge transfer occurs, the lower is the charge transfer resistance value.

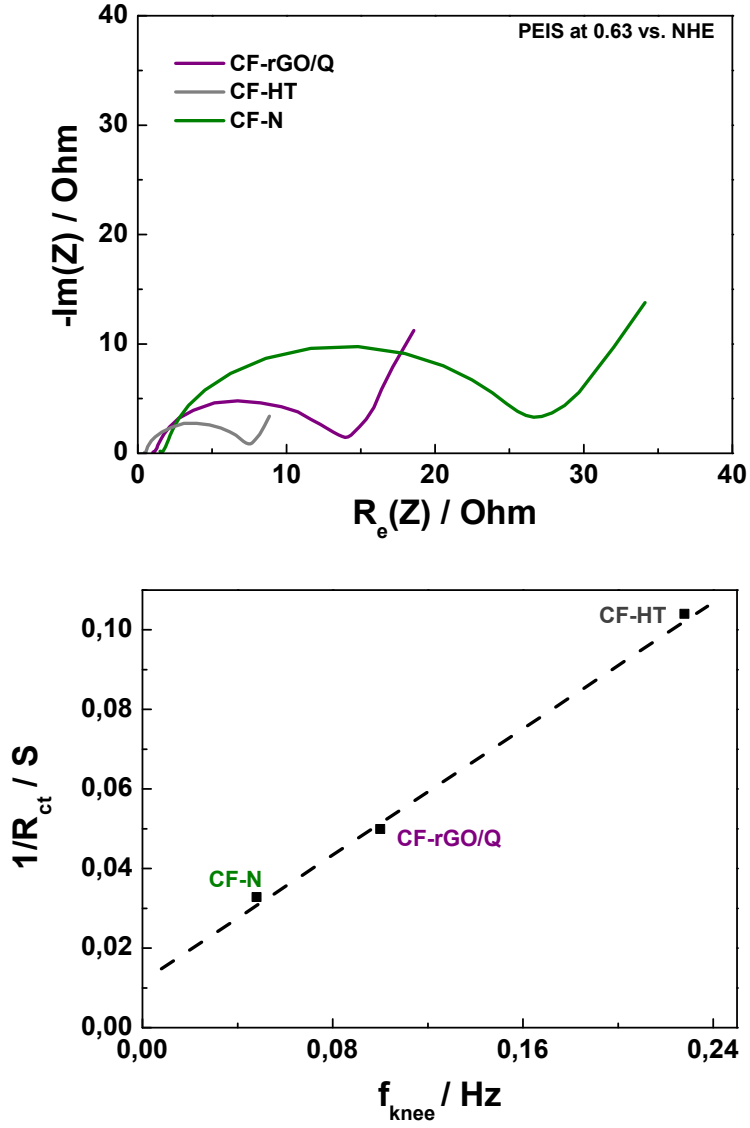

Figure 7.18.-Top. EIS for the electrodes CF-HT, CF-N and CF-rGO/Q at a fixed potential of 0.63 V vs. NHE, using CF as counter electrode and Hg/Hg_2SO_4 as reference in a 0.05M Tiron 3 M $MeSO_3H$ solution. **Bottom.** linear tendency of the inverse of the charge transfer resistance (conductivity) versus the knee frequency.

Thus, considering charge-discharge plots at high current (**Figure 7.19a**), 100 mA/cm^2, overall charge and discharge capacity (mAh) are larger for CF-HT (0.272) > CF-rGO/Q (0.256) ≈ CF-N (0.256). However, in case it is taking into account only the larger plateau (Reaction 1) the capacity is greater for the GF-rGO/Q and GF-N

(0.202 mAh) electrode due to a minor secondary reaction effect (21.4% Reaction 2). In spite that fact, it is not viable further reduce the potential window as the coulombic efficiency will drop due to lowered reversibility between the charge and discharge processes. Moreover, as seen in **Figure 7.19b**, discharge capacity retention ,from 25 to 100 mA/cm^2, decreases as the quinone reaction does not occur as fast as it would be needed when large current densities are applied. Besides, discharge capacity retention follows the trend: CF-HT > CF-rGO/Q > CF-N at any current density applied. In case of 100 mA/cm^2 is applied, the following values are obtained (%): CF-HT (77.9) > CF-N (70.7) > CF-rGO/Q (65.8). Therefore, the electrodes treated by oxygen plasma perform better electrochemically in galvanostatic conditions, which is mainly caused by the nitrogen surface content, as well as, C=O oxygenated surface groups.

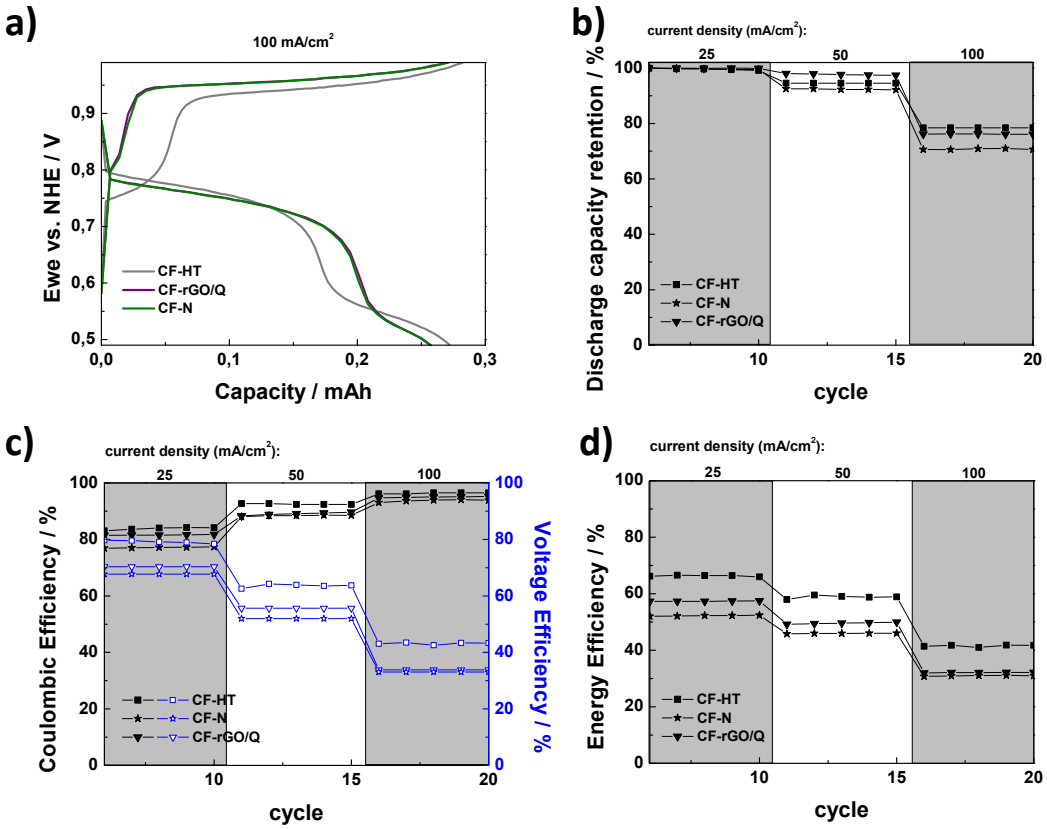

Figure 7.19.- Galvanostatic experiments of a 3 electrodes system with CF as counter electrode and Hg/Hg_2SO_4 as reference in a 0.05M Tiron 3 M $MeSO_3H$ solution at different current densities (10 to 150 mA/cm^2) displaying **a)** Charge-discharge plots for the electrodes used at current density of 100 mA/cm^2. **b)** Discharge capacity retention from the initial value for each electrode. **c)** Coulombic and voltage efficiencies (CE and VE). **d)** Energy efficiency (EE).

Additionally, efficiencies (Coulombic Voltage and Energy efficiencies) are screened at different current densities, from 25 to 100 mA/cm^2. Obtaining larger values of coulombic efficiency as the current is raised due to minor side reactions (i.e. OER), as well as less time for cross over trough the membrane (**Figure 7.19c**). The

electrodes at a current applied of 100 mA/cm^2 has a Coulombic efficiency values that follows: CF-HT (96.6)> CF-rGO/Q (96.2)> CF-N (93.7). Although the three samples present closer values and above 95%, the voltage efficiency decreases when large current densities are handled. It is due to the redox reaction does not have enough time to take place. Energy efficiencies are limited by the voltage efficiency, and therefore has the same tendency of the values obtained (**Figure 7.19d**). The energy efficiency values for a current applied of 50 mA/cm^2 have values around a 60%, following the same trend as for Coulombic and voltage efficiencies: CF-HT (59.1)> CF-rGO/Q (49.6)> CF-N (45.8).

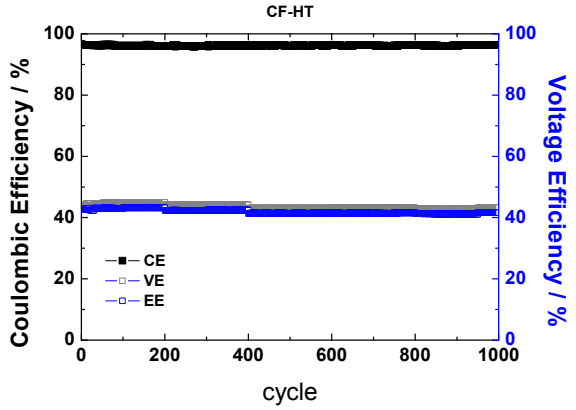

100 mA/cm^2 (cycle 1000)	CE / %	VE / %	EE / %
CF-HT	96.2	43.2	41.6

Figure 7.20.- Long term cycling in galvanostatic conditions for 1000 cycles of a 3 electrodes system with GF as counter electrode and Hg/Hg_2SO_4 as reference in a 0.05M Tiron 3 M $MeSO_3H$ solution at a current densities of 100 mA/cm^2 displaying **a)**Coulombic and voltage efficiency (CE and VE). **b)** Coulombic efficiencies zoomed (CE). **c)** Energy efficiency (EE). **d)** Efficiency values after 1000 cycles for the electrodes used at current density of 100 mA/cm^2.

Finally, the CF-HT electrode was tested for 1000 cycles in order to study its long term viability towards the battery application, as it is the one performing better towards the Tiron redox reaction. Those cycles were done at high current density (100 mA/cm^2). As seen in **Figure 7.20**, the coulombic efficiency performed for the GF-HT electrode is high enough, around 96%, and remains constant during cycling. Moreover, Voltage efficiency and therefore Energy efficiency are quite stable, as the Voltage efficiency is the limiting factor. The GF-HT electrode boost the efficiency more than 10% compare with the other electrodes for similar currents, as seen in **Figure 7.19**. This improvement can be maintained along the life cycling with an energy efficiency of 41.6%.

In brief, the treatments done on the cathode electrodes for aqueous organic redox flow batteries has the objective to increase the surface active area by electrode functionalization with nitrogen and oxygen groups, especially active are the oxygenated-N and C=O groups. These are more abundant on the CF-HT surface. Therefore the electrodes become more electrochemically active, as CV showed by an increase in the reversibility and mass transfer towards the Tiron redox reaction on CF-HT comparatively to the other two electrodes (CF-N and CF-rGO/Q). Moreover, the charge transfer resistance is reduced due to that functionalization.

This facilitates the migration of the Tiron redox species towards the interface electrode-electrolyte. Additionally, the CF-HT electrode is stable at least for 1000 cycles, which evidences the good performance and low degradation. Therefore, this study helps to know which functional groups, obtained by several methods, are more active towards the reaction that needs to be enhanced..

7.3.3 Anodic electroactive species

In this section we are going to focus on Anthraquinone 2,7-Disulfonic acid disodium salt as anode active material (**Figure 7.21**) used in acidic electrolyte conditions, methanosulfonic acid. In order to improve the electrode-electrolyte active material interactions, several electrode treatments have been done and studied afterwards as follows described.

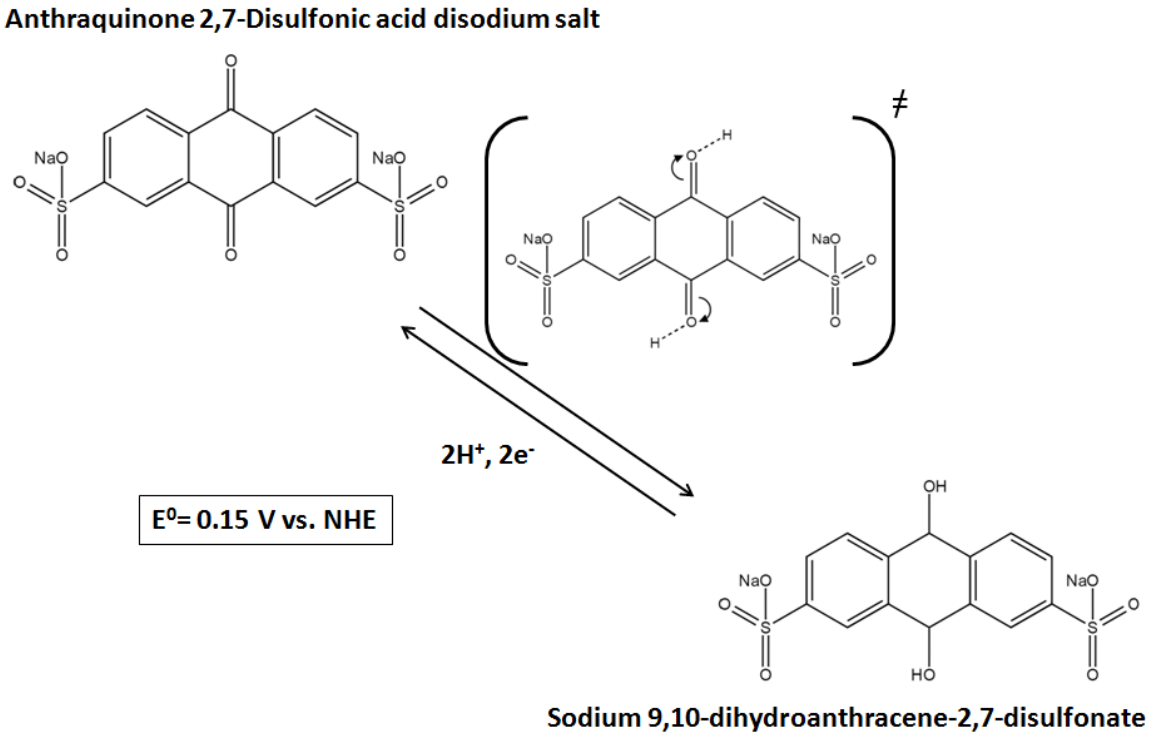

Figure 7.21.- Anodic quinone redox reaction from anthraquinone 2,7-disulfonic acid disodium salt to sodium 9,10-dihydroanthracene-2,7-disulfonate, showing the standard potential of it, as E^0=0.15 V vs. NHE.

7.3.3.1 Electrode enhancement

Initially, , similarly as the treatment done for the cathode electrode, the commercial pristine carbon felt electrode (CF) is subjected to a plasma treatment in oxygen atmosphere, with the purpose of increase its active surface area, as well as hydrophilicity, as the oxygen groups are boost[269]. Next, a similar hydrothermal process, but this time, it is used graphene oxide (GO) with the purpose of elevate the electron transfer rate due to the great graphene conductivity nature, which has not worked for t. Afterwards, two different pathways are followed. Firstly, a hydrothermal process introducing the quinone molecule, p-benzoquinone, as aromatic electron transfer material which can interact between the carbon substrate (CF-rGO) and the quinone active material (AQ27DS) solved in the electrolyte. It is done with the objective of facilitate the interactions electrode-electrolyte. Secondly a similar molecule but in this case an aliphatic hydrocarbon molecule with the aim of confirm the previous statement and observe if this molecule can also enhance the interactions between the electrode and the electrolyte.

7.3.3.1.1 Characterization

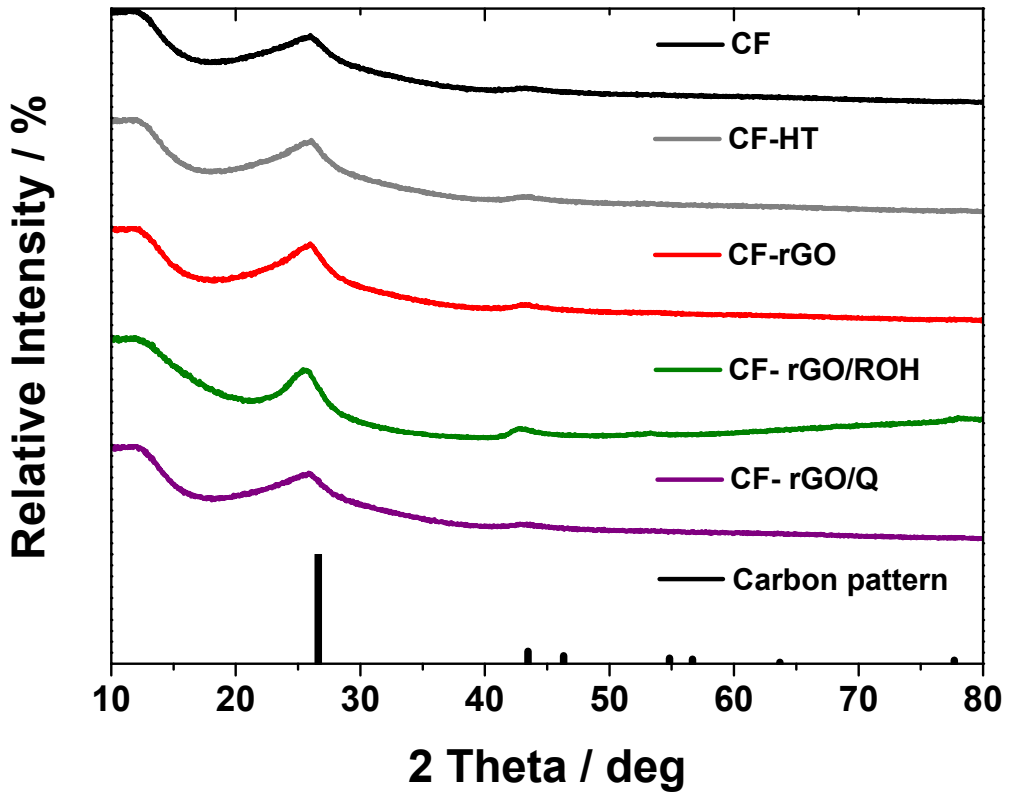

Figure 7.22. - XRD spectra for the samples CF, CF-HT, CF-rGO, CF-rGO/ROH and CF-rGO/Q compared with the graphite pattern.

Besides, the material synthesis is characterized by several methods, the XRD diffractogram (**Figure 7.22**) showed two main peaks around 12º and 26.4, which correspond to the G and D bands related to carbon structures[271]. Also there is a hardly noticeable peak at 44.4º correspond to (101). There is not an appreciable difference in the XRD peaks between the various electrodes, as all of them are hydrocarbon based materials, and therefore other specialized techniques are more appropriate. SEM images of the various electrodes companied by its EDX elementary composition, **Figure 7.23a**, show initial activated graphite felt electrode containing approximately 1% in weight of oxygen as well as a smooth surface with just a few carbon grains. It also evidences increased rGO deposits over the felt substrate after the consequently treatment, as it can be seen in **Figure 7.23b**. Moreover, the CF into the glycerol hydrothermal treatment gives a surface containing oxygen groups slightly improved (**Figure 7.23c**). Lastly, the case that includes quinone on the felt complex CF-rGO structure gives 10 times higher oxygen content carbon felt plasma activated. The **Figure 7.23d** offers a vision of the graphene flake coating the CF, the presence of the quinone cannot be seen by this technique due to the small size of the quinone molecules. For that reason, XPS measurements are done in order to study the electrodes surface composition.

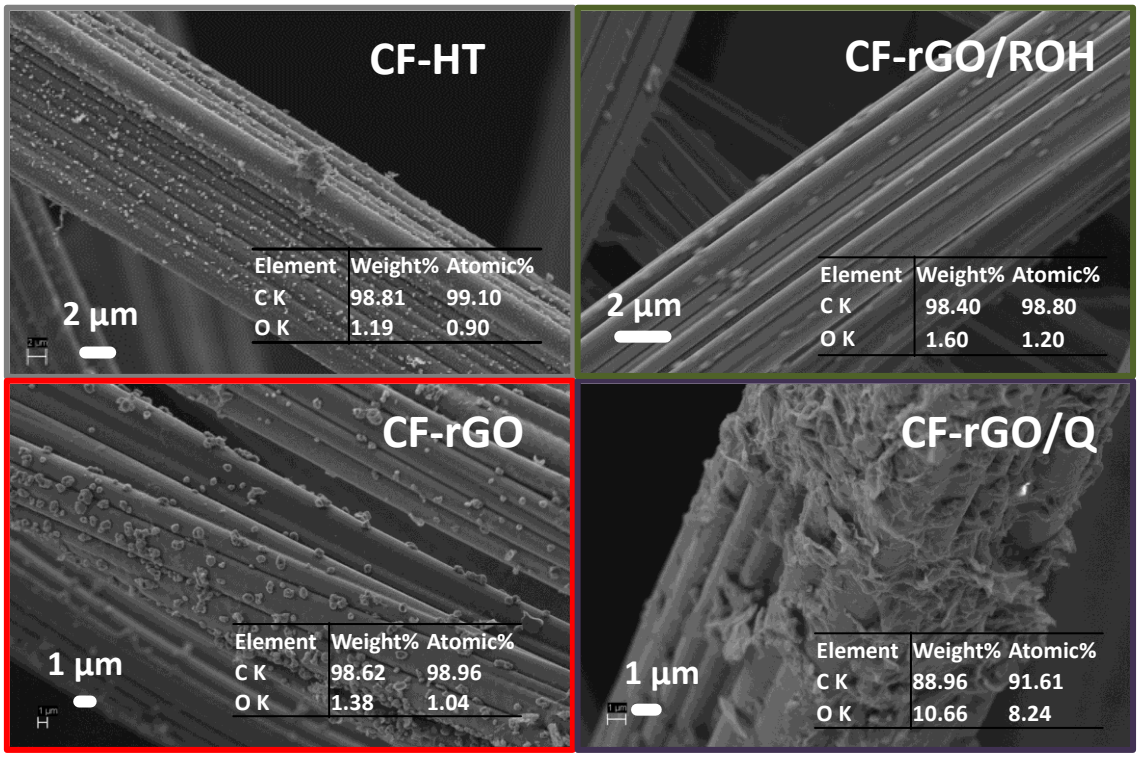

Figure 7.23.- SEM images for several electrodes **a)** CF-HT **b)** CF-rGO **c)** CF-rGO/ROH **d)** CF-rGO/Q.

Additionally, XPS spectra analysis (**Figure 7.24**) shows the surface effects of the different functionalization processes done on the carbonaceous electrodes. First,

considering the C1s contribution for the different electrodes it is obvious a larger intensity peak for CF-rGO/ROH (81% at.), with a larger contribution of unsaturated carbon bonding (C=C, 284.9 eV). When compare to CF-HT C1s peak area is reduced to 73% at., and 67% at. considering CF-rGO/Q. However, single C-C (285.2 eV) bonding has a different tendency: CF-rGO/Q > CF-rGO/ROH > CF-HT, with. a larger contribution into the C1s peak for CF-rGO/Q electrode.

Furthermore, In terms of overall contribution of O1s signal the trend followed is: CF-rGO/Q (30% at.)> CF-HT (24% at.) > CF-rGO/ROH (17% at.). Besides, the oxygen band in **Figure 7.24** confirms the increasing contribution of C-O bonding (533.3 eV) in case of CF-rGO/Q electrode to a 12% at., while CF-HT has only a 6% and slightly higher for CF-rGO/ROH with an 8%. Moreover, O-C=O bonding (531.4 eV) is also slightly greater in case of CF-rGO/Q (4.3% at.), while the contributions for CF-HT and CF-N are a 3.7 and 2.3% at, respectively (**Figure 7.25**). Therefore, these facts evidence that the rGO/Q contribution increases the quantity of C-O groups (533.2 eV), while the C=O groups (532.2 eV) are decreased when compared to CF-HT electrode, as the Quinone's oxygen groups are bonded to the carbon surface by these C=O groups.

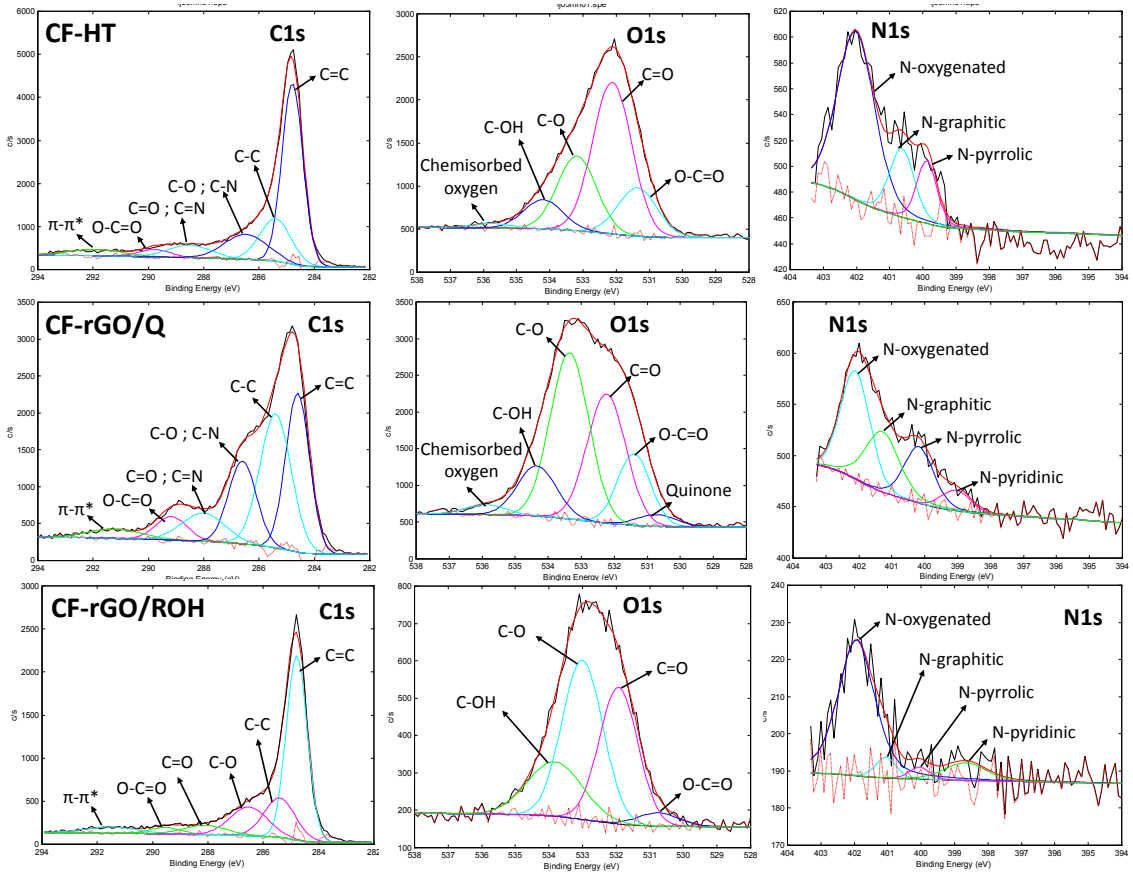

Figure 7.24.- XPS deconvoluted spectra of C1s, O1s and N1s for the electrodes CF-HT, CF-rGO/Q and CF-N.

Additionally, the N1s XPS band spectra (**Figure 7.24**) in terms of overall contribution of N1s signal follows the tendency: CF-rGO/Q (3% at.) ≈ CF-HT (3% at.) > CF-rGO/ROH (2% at.). Moreover, it is shown a main contribution due to

oxygenated-N group (402.1 eV) for CF-HT (2.1% at.), CF-rGO/ROH (1.4% at.) and CF-rGO/Q (1.1% at.). There are also minor contributions for the CF-rGO/Q coming from graphitic-N (0.8% at, 401.2 eV) and pyrrolic-N (0.6% at, 400.1 eV). The pyridinic-N is (399 eV) only exhibited in case of CF-rGO/Q (**Figure 7.25**). The CF-HT nitrogen groups come from the commercial synthesis process.

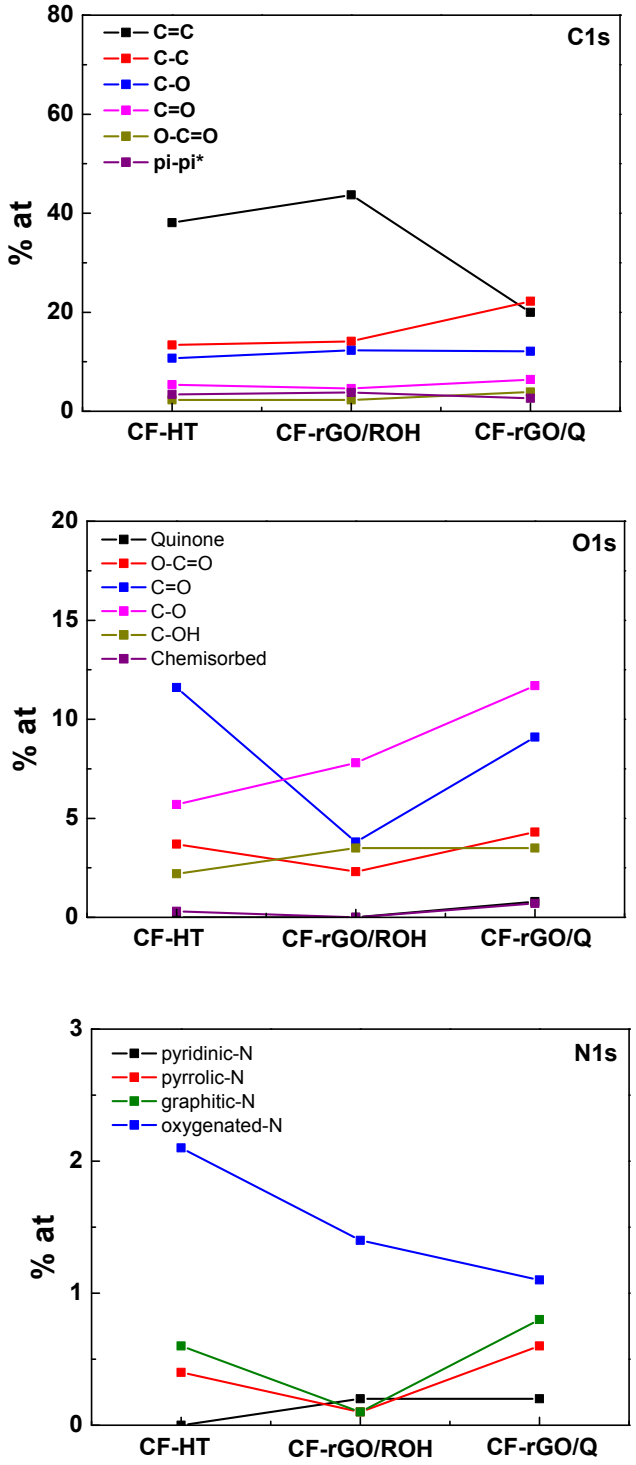

Figure 7.25. - Table chart showing the specific different groups content, from the top to the bottom, of C, O and N in atomic percentage.

Besides, considering the structural surface differences between the studied electrodes, as seen in **Figure 7.26**, there is a similar tendency for the O/C and N/C ratio. Both follow the trend: CF-rGO/Q > CF-HT > CF-rGO/ROH. The values for O/C are 0.4, 0.3 and 0.2, respectively. In case of N/C ratio the values are 0.04, 0.04 and 0.02. This evidences the larger proportion of O and N groups on the carbon surface in case of the CF-rGO/Q electrode.

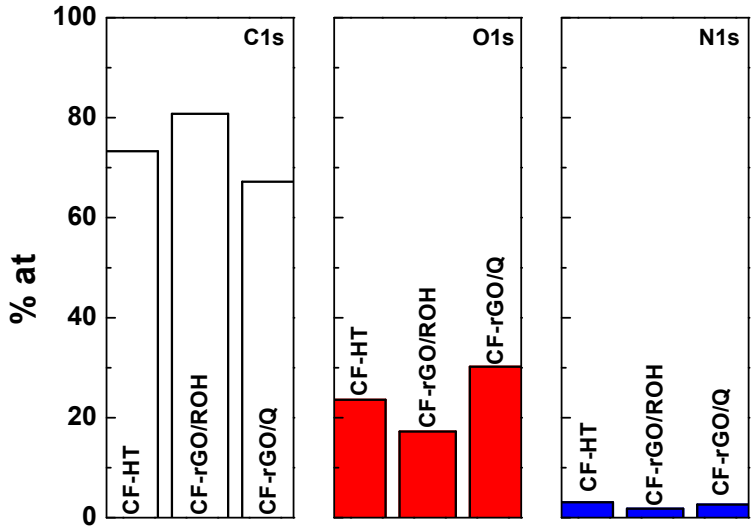

Figure 7.26. - Overall table chart showing the content of C, O and N in atomic percentage.

7.3.3.1.2 Electrochemical characterization

Concurrently, Physical characterization is followed by the electrochemical characterization. Cyclic voltammetry (**Figure 7.27**) at two different scan rates, 1 and 20 mV/s are done for the electrodes CF-HT, CF-rGO/ROH and CF-rGO/Q gives a quasi-reversible redox peak, which corresponds to the two electrons involve in the quinone redox reaction (**Figure 7.27**), which outcome is a reduction-oxidation ratio following the trend: CF-rGO/ROH (0.87) < CF-rGO/Q (0.95) < CF-HT (0.96). In spite the fact that the CF-HT performs slightly better than the rGO quinone modified electrode, the voltage differential between reduction and oxidation does not follow the same tendency (V): CF-rGO/ROH (0.59) > CF-HT (0.53) > CF-rGO/Q (0.40), seen in **Table 7.7**. It is the reason to initially suggest an enhanced performance for CF-rGO/Q electrode towards the anthraquinone molecule (2,7-AQDS) in the anolyte, which is a consequence of the large O/C and N/C ratio on the surface electrode, as well as the larger C-O group's content.

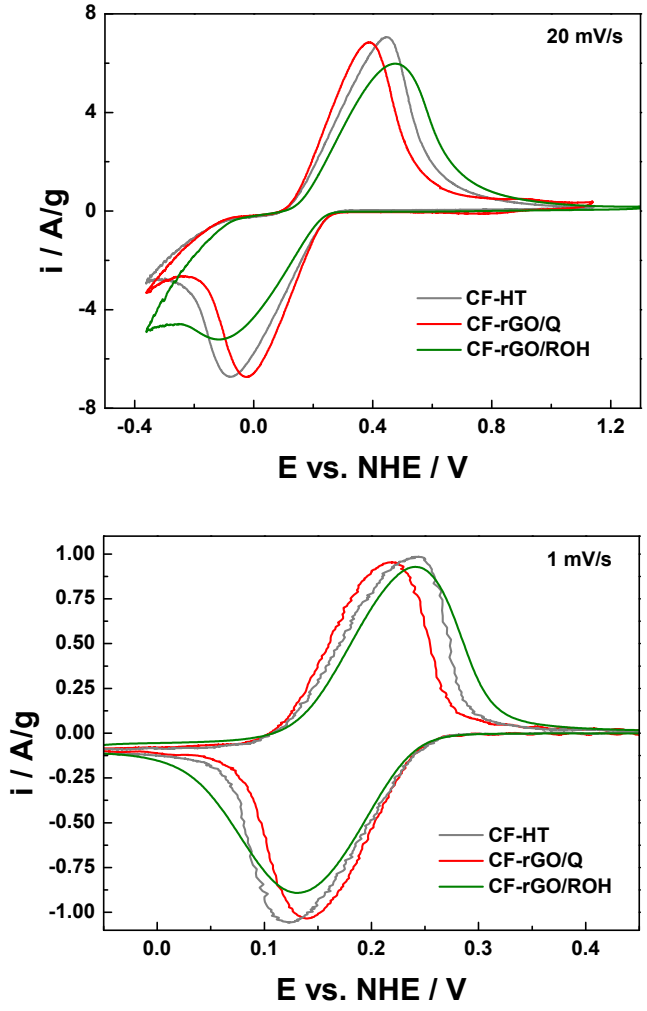

Figure 7.27. – Top. Cyclic voltammetry done for the electrodes CF-HT, CF-rGO/ROH and CF-rGO/Q as working electrodes of a 3 electrodes system with CF as counter electrode and Hg/Hg_2SO_4 as reference in a 0.05M Anthraquinone-2,7-disulfonic acid disodium salt 3 M $MeSO_3H$ solution run at a scan speed of 20 mV/s. **Bottom.** Cyclic voltammetry done for the electrodes CF-HT, CF-rGO/ROH and CF-rGO/Q as working electrodes of a 3 electrodes system with GF as counter electrode and Hg/Hg_2SO_4 as reference in a 0.05M Anthraquinone-2,7-disulfonic acid disodium salt 3 M $MeSO_3H$ solution run at a scan speed of 1 mV/s.

Table 7.7.- Electrochemical values obtained from the cyclic voltammetry showed in **Figure 7.27 Left** for the initial cycle.

Electrode	Eox /V	Ered /V	ΔE / V	Iox / mAg^{-1}	Ired / mAg^{-1}	Ired/Iox
CF-HT	0.448	-0.0797	0.528	7046.3	-6727.6	0.955
CF-rGO/Q	0.378	-0.0254	0.403	7064.4	-6727.6	0.952
CF-rGO/ROH	0.476	-0.116	0.592	5983.2	-5224.0	0.873

Furthermore, for the electrochemical analysis several cyclic voltammetries have been done at different scan rates, from 20 to 1 mV/s, in order to plot the Randles-Sevcik equation and therefore knows the mass transfer tendency for each one of the electrodes and redox reactions taking place (**Figure 7.28**). Considering the plotted graph results for the Ox/Red the mass transfer follows (cm^2/s): CF-rGO/ROH < CF-HT < CF-rGO/Q. It shows the same behavior as the CV data obtained, which confirms that the electrochemical enhancement of the electrodes could be due to the nitrogen and oxygen groups, especially C-O and O-C=O, as well as graphitic and pyrrolic-N, favoring Anthraquinone-2,7-disulfonic acid disodium salt electrode-electrolyte mass transfer involved on the 2-electron reaction.

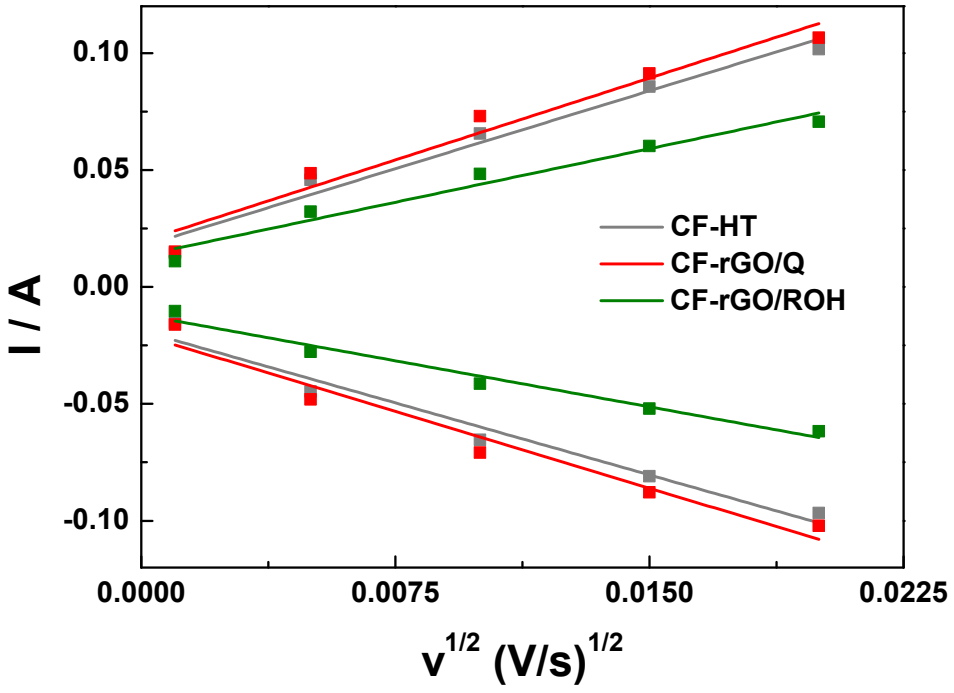

Figure 7.28. - - Randles-Sevcik plot obtained from cyclic voltammetry at different scan rates (1 to 20 mV/s), which shows the increasing mass-transfer over the electrode as the slope increases.

Hence, electrochemical impedance spectroscopy highlights the previous results. CF-rGO/Q as the nitrogen and oxygen content increases (more electrochemically active surface area), as well as the quinone groups, which favor the conductivity electrode-electrolyte towards the 2,7-AQDS redox reaction, and therefore the charge transfer resistance decreases (**Figure 7.29**). This fact is corroborated by the sample CF-rGO/ROH due to the lack of oxygen content, especially C-O groups, has a lower conductivity towards the reaction probably caused also by the insufficient nitrogen groups, as graphitic and pyrrolic-N. On the contrary, the CF-rGO/Q electrode, as the nitrogen and oxygen groups increase and activate the

surface towards the negative anthraquinone redox reaction, the charge transfer resistance (**Table 7.8**) follows the same direction as the reversibility values studied on the electrodes as shown in the cyclic voltammetry (**Figure 7.27**).

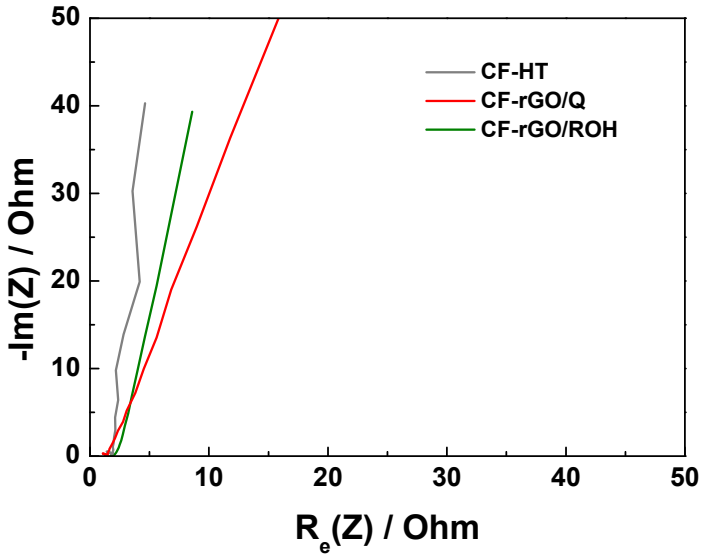

Figure 7.29. – PEIS for the electrodes CF-HT, CF-rGO/Q and CF-rGO/ROH at a fixed potential of 0.15 V vs. NHE, using GF as counter electrode and Hg/Hg_2SO_4 as reference in a 0.05M Anthraquinone-2,7-disulfonic acid disodium 3 M $MeSO_3H$ solution.

Table 7.8.- Charge transfer resistance, double layer capacitance and knee frequency values for the electrodes CF-HT, CF-rGO/Q and CF-rGO/ROH.

Electrode	R_{ct} / Ohm
CF-HT	0.44
CF-rGO/Q	0.29
CF-rGO/ROH	0.30

Thus, treated electrodes are studied in galvanostatic conditions considering charge discharge plots at high current (**Figure 7.30a**), 200 mA/cm^2, overall charge and discharge capacity (mAh) are larger for CF-rGO/Q (0.325) > CF-HT (0.263) > CF-rGO/ROH (0.1). Contrary to the case it is used CF-rGO/Q as cathode electrode, as anode, the capacity is greater for this electrode due to two synergetic effects. First, great amount of oxygen groups, especially C-O and O-C=O groups, enhancing the active surface area over the electrode. Second, the nitrogen groups, especially graphitic and pyrrolic, that helps more active material to be reduced and oxidized. Moreover, this effect can be clearly seen not only in **Figure 7.30a**, but also in

Figure 7.30b where discharge capacity retention decreases faster, from 25 to 200 mA/cm^2, in case of CF-rGO/ROH electrode than any other while CF-rGO/Q can achieve 300 mA/cm^2 with the best electrode capacity retention. When applied too low current densities (10 mA/cm^2) the side reactions and cross-over rise due to the charge and discharge time. This is a reason for the low coulombic efficiency at such current density applied. Moreover, discharge capacity retention follows the trend: CF-rGO/Q (79) > CF-HT (75) > CF-rGO/ROH (50) up to 150 mA/cm^2 current density applied. In case a larger current density, as 300 mA/cm^2, is applied, the values of capacity retention obtained are slightly different (%): CF-rGO/Q (53) > CF-rGO/ROH (0) ≥ CF-HT (0).

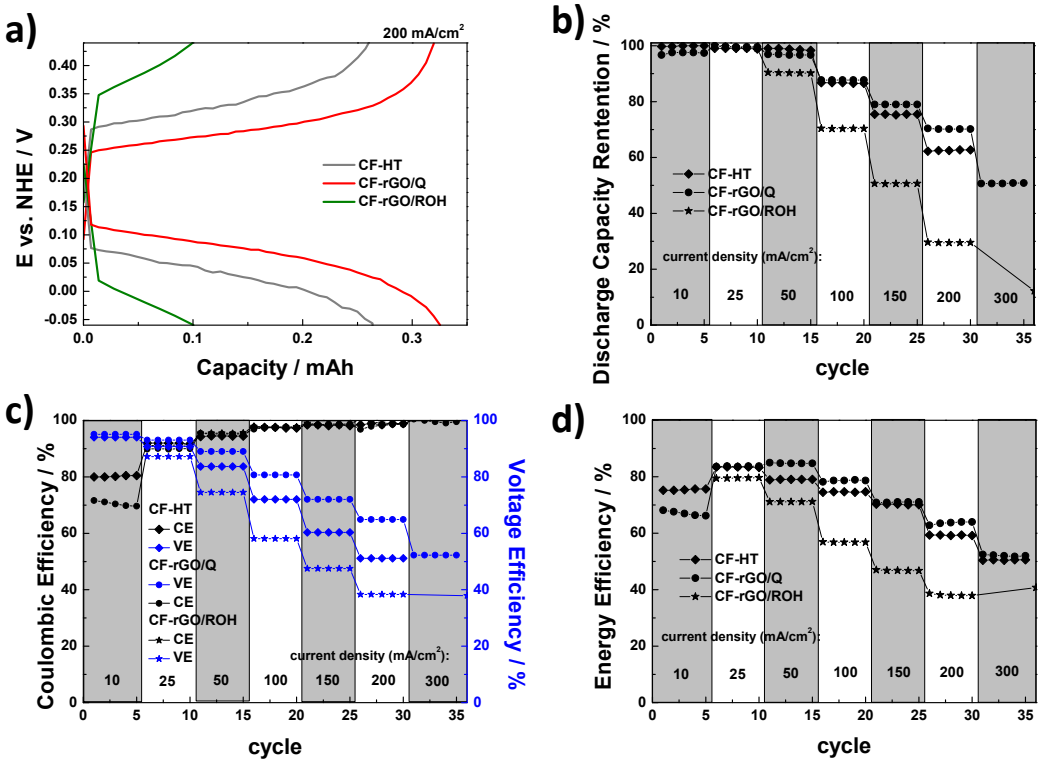

Figure 7.30.- Galvanostatic experiments of a 3 electrodes system with CF as counter electrode and Hg/Hg_2SO_4 as reference in a 0.05M Anthraquinone-2,7-disulfonic acid disodium 3 M $MeSO_3H$ solution at different current densities (10 to 300 mA/cm^2) displaying **a)** Charge-discharge plots for the electrodes used at current density of 200 mA/cm^2. **b)** Discharge capacity retention from the initial value for each electrode. **c)** Coulombic and voltage efficiencies (CE and VE). **d)** Energy efficiency (EE).

Additionally, efficiencies (Coulombic Voltage and Energy efficiencies) are screened at different current densities, from 10 to 300 mA/cm^2. Obtaining larger values of Coulombic efficiency as the current is raised due to minor cross-over and side reactions (HER and OER) (**Figure 7.30c**). All the samples perform well, showing a Coulombic Efficiency between 98 and 99% which evidence the low cross-over and side reactions that occurs at such current density. On the other hand, Voltage efficiency, which acts as a limiting factor and therefore Energy efficiency follows the analogous trend, decreases when large current densities are handled. Therefore as

the redox reaction does not have enough time to take place or does not have enough active sites due to low surface active groups. In this case the voltage efficiency trend at 200 mA/cm^2 is (%): CF-rGO/Q (64.9) > CF-HT (51.2)> CF-rGO/ROH (38.3). This could be a consequence of the nitrogen and oxygen active functional groups over CF-rGO/Q are larger, as XPS shows (**Figure 7.26**). Especially larger amount of C-O, O-C=O, graphitic-N and pyrrolic-N are found on CF-rGO/Q surface compared with the other electrodes (**Figure 7.25**). Moreover, as the $1/R_{ct}$ is also greater for CF-rGO/Q, when large current densities are applied these active groups facilitate the redox reaction on the electrode surface. Energy efficiency is limited by the Coulombic efficiency when low currents are applied, but by the Voltage efficiency when the current density it is high (**Figure 7.30d**).

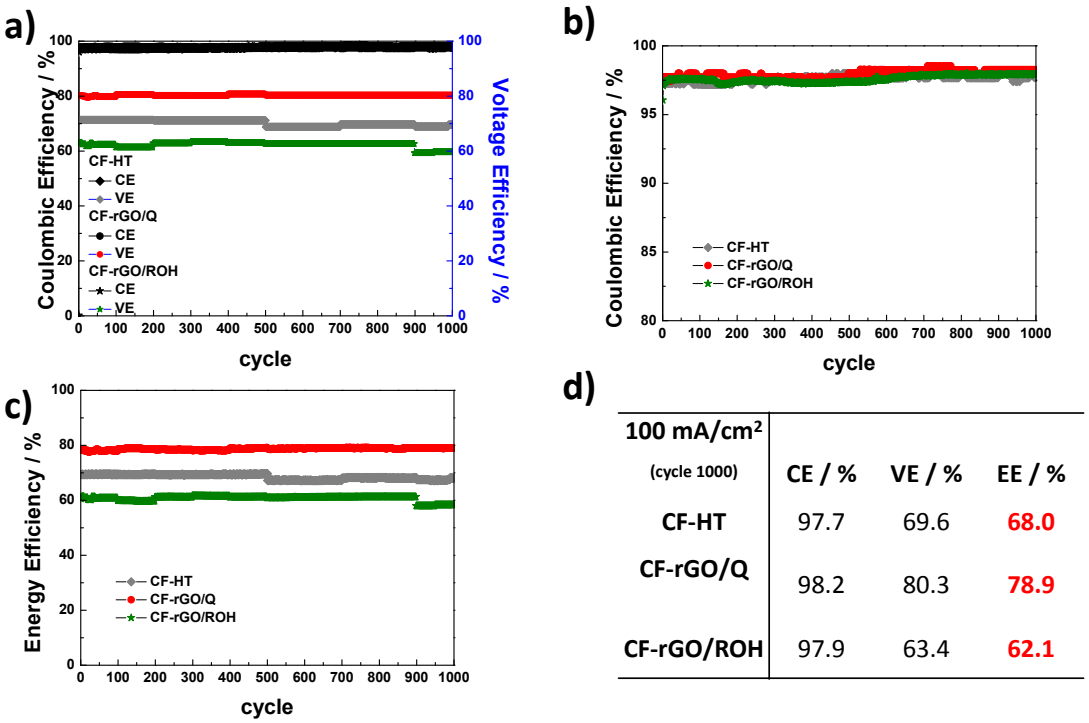

100 mA/cm^2 (cycle 1000)	CE / %	VE / %	EE / %
CF-HT	97.7	69.6	68.0
CF-rGO/Q	98.2	80.3	78.9
CF-rGO/ROH	97.9	63.4	62.1

Figure 7.31.- Long term cycling in galvanostatic conditions for 1000 cycles of a 3 electrodes system with CF as counter electrode and Hg/Hg_2SO_4 as reference in a 0.05M Anthraquinone-2,7-disulfonic acid disodium 3 M $MeSO_3H$ solution at a current densities of 100 mA/cm^2 displaying **a)**Coulombic and voltage efficiency (CE and VE). **b)** Coulombic efficiencies zoomed (CE). **c)** Energy efficiency (EE). **d)** Efficiency values after 1000 cycles for the electrodes used at current density of 100 mA/cm^2.

Finally, the electrodes were tested for 1000 cycles in order to study their long term viability towards the battery application. Those cycles were done at high current density, 100 mA/cm^2. As seen in **Figure 7.31**, Coulombic efficiency for all the electrodes is high, above 95%, and remains constant during cycling. Besides, all samples perform in the range of 97-98% showing the lack of cross-over, OER and HER. Additionally, Voltage efficiency and therefore Energy efficiency are quite stable, as the Voltage efficiency is the limiting factor. The CF-rGO/Q electrode boost the efficiency more than 10% compare with the other electrodes. This improvement

can be maintain along the life cycling, following the energy efficiency tendency: CF-rGO/Q (78.9) > CF-HT (68.0)> CF-rGO/ROH (62.1).

As a summary, the treatments done on the anode electrodes towards the Anthraquinone-2,7-disulfonic acid disodium salt has the objective of increase the electrochemically active surface area by the formation of nitrogen, mainly as graphitic-N as well as pyrrolic-N, and oxygen groups, especially C-O and O-C=O groups. Therefore the electrodes become more active towards the previously mentioned 2,7-AQDS. It is confirmed as CV showed by an increase in the reversibility and electrode-electrolyte mass transfer for the CF-rGO/Q electrode comparatively to CF-HT and CF-rGO/ROH. Moreover, when fitting PEIS done at 0.15V vs. NHE which is the potential Anthraquinone-2,7-disulfonic acid disodium keto/enol reaction takes place, CF-rGO/Q performance reduces its charge transfer resistance (R_{ct}). Moreover, charge-discharge plots at high current in a three electrode set-up, shows a larger overall charge and discharge capacity, as well as voltage efficiency (72%) for CF-rGO/Q due to a lower polarization of the electrode caused by all the modifications previously mentioned increasing the N/C and O/C ratio by oxygen and nitrogen functional groups. Additionally, the electrode cycling is stable at least for 1000 cycles with a large Coulombic efficiency (98%), which evidences the good performance, low electrolyte degradation (HER and OER) and cross-over.

7.3.4 Single cell performance

7.3.4.1 Carbon-based electrodes

Once the quinones molecules have been studied independently and systematically in half-cell systems, now it is the turn to couple the negative and positive active molecules, commonly benzoquinones in the positive cell and anthraquinones in the negative compartment due to their standard electrode potential. Consequently, put them together into a single-cell device in order to study their overall properties and behavior. Following this path, three different approaches have been done to obtain the best possible combination, continue its development and, eventually, stack several single-cell devices into a larger battery.

7.3.4.1.1 1,4-benzoquinone (+) vs. anthraquinone 2,7- Disulfonic acid disodium salt (-)

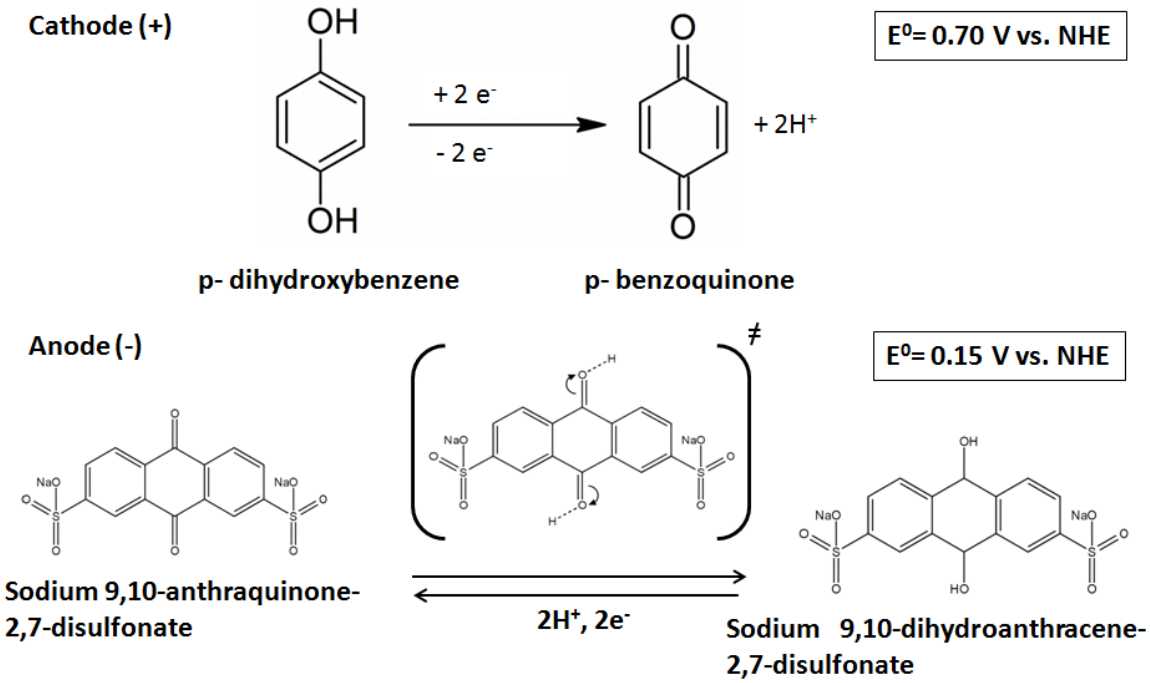

Figure 7.32.-. Scheme of cathodic redox reaction of p-benzoquinone at 0.70 V vs. NHE potential, as well as, anodic redox reaction of Sodium 9,10-anthraquinone-2,7-disulfonate molecule at 0.15 V vs. NHE potential.

Firstly, the system of study, as shown in **Figure 7.32**, is made of a combination of 0.4M p-hydroxybenzene on the positive side of the battery with a standard potential of 0.70 V vs. NHE, while 0.4M sodium 9,10-Anthraquinone-2,7-Disulfonate on the negative side with a standard potential of 0.15 V vs. NHE. Both compounds have been solved in 3M methanosulfonic acid (MSA), as this acid shows the better performance towards quinones redox reaction. The electrodes used for both compartments are Carbon felt. Moreover, some charge-discharge cycling has been done at a current density of 25 mA/cm^2 in order to do an initial experimentally screening of the system. The charge-discharge plot of the single cell, which is shown in **Figure 7.33**, evidences the easily visual changes happening in the electrolytes. In a first instance, the electrolytes are completely discharged showing a transparent-pink colored catholyte and an orange colored anolyte. When charged the color changes, the catholyte turns to a light orange color while the anolyte does it to a dark-green color.

Besides, considering the charge-discharge plot, shown in **Figure 7.33**, it is found two plateaus for charge and discharge as well. They fit with two redox reactions which are reversible as the Coulombic efficiency performance is above 95%, exactly 97.2%. In consequence, there will not have significant electrolyte degradation or cross-over to make the cycling to fail. However, as it is also shown, the voltage

efficiency is the limiting factor of the battery. One of the main reasons could be the high electrode resistivity due to its minor carbon felt (CF) hydrophilicity, as well as a low of the electrolyte ionic conductivity as there are not metallic ions facilitating the electronic movement in the bulk, obtaining only a final 51.1% energy efficiency.

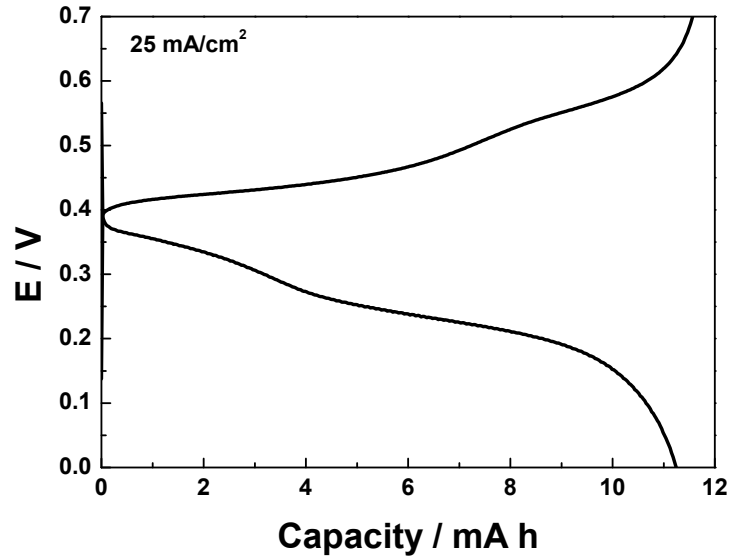

Discharged

Charged

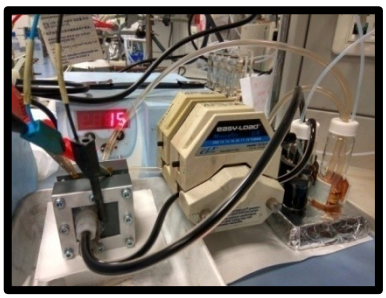

	CE / %	VE / %	EE / %
GF pristine 25 mA/cm²	97.2	52.6	51.1

Figure 7.33.-. Single cell charge-discharge plot of the potential of the cell vs. capacity at 25 mA/cm^2, showing the values of Coulombic, voltage and energy efficiency (CE, VE and EE), as well as, the pictures of the device completely charged and discharged.

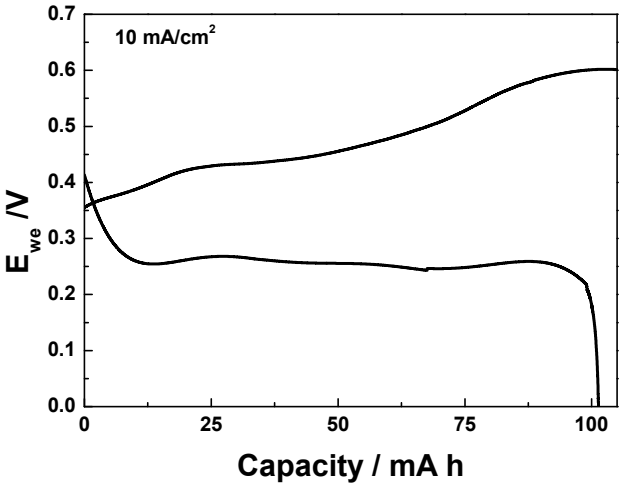

GF pristine	CE / %	VE / %	EE / %
10 mA/cm²	96.5	55.7	53.8

Figure 7.34. - Single cell charge-discharge plot of the potential of the cell vs. capacity at 10 mA/cm^2, showing the values of Coulombic, voltage and energy efficiency (CE, VE and EE), as well as, the pictures of the anolyte and catholyte.

Additionally, as seen in **Figure 7.34**, the charge-discharge of the single cell is repeated at lower current density (10 mA/cm^2) to verify if it is possible to increase the low voltage efficiency in this regard. Although the voltage efficiency just increases a 2.1%, the low current applied makes it possible to reach 10 times more capacity (100 mAh) compare to the previous chare-discharge plot at 25 mA/cm^2. Moreover, the Coulombic efficiency slightly decreases which is an indicator of small side reactions or cross-over. For this reason two approaches have been made i) introduce a reference electrode to follow positive and negative redox reaction independently and ii) reduce the cut-off voltage of the cell in order to avoid side reactions.

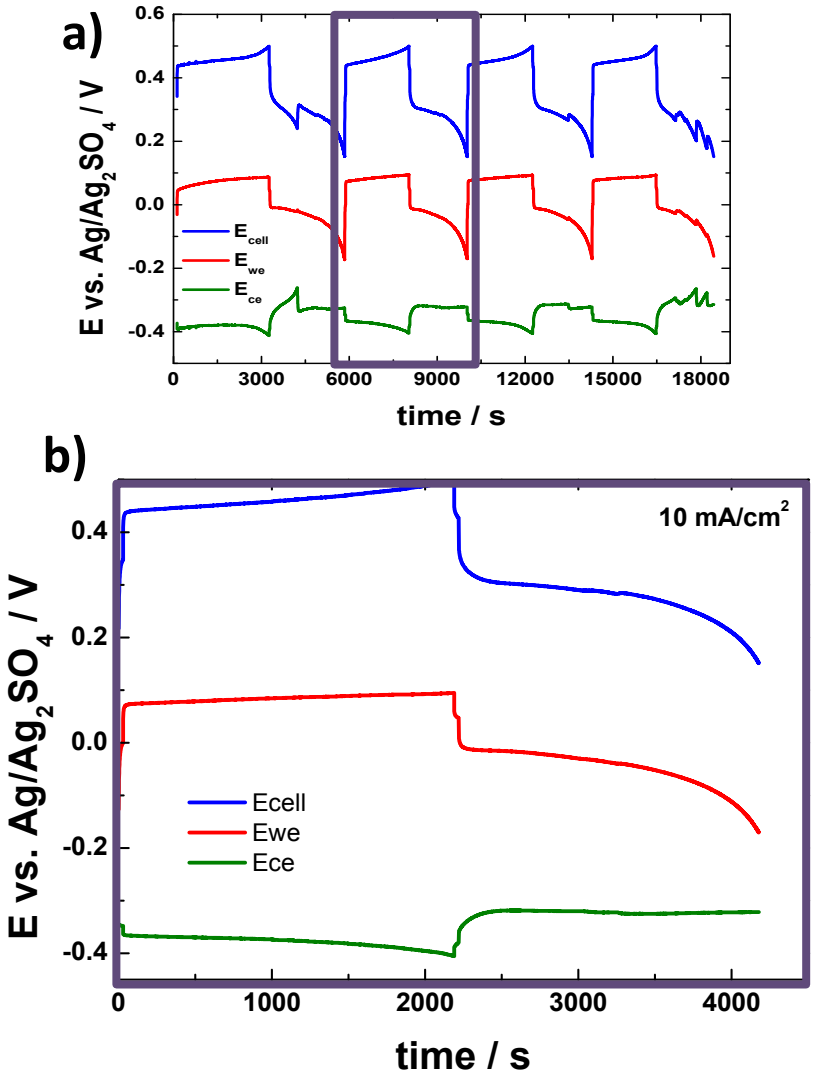

Figure 7.35. - a) Single cell several charge-discharge plot of the potential of the cell vs. time for the working, counter and the difference between these two electrodes at a current density of 10 mA/cm^2. **b)** inset caption of one of the previous cycles.

Therefore, while cycling the battery it is possible to follow the charge and discharge of both compartments independently, as seen in **Figure 7.35**. A 10 mA/cm^2 current density is applied with a lower cut of potential, up to 0.5 V, to avoid side reactions and cross-over within the cell. Focusing now on the plots, while charging the cell it is obvious an oxidation is happening on the positive side, p-hydroxibenzene as initial molecule solved is reacting to form p-benzoquinone. Similarly, on the negative side there is a reduction occurring, the initial sodium 9,10-anthraquinone-2,7-disulfonate is reduced to its enol form (sodium 9,10-dihydroanthracene-2,7-disulfonate). Deducting from the plot, it can be clearly seen that the negative reaction acts as a limiting factor in the overall single-cell charge, and as a consequence the positive reaction limits the discharge of the battery. Analyzing in deep these results, it can be found a plausible explanation to the negative reaction as limiting factor, which is the faster kinetics considering the same quantity of

active material (molarities of quinones) for the anolyte and catholyte. It can be observed a lower overpotential (η_a) in case of 2,7-AQDS redox reaction while charging, 25 mV, compare to the positive one (p-benzoquinone) which at least doubles that value (η_c = 63 mV). The overall charge overpotential of the single cell is 80 mV. The discharge overpotential follows the same trend, but with lower values than the charge process, as expected, which corresponds to 15mV, 47 mV and 73 mV for the negative side, positive side and overall cell, respectively.

Additionally, the efficiencies has been analyzed from **Figure 7.36**, visually it is quite obvious the larger voltage efficiency in case of 2,7-AQDS (green line), 87.8% VE. The voltage efficiency of the positive redox reaction of p-benzoquinone (red line) is significantly lower, 79.8% VE, which will limit the voltage efficiency of the battery to 70% (blue line). Moreover, the Coulombic efficiency will be the same value for both compartments and the overall cell as the negative side limits it, which is equal to 90.5%. Although is above 90% of efficiency, it still need to be improved due to the presence of a moderate cross-over and side reaction effect. Considering all of that, the energy efficiency when applying 10 mA/cm^2 are 79.4, 72.2 and 63.4 % for the negative side, positive side and overall single-cell device.

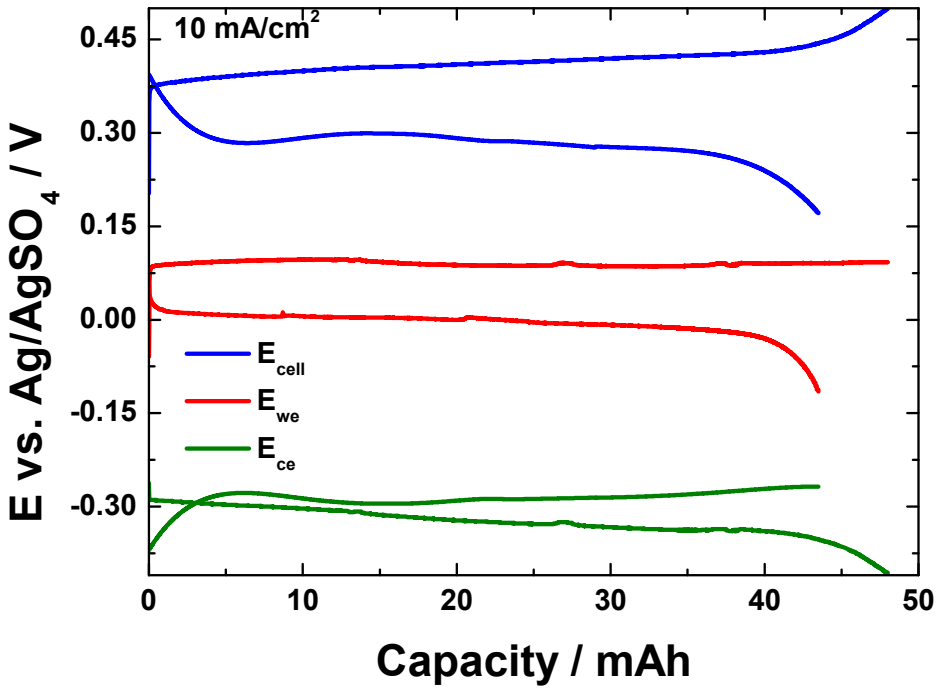

Figure 7.36. - Single cell charge-discharge plot of the potential of the cell vs. capacity for the working, counter and the difference between these two electrodes at a current density of 10 mA/cm^2.

Once all these factors of the primary single cell made of organic active material has been analyzed, it could be extract from the data the satisfactory efficiency of the single cell, and especially the negative side. However, further enhancements should be done especially the active material solubility which can be functional up to 0.4

M, as well as the current density and the potential of the battery. For this purpose, the cathode active material, p-hydrozybenzene, has been substituted by o-dihydroxybenzene mainly due to its larger solubility, as previously mentioned up to 2 M, which also increases the potential of the battery.

7.3.4.1.2 1,2-benzoquinone (+) vs. anthraquinone 2,7- Disulfonic acid disodium salt (-)

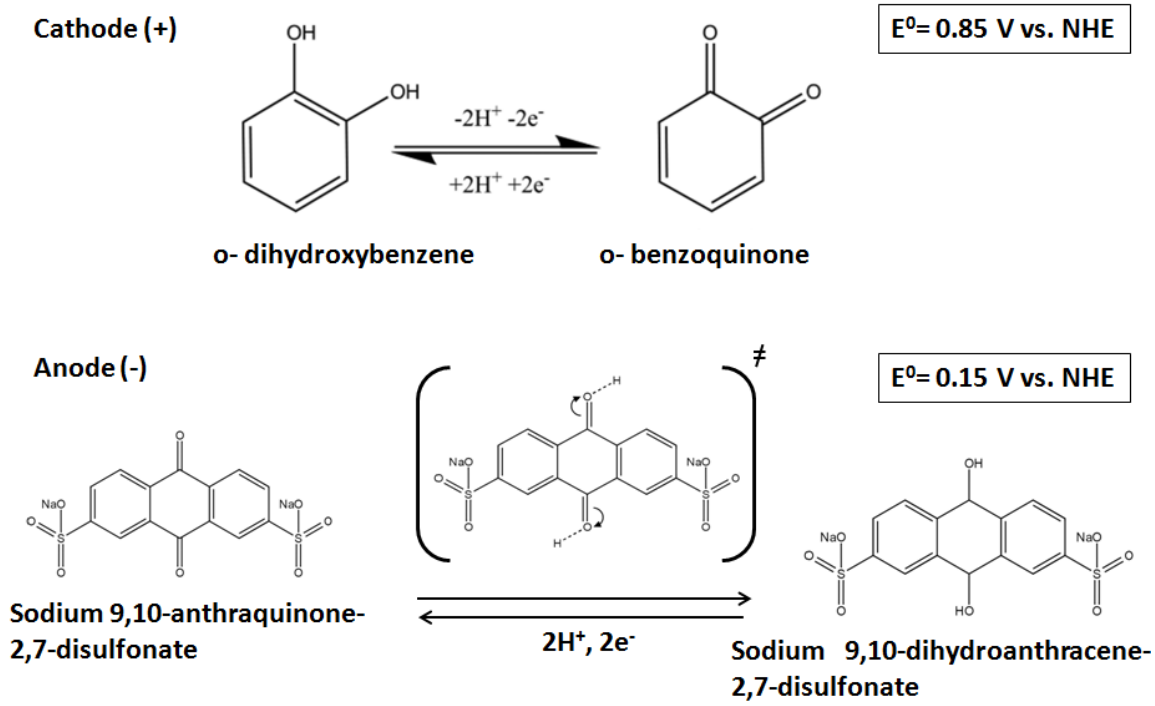

Figure 7.37.- Scheme of cathodic redox reaction of o-benzoquinone at 0.85 V vs. NHE potential, as well as, anodic redox reaction of Sodium 9,10-anthraquinone-2,7-disulfonate specie at 0.15 V vs. NHE potential.

Secondly, the battery active materials, as shown in **Figure 7.37**, are initially composed of 0.4M o-hydroxybenzene on the positive side of the battery, which has a standard potential of 0.85 V vs. NHE, while 0.4M sodium 9,10-Anthraquinone-2,7-Disulfonate performing a standard potential of 0.15 V vs. NHE on the negative side. Both of the compounds have been solved in 3M methanosulfonic acid (MSA), as well as the prior case using the p-benzoquinone. The electrode used for both compartments is Carbon felt material. Additionally, some charge-discharge cycles have been done at 25 mA/cm^2 current density in order to do an initial experimentally screening of the system at different cut off potentials. Considering the charge-discharge plot, shown in **Figure 7.38**, it is found that above 0.55 V there is a highly irreversible reaction (side reaction) happening while charging, which is evidenced in a low Coulombic efficiency (66% for 0.6 V and 47% for 1 V) for a single cell. Therefore, the optimum value of Coulombic efficiency is obtained

for 0.5 V (99.1%), fitting with a reversible redox reaction. However, the voltage efficiency reached for this potential limit is remarkable low, 18.2%, which limit its application at such high current density for this system. In order to increase this value it is mandatory to increase the reversibility of the positive redox reaction, as well as reduce the electrode's polarization.

On the bright side, the Coulombic efficiency performed is above 95%, exactly 99.1%. In consequence, there will not have significant electrolyte degradation to stop the process. It can be appreciated in **Figure 7.38** showing several charge discharge plots without degradation. However, as it is also shown, the voltage efficiency is the limiting factor of the process. One of the main reasons is the large electrode polarization increasing the ohmic drop, which limits the battery to perform just an 18% of energy efficiency.

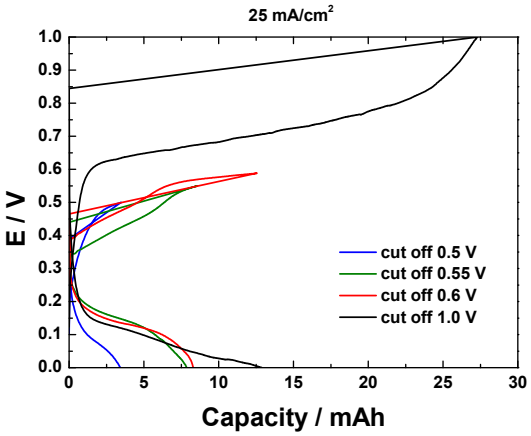

25 mA/cm² GF pristine	CE / %	VE / %	EE / %
0.5 V	**99.1**	18.2	18.0
0.55 V	**91.7**	**29.6**	**27.1**
0.6 V	66.3	23.7	15.7
1.0 V	47.2	10.6	5.00

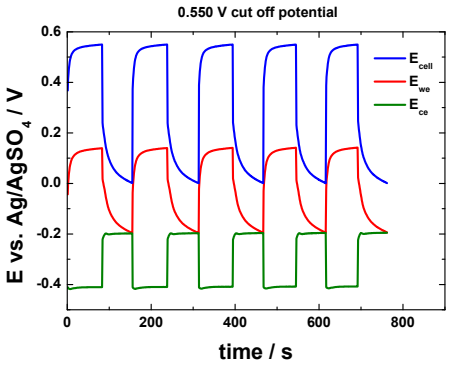

Figure 7.38.- a) Single cell charge-discharge plots of different cut off potentials (0.5, 0.55, 0.6 and 1 V) vs. capacity at a current density of 25 mA/cm^2. **b)** CE, VE and EE for the different cut off potentials at a current density of 25 mA/cm^2. **c)** Single cell charge-discharge plot of the potential with a cut off 0.55 V vs. time for the working electrode, counter electrode and the difference between these two at a current density of 25 mA/cm^2.

Additionally, the charge-discharge of the single cell is repeated at lower current density (10 mA/cm^2) to verify if it is possible to increase the low voltage efficiency in this regard, as seen in **Figure 7.39**. Certainly, the voltage efficiency is highly increased, from 18 to 56%, reaching values close to the electrolyte configuration showed before with p-hydroxibenzene as positive active material. Moreover, the capacity is also increased from 3.4 to 15 mAh for the optimum 0.5 V as cut off voltage. However, the coulombic efficiency decreases abruptly when the current density applied is lowered, from 99 to 87%, an indicator of non reversible process increasing during cycling. As previously said, it may be caused by side reactions

and cross-over through the membrane of the o-benzoquinone while cycling, which also could be the main reason for the difference between the discharge capacities between the two configurations, from 44 mAh for p-benzoquinone to 15 for o-benzoquinone. Although the solubility may be increased with the solution composed by the orto-benzoquinone, it is needed to solve the lack of voltage efficiency (electrode-electrolyte conductivity) and irreversible side reactions happening to the organic active molecules, before this solved o-benzoquinone became really active.

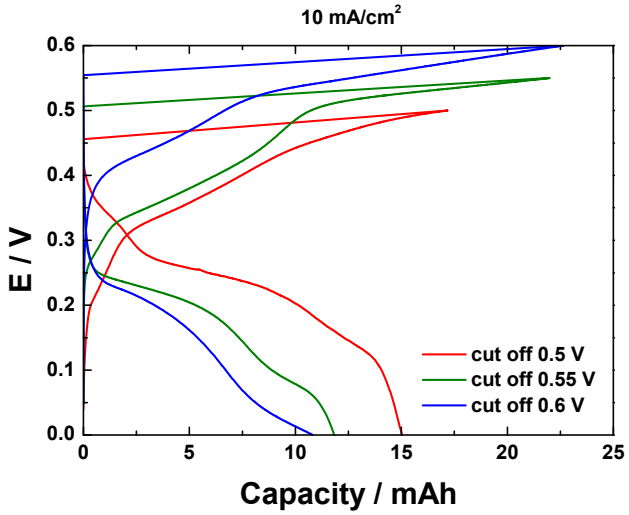

10 mA/cm² GF pristine	CE / %	VE / %	EE / %
0.5 V	**87.4**	**56.4**	**49.3**
0.55 V	53.8	37.6	20.3
0.6 V	47.8	27.6	13.2

Figure 7.39.- a) Single cell charge-discharge plots of different cut off potentials (0.5, 0.55 and 0.6V) vs. capacity at a current density of 10 mA/cm^2. **b)** CE, VE and EE for the different cut off potentials at a current density of 10 mA/cm^2.

7.3.4.1.3 Sodium 4,5-dihydroxybenzene-1,3-disulfonate (+) vs. anthraquinone 2,7-Disulfonic acid disodium salt (-)

Thirdly, the battery assembled, as shown in **Figure 7.40**, is initially composed of 0.4 M sodium 4,5-dihydroxybenzene -1,3-disulfonate (Tiron) on the positive side of the battery, which has a standard potential of 0.85 V vs. NHE, while 0.4M sodium 9,10-Anthraquinone-2,7-Disulfonate performing a standard potential of 0.15 V vs. NHE is used on the negative side. Both compounds have been solved in 3M methanosulfonic acid (MSA), as well as the previous cases. Analogously, the electrode used for both compartments is carbon felt.

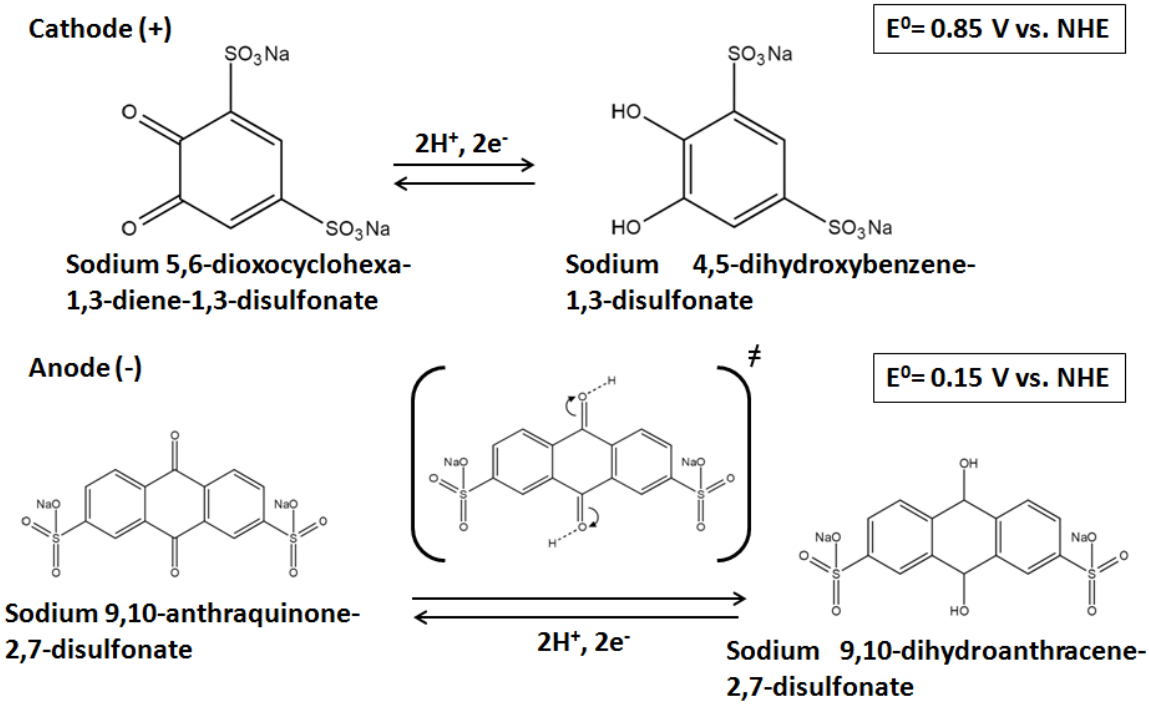

Figure 7.40.- Scheme of cathodic redox reaction of Sodium 4,5-dihydroxybenzene-1,3-disulfonate at 0.85 V vs. NHE potential, as well as, anodic redox reaction of Sodium 9,10-anthraquinone-2,7-disulfonate specie at 0.15 V vs. NHE potential.

Initially, it is studied the self-discharge of the battery for that purpose a reference electrode is introduce in the battery, as shown in **Figure 7.35**. Afterwards, the OCV potential is followed once the cell is fully charged. There is no significantly self-discharge of the system among time (**Figure 7.41a**). However, after cycling it is more sensitive to a smooth auto-discharge in the negative side of the cell, remaining the positive side unchanged after cycling.

At the beginning, a new cut-off voltage screening has been done from 0.7 to 1.4 V with an increment of 0.1V each cycle (**Figure 7.41b**). As the voltage is increased, the capacity of the battery also increases up to 1.1 V, from this value the capacity starts to decay which is probably caused by a non-reversible processes. As **Figure 7.41c** shows, there is a rapid decay in the charge-discharge cycling time, confirmed by the Coulombic efficiency for each potential. The Coulombic efficiency increases from 76.6% when 1.1 V is applied up to 96.8% when the potential cell is 1.4 V (**Figure 7.41d**).

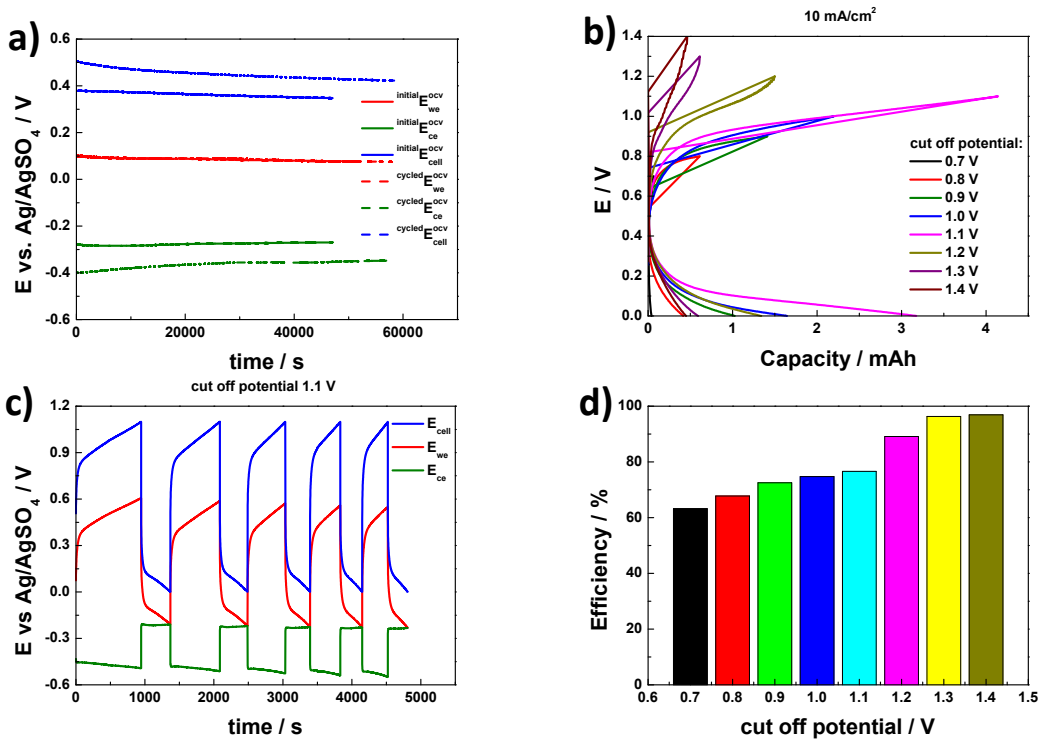

Figure 7.41.- a) Single cell E_{ocv} vs. time after charge. **b)** Single cell charge discharge-plot of potential vs. capacity for several cut off potentials, showed on the picture, at 10 mA/cm^2 current density. **c)** Single cell charge-discharge plot for working electrode, counter electrode and the difference between these two of the potential vs. time. **d)** Bar chart of single cell efficiency vs. cut off potential at 10 mA/cm^2 current density.

Furthermore, some charge-discharge has been done at a current density of 10 mA/cm^2 setting different values of flow speed, in order to set the most efficient for the aqueous organic redox flow batteries. In this case, the cut off potential is highly increased up to 1.4 V. As **Figure 7.42** shows, the efficiency (87 to 96.9 CE%) and capacity of the battery increase as the flow speed is raised from 10 mL/min to 50 mL/min quite significantly. Once this value is obtained, the capacity minimally increases when setting 75 and 100 mL/min, as well as happens to the efficiency (97.1% for 75 mL/min), which could even decrease its value when 100 mL/min is set (96.1%). Moreover, long term stability has been done up to 100 cycles with a cut of potential of 1.4V and 50 mL/min of flow speed. Even though the battery increases its Coulombic efficiency among cycling, the capacity retention decays rapidly to 40% in less than 20 cycles and giving a final value of 20% after 100 cycles. This fact evidences the low stability of the system, which suffers from an important non-reversible process of the active material.

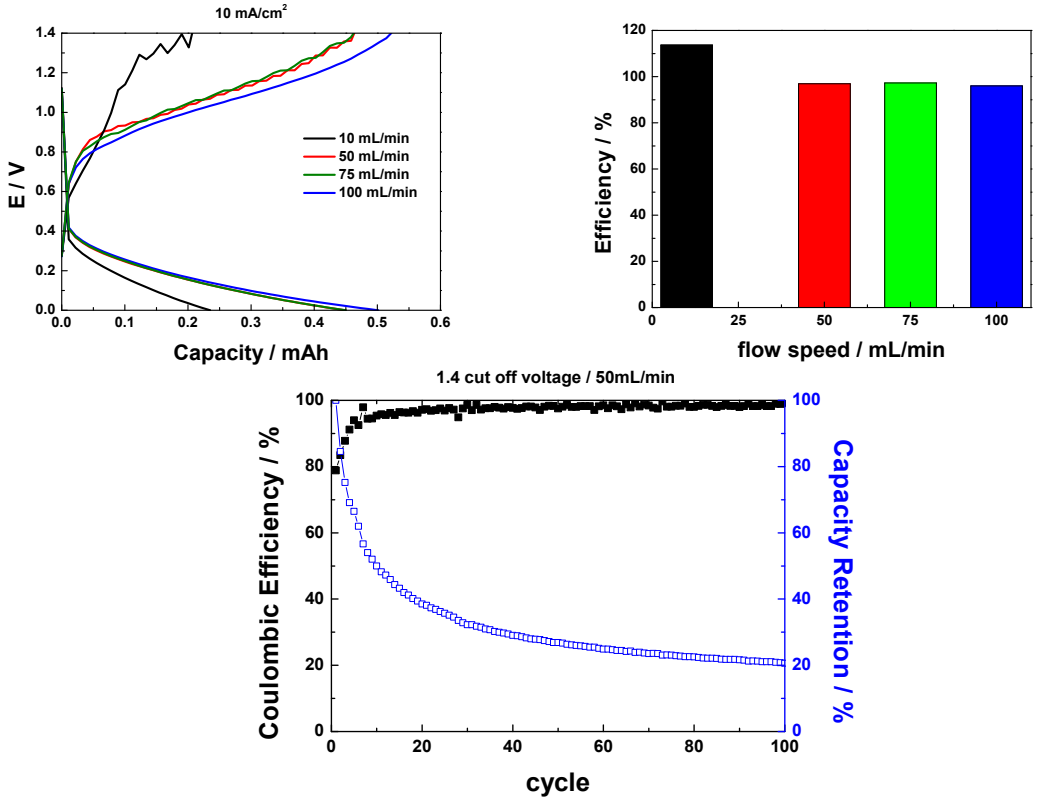

Figure 7.42. - a) Single cell charge-discharge plots for different flow speed (10, 50, 75 and 100 mL/min) vs. capacity at a current density of 10 mA/cm^2. **b)** Bar chart of Efficiency vs. flow speed at a current density of 25 mA/cm^2. **c)** Single cell Coulombic efficiency and capacity retention plot for 100 cycles for a cut off potential of 1.4 V and 50 mL/min of flow speed at a current density of 25 mA/cm^2.

Therefore, considering just electrochemical factors related to the different active molecules solved in the positive electrolyte. The best values are obtained for the p-benzoquinone molecule. Always working with sodium 9,10-anthraquinone-2,7-disulfonate as negative active electrolyte molecule as the one showing better electrochemical output. Although all this facts are true, more intensive research need to be done in single-cell configuration, as study deeply electrodes modifications to increase the active area in the interface electrode-electrolyte. It can enhance the voltage efficiency of the cell which is one of the main lacks of the system. Moreover, include new additives into the electrolyte to make it more conductive and also to avoid any gas evolution, cross-over and non reversible redox reaction taking place in the device. It should be always consider aqueous organic redox flow batteries as a new redox system with less than 5 years of development comparatively to VRFBs, which origins are place in 1980s more than 30 years ago. In this matter there is still room to improve this technology, which has a limitless potential to exploit yet.

7.3.4.2 Enhanced carbon-based electrodes

7.3.4.2.1 Sodium 4,5-dihydroxybenzene-1,3-disulfonate (+) vs. anthraquinone 2,7-Disulfonic acid disodium salt (-)

Finally, once the studies of the quinones molecules, following three different approaches, have been done to obtain the best possible combination, it is continued its development including the treated electrodes previously verified into half-cell systems. CF-HT is included as positive electrode using 4,5-dihydroxybenzene-1,3-disulfonate (1,2-BQDS) active material, analogously CF-rGO/Q electrode is implemented as negative electrode using anthraquinone 2,7- Disulfonic acid disodium salt (2,7-AQDS) negative active material. In Both cases methanosulfonic acid is used as solvent.

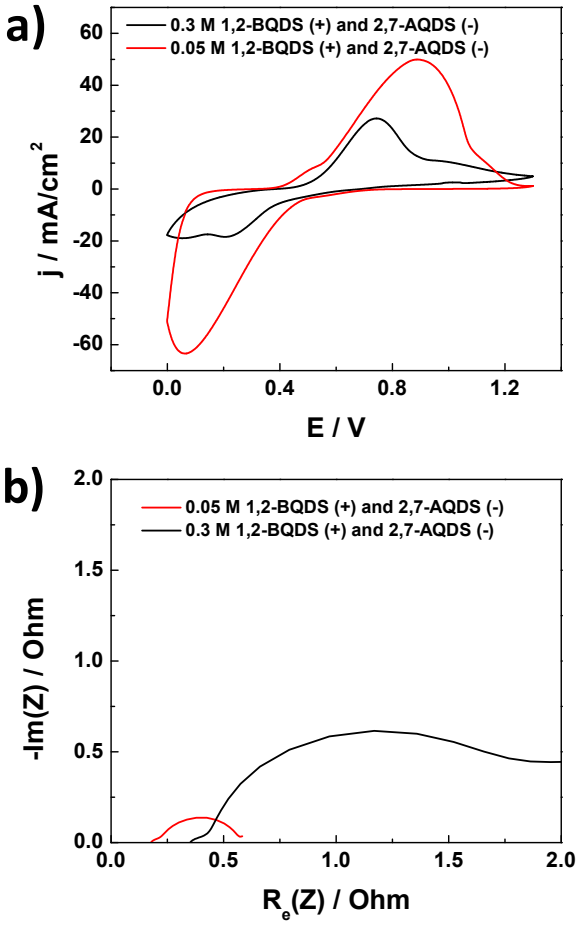

Figure 7.43. – a) Cyclic voltammetry for the single cell in a potential range from 0 to 1.2 V, using GF-N as positive electrode and GF-rGO/Q as negative electrode containing an electrolyte of 0.05 M 1,2-BQDS(+) and 2,7-AQDS in 3 M $MeSO_3H$ solution (red line) and 0.3 M 1,2-BQDS(+) and 2,7-AQDS in 3 M $MeSO_3H$ solution (black line). **b)** PEIS for the single cell at a fixed potential of 0 V vs. NHE, using GF-N as positive electrode and GF-rGO/Q as negative electrode containing an electrolyte of 0.05 M 1,2-BQDS(+) and 2,7-AQDS in 3 M $MeSO_3H$ solution (red line) and 0.3 M 1,2-BQDS(+) and 2,7-AQDS in 3 M $MeSO_3H$ solution (black line).

Initially, cyclic voltammetry (**Figure 7.43a**) is used to screening the potential range in which the single cell system studied can operate. Obviously is observed a cell potential around 1 V, which current density reached on the redox process is larger in case of 0.05 M of active material compare to higher concentration of active material , as it is 0.3 M. This indicates that the electrode's surface is saturated at larger concentrations, which is due to a larger polarization over the electrodes when larger amount of active material is solved, inhibiting the cell with lower concentrations of active material will be able to generate larger current densities. Besides, this fact is coherent with the results of potentiostatic electrochemical impedance spectroscopy (PEIS) (**Figure 7.43b**), showing that the single cell containing just 0.05 M of active material has a lower electrical resistance (R_e = 0.17 Ohm), as well as charge transfer resistance (R_{ct} = 0.4 Ohm). When the active material's concentration is raised to 0.3 M, the resistances also increase, R_s = 0.35 Ohm and R_{ct} = 1.5 Ohm.

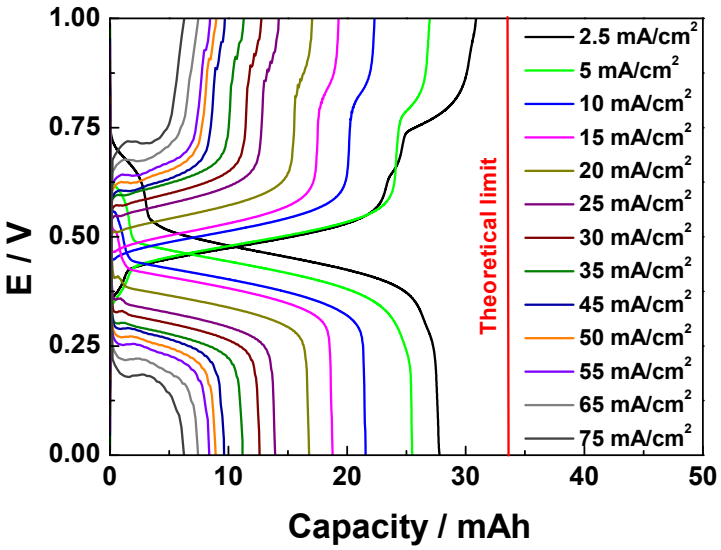

Figure 7.44. - Galvanostatic charge-discharge plots at increasing current densities, from 2.5 to 75 mA/cm^2, for a single cell containing an electrolyte of 0.05 M 1,2-BQDS(+) and 2,7-AQDS in 3 M $MeSO_3H$ solution (12.5 mL each reservoir).

Furthermore, galvanostatic charge-discharge cycles are done for 0.05 M organic active material in each compartment of a single-cell device, for that purpose increasing current densities, from 2.5 to 75 mA/cm^2, are applied to observe its behavior among cycling and also more demanding conditions. **Figure 7.44** evidences a charge-discharge capacity near the theoretical limit value for low current densities as it is 2.5 mA/cm^2. In case the current is increased, these values are getting apart from the theoretical capacity. Moreover, when the capacity retention in the same conditions is analyzed, seen **Figure 7.45a**. The values reach an outstanding 77% for a 10 mA/cm^2 current density, which decay to an acceptable 50% when increased up to a current density of 25 mA/cm^2.

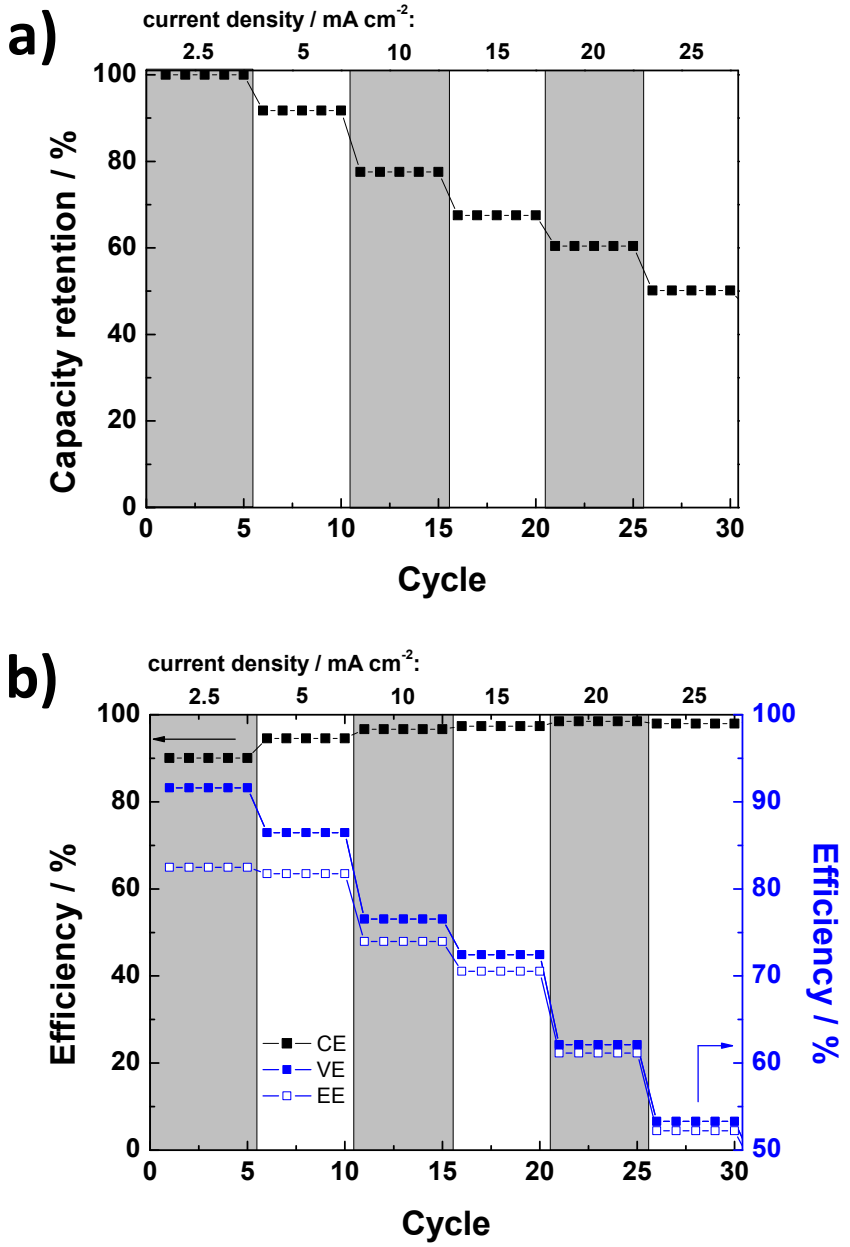

Figure 7.45. – a) Capacity retention obtained among cycling, while increasing the current density (2.5 to 25 mA/cm^2) for a single cell containing an electrolyte of 0.05 M 1,2-BQDS(+) and 2,7-AQDS in 3 M $MeSO_3H$ solution. **b)** Coulombic, voltage and energy efficiency obtained among cycling, while increasing the current density (2.5 to 25 mA/cm^2) for a single cell containing an electrolyte of 0.05 M 1,2-BQDS(+) and 2,7-AQDS in 3 M $MeSO_3H$ solution.

Additionally, the coulombic efficiency (CE) for the charge-discharge cycles is also deeply analyzed. Related to this, as seen in **Figure 7.45b**, the values increase from 95% CE at a low current of 2.5 mA/cm^2 up to 99% in case the current is raised ten times (25 mA/cm2). This effect is due to the presence of a lower contribution of side reactions, as well as lower active species cross-over trough the membrane. However, it is the voltage efficiency (VE) the limiting factor to the overall efficiency (energy efficiency - EE). In this regard, as seen previously in **Figure 7.44**, the polarization effect while the current is raised follows the same tendency as the voltage efficiency. Obtaining extraordinary values of 76% VE for 10 mA/cm^2 of

current density applied, which turn into 74% EE. These efficiency values are diminished to 53% VE and 52% EE when the current density is raised up to 25 mA/cm^2.

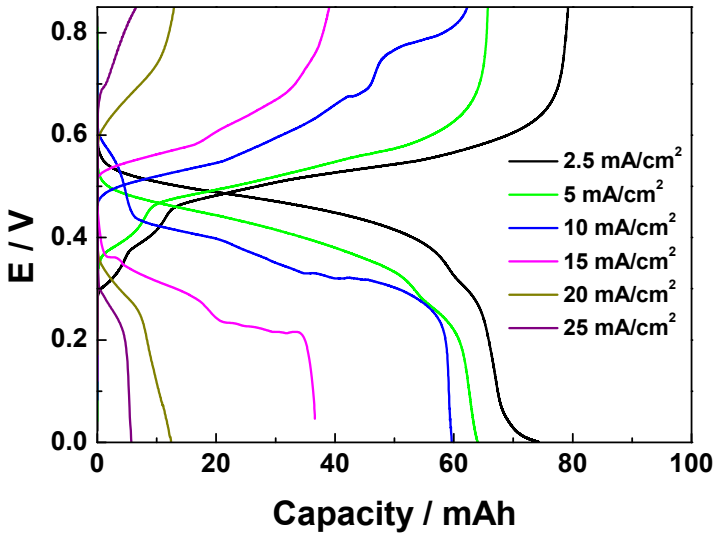

Figure 7.46. - Galvanostatic charge-discharge plots at increasing current densities, from 2.5 to 25 mA/cm^2, for a single cell containing an electrolyte of 0.3 M 1,2-BQDS(+) and 2,7-AQDS in 3 M $MeSO_3H$ solution.

Last but not least, the galvanostatic charge-discharge cycles are done for larger concentration of 0.3 M organic active material in each compartment for a single-cell device with a theoretical capacity of 241.2 mAh. Similarly, increasing current densities, from 2.5 to 25 mA/cm^2, are applied to observe its behavior among cycling and also more demanding conditions. **Figure 7.46** evidences a charge-discharge capacity values above the one shown in **Figure 7.45**. In case the current is increased, these values are getting lower. Reaching that point is worth mention, the exceptional improvement of the charge-discharge cycle capacity and polarization, when the enhanced electrode are included in the flow battery comparatively to the performance of the pristine electrodes, seen in **Figure 7.42**. Moreover, when the capacity retention is analyzed, seen **Figure 7.47a**. The values reach an outstanding 80% for a 10 mA/cm^2 current density, which is far greater value than the 77% obtained for a lower 0.05 M organic active material conditions. In addition, the coulombic efficiency (CE) for the charge-discharge cycles is also analyzed. In which regard, as seen in **Figure 7.47b**, the values increase from 94% CE for a low current, 2.5 mA/cm^2, up to 96% CE in case the current is raised up to 10 mA/cm^2. This effect is due to the presence of a even lower contribution of side reactions, as well as lower active species cross-over trough the membrane. However, the voltage efficiency (VE) is the limiting factor on the overall efficiency (energy efficiency - EE). Therefore, as seen previously in **Figure 7.43b**, the polarization effect is more dominant in larger concentration of active material. Moreover, the polarization in both cases, low and high organic active material concentration follows the same tendency, increases similarly as the voltage efficiency when the current density is raised. Obtaining values of 58% VE for 10 mA/cm^2 of current density applied, which turn into 56% EE. These efficiency values evidences the previous explained fact, as for 0.05 M of active material the efficiency

values give a 76% VE for 10 mA/cm^2 of current density applied, which turn into 74% EE.

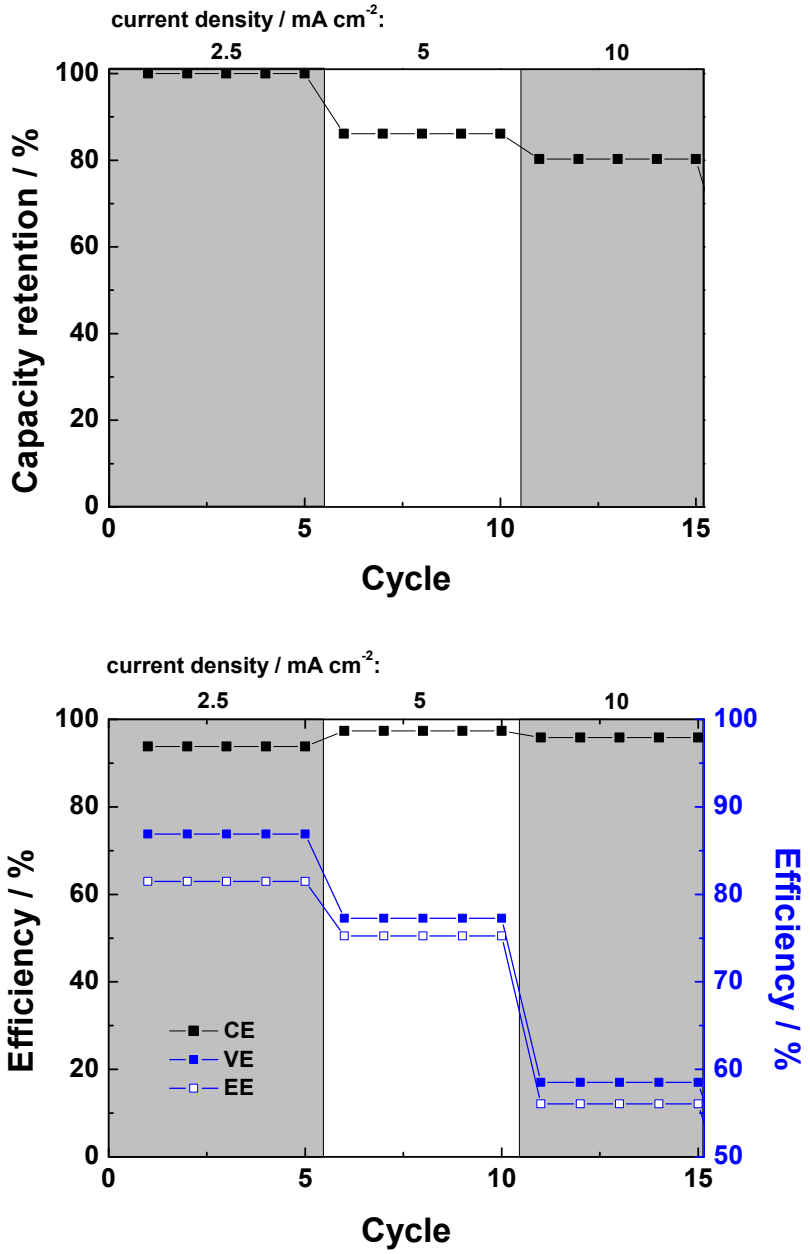

Figure 7.47. - Top. Capacity retention obtained among cycling, while increasing the current density (2.5 to 10 mA/cm^2) for a single cell containing an electrolyte of 0.3 M 1,2-BQDS(+) and 2,7-AQDS in 3 M $MeSO_3H$ solution. **Bottom.** Coulombic, voltage and energy efficiency obtained among cycling, while increasing the current density (2.5 to 10 mA/cm^2) for a single cell containing an electrolyte of 0.3 M 1,2-BQDS(+) and 2,7-AQDS in 3 M $MeSO_3H$ solution.

Besides, knowing this performance it would be useful an additive or some modification capable of increase the obtained efficiency values, which are already outstanding comparatively with similar aqueous organic redox flow batteries using the same molecules only being able to reach 8 mAcm^{-2} as current densities and a functional charge-discharge into a single cell with a 0.2M of active material in each

comparment[1]. Another interesting future feature would be increasing even more the concentration of the solvated redox material into a functional battery.

As a summary, the prior showed studies done in half-cell systems considering specially the electrodes (cathode and anode) enhancement, are capable of take into a single cell device (battery) these improvement. After implementing these electrodes, CF-HT (+) and CF-rGO/Q (-), the battery is capable to achieve an outstanding performance, in 0.05 M active material concentration, obtaining 98% CE, 76% VE and 74% EE for 10 mA/cm^2 of current density applied. These efficiency values are reduced when increased to 0.3 M of active material, getting 96% CE, 58% VE and 56% EE for 10 mA/cm^2 of current density applied. However, the capacity retention is increased from 77% to 80%, as the amount of active material is raised.

7.4 Conclusions

Along the experimental work done within the group, it has been accomplished much, obtaining the following conclusion points that summarize this chapter about aqueous organic redox flow batteries:

1. The treatments done on the cathode electrodes for metal-free redox flow batteries has the objective to increase the surface area by electrode functionalization with nitrogen and oxygen groups, especially active are the oxygenated-N and C=O groups. These are more abundant on the CF-HT surface. Therefore the electrodes become more electrochemically active, as CV showed by an increase in the reversibility and diffusion towards the Tiron redox reaction on CF-HT comparatively to the other two electrodes (CF-HT and CF-rGO/Q). In spite the fact that the kinetic values for all the electrodes are similar, which shows that these N and O groups do not act as a catalyst, the charge transfer resistance is reduced due to that functionalization. This facilitates the migration of the Tiron redox species towards the interface electrode-electrolyte. Moreover, the CF-HT electrode is stable at least for 1000 cycles, which evidences the good performance and low degradation (HER and OER) of it.

2. The treatments done on the anode electrodes towards the Anthraquinone-2,7-disulfonic acid disodium salt has the objective of increase the electrochemically active surface area by the formation of nitrogen, mainly as graphitic-N as well as pyrrolic-N, and oxygen groups, especially C-O and O-C=O groups. Therefore the electrodes become more active towards the previously mentioned 2,7-AQDS redox reaction. It is confirmed as CV showed by an increase in the reversibility and electrode-electrolyte mass transfer for the CF-rGO/Q electrode comparatively to CF-HT and CF-rGO/ROH. Moreover, when fitting PEIS done at 0.15V vs. NHE which is the potential Anthraquinone-2,7-disulfonic acid disodium keto/enol reaction

takes place, CF-rGO/Q performance reduces its charge transfer resistance (R_{ct}). In case considered charge-discharge plots at high current in a three electrode set-up, the overall charge and discharge capacity, as well as the voltage efficiency (72%) is larger for CF-rGO/Q due to a lower polarization of the electrode caused by all the modifications previously mentioned. Additionally, the electrode cycling is stable at least for 1000 cycles with a large Coulombic efficiency (98%), which evidences the good performance, low electrolyte degradation (HER and OER) and limited cross-over.

3. When couple the negative and positive active molecules previously mentioned, commonly benzoquinones in the positive cell and anthraquinones in the negative compartment, into a single-cell device in order to study their overall properties and behavior. Three different approaches have been done to obtain the best possible combination. Considering just electrochemical factors related to the different active molecules solved in the positive electrolyte. The best values are obtained for the p-benzoquinone molecule. Always working with sodium 9,10-anthraquinone-2,7-disulfonate as negative active electrolyte molecule as the one showing better electrochemical output. Although all this facts are true, it happens to p-benzoquinone to self-oxidize when solved in the acidic electrolyte. For that reasons the single cell studies using the modified electrodes have 1,2-BQDS as cathodic active material and continuing with 2,7-AQDS as anode material.

4. After implementing these electrodes, CF-HT (+) and CF-rGO/Q (-), the battery is capable to achieve an outstanding performance, in 0.05 M active material concentration, obtaining 98% CE, 76% VE and 74% EE for 10 mA/cm^2 of current density applied. These efficiency values are reduced when increased to 0.3 M of active material, getting 96% CE, 58% VE and 56% EE for 10 mA/cm^2 of current density applied. However, the capacity retention is increased from 77% to 80%. In any case, when the modified electrodes are introduced not only the overall efficiency is enhanced, from 63.4% EE for CF-P p-benzoquinone (+) vs. 2,7-AQDS to 74% EE for CF-HT in 1,2-BQDS (+) vs. CF-rGO/Q in 2,7-AQDS, but the capacity reached raised from 45 mAh to 60 mAh and not only for one cycle but for few of them. It should be always consider aqueous organic redox flow batteries as a new redox systems with less than 5 years of development comparatively to a well-developed technology, as VRFBs, which origins are place in 1980s more than 30 years ago. In this matter there is still room to improve this technology, which has a limitless potential to exploit yet.

7.5 Perspective of Organic Redox Flow Devices

Usually, capacity loss in flow batteries can be attributed to redox species crossover through the membrane, oxidation from the outside environment and chemical degradation of redox species. Here major external oxidation is not likely since sealed and purged reservoirs are used. Moreover, a dense and highly selective Nafion 117 membrane was used in all RFB tests displayed and crossover has been shown to be unlikely for the relatively large quinone molecules (p-benzoquinone, o-benzoquinone and sodium 9,10-anthraquinone 2,7-disulfonate). For this reason we attribute the capacity loss to chemical degradation of the organic redox species. According to recent work, o-benzoquinones derivates, as Tiron, transforms to the tri- and tetrahydroxylated versions shortly after the oxidation to the quinone form, since water performs a Michael addition (1,4 to the α,β unsaturated carbonyl compound) as exemplified in **Figure 7.16**.

The multi-hydroxylated quinones are usually found to be electrochemically irreversible and/or insoluble. In the case of increasing the pH, a stronger nucleophile (OH-) is predominant and thus the reduction/oxidation peak ratio is even smaller than in acidic and neutral solution. This is confirmed in a redox flow battery test in **Figure 7.42**, where an acidic metal free redox flow battery with Tiron losses more than half of its capacity after only 20 cycles.

Consequently, quinones with possible leaving groups and unsubstituted sites are likely to be unstable in aqueous solutions. However, the degradation reaction rate depends on the electrolyte used. A further complication is that as both oxidation states are present in the battery during operation and hydroquinones can act as nucleophiles and react with the benzoquinones, there can be unwanted polymerizations at both, low and large pH. Thus, when considering stability the use of only partially substituted BQs and those substituted with possible leaving groups in aqueous RFBs is very limited.

As an alternative to single quinone molecules solved in the electrolyte, it could be possible to do a controlled polymerization analogously to Janoschka et al. that has evaluated numerous water-soluble polymers (polymethacrylates and polystyrenes) for application in an aqueous RFB[274]. A special focus should be placed on their rheological, thermal, and electrochemical properties with a target of < 20mPas to ensure the efficient operation of a pumped RFB. Similarly as they do with TEMPO and viologen as redox active moieties (**Figure 7.48**)[274,275], it can also be done a novel battery type not only to replace common ion-exchange membranes and highly corrosive acidic electrolyte solutions with inexpensive dialysis membranes and pH-neutral sodium chloride solutions, but also avoiding the chemical degradation of single quinones molecules.

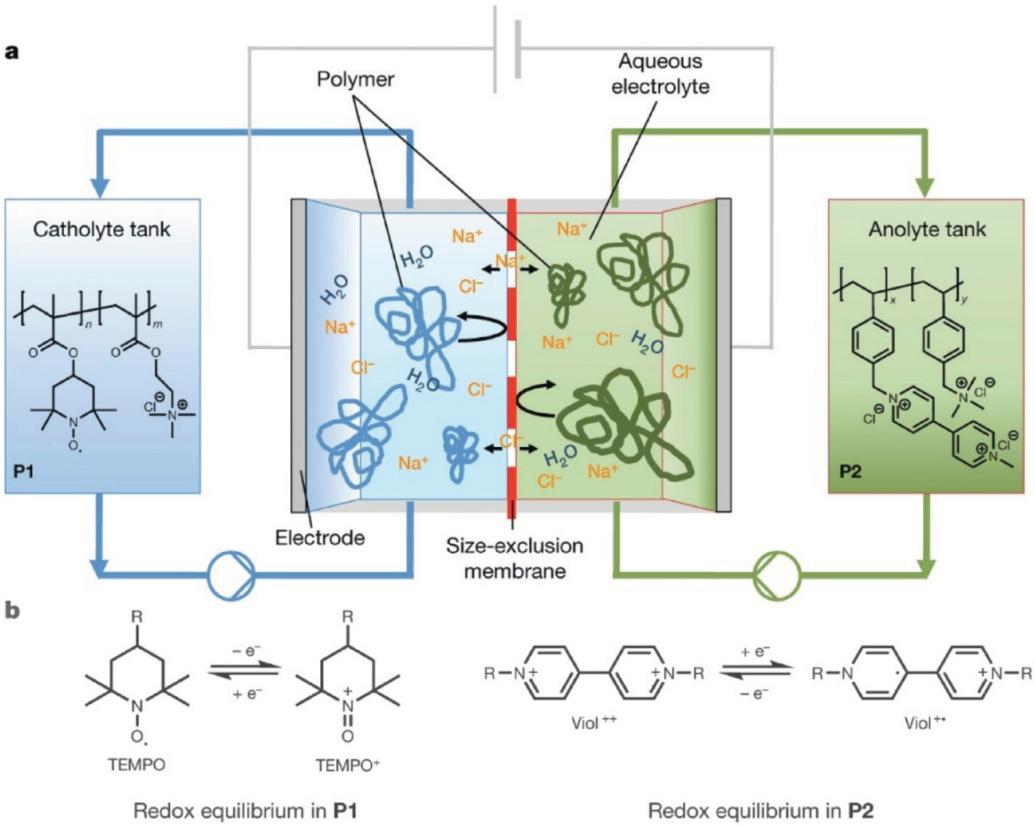

Figure 7.48. -. a) Schematic representation of a polymer-based RFB consisting of an electrochemical cell and two electrolyte reservoirs. The anolyte and catholyte cycle are separated by a semi-permeable size-exclusion membrane, which retains the redox-active macromolecules while allowing small salt ions to pass. b) Fundamental electrode reactions of P1 (TEMPO radical) and P2 (viologen).[275]

8 Conclusions

1. A reference electrode based on silver/silver sulfate to be inserted in filter press cells of VRFB has been proposed. This easy-to-make reference electrode provides valuable information for "in-operando" conditions. For ammoxidized graphite felts, the hydrogen evolution at the negative electrode during the charge decreases the coulombic efficiency whereas the slower kinetics of the positive electrode contributes more to the decrease in voltage efficiency. The use of this easy-to-make reference electrode also opens new perspectives for the experimental routes allowing a fast, reliable and feasible way for proceeding in the study, analysis and control of VRFBs.

2. In order to overcome the drawbacks of VFRB related to thermal stability at 60ºC, several charge and discharge experiments at 20 $mAcm^{-2}$ were carried out to demonstrate the outstanding performance of the dPEI-containing positive electrolyte. Stable performance with an energy efficiency of 88% was observed during a course of 40 cycles. This is probably due to the stabilization of the V (V) ions carried out by the dPEI- containing electrolyte. The energy density at 60 º C was 19.5 W h L^{-1}. Note this value is higher than that obtained at 25º C (ca.18 WhL^{-1}). This is probably due to the water evaporation in each compartment leading to an increment of proton concentration. Therefore, a cost-effective formulation of dPEI-based positive electrolyte for VFRB was successfully demonstrated in term of the thermal stability and energy density. The highly improved energy capacity (ca. 18 WhL^{-1}) and the excellent electrochemical performance (ca. 85 % of energy efficiency) over 60ºC of operation temperature could boost the marketability of VRFB technology.

3. Along the experimental work done within the group, it has been accomplished much in terms of electrode modifications, obtaining the following conclusion points that summarize them:

   a) Titanium dioxide especially in its rutile (110) phase acts as a powerful electrocatalyst towards the VRFBs negative half-cell reaction. Increasing the active groups on the electrode surface and decreasing the side reactions taking place (HER). However, when the TiO_2 thickness increases above certain limit the semiconductor properties enlarge the charge transfer resistance towards the vanadium negative redox reaction due to an ohmic drop. In spite that fact, kinetically the reaction towards V^{3+}/V^{2+} is faster when the graphite felt is completely covered by the nanorods (GF-TiO_2(MNRs)). In order to improve the electrodes performance, it would be relevant to improve the conductivity when the fibers are completely covered by titanium dioxide nanorods in its rutile phase.

b) TiO_2:H based graphite felt electrode, as a low-cost, efficient and novel electrocatalyst towards the negative reaction was demonstrated to enhance the electrochemical performance in all-vanadium redox flow battery, especially at high charge/discharge rates. GF@TiO_2:H electrodes showed greatly improved electrochemical properties (i.e. fast electron charge process) in combination with a better selectivity to V^{3+}/V^{2+} reaction, inhibiting hydrogen-evolution reaction. Furthermore, the electronic donor properties were increased, comparatively with pristine and thermal treated, as a consequence of the oxygen-vacancies formation in the structure of titanium dioxide. A specific discharge capacity of around 11 Ah/L with a 66.1% of energy efficiency was observed after 100 cycles of charge/discharge at high current densities rates up to 150mA/cm^2. In addition, significantly improved the electrolyte-utilization ratio to 87% was achieved using 1 M in vanadium solution. Afterwards, the performance of 2 M vanadium ion concentrations has been evaluated at high current density as well, (300 mA/cm^2) during 140-cycles, showing the great durability of the battery especially when reached 200 mA/cm^2. The CE value was > 96%; electrolyte-utilization ratio was 80%, with a specific capacity of 22 Ah/L, demonstrating the total suppression of HER and long term stability of VRFB. These results suggest that the TiO_2:H based graphite felt is a powerful electrocatalyst for high-performance VRFB application.

c) The partially reduced sample (TiO_2:N) favours the V^{3+}/V^{2+} due to a reduction of the charge transfer resistance as an increasing active sites are present on the surface, and therefore, more vanadium ions are capable of react simultaneously. TiN is formed over the TiO_2 decorating the carbon felt, consequently two conditions favour the V^{3+} reduction: i) The increase of O and N groups due to the presence of the catalyst formed (TiN-TiO_2) itself that promote the number of active sites for the reaction to happen, enhancing the electron charge transfer at the interface electrode/vanadium. ii) The increase of O and N groups due to the presence of them over the carbon felt structure. All these qualities have allowed us to achieve a high-power output of the cell up to 700 mW/cm^2), as well as work at high current density (150 mA/cm^2) with low ohmic losses and high redox reversibility. It allows our system to be able to obtain great energy efficiency (71%). We firmly believe this is a highly promising material in order to obtain a VRFB capable of give a strong energy momentum, from which this types of battery possess an undeniable lack. It could be a future perspective focus on the implementation of this enhanced electrode in a cell where other components of the battery has been improved, as the membrane and/or the electrolyte, and therefore obtain not yet reported values capable of compete with lithium technology.

d) Hydrogen treated TiO_2-based couple with defective Ceria-based graphite felt electrodes for negative and positive cell are an excellent option as low-cost, efficient and novel electrocatalysts that enhance the electrochemical performance in vanadium redox flow battery, especially at high charge/discharge rates. GF@TiO_2:H electrodes showed greatly improved electrochemical properties (i.e. low charge transfer resistance) in combination with the inhibition of hydrogen-evolution reaction. GF@CeO_2 exhibits an improved kinetic over the positive reaction, as well as, delay the oxygen evolution due to its standard potential. Moreover, the electronic donor properties were enhanced as a consequence of the oxygen-vacancies generation in the GF@TiO_2:H and GF@CeO_2 electrodes, in case we compare to heat treated and thermally annealed in argon atmosphere. A specific discharge capacity around 10 AhL^{-1} with a 50% of energy efficiency was observed after more than 100 cycles of charge/discharge at high current densities rates up to 200$mAcm^{-2}$. The battery was capable of several docents more of cycles at high current (150 mA/cm^2) before reaching the capacity fading. In addition, it has been significantly improved the electrolyte-utilization ratio to 80% using 1.5 M in vanadium solution at 150 mA/cm^2. Additionally, at 200 mA cm^{-2}, the CE value was > 97%, electrolyte-utilization ratio was 60%, with a specific capacity of 12.3 AhL^{-1}, demonstrating the highly suppression of HER, OER, ion species cross-over and long term stability of VRFB. These results are presented in the literature for the first time, suggesting that the combination of these two electrodes can be powerful electrocatalysts for high-performance VRFB application.

4. Furthermore, there are several accomplishment that summarize the goals obtained for aqueous organic redox flow batteries:

a) The treatments done on the cathode electrodes for metal-free redox flow batteries has the objective to increase the surface area by electrode functionalization with nitrogen and oxygen groups, especially active are the oxygenated-N and C=O groups. These are more abundant on the GF-HT surface. Therefore the electrodes become more electrochemically active, as CV showed by an increase in the reversibility and diffusion towards the Tiron redox reaction on CF-HT comparatively to the other two electrodes (CF-HT and CF-rGO/Q). In spite the fact that the kinetic values for all the electrodes are similar, which shows that these N and O groups do not act as a catalyst, the charge transfer resistance is reduced due to that functionalization. This facilitates the migration of the Tiron (1,2-BQDS) redox species towards the interface electrode-electrolyte. Moreover, the GF-HT electrode is stable at least for 1000 cycles, which

evidences the good performance and low degradation (HER and OER) of it.

b) The treatments done on the anode electrodes towards the Anthraquinone-2,7-disulfonic acid disodium salt has the objective of increase the electrochemically active surface area by the formation of nitrogen, mainly as graphitic-N as well as pyrrolic-N, and oxygen groups, especially C-O and O-C=O groups. Therefore the electrodes become more active towards the previously mentioned 2,7-AQDS redox reaction. It is confirmed as CV showed by an increase in the reversibility and electrode-electrolyte mass transfer for the CF-rGO/Q electrode comparatively to CF-HT and CF-rGO/ROH. Moreover, when fitting PEIS done at 0.15V vs. NHE which is the potential Anthraquinone-2,7-disulfonic acid disodium keto/enol reaction takes place, CF-rGO/Q performance reduces its charge transfer resistance (R_{ct}). In case considered charge-discharge plots at high current in a three electrode set-up, the overall charge and discharge capacity, as well as the voltage efficiency (72%) is larger for CF-rGO/Q due to a lower polarization of the electrode caused by all the modifications previously mentioned. Additionally, the electrode cycling is stable at least for 1000 cycles with a large Coulombic efficiency (98%), which evidences the good performance, low electrolyte degradation (HER and OER) and limited cross-over.

c) When couple the negative and positive active molecules previously mentioned, commonly benzoquinones in the positive cell and anthraquinones in the negative compartment, into a single-cell device in order to study their overall properties and behavior. Three different approaches have been done to obtain the best possible combination. Considering just electrochemical factors related to the different active molecules solved in the positive electrolyte. The best values are obtained for the p-benzoquinone molecule. Always working with sodium 9,10-anthraquinone-2,7-disulfonate as negative active electrolyte molecule as the one showing better electrochemical output. Although all this facts are true, it happens to p-benzoquinone to self-oxidize when solved in the acidic electrolyte. For that reasons the single cell studies using the modified electrodes have 1,2-BQDS as cathodic active material and continuing with 2,7-AQDS as anode material.

d) After implementing these electrodes, CF-HT (+) and CF-rGO/Q (-), the battery is capable to achieve an outstanding performance, in 0.05 M active material concentration, obtaining 98% CE, 76% VE and 74% EE for 10 mA/cm^2 of current density applied. These efficiency values are reduced when increased to 0.3 M of active material, getting 96% CE, 58% VE and 56% EE for 10 mA/cm^2 of current density applied. However,

the capacity retention is increased from 77% to 80%. In any case, when the modified electrodes are introduced not only the overall efficiency is enhanced, from 63.4% EE for CF-P p-benzoquinone (+) vs. 2,7-AQDS to 74% EE for CF-HT in 1,2-BQDS (+) vs. CF-rGO/Q in 2,7-AQDS, but the capacity reached raised from 45 mAh to 60 mAh and not only for one cycle but for few of them. It should be always consider aqueous organic redox flow batteries as a new redox systems with less than 5 years of development comparatively to a well-developed technology, as VRFBs, which origins are place in 1980s more than 30 years ago. In this matter there is still room to improve this technology, which has a limitless potential to exploit yet.

9 Appendix

9.1 Kinetics of redox reactions

9.1.1 One step, one-electron process

Considering the simplest possible electrode process, wherein species O and R engage in one-electron transfer at the interface without being involved in any other chemical step,

$$\mathrm{O} + \mathrm{e}^- \overset{k_f}{\rightarrow} \mathrm{R} \qquad \textbf{(9.1)}$$

$$\mathrm{R} \overset{k_b}{\rightarrow} \mathrm{O} + \mathrm{e}^- \qquad \textbf{(9.2)}$$

Suppose also that the standard free energy profiles along the reaction coordinate have the parabolic shapes shown in **Figure 9.1.** The left frame of that figure depicts the full path from reactants to products, while the right is an enlargement of the region near the transition state. It is not important for this discussion that we know the shapes of these profiles in detail[222].

In developing a theory of electrode kinetics, it is convenient to express potential against a point of significance to the chemistry of the system, rather than against an arbitrary external reference, such as SCE. There are two natural reference points, *viz.* the equilibrium potential of the system and the standard (or formal) potential of the couple under consideration. It was actually used the equilibrium potential as a reference point in the discussion of the preceding section, and we will use it again in this section. However, it is possible to do so only when both members of the couple are present, so that the equilibrium is defined. The more general reference point is $E^{0'}$. Suppose the upper curve on the O + e^- side of **Figure 9.1** applies when the electrode potential is equal to $E^{0'}$. The cathodic and anodic activation energies are then $\Delta G^{\ddagger}_{0c}$ and $\Delta G^{\ddagger}_{0a}$ respectively.

If the potential is changed by ΔE to a new value, E, the relative energy of the electron resident on the electrode changes by $-F\Delta E = -F(E-E^{0'})$; hence the O+$e^-$ curve moves up or down by that amount. The lower curve on the left side of **Figure 9.1** shows this effect for a positive ΔE. It is readily apparent that the barrier for oxidation, $\Delta G^{\ddagger}_{a}$, has become less than $\Delta G^{\ddagger}_{0a}$ by a fraction of the total energy change.

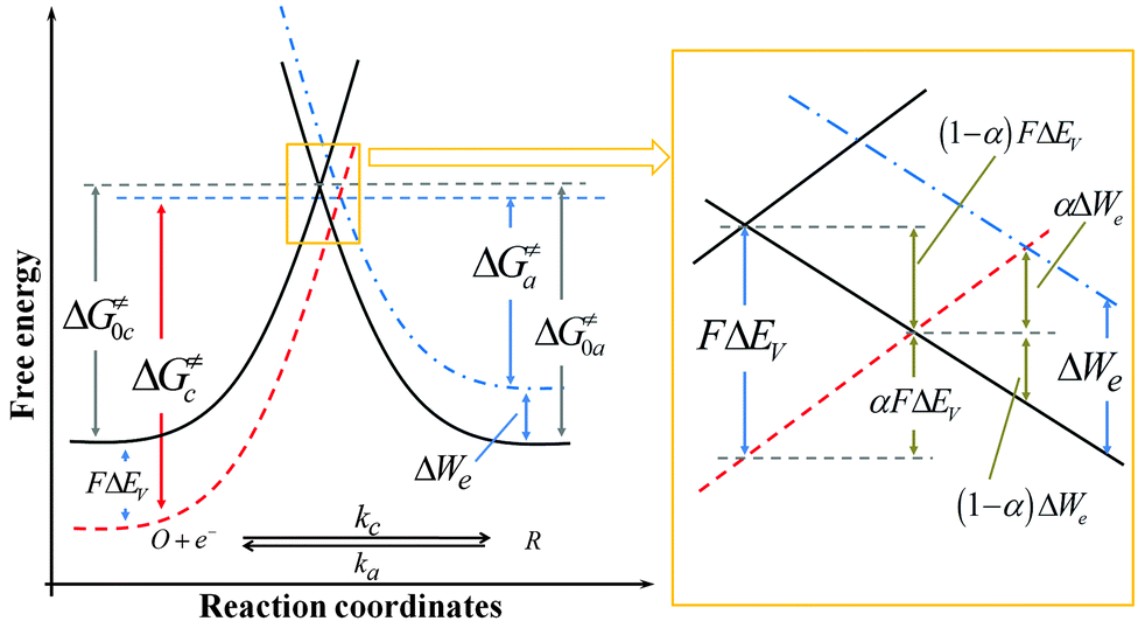

Figure 9.1 – Effects of a potential change on the standard free energies of activation for oxidation and reduction. The right frame is a magnified picture of the boxed area.

Let us call that fraction 1-α, where α is the *transfer coefficient*, can range from zero to unity, depending on the shape of the intersection region. Thus,

$$\mathbf{\Delta G_a^{\ddagger} = \Delta G_{0a}^{\ddagger} - (1-\alpha)F(E - E^{0\prime})} \qquad \textbf{(9.3)}$$

A brief study of the figure also reveals that at potential E the cathodic barrier, $\Delta G^{\ddagger}_{c}$, is higher than $\Delta G^{\ddagger}_{0c}$ by $\alpha F(E\text{-}E^{0\prime})$; therefore,

$$\mathbf{\Delta G_c^{\ddagger} = \Delta G_{0c}^{\ddagger} + \alpha F(E - E^{0\prime})} \qquad \textbf{(9.4)}$$

Now let us assume that the rate constants k_f and k_b have an Arrhenius form that can be expressed as

$$\mathbf{k_f = A_f \exp(-\frac{\Delta G_c^{\ddagger}}{RT})} \qquad \textbf{(9.5)}$$

$$\mathbf{k_b = A_b \exp(-\frac{\Delta G_a^{\ddagger}}{RT})} \qquad \textbf{(9.6)}$$

Inserting the activation energies, **(9.3)** and **(9.4)**, gives

$$\mathbf{k_f = A_f \exp(-\frac{\Delta G_{0c}^{\ddagger}}{RT}) \exp[-\alpha f(E - E^{0\prime})]} \qquad \textbf{(9.7)}$$

$$\mathbf{k_b = A_b\,exp(-\frac{\Delta G^{\ddagger}_{0a}}{RT})exp[(1-\alpha)f(E-E^{0\prime})]} \qquad \textbf{(9.8)}$$

Where $f=F/RT$. The first two factors in each of these expressions form a product that is independent of potential and equal to the rate constant at $E=E^{0'}$.

Now consider the special case in which the interface is at equilibrium with a solution in which $C^*_O = C^*_R$. In this situation, $E=E^{0'}$ and $k_f C^*_O = k_b C^*_R$, so that $k_f = k_b$. Thus, $E^{0'}$, is the potential where the forward and reverse rate constants have the same value. That value is called the *standard rate constant*, $k^{0.5}$. The rate constants at other potentials can then be expressed simply in terms of k^0:

$$\mathbf{k_f = k^0 exp[-\alpha f(E-E^{0\prime})]} \qquad \textbf{(9.9)}$$

$$\mathbf{k_b = k^0 exp[(1-\alpha)f(E-E^{0\prime})]} \qquad \textbf{(9.10)}$$

Insertion of these relations into

$$\mathbf{i = i_c - i_a = nFA[k_f C_O(0,t) - k_b C_R(0,t)]} \qquad \textbf{(9.11)}$$

Yields the complete *current-potential characteristics*:

$$\mathbf{i = FAk^0\left[C_O(0,t)e^{-\alpha f(E-E^{0\prime})} - C_R(0,t)e^{(1-\alpha)f(E-E^{0\prime})}\right]} \qquad \textbf{(9.12)}$$

This relation is very important. It, or a variation derived from it, is used in the treatment of almost every problem requiring an account of heterogeneous kinetics. There results and the inferences derived from them are known broadly as the *Butler-Volmer* formulation of electrode kinetics, in honor of the pioneers in this area[276,277].

One can derive the Butler-Volmer kinetic expressions by an alternative method based on electrochemical potentials[278–283]. Such an approach can be more convenient for more complicated cases, such as requiring the inclusion of double-layer effects or sequences of reactions in a mechanism.

9.1.2 Implications of Butler-Volmer model for the one-step, one-electron process

In this section, it will be developed a number of operational relationships that will prove valuable in the interpretation of electrochemical experiments. Each is derived under the assumption that the electrode reaction is the one-step, one-electron process for which the primary relations were derived above. The validity of the conclusions for a multistep process will be considered separately.

9.1.2.1 Equilibrium conditions. The exchange current

At equilibrium, the net current is zero, and the electrode is known to adopt a potential based on the bulk concentration of O and R as dictated by the Nernst equation. Let us see now if kinetic model yields that thermodynamic relation as a special case. From equation **(9.12)** we have, at zero current,

$$\mathbf{FAk^0C_O(0,t)e^{-\alpha f\left(E_{eq}-E^{0\prime}\right)} = FAk^0C_R(0,t)e^{(1-\alpha)f(E_{eq}-E^{0\prime})}} \qquad \mathbf{(9.13)}$$

Since equilibrium applies, the bulk concentrations of O and R are found also at the surface; hence

$$\mathbf{e^{f(E_{eq}-E^{0\prime})} = \frac{C_O^*}{C_R^*}} \qquad \mathbf{(9.14)}$$

which is simply an exponential form of the Nernst relation:

$$\mathbf{E_{eq} = E^{0\prime} + \frac{RT}{F}\ln\frac{C_O^*}{C_R^*}} \qquad \mathbf{(9.15)}$$

Thus, the theory has passed its first test of compatibility with reality.

Even though the net current is zero at equilibrium, we still envision balanced faradic activity that can be expressed in terms of the *exchange current*, i0, which is equal in magnitude to either component current, i_c or i_a. That is,

$$\boldsymbol{i_0 = FAk^0C_o^*e^{-\propto f(E_{eq}-E^{0\prime})}} \qquad \mathbf{(9.16)}$$

If both sides of **(9.14)** are raised to the –α power, we obtain

$$\mathbf{e^{-\alpha f(E_{eq}-E^{0\prime})}} = \left(\frac{\mathbf{C_O^*}}{\mathbf{C_R^*}}\right)^{-\alpha} \qquad \textbf{(9.17)}$$

Substitution of **(9.17)** into **(9.16)** gives

$$\boldsymbol{i_0 = FAk^0 C_O^{*(1-\propto)} C_R^{*\propto}} \qquad \textbf{(9.18)}$$

The exchange current is therefore proportional to k^0 and can often be substituted for k^0 in kinetic equation. For the particular case where $C^*_O = C^*_R = C$,

$$\boldsymbol{i_0 = FAk^0 C} \qquad \textbf{(9.19)}$$

Often the exchange current is normalized to unit are to provide the *exchange current density*, $j_0 = i_0/A$.

9.1.2.2 The current-overpotential equation

An advantage of working with i_0 rather than k^0 is that the current can be described in terms of the deviation from the equilibrium potential, that is, the overpotential, η, rather than the formal potential, $E^{0'}$. Dividing **(9.12)** by **(9.18)**, we obtain

$$\frac{\mathbf{i}}{\mathbf{i_0}} = \frac{\mathbf{C_O(0,t)e^{-\alpha f\left(E-E^{0\prime}\right)}}}{\mathbf{C_O^{*(1-\alpha)} C_R^{*\alpha}}} - \frac{\mathbf{C_R(0,t)e^{(1-\alpha)f(E-E^{0\prime})}}}{\mathbf{C_O^{*(1-\alpha)} C_R^{*\alpha}}} \qquad \textbf{(9.20)}$$

or

$$\frac{\mathbf{i}}{\mathbf{i_0}} = \frac{\mathbf{C_O(0,t)}}{\mathbf{C_O^*}} \mathbf{e^{-\alpha f\left(E-E^{0\prime}\right)}} \left(\frac{\mathbf{C_O^*}}{\mathbf{C_R^*}}\right)^{\alpha} - \frac{\mathbf{C_R(0,t)}}{\mathbf{C_R^*}} \mathbf{e^{(1-\alpha)f(E-E^{0\prime})}} \left(\frac{\mathbf{C_O^*}}{\mathbf{C_R^*}}\right)^{-(1-\alpha)} \qquad \textbf{(9.21)}$$

The ratios $(C^*_O/\ C^*_R)^{\alpha}$ and $(C^*_O/\ C^*_R)^{1-\alpha}$ are easily evaluated from equations **(9.14)** and **(9.17)**, and by substitution we obtain

$$\mathbf{i = i_0}\left[\frac{\mathbf{C_O(0,t)}}{\mathbf{C_O^*}} \mathbf{e^{-\alpha f \eta}} - \frac{\mathbf{C_R(0,t)}}{\mathbf{C_R^*}} \mathbf{e^{(1-\alpha)f\eta)}}\right] \qquad \textbf{(9.22)}$$

where $\eta = E - E_{eq}$. This equation is known as the *current-overpotential equation*. Note that the first term describes the cathodic component current at any potential, and the second gives the anodic contribution.

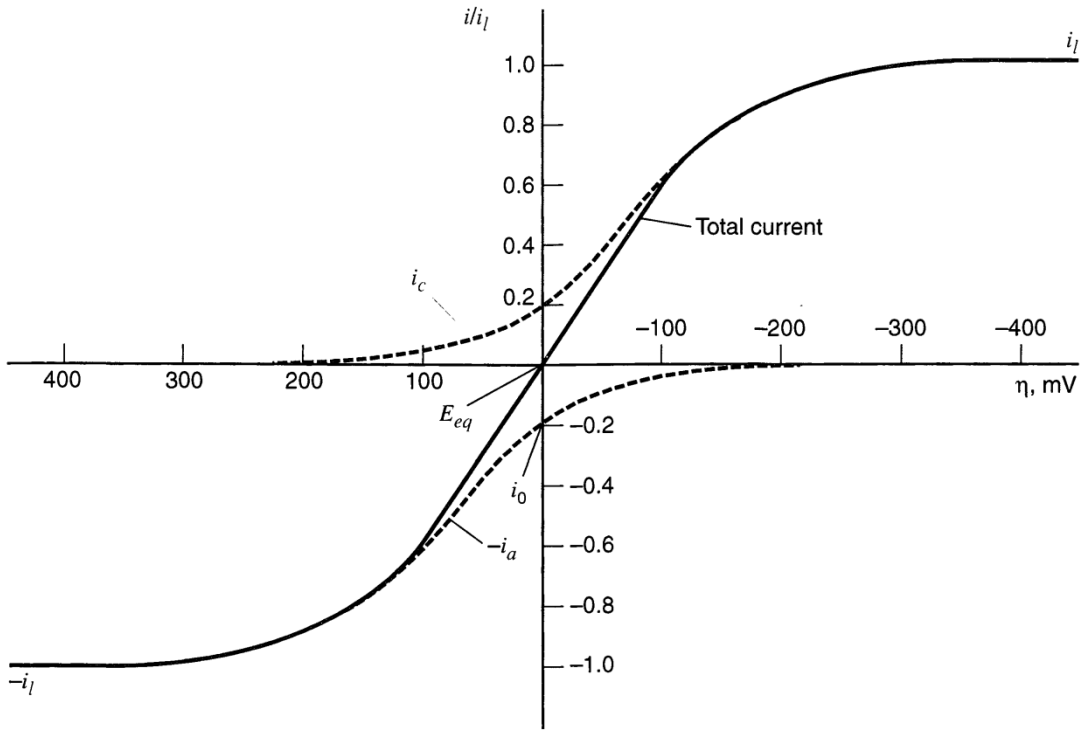

Figure 9.2 – Current-overpotential curves for the system $O+e^-=R$ with α=0.5, T=298 K, $i_{l,c}=-i_{l,a}=i_l$ and i_0/i_l =0.2. The dashed lines show the component currents i_c and i_a.

The behavior predicted by **(9.22)** is depicted in **Figure 9.2**. The solid curve shows the actual total current, which is the sum of the components i_c and i_a, shown as dashed traces. For large negative over-potentials, the anodic component is negligible; hence the total current curve merges with that for i_c. At large positive over-potentials, the cathodic component is negligible, and the total current is essentially the same as i_a. In going either direction from E_{eq}, the magnitude of the current rises rapidly, because the exponential factors dominate behavior, but extreme η, the current levels off. In these level regions, the current is limited by mass transfer rather than heterogeneous kinetics. The exponential factors in **(9.22)** are then moderated by the factors $C_O(0,t)/C^*_O$ and $C_R(0,t)/C^*_R$, which manifest the reactant supply.

9.1.2.3 Approximate Form of the i-η Equation

9.1.2.3.1 Tafel plots

A plot of log i vs. η, known as a Tafel plot, is a useful device for evaluating kinetic parameters. In general, there is an anodic branch with slope (1-α)F/2.3RT and a cathodic branch with slope −αF/2.3RT. As shown in **Figure 9.3**, both linear segments extrapolate to an intercept of log i_0. The plots deviate sharply from linear behavior as η approaches zero, because the back reactions can no longer be

regarded as negligible. The transfer coefficient, α, and the exchange current, i_0, are obviously readily accessible from this kind of presentation, when it can be applied.

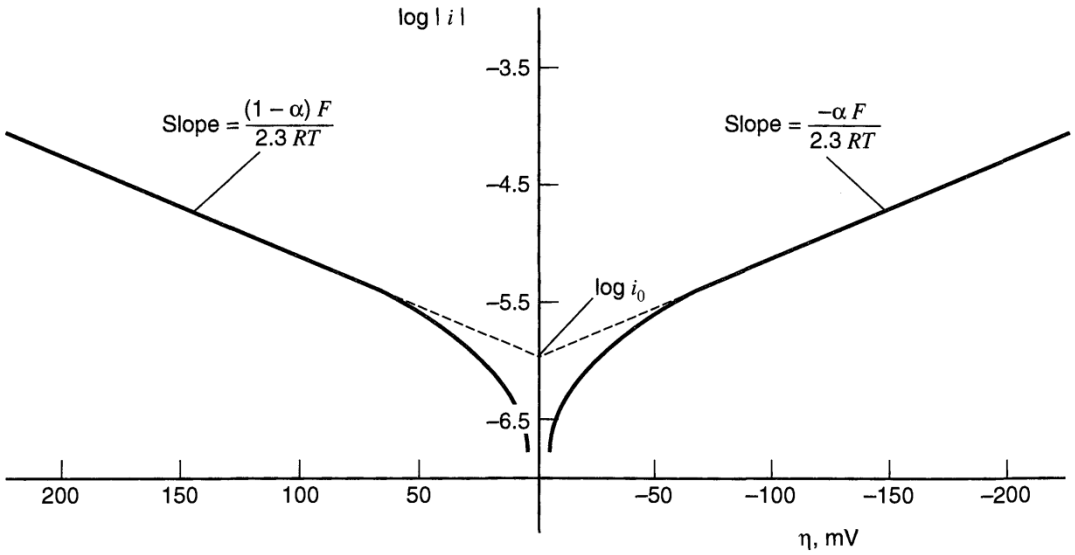

Figure 9.3 – Tafel plots for anodic and cathodic branches of the current-overpotential curve for O + e = R with α = 0.5, T = 298K, and $j_0 = 10^{-6}$ A/cm^2.

Some real Tafel plots are shown in **Figure 9.4** for the Mn(IV)/Mn(III) system in concentrated acid. The negative deviations from linearity at very large overpotentials come from limitations imposed by mass transfer. The region of very low overpotentials shows sharp falloffs for the reasons outlined just above.

Allen and Hickling suggested an alternative method allowing the use of data obtained at low overpotentials. Butler-Volmer equation

$$\boldsymbol{i = i_0\left[e^{-\alpha f n} - e^{(1-\alpha) f n}\right]} \qquad \textbf{(9.23)}$$

can be rewritten as

$$\boldsymbol{i = i_0 e^{-\alpha f n}(1 - e^{f n})} \qquad \textbf{(9.24)}$$

or

$$\boldsymbol{log \frac{i}{1 - e^{f n}} = log\ i_0 - \frac{\alpha F \eta}{2.3 RT}} \qquad \textbf{(9.25)}$$

so a plot of log [i/(1-e^{fn})] vs. η yields an intercept of log i_0 and a slope of –αF/2.3RT. This approach has the advantage of being applicable to electrode reactions that are not totally irreversible, that is, those in which both anodic and cathodic processes contribute significantly to the currents measured in the overpotential range where mass-transfer effects are not important. Such systems are often quasi-reversible, because the opposing charge-transfer reactions must

both be considered; yet noticeable activation overpotential is required to drive a given net current through the interface.

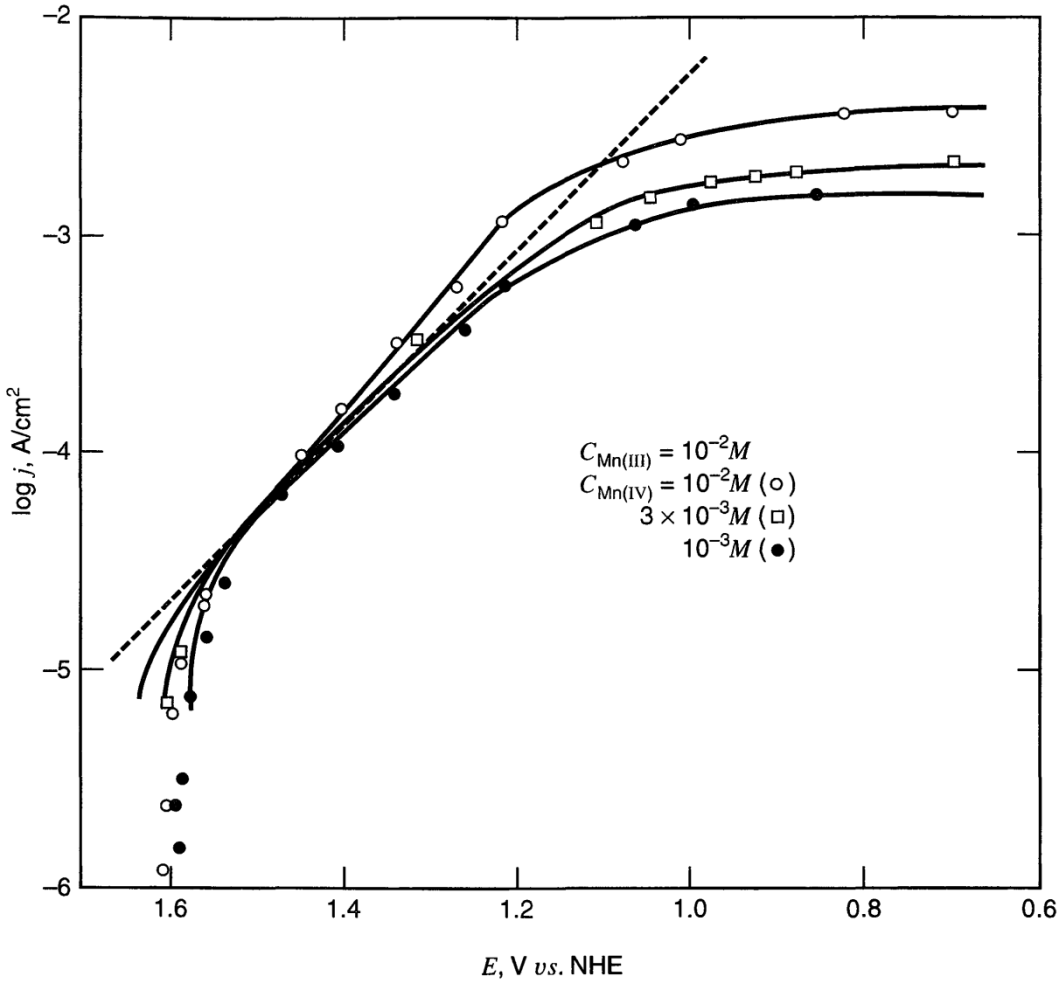

Figure 9.4 – Tafel plots for anodic and cathodic branches of the current-overpotential curve for O + e = R with α = 0.5, T = 298K, and $j_0 = 10^{-6}$ A/cm^2.

9.1.2.4 Effects of Mass Transfer

A more complete *i*-η relation can be obtained from **(9.22)** by substituting for $C_O(0,t)/C^*_O$ and $C_R(0,t)/C^*_R$ according to $C_R(x=0)/C^*_R=1-(i/i_{l,c})$:

$$\frac{\mathbf{i}}{\mathbf{i_0}} = \left(\mathbf{1} - \frac{\mathbf{i}}{\mathbf{i_{l,c}}}\right)\mathbf{e}^{-\alpha \mathbf{f}\eta} - \left(\mathbf{1} - \frac{\mathbf{i}}{\mathbf{i_{l,a}}}\right)\mathbf{e}^{(1-\alpha)\mathbf{f}\eta} \qquad \textbf{(9.26)}$$

This equation can be rearranged easily to give *i* as an explicit function of η over the whole range of η. In **Figure 9.5**, one can see *i*- η curves for several ratios of i_0/i_l,

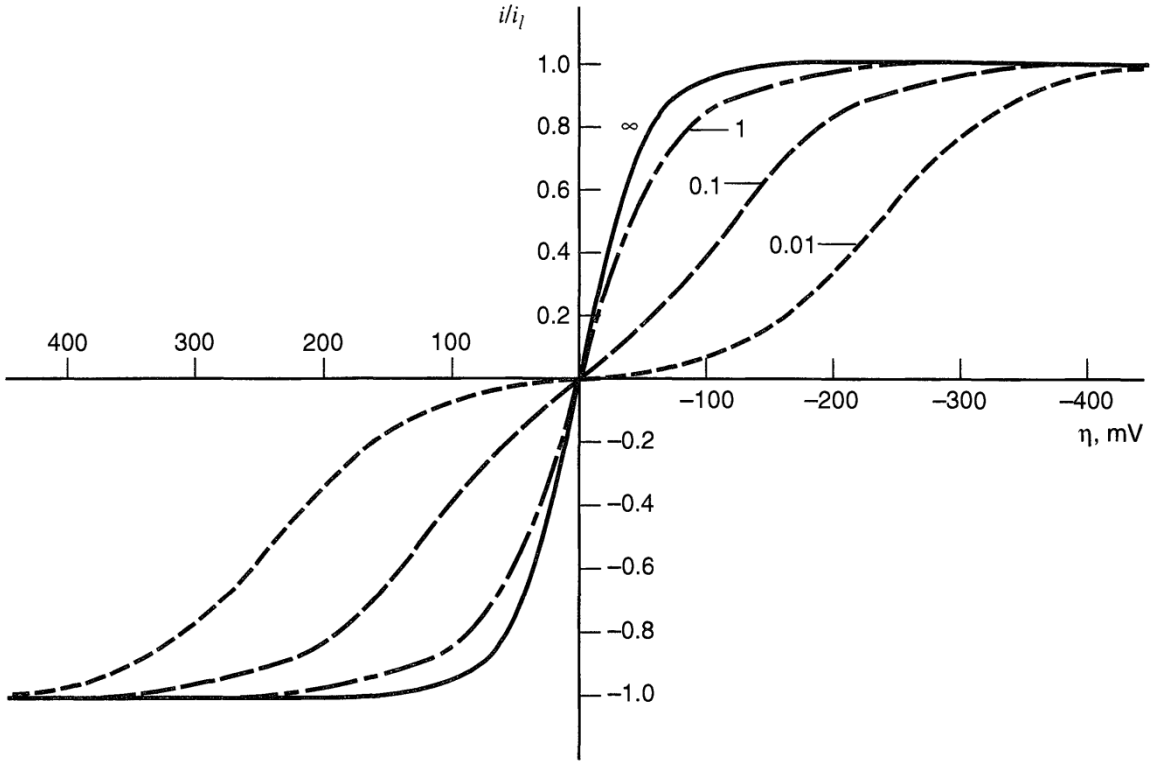

Figure 9.5 – Relationship between the activation overpotential and net current demand relative to the exchange current. The reaction is $O+e^-=R$ with $\alpha=0.5$, T=298 K, $i_{l,c}=-i_{l,a}=i_l$. Numbers by curves show i_0/i_l.

where $i_l=i_{l,c}=-i_{l,a}$.

For small over-potentials, a linearized relation can be used. The complete Taylor expansion gives, for $af\eta<<1$,

$$\frac{\mathbf{i}}{\mathbf{i_0}} = \frac{\mathbf{C_O(0,t)}}{\mathbf{C_O^*}} - \frac{\mathbf{C_R(0,t)}}{\mathbf{C_R^*}} - \frac{\mathbf{F\eta}}{\mathbf{RT}} \qquad \textbf{(9.27)}$$

which can be substituted as above and rearranged to give

$$\boldsymbol{\eta} = \mathbf{i}\frac{\mathbf{RT}}{\mathbf{F}}\left(\frac{\mathbf{1}}{\mathbf{i_0}} + \frac{\mathbf{1}}{\mathbf{i_{l,c}}} - \frac{\mathbf{1}}{\mathbf{i_{l,a}}}\right) \qquad \textbf{(9.28)}$$

In terms of the charge- and mass-transfer pseudo resistances is

Here we see very clearly that when i_0 is much greater than the limiting currents,

$$\eta = -i\left(R_{ct} + R_{mt,c} + R_{mt,a}\right) \quad \textbf{(9.29)}$$

$R_{ct} << R_{mt,c} + R_{mt,a}$ and the overpotential, even near E_{eq}, is a concentration overpotential. On the other hand, if i_0 is much less than the limiting currents, then $R_{mt,c} + R_{mt,a} << R_{ct}$, and the overpotential near E_{eq} is due to activation of charge transfer.

In Tafel regions, other useful forms of **(9.26)** can be obtained. For the cathodic branch at high η values, the anodic contribution is insignificant, and **(9.26)** becomes

$$\frac{i}{i_0} = \left(1 - \frac{i}{i_{l,c}}\right) e^{-\alpha f \eta} \quad \textbf{(9.30)}$$

or

$$\eta = \frac{RT}{\alpha F} \ln \frac{1}{i_{l,c}} + \frac{RT}{\alpha F} \ln \frac{\left(i_{l,c} - i\right)}{i} \quad \textbf{(9.31)}$$

This equation can be useful for obtaining kinetic parameters for systems in which the normal Tafel plots are complicated by mass-transfer effects.

One can estimate the rough order of magnitude that the kinetic rate must be for a practical RFB. For example, using some of the metrics that suggest RFB must have high electrical efficiency, at least 80% round-trip, or 90% in each direction, and assuming a typical cell voltage of 1.5 V, then the kinetic overpotential must be less than 150 mV throughout the charge/discharge cycle. Assuming a minimum practical current density of at least 50 mA/cm^2, a roughness factor of 10, i.e. 10 cm^2 surface per unit of electrode geometric area and a transfer coefficient of 0.5, the exchange current density must be greater than 0.3 mA/cm^2 (real) throughout the charge/discharge cycle. Assuming 1 M solutions at 50% state of charge, and 90% utilization of the redox ions in the cycle, the minimum value of standard rate constant k^0 is ca. 10^{-5} cm/s. If the rate constant is significantly less than this value, some compromises must be made to achieve a practical device which may increase cost and/or utility. For example, higher surface area/porosity electrodes will compromise a simple flow-by/through design. Reduced current density will lower the power density and result in larger electrodes and more material per unit volume in the RFB. The estimated value above can be compared to those in literature as shown in **Table 9.1** .

The results in **Table 9.1** show that all of the redox couples recently or currently in used in practical RFBs, only VO^{2+}/VO_2^+ couple has a clear kinetic limitation and, in fact, is clearly problematic. This is not surprising since this redox is not a simple one-electron transfer reaction, but is in modern terminology an oxygen transfer

reaction as shown in Eq. **(9.2)**. As discussed in detail by Gattrell et al.[284], this reaction is a multi-step reaction in which oxygen transfer (a chemical step) may precede or follow an electron-transfer step, denoted in modern terminology as a CE or EC mechanism. Such reactions usually have current-potential relations which differ significantly from the ideal Butler-Volmer form, and that is the case here.

Table 9.1 – Kinetics parameters for redox reactions used in flow batteries.

Redox couple	α	K^0 / cm s^{-1}	Electrode	Reference
Fe^{3+}/Fe^{2+}	0.59	2.2 x 10^{-5}	Au(poly)	285
	0.55	1.2 x 10^{-5}	Au(111)	286
Cr^{3+}/Cr^{2+}	~0.5	2 x 10^{-4}	Hg	287
VO_2^+/VO^{2+}	0.42	3.0 x 10^{-7}	Graphite	284
	0.3	1-3 x 10^{-6}	Carbon	59
V^{3+}/V^{2+}	~0.5	4 x 10^{-3}	Hg	287
Ce^{4+}/Ce^{3+}	~0.5	1.6 x 10^{-3}	Pt	288
Br_2/Br^-	0.35	1.7 x 10^{-2}	Pt(poly)	289
	0.46	5.8 x 10^{-4}	Vitreous C	290

9.1.3 Multistep mechanisms

The foregoing sections have concentrated on the potential dependences of the forward and reverse rate constants governing the simple one-step, one-electron electrode reaction. By restricting our view in this way, we have achieved a qualitative and quantitative understanding of the major features of electrode kinetics.

But we must now recognize that most electrode processes are mechanisms of several steps. For example, the important reaction (2.7) clearly must involve several elementary reactions. The hydrogen nuclei are separated in the oxidized form, but are combined by reduction. Somehow, during reduction, there must be a pair of charge transfers and some chemical means for linking the two nuclei. Consider also the reduction

$$\mathbf{Sn^{4+} + 2e^- \leftrightarrow Sn^{2+}, E^0 = 0.151\ V\ vs.\ NHE} \qquad \textbf{(9.32)}$$

Is it realistic to regard two electrons as tunneling simultaneously through the interface? Or must we consider the reduction and oxidation sequences as two one-electron processes proceeding through the ephemeral intermediate Sn^{3+}. Another

case that looks simple at first glance is the deposition of silver from aqueous potassium nitrate:

$$\mathbf{Ag^+ + e^- \leftrightarrow Ag, E^0 = 0.8\ V\ vs.\ NHE} \qquad \textbf{(9.33)}$$

However, there is evidence that this reduction involves at least a charge-transfer step, creating an adsorbed silver atom, and a crystallization step, in which the atom migrates across the surface until it finds a vacant lattice site. Electrode processes may also involve adsorption and desorption kinetics of primary reactants, intermediates, and products.

Thus, electrode reactions generally can be expected to show complex behavior, and for each mechanistic sequence, one would obtain a distinct theoretical linkage between current and potential. That relation would have to take into account the potential dependences of all steps and the surface concentrations of all intermediates, in addition to the concentrations of the primary reactants and products.

A great deal of effort has been spent in studying the mechanism of complex electrode reactions. One general approach is based on steady-state current-potential curves. Theoretical responses are derived on the basis of mechanistic alternatives, then one compares predicted behavior, such as the variation of exchange current with reactant concentration, with the behavior found experimentally. A number of excellent expositions of this approach are available in the literature[278–280,291–295]. More commonly, complex behavior is elucidated by studies of transient responses, such as cyclic voltammetry at different scan rates.

9.1.3.1 Rate-determining electron transfer

In the study of chemical kinetics, one can often simplify the prediction and analysis of behavior by recognizing that a single step of a mechanism is much more sluggish than all the others, so that it controls the rate of the overall reaction. If the mechanism is an electrode process, this rate-determining step (RDS) can be a heterogeneous electron-transfer reaction.

A widely held concept in electrochemistry is that truly elementary electron-transfer reactions always involve the exchange of one electron, so that an overall process involving a change of *n* electrons must involve *n* distinct electron-transfer steps. Of course, it may also involve other elementary reactions, such as adsorption, desorption, or various chemical reactions away from the interface. Within this view, a rate-determining electron transfer is always a one-electron-process, and the results that we derived above for the one-step, one-electron process can be used to describe the RSD, although the concentrations must often be understood as applying to intermediates, rather than to starting species or final products.

For example, consider an overall process in which O and R are coupled in an overall multielectron process

$$O + ne^- \leftrightarrow R \qquad (9.34)$$

by a mechanism having the following general character:

$$O + n'e^- \leftrightarrow O' \qquad \text{(net result of steps preceding RDS)} \qquad (9.35)$$

$$O' + e^- \overset{k_f/k_b}{\longleftrightarrow} R' \qquad \text{(RDS)} \qquad (9.36)$$

$$R' + n''e^- \leftrightarrow R \qquad \text{(net result of steps following RDS)} \qquad (9.37)$$

Obviously $n' + n'' + 1 = n$

The current-potential characteristic can be written as

$$i = nFAk^0_{rds}[C_{O'}(0,t)e^{-\alpha f\left(E-E^{0'}_{rds}\right)} - C_{R'}(0,t)e^{(1-\alpha)f\left(E-E^{0'}_{rds}\right)}] \qquad (9.38)$$

where k^0_{rds}, α, and $E^{0'}_{rds}$ apply to the RDS. This relation is **(9.12)** written for the RDS and multiplied by *n*, because each net conversion of O' to R' result in the flow of *n* electrons, not just one electron, across the interface. The concentrations $C_{O'}(0,t)$ and $C_{R'}(0,t)$ are controlled not only by the interplay between mass transfer and the kinetics of heterogeneous electron transfer, as we found in the Butler-Volmer model for one-step, one-electron process, but also by the properties of the preceding and following reactions. The situation can become quite complicated, so we will make no attempt to discuss the general problem. However, a few important simple cases exist, and we will develop them briefly now.

9.1.3.2 Multistep Process at Equilibrium

If a true equilibrium exists for the overall process, all the steps in the mechanism are individually at equilibrium. Thus, the surface concentrations of O' and R' are the values in equilibrium with the bulk concentrations of O and R, respectively. We designate them as $(C_{O'})_{eq}$ and $(C_{R'})_{eq}$. Recognizing that i=0, we can proceed through the treatment leading to **(9.14)** to obtain the analogous relation

$$e^{f(E_{eq}-E^{0'}_{rds})} = \frac{(C^*_O)_{eq}}{(C^*_R)_{eq}} \qquad (9.39)$$

For the mechanism in **(9.35)** and **(9.37)**, Nerstian relationships define the equilibrium for the pre- and postreactions, and they can be written in the following forms:

$$\mathbf{e^{n'f(E_{eq}-E^{0'}_{pre})} = \frac{C^*_O}{(C_{O'})_{eq}}} \qquad \mathbf{e^{n''f(E_{eq}-E^{0'}_{post})} = \frac{(C^*_{R'})_{eq}}{C^*_R}} \qquad \textbf{(9.40)}$$

where $E^{0'}_{pre}$ and $E^{0'}_{post}$ apply to **(9.35)** and **(9.37)**, respectively. Substitution for the equilibrium concentrations of O′ and R′ in **(9.39)** gives

$$\mathbf{e^{f(E_{eq}-E^{0'}_{rds})}e^{n'f(E_{eq}-E^{0'}_{pre})}e^{n''f(E_{eq}-E^{0'}_{post})} = \frac{C^*_O}{C^*_R}} \qquad \textbf{(9.41)}$$

Recognizing that $n = n' + n'' + 1$ and that $E^{0'}$ for the overall process is

$$\mathbf{E^{0'} = \frac{E^{0'}_{rds} + n'E^{0'}_{pre} + n''E^{0'}_{post}}{n}} \qquad \textbf{(9.42)}$$

it can be distilled **(9.41)** into

$$\mathbf{e^{nf(E_{eq}-E^{0'})} = \frac{C^*_O}{C^*_R}} \qquad \textbf{(9.43)}$$

which the exponential form of the Nernst equation for the overall reaction is,

$$\mathbf{E_{eq} = E^{0'} + \frac{RT}{nF}\ln\frac{C^*_O}{C^*_R}} \qquad \textbf{(9.44)}$$

Of course, this is a required result if the kinetic model has any pretense to validity, and it is important that the BV model attains it for the limit of i=0, not only for the simple one-step, one-electron process, but also in the context of an arbitrary multistep mechanism. The derivation here was carried out for a mechanism in which the prereactions and postreactions involve net charge transfer; however the same outcome can be obtained by a similar method for any reaction sequence, as long as it is chemically reversible and a true equilibrium can be established.

9.1.3.3 Quasirreversible and Irreversible Multistep Processes

If a multistep process is neither Nerstian nor at equilibrium, the details of the kinetics influence its behavior in electrochemical experiments, and one can use the results to diagnose the mechanism and to quantify kinetic parameters. As in the study of homogeneous kinetics, one proceeds by devising a hypothesis about the mechanism, predicting experimental behavior on the basis of the hypothesis, and comparing the predictions against the results. In the electrochemical sphere, an important part of predicting behavior is developing the current-potential characteristic in terms of controllable parameters, such as the concentrations of participating species.

If the RDS is a heterogeneous electron-transfer step, then the current-potential characteristic has the form of **(9.38)**. For most mechanisms, this equation is of limited direct utility, because O′ and R′ are intermediates, whose concentration cannot be controlled directly. Still, **(9.38)** can serve as the basis for a more practical current-potential relationship, because one can use the presumed mechanism to re-express $C_{O'}(0,t)$ and $C_{R'}(0,t)$ in terms of the concentrations of more controllable species, such as O and R.

Unfortunately, the results can easily become too complex for practical application. For example, consider the simple mechanism in **(9.35)-(9.37)**, where the pre- and postreactions are assumed to be kinetically facile enough to remain in local equilibrium. The overall Nerstian relationships connect the surface concentrations of O and R to those of O′ and R′. Thus, the current-potential characteristic, **(9.38)**, can be expressed in terms of the surface concentrations of the initial reactant, O, and the final product, R.

$$\mathbf{i = nFAk^0_{rds}C_O(0,t)e^{-n'f\left(E-E^{0'}_{pre}\right)}e^{-\alpha f\left(E-E^{0'}_{rds}\right)}} \\ \mathbf{- nFAk^0_{rds}C_R(0,t)e^{n''f\left(E-E^{0'}_{post}\right)}e^{(1-\alpha)f\left(E-E^{0'}_{rds}\right)}]} \qquad \textbf{(9.45)}$$

This relationship can be rewritten as

$$\mathbf{i = nFA[k_fC_O(0,t) - k_bC_R(0,t)]} \qquad \textbf{(9.46)}$$

where

$$\mathbf{k_f = k^0_{rds}e^{f\left[n'E^{0'}_{pre}+\alpha E^{0'}_{rds}\right]}e^{-(n'+\alpha)fE}]} \qquad \textbf{(9.47)}$$

$$\mathbf{k_b = k^0_{rds}e^{-f\left[n''E^{0'}_{post}+(1-\alpha)E^{0'}_{rds}\right]}e^{(n''+1-\alpha)fE}} \qquad \textbf{(9.48)}$$

The point of these results is to illustrate some of the difficulties in dealing with multistep mechanism involving embedded RDS. No longer is the potential dependence of the rate constant expressible in two parameters, one of which is interpretable as a measure of intrinsic kinetic facility. Instead, k^0 becomes obscured by the first exponential factors in **(9.47)** and **(9.48)**, which express thermodynamic relationships in the mechanism. One must have ways to find out the individual values of n', n'', $E^{0'}_{pre}$, $E^{0'}_{post}$, and $E^{0'}_{rds}$ before one can evaluate the kinetics of the RDS in a fully quantitative way. This is normally a difficult requirement.

The kinetic data by Gattrell et al. were obtained using graphite rotating disk electrode (RDE), which should be directly applicable to practical cells which use carbon-felt electrodes. Although the quantitative data **Table 9.1** was obtained using a Hg electrode, the polarization curves shown for the V2+/V3+ electrode with graphite RDE in Gattrell et al. indicate a rate constant $>>10^{-5}$ cm/s.

The dependence of the VO^{2+}/VO_2^+ couple on electrode material has not been very well-studied. Skyllas-Kazacos and co-workers[59] reported somewhat larger exchange-current densities for less well-characterized "carbon" electrodes than Gattrell et al. and suggested it is possible to enhance kinetics by surface treatment of carbon-based electrodes. Zhong et al. fabricated conducting polyethylene (PE) composite electrodes with low resistivity by mixing PE with conducting fillers (carbon black, graphite powder and fiber). The chemical treatment of graphite fiber-based composite polymer electrodes with chromate-sulfuric acid was shown to enhance the surface and improve reactivity for the electrode reactions. Carbon-polypropylene (PP) composite electrodes modified with rubber show better mechanical properties, better impermeability and better overall conductivity compared to the PE composite electrodes[65]. Graphene oxide nanoplatelets (GONPs) demonstrated a more favorable electrocatalytic activity for V(V)/V(IV) and V(III)/V(II) redox couples than pristine graphite for the VRFBs. It is found that the V(III)/V(II) redox reaction strongly depends on the formation of surface active functional groups of C-OH and COOH[296]. However, it is not clear that using an electrode material other than graphite/carbon would be cost effective.

Before examining surface-area effects, a mention should be made about typical RFB electrode materials. As noted above, graphitic or vitreous carbon materials are widely used in RFBs[36,39,134,297], such as graphite, carbon felt, carbon fiber, thermal and acid treated graphite, carbon polymer composite materials, carbon nanotubes, Ir-modified carbon felt and graphene-oxide nanoplatelets. In general, RFB couples are chosen for the facile kinetics so highly active catalytic materials are not necessary. Nonetheless, it has been found that various surface treatments can lead to improved reaction kinetics on carbon electrodes. Chemical etching[298], thermal treatment[299], chemical doping, carbon nanotubes addition, and addition of metallic catalyst sites to the carbon fibers have all been attempted[138]. Aside from catalytic activity, the main criteria for electrode materials are electrical conductivity, chemical stability and durability in the reaction environment. Carbon and graphite materials meet both these requirements, though metal foams and meshes are also candidates[300,301]. The search for improved electroactive materials for RFBs will no doubt continue to be actively pursued.

9.2 Active surface area

The previously explained kinetic constants and equations (e.g. **(9.22)**) are for rates per unit catalyst area. As mentioned, one way to compensate for a slower reaction is to increase the roughness factor or catalyst surface area per unit geometric area. For example, ignoring double-layer charging and assuming electro neutrality, one can write a current balance between ionic and electronic current,

$$\nabla \cdot \mathbf{i_2} = -\nabla \cdot \mathbf{i_1} = \mathbf{a_{1,2}} \mathbf{i_{h,1-2}} \qquad \textbf{(9.49)}$$

where is evident that the current generation source term is directly proportional to the specific interfacial area, $a_{1,2}$, which can be related to the roughness factor discussed above **Table 9.1** by accounting for the thickness of the electrode. In the above equation, $-\nabla \cdot \mathbf{i_1}$ represents the total anodic rate of electrochemical reactions per unit volume of electrode and $i_{h,1\text{-}2}$ is the transfer current for reaction *h* between the ionic and electronic materials; for RFBs, the electronic current (i) is the electrons and the ionic current (ii) are the reactive ion species. Thus, the surface area in the porous electrode is critical to RFB performance.

An optimum surface area in a porous medium is directly linked to the physical and transport properties of the medium, namely, porosity and permeability, respectively. From an electrochemical standpoint it is desirable to have the need to minimize pressure drop and pumping costs, which favor high permeability. A brief analysis of the interplay between these two key parameters follows. Typical RFB carbon-fiber-paper or carbon-felt electrode materials have a porosity around 0.8, a fiber diameter of approximately 10 μm and a permeability of 2 x 10^{-8} cm^2. A qualitative estimate of the surface area variation with fiber diameter can be obtained using a filament analogue model which simply involves finding the number of cylinders *N* of a given diameter d_f that give a specific porosity ε (cm^3/cm^2), then determining the specific surface area $a_{1,2}$ (cm^2/cm^3) of *N* cylinders. A simple formula for this relationship is given by Carta et al.[302]

$$\mathbf{a_{1,2}} = \frac{\mathbf{4(1-\varepsilon)}}{\mathbf{d_f}} \qquad \textbf{(9.50)}$$

The actual surface area in a real fiber bed may be less than this value since fibers contact and overlap each other. Even more if the fibers are not truly cylindrical but rough or ridged. In terms of a roughness factor, using a typical felt properties and a thickness of a few millimeters, a value of around 50 is obtained. Also the absolute permeability change expected as calculated from the Carman-Kozeny equation[303], which has been shown to adequately describe the variation of permeability with porosity due to compression in fibrous materials[304] and is assumed to apply here.

Clearly, the fiber diameter dramatically impacts both aspects and unfortunately in opposing directions. Increasing the fiber diameter from 10 to 100 μm improves the permeability by a factor of 100, but reduces the surface area by a factor of 10. The

same general trend would be true for other random electrodes such as particulate beds. Effort to increase active surface area in a flowing electrolyte by using particles with microporosity have been reported[91], but, not surprisingly, this additional surface area does not contribute significantly to the electrochemically active area since such internal surfaces are highly diffusion limited. Attempts to increase the roughness of the electrode surface could be beneficial, but typically it is more profitable to modify the surface for increased kinetic or catalytic behavior rather than just surface area.

Another aspect of the active solid surface area that must be considered is the intimacy of the solid/electrolyte contact[72,91]. Carbon and graphite materials have a neutral wettability to water[305] which prevents the spreading of electrolyte over the electrode surface. The trapped air pockets resulting from incomplete wetting reduce the electroactive surface area owing to the Cassie-Baxter effect. Such incomplete wetting would be exacerbated on roughness surfaces. Sun and Skyllas-Kazacos found that certain electrode pretreatments intended to improve catalytic activity also lead to somewhat improved wettability behavior[72]. Litster et al.[306] report that briefly heating carbon fiber materials at 300ºC in an air environment rendered them fully hydrophilic, and Yan et al. review various treatment procedures for altering carbon wettability[307]. The presence of a gas phase at the solid/electrolyte interface could be due to residual air trapped during initial flooding of the electrode, or could appear due to evolution of gases such as the parasitic evolution of hydrogen and/or oxygen[308].

9.3 Transport phenomena

Mass transfer, that is, the movement of material from one location in the solution to another, arises either from differences in electrical or chemical potential at the two locations or from movement of a volume element solution. The modes of mass transfer are:

1. *Migration*. Movement of a charged body under the influence of an electric field (a gradient of electrical potential).

2. *Diffusion*. Movement of a species under the influence of a gradient of chemical potential (i.e. a concentration gradient).

3. *Convection*. Stirring or hydrodynamic transport. Generally fluid flow occurs because of *natural convection* (convection caused by density gradients) and *forced convection*, and may be characterized by stagnant regions, laminar flow, and turbulent flow.

There is various mechanism of transport that occurs within a RFB. Typically, electron flow is not limiting due to the use of conductive additives or just carbon materials. This transport is adequately described by Ohm's law,

$$\mathbf{i_1} = -\boldsymbol{\sigma}\nabla\boldsymbol{\phi_1} \qquad \textbf{(9.51)}$$

where σ is the electronic conductivity. The other major transport issue is that reactants and products. Typically, this can be separated into two different regions, namely, that of the electrode and that of the membrane or separator. These two regions have different properties; their transport species and mechanisms are discussed in turn below. For the electrolyte in the electrodes, diffusion is often the most important process while conduction is for the membrane. While diluted-solution theory does not necessarily strictly apply in the electrolyte systems of interest, diffusivities of the ions give a good indication of the relative motions of the relevant ions. Cation exchange-membranes, such as H^+ and Na^+, are widely used in the aqueous RFBs due to their high ionic conductivity. Anion exchange membranes are used mainly in non-aqueous systems to be compatible with the supporting electrolytes used and suppress unwanted crossover. Generally, the open-circuit potential (OCP) of an aqueous system is constrained to be lower due to the reduced electrochemical stability window of water compared to that of non-aqueous RFB's, in which organic solvents with a higher electrochemical stability voltage window are used. The diffusivities of active species should be in the range of $10^{-6}cm^2/s$ to be suitable for a RFB. Finally, while there is some other, less critical issues such as thermal management and heat transport within the cell.

9.3.1 Rotating disk electrode

The rotating disk electrode (RDE) is one of the few convective electrode systems for which the hydrodynamic equations and the convective-diffusion equation have been solved rigorously for the steady state. This electrode is rather simple to construct and consists of a disk of the electrode material imbedded in a rod of an insulating material. For example, a commonly used form involves a platinum wire sealed in glass tubing with the sealed end ground smooth and perpendicularly to the rod axis. More frequently, the metal is imbedded into Teflon, epoxy resin, or another plastic (**Figure 9.6**). Although the literature suggests that the shape of the insulating mantle is critical and that exact alignment of the disk is important, these factors are usually not troublesome in practice, except perhaps at high rotation rates, where turbulence and vortex formation may occur. It is more important that there is no leakage of the solution between the electrode material and the insulator. The rod is attached to a motor directly by a chuck or by a flexible rotating shaft or pulley arrangement and is rotated at a certain frequency, f (revolutions per second). The more useful descriptor of rotation rate is the angular velocity, ω (s^{-1}), where $\omega = 2\varpi f$. Electrical connection is made to the electrode by means of a brush contact; the noise level observed in the current at the RDE depends on this contact. Carbon-silver (graph-alloy) materials are frequently used. RDE are available commercially.

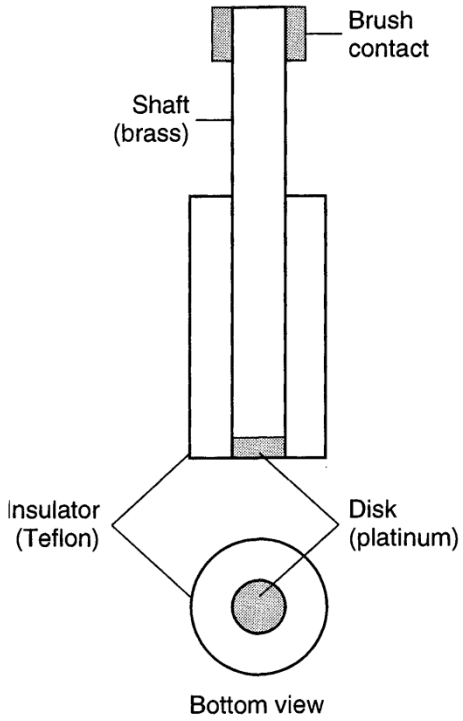

Figure 9.6 – Rotating disk electrode.

9.3.1.1 Solution of the Convective-Diffusion Equation

The current is the flux at the electrode surface, that is,

$$\boldsymbol{i = nFAD_O\left(\frac{\partial C_O}{\partial y}\right)_{y=0}} \qquad \textbf{(9.52)}$$

Where, under the chosen current conditions, $i=i_{l,c}$. From **(9.52)** and

$$\boldsymbol{C_O^* = \left(\frac{\partial C_O}{\partial y}\right)_{y=0} 0.8934\left(\frac{3D_O\omega^{-3/2}\nu^{1/2}}{0.51}\right)^{1/3}} \qquad \textbf{(9.53)}$$

We obtain the *Levich equation*:

$$\boldsymbol{i_{l,c} = 0.62nFAD_O^{2/3}\omega^{1/2}\nu^{-1/6}C_O^*} \qquad \textbf{(9.54)}$$

This equation applies to the totally mass-transfer-limited condition at the RDE and predicts that $i_{l,c}$ is proportional to C_O^* and $\omega^{1/2}$. One can define the *Levich constant* as $i_{l,c}/\omega^{1/2}C_O^*$, which is the RDE analog of the diffusion current constant or current function in voltammetry or the transition time constant in chronopotentiometry.

9.3.1.2 General Current-Potential Curves at the RDE

For no limiting-current conditions, only a change in integration limits is required. In general, at y=0, C_O=C_O(y=0) and $(\partial C_O/\partial y)_{y=0}$ is given by an analogue to **(9.53)**, which yields

$$\boldsymbol{C_O^* - C_O(y=0) = \left(\frac{\partial C_O}{\partial y}\right)_{y=0} \int_0^\infty exp\left(\frac{-y^3}{3B}\right) dy} \qquad \textbf{(9.55)}$$

Thus,

$$\boldsymbol{i = 0.62nFAD_O^{2/3}\omega^{1/2}\nu^{-1/6}[C_O^* - C_O(y=0)]} \qquad \textbf{(9.56)}$$

For a Nerstian reaction, combination of the Nernst equation for the O,R couple with the equations for the various currents yields the familiar voltammetric wave equation:

$$\boldsymbol{E = E_{1/2} + \frac{RT}{nF} ln \frac{(i_{l,c} - i)}{(i - i_{l,a})}} \qquad \textbf{(9.57)}$$

where

$$\boldsymbol{E_{1/2} = E^{0\prime} + \frac{RT}{nF} ln \left(\frac{D_R}{D_O}\right)^{2/3}} \qquad \textbf{(9.58)}$$

Note that the shape of the wave for a reversible reaction is independent of ω. Thus, since i_l varies as $\omega^{1/2}$, I at any potential should also vary as $\omega^{1/2}$. A deviation of a plot of i vs. $\omega^{1/2}$ from a straight line intersecting the origin suggests that a kinetic limitation is involved in the electron-transfer reaction. For example, for a totally irreversible one-step, one-electron reaction, the disk current is

$$\boldsymbol{i = FAk_f(E)C_O(y=0)} \qquad \textbf{(9.59)}$$

where $k_f(E) = k^0 \exp[-\alpha f(E-E^{0\prime})]$.

$$\boldsymbol{i = FAk_f(E)C_O^*\left(1 - \frac{i}{i_{l,c}}\right)} \qquad \textbf{(9.60)}$$

Or, with rearrangement and defining

$$\boldsymbol{i_K = FAk_f(E)C_O^*} \qquad \textbf{(9.61)}$$

One obtains the *Koutecký-Levick equation*:

$$\frac{\mathbf{1}}{\boldsymbol{i}} = \frac{\mathbf{1}}{\boldsymbol{i_K}} + \frac{\mathbf{1}}{\boldsymbol{i_{l,c}}} = \frac{\mathbf{1}}{\boldsymbol{i_K}} + \frac{\mathbf{1}}{\mathbf{0.62}\boldsymbol{nFAD_O^{2/3}\omega^{1/2}\nu^{-1/6}C_O^*}} \qquad \textbf{(9.62)}$$

Here, i_k represents the current in the absence of any mass-transfer effects, that is, the current that would flow under the kinetic limitation if the mass transfer were efficient enough to keep the concentration at the electrode surface equal to the bulk value, regardless of the electrode reaction. Clearly, $i/\omega^{1/2}C$ is a constant only when i_k [or k_f (E)] is very large. Otherwise, a plot of i vs. $\omega^{1/2}$ will be curved and tend toward the limit $i = i_k$ as $\omega^{1/2}$ tend to infinite (**Figure 9.7**).

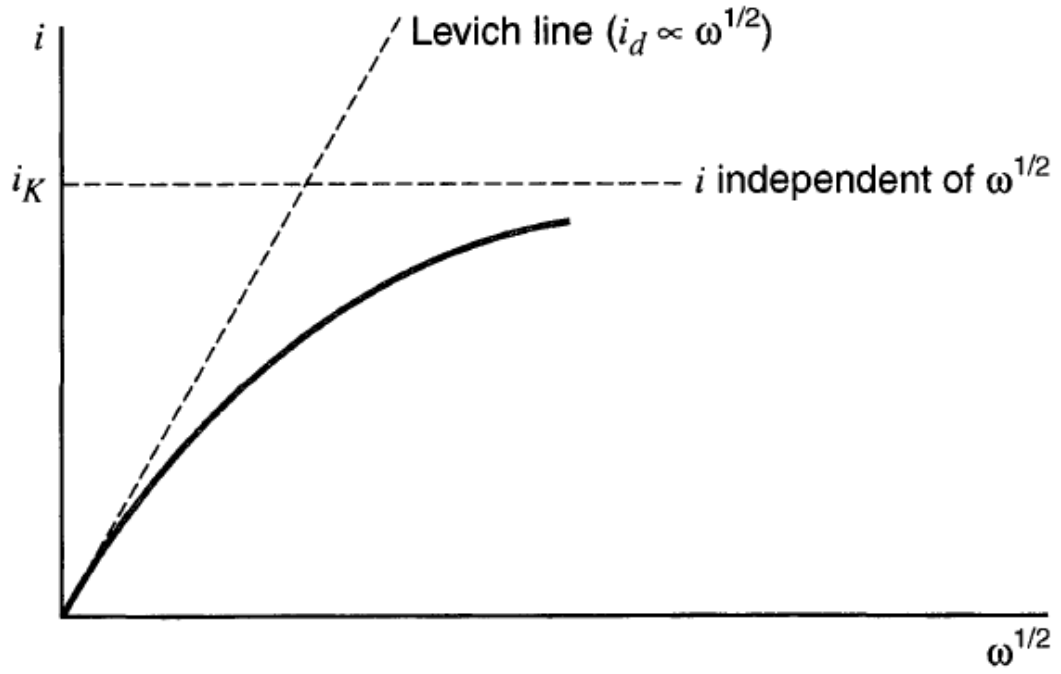

Figure 9.7 – Variation of i with $\omega^{1/2}$ at an RDE (at constant E_D) for an electrode reaction with slow kinetics.

A plot of 1/i vs. $1/\omega^{1/2}$ should be linear and can be extrapolated to $\omega^{-1/2} = 0$ to yield $1/i_K$. Determination of i_K at different values of E then allows determination of the kinetic parameter k^0 and α (**Figure 9.8**).

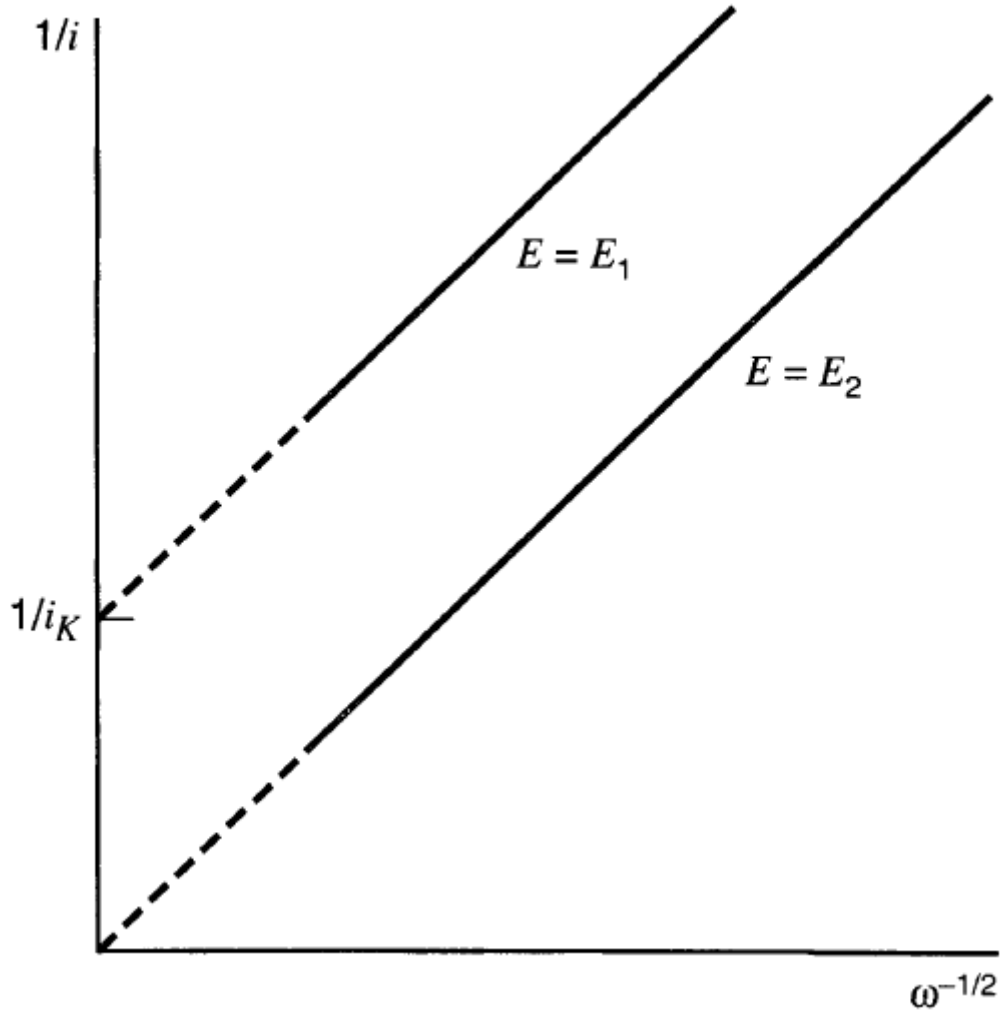

Figure 9.8 – Koutecký-Levick plots at potential E_1, where the rate of electron transfer is sufficiently slow to act as a limiting factor, and at E_2, where electrons transfer is rapid, for example, in the limiting-current region. The slope of both lines is $(0.62nFAC_O^*D_O^{2/3}v^{-1/6})^{-1}$.

9.3.2 Electrolyte flow

Within the electrode, the flux of the various species can be described using the Nernst-Planck equation assuming that dilute-solution theory holds[309].

$$\mathbf{N_i} = -\mathbf{z_i u_i F c_i \nabla \phi_2} - \mathbf{D_i \nabla c_i} + \mathbf{c_i \nu} \qquad \textbf{(9.63)}$$

The first term in the expression is a migration term, representing the motion of charged species that results from a potential gradient. The migration flux is related to the potential gradient ($-\nabla\phi_2$) by a charge number, z_i, concentration, c_i, and mobility, u_i. The second term relates the diffusive flux to the concentration gradient. The final term is a convective term and represents the motion of the species as the bulk motion of the solvent carries it along. For non-charged

reactants and products, the same equation can be used with the migration term set to zero, resulting in the equation of convective diffusion[310]. Dilute-solution theory considers only the interactions between each dissolved species and the solvent, and thus one can consider the conductivity of the solution to be given by

$$\kappa = F^2 \sum_i z_i^2 c_i u_i \qquad (9.64)$$

The motion of each charged species is described by its transport properties, namely, the mobility and the diffusion coefficient. These transport properties con be related to one another at infinite dilution vie Nernst-Einstein equation[309,311,312]

$$D_i = RTu_i \qquad (9.65)$$

For more complicated systems than binary electrolytes or where the interactions between species are important and/or non-ideal, concentrated-solution theory can be used as discussed by Newman and Thomas-Alyea[308]. In this approach, the transport coefficients of merit include the conductivity of the solution, and the transference numbers and diffusivities of the ions. It should be noted that many RFBs operate at higher concentrations such that concentrated-solution theory may be required; however, the use of supporting electrolytes does mitigate this to a certain extent in that detailed speciation is not required to predict cell performance fairly well.

The total current in the electrolyte can be expressed as

$$i_2 = F \sum_i z_i N_i \qquad (9.66)$$

and the ionic conductivity of the electrolyte can be related to the above transport properties[308].

For most RFB applications, the system is one phase (liquid) and so complicated expressions for multiphase flow are unnecessary, in stark contrast to low-temperature fuel cells. Thus, for the convective flow one can use the Navier-Stokes equations[309]

$$v \cdot \nabla(\rho v) = -\nabla p + \mu \nabla^2 v \qquad (9.67)$$

where p is the pressure, and μ and ρ are the viscosity and density of the liquid, respectively. Since most RFB electrodes are porous, the above equation can be extended using various methodologies such as Brinkman[303,309,313], or even replaced by Darcy's law[303].

$$\mathbf{v} = -\frac{\mathbf{k}}{\mu}\nabla \mathbf{p} \qquad \textbf{(9.68)}$$

Flowing electrolyte through porous electrodes presents a number of challenges, both at the single-cell and full-stack level. At the pore scale within each electrode there will be significant differences in the interstitial flow rate in each pore owing to size differences, with flow largely confined to the largest pores in the medium. Such pore-scale-channeling behavior provides convective mass transport at a limited number of surfaces, while dead zones of relatively stagnant flow and localized limiting currents would exist elsewhere throughout the electrode. Fibrous materials are the favored porous-electrode substrate for several reasons because high porosity can be achieved while still maintaining electrical conductivity and percolation in the solid phase due to the bridging between long fibers. As discussed above, high porosity is advantageous since i) there is a strong positive correlation between porosity and permeability[308], thereby resulting in reduced pressure drop and associated pumping cost; and ii) the effective ionic conductivity of the electrolyte is directly proportional to porosity[314] and inversely proportional to tortuosity which tends to increase with decreasing porosity[308].

Due to the wide spread use of fibrous electrodes for various applications, a number of studies have looked at mass transfer in carbon-fiber electrodes[61,62,315,316]. Schmal et al. [117] compared mass transfer at single fibers to fiber assemblies (bundles and felts) and found that per unit length of fiber the mass transfer to a single fiber was significantly higher. This was attributed to channeling within the fiber assemblies causing dead-zones or stagnant regions, effectively reducing the active area for reaction. A porous material with very uniform pore-size distribution would help alleviate this problem, but such materials may be impractical. Saleh[317] studied the effectiveness factor in packed bed electrodes and found that ohmic resistance, which is a combination of fluid properties and bed geometry, also played a key role in determining the extent to which porous electrode was utilized.

Another cell-scale issue arising from the convective flow in porous electrodes is large scale heterogeneities due to assembly tolerances or uneven thermal expansion, which could lead to bypassing of large sections of a cell. Moreover, flow though porous electrodes presents major manifolding issues at the stack-scale since each cell must have nearly identical permeability. This would be difficult to achieve since stacks may be compressed significantly when assembled. This situation is analogous to interdigitated flow fields proposed for low-temperature fuel cells, which showed very promising performance results in single-cell tests, but the inevitable differences in permeability from cell to cell in a stack created uneven flow distribution among cells[318].

To enhance flow and electrolyte utilization during deep discharge where high flow rates are required, physical barriers or roughened electrode materials can be used inside cell to promote turbulence and mass transport. Lessner et al. designed a flow-through porous electrode for bromine/polysulphide RFBs[96]. To ensure uniform flow distribution and prevent channeling, quartz particle, with a diameter of 0.5 to 1.0 mm, were placed 0.5 cm above the inlet.

Leung et al. also investigated the effect of the mean linear flow velocity of the electrolyte on the cell performance both under constant current charge and discharge[83]. **Figure 9.9** presents the effect of the mean linear flow velocity on the discharge voltage with different constant discharge current densities. It is shown that there is a maximum cell voltage at the mean linear flow velocity of 3.9 cm/s.

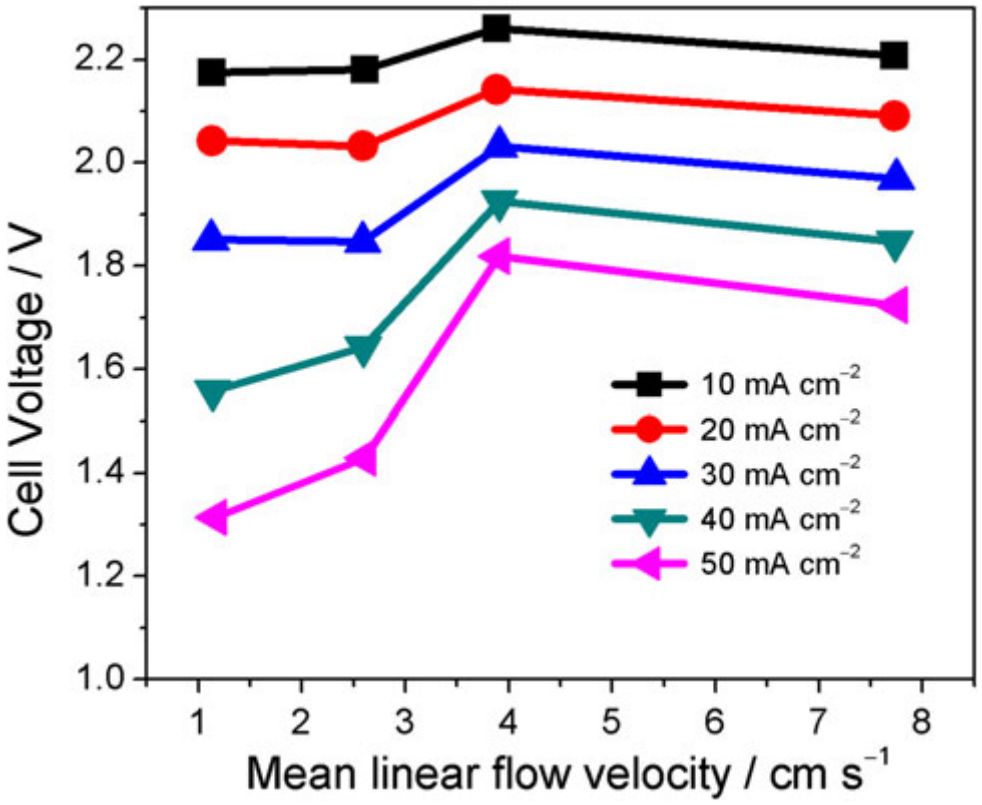

Figure 9.9 – Effect of the mean linear flow velocity of the electrolyte on the cell voltage of a RFB[83].

9.3.3 Reactant concentration effects

The issue of reactant solubility in the flowing electrolyte solution can be important. The energy density of a RFB system is set by the concentration of dissolved species, but the maximum concentration in any stream is limited by the solubility of at least soluble species. Precipitation of reactants or products in the porous electrode is calamitous. Concentration limits on the electroactive species not only reduces the energy density of a system, but also negatively impacts the power density and cell efficiency as well. Lower concentrations mean reduced mass-transfer rates and current density, thus increasing concentration polarization and/or pumping power. Solubility is a function of temperature as well, which must be factored into cell design. For instance, it is observed that V_2O_5 precipitation occurs at elevated temperature, limiting the operating temperature to the range 10 to 40ºC[99,319]. Li et al. improved this situation with the development of a vanadium sulfate and chloride mixed electrolyte, enabling a vanadium concentration up to 2.5

M over a temperature range of -5 to 50ºC[319]. However, temperature excursion in an operating cell could cause a precipitation event and lead to cell failure[91].

Other issues regarding concentrations include the fact that for many systems increasing the concentration of the reactant can lead to more complexing and lower diffusivities and perhaps even more viscous solutions. Such tradeoffs require optimization for the specific system.

10 References

(1) Yang, B.; Hoober-Burkhardt, L.; Wang, F.; Surya Prakash, G. K.; Narayanan, S. R. An Inexpensive Aqueous Flow Battery for Large-Scale Electrical Energy Storage Based on Water-Soluble Organic Redox Couples. *Journal of the Electrochemical Society* **2014**, *161* (9), A1371–A1380.

(2) Huskinson, B.; Marshak, M. P.; Suh, C.; Er, S.; Gerhardt, M. R.; Galvin, C. J.; Chen, X.; Aspuru-Guzik, A.; Gordon, R. G.; Aziz, M. J. A Metal-Free Organic–inorganic Aqueous Flow Battery. *Nature* **2014**, *505* (7482), 195–198.

(3) Alotto, P.; Guarnieri, M.; Moro, F. Redox Flow Batteries for the Storage of Renewable Energy: A Review. *Renewable and Sustainable Energy Reviews* **2014**, *29*, 325–335.

(4) Badwal, S. P. S.; Giddey, S. S.; Munnings, C.; Bhatt, A. I.; Hollenkamp, A. F. Emerging Electrochemical Energy Conversion and Storage Technologies. *Frontiers in Chemistry* **2014**, *2*, 79.

(5) Linden, D.; Reddy, T. B.; York, N.; San, C.; Lisbon, F.; Madrid, L.; City, M.; New, M.; San, D.; Singapore, J. S.; et al. HANDBOOK OF BATTERIES McGraw-Hill Library of Congress Cataloging-in-Publication Data.

(6) Noack, J.; Roznyatovskaya, N.; Herr, T.; Fischer, P. The Chemistry of Redox-Flow Batteries. *Angewandte Chemie International Edition* **2015**, *54* (34), 9776–9809.

(7) Zhang, J.-G.; Bruce, P. G.; Zhang, X. G. Metal-Air Batteries. In *Handbook of Battery Materials*; Wiley-VCH Verlag GmbH & Co. KGaA: Weinheim, Germany, 2011; pp 757–795.

(8) Duduta, M.; Ho, B.; Wood, V. C.; Limthongkul, P.; Brunini, V. E.; Carter, W. C.; Chiang, Y.-M. Semi-Solid Lithium Rechargeable Flow Battery. *Advanced Energy Materials* **2011**, *1* (4), 511–516.

(9) Pickard, W. F.; Shen, A. Q.; Hansing, N. J. Parking the Power: Strategies and Physical Limitations for Bulk Energy Storage in Supply–demand Matching on a Grid Whose Input Power Is Provided by Intermittent Sources. *Renewable and Sustainable Energy Reviews* **2009**, *13* (8), 1934–1945.

(10) Kaldellis, J. K.; Zafirakis, D.; Kavadias, K. Techno-Economic Comparison of Energy Storage Systems for Island Autonomous Electrical Networks. *Renewable and Sustainable Energy Reviews* **2009**, *13* (2), 378–392.

(11) Shigematsu, T. Redox Flow Battery for Energy Storage. *SEI Technical Review* **2011**, No. 73, 4–13.

(12) Ponce de Le?n, C.; Fr?as-Ferrer, A.; Gonz?lez-Garc?a, J.; Sz?nto, D. A.; Walsh, F. C. Redox Flow Cells for Energy Conversion. *Journal of Power Sources* **2006**, *160* (1), 716–732.

(13) Bartolozzi, M. Development of Redox Flow Batteries. A Historical Bibliography. *Journal of Power Sources* **1989**, *27* (3), 219–234.

(14) Ashimura, S.; Miyake, Y. Denki Kagaku, Vol. 39. **1971**.

(15) G. Ciprios, W. Erstoine, Jr. and P. G. Grimes (Exxon/GRU, 1, 77-V, 1 and Exxon/ GRU. 2, BH, 77-V) NASA Contract Rep. No. NAS3-135-206, Vols. 1 & 2, 1977.

(16) J. Giner, L. Swette and K. Cahill, NASA Contract NAS3-19760, NASA CR-134705, 1976. 8.

(17) Beccu, K.-D. Umweltbelastung Und Sicherheitsfaktoren Elektrochemischer Speichersysteme Zur Spitzenlastdeckung. *Chemie Ingenieur Technik* **1979**, *51* (6), 659–662.

(18) Warshay, M.; Wright, L. O. Cost and Size Estimates for a Redox Bulk Energy Storage Concept. *Journal of The Electrochemical Society* **1977**, *124* (2), 173.

(19) R. D. Weaver, Final Rep., Stanford Res. Inst., for EPRI (EPRI Proj. RP 370-2, SRI Proj. 3974-2), January, 1976.

(20) Thaller, L. H. RECENT ADVANCES IN REDOX FLOW CELL STORAGE SYSTEMS.

(21) 27 J. D. Giner and K. J. Cahill, U.S. Pat. 61 555 (June 20, 1980).

(22) T. Nozaki, N. Kaneko and T. Ozawa, Denki Toronkai (Japan), 18 (1979) 33 https://docs.google.com/viewer?url=patentimages.storage.googleapis.com/pdfs/US5993986.pdf (accessed Jun 1, 2017).

(23) N. H. Hagedorn and L. H. Thaller, NASA Tech. Mem, NASA-TM-81464, E-383,1980.

(24) Sept. N. H. Hagedorn, Proc. 16th Intersoc. Energy Conv. Eng. Conf., Vol. 1, 1981, p. 805. *CPIA Publication 1* (1), 129–137.

(25) Liu, C. C.; Galasco, R. T.; Savinell, R. F. Enhancing Performance of the Ti(III)/Ti(IV) Couple for Redox Battery Applications. *Journal of The Electrochemical Society* **1981**, *128* (8), 1755.

(26) Trainham, J. A.; Newman, J. A Comparison between Flow-through and Flow-by Porous Electrodes for Redox Energy Storage. *Electrochimica Acta* **1981**, *26* (4), 455–469.

(27) J. S. Ling and J. Charleston, NASA Tech. Mem. 1980, NASA-TM-82701, DOE/ NASA/12726-12, E798.

(28) J. Giner, V. Jalan and L. Swette, Dechema - Monograf. 1982,92-1885 https://docs.google.com/viewer?url=patentimages.storage.googleapis.com/pdfs/US5104497.pdf (accessed Jun 2, 2017).

(29) Liu, C. C.; Galasco, R. T.; Savinell, R. F. Operating Performance of an Fe-Ti Stationary Redox Battery in the Presence of Lead. *Journal of The Electrochemical Society* **1982**, *129* (11), 2502.

(30) Yang, C. Y. Catalytic Electrodes for the Redox Flow Cell Energy Storage Device. *Journal of Applied Electrochemistry* **1982**, *12* (4), 425–434.

(31) Oei, D.-G. Chemically Regenerative Redox Fuel Cells. *Journal of Applied Electrochemistry* **1982**, *12* (1), 41–51.

(32) Fedkiw, P. S.; Watts, R. W. A Mathematical Model for the Iron/Chromium Redox Battery. *Journal of The Electrochemical Society* **1984**, *131* (4), 701.

(33) H. Ohya, K. Emori, T. Ohto and Y. Negishi, Denki Kagaku, 52 (1984) 341. -

Google Search https://www.google.es/search?q=H.+Ohya%2C+K.+Emori%2C+T.+Ohto+and+Y.+Negishi%2C+Denki+Kagaku%2C+52+(1984)+341.&rlz=1C1KMZB_enES555ES555&oq=H.+Ohya%2C+K.+Emori%2C+T.+Ohto+and+Y.+Negishi%2C+Denki+Kagaku%2C+52+(1984)+341.&aqs=chrome..69i57.1105j0j9&sourceid= (accessed Jun 2, 2017).

(34) 79 R. J. Remick and P. G. Ang, U.S. Pat. 4 485 154 (NOV. 27,1984). https://docs.google.com/viewer?url=patentimages.storage.googleapis.com/pdfs/US4485154.pdf (accessed Jun 2, 2017).

(35) Mitsui Eng. Shipbuilding Co. Ltd., Jpn. Pat. 60 70 672 (Apr. 22, 1985 https://www.google.es/search?q=Mitsui+Eng.+Shipbuilding+Co.+Ltd.%2C+Jpn.+Pat.+60+70+672+(Apr.+22%2C+1985&rlz=1C1KMZB_enES555ES555&oq=Mitsui+Eng.+Shipbuilding+Co.+Ltd.%2C+Jpn.+Pat.+60+70+672+(Apr.+22%2C+1985&aqs=chrome..69i57.857j0j9&sourceid=chrome&ie=UTF (accessed Jun 2, 2017).

(36) Sum, E.; Skyllas-Kazacos, M. A Study of the V(II)/V(III) Redox Couple for Redox Flow Cell Applications. *Journal of Power Sources* **1985**, *15* (2–3), 179–190.

(37) *Energía : Revista de Ingeniería Energética.*; Ingeniería Química, 1975.

(38) Sumitomo Electric Industr. Ltd., Jpn. Pat. 60 101 881 (Jun. 05, 1985). - Google Search https://www.google.es/search?q=Sumitomo+Electric+Industr.+Ltd.%2C+Jpn.+Pat.+60+101+881+(Jun.+05%2C+1985).&rlz=1C1KMZB_enES555ES555&oq=Sumitomo+Electric+Industr.+Ltd.%2C+Jpn.+Pat.+60+101+881+(Jun.+05%2C+1985).&aqs=chrome..69i57.768j0j9&sourceid=chrome&ie=U (accessed Jun 2, 2017).

(39) Sum, E.; Rychcik, M.; Skyllas-kazacos, M. Investigation of the V(V)/V(IV) System for Use in the Positive Half-Cell of a Redox Battery. *Journal of Power Sources* **1985**, *16* (2), 85–95.

(40) Y. Hibino, T. Shigematsu and M. Kondo, Jpn. Pat. 60 163 177 (Aug. 26,1985).

(41) M. Kondo and T. Shigematsu, Jpn. Pat. 60225 366 (Nov. 09,1985). - Google Search https://www.google.es/search?q=M.+Kondo+and+T.+Shigematsu%2C+Jpn.+Pat.+60225+366+(Nov.+09%2C1985).%2B&rlz=1C1KMZB_enES555ES555&oq=M.+Kondo+and+T.+Shigematsu%2C+Jpn.+Pat.+60225+366+(Nov.+09%2C1985).%2B&aqs=chrome..69i57.492j0j4&sourceid=chrome&ie=UTF-8#q=M (accessed Jun 2, 2017).

(42) H. Matsubara, M. Kondo and T. Shigematsu, Jpn. Pat. 60297 076 (Dec. 18,1985). - Google Search https://www.google.es/search?q=H.+Matsubara%2C+M.+Kondo+and+T.+Shigematsu%2C+Jpn.+Pat.+60297+076+(Dec.+18%2C1985).&rlz=1C1KMZB_enES555ES555&oq=H.+Matsubara%2C+M.+Kondo+and+T.+Shigematsu%2C+Jpn.+Pat.+60297+076+(Dec.+18%2C1985).&aqs=chrome..69i57.809j0j9&so (accessed Jun 2, 2017).

(43) J. Doria, M. C. De Andres and C. Armenta, Inter-sol 85, Proc. 9th Solar Energy Sot., 3 (1985) 1500. - Google Search https://www.google.es/search?q=J.+Doria%2C+M.+C.+De+Andres+and+C.+Armenta%2C+Inter-

sol+85%2C+Proc.+9th+Solar+Energy+Sot.%2C+3+(1985)+1500.&rlz=1C1KMZB_enES555ES555&oq=J.+Doria%2C+M.+C.+De+Andres+and+C.+Armenta%2C+Inter-sol+85%2C+Proc.+9th+Solar+Energy+Sot (accessed Jun 2, 2017).

(44) Kummer, J. T.; Oei, D.-G. A Chemically Regenerative Redox Fuel Cell. II. *Journal of Applied Electrochemistry* **1985**, *15* (4), 619–629.

(45) Skyllas-Kazacos, M.; Rychcik, M.; Robins, R. G.; Fane, A. G.; Green, M. A. THE New All-Vanadium Redox Flow Cell. *Journal of The Electrochemical Society* **1986**, *133* (5), 1057–1058.

(46) T. Nozaki, T. Ozawa, H. Kaneko and A. Kidoguchi, Jpn. Pat. 6124 172 (Feb. 01, 1986). - Google Search https://www.google.es/search?q=T.+Nozaki%2C+T.+Ozawa%2C+H.+Kaneko+and+A.+Kidoguchi%2C+Jpn.+Pat.+6124+172+(Feb.+01%2C+1986).&rlz=1C1KMZB_enES555ES555&oq=T.+Nozaki%2C+T.+Ozawa%2C+H.+Kaneko+and+A.+Kidoguchi%2C+Jpn.+Pat.+6124+172+(Feb.+01%2C+1986).&aqs=chrome (accessed Jun 2, 2017).

(47) L. L. Swette and V. M. Jalan, Proc. Electrochem. Sot., 86-10 (1986) 195. - Google Search https://www.google.es/search?q=L.+L.+Swette+and+V.+M.+Jalan%2C+Proc.+Electrochem.+Sot.%2C+86-10+(1986)+195.&rlz=1C1KMZB_enES555ES555&oq=L.+L.+Swette+and+V.+M.+Jalan%2C+Proc.+Electrochem.+Sot.%2C+86-10+(1986)+195.&aqs=chrome..69i57.1352j0j9&sourceid=chrome (accessed Jun 2, 2017).

(48) Mathur, P. B.; Rajagopalan, C. S.; Bhatt, D. P. Studies on the Fe2+/Fe3+ Redox System Using D.C. Linear Polarisation and Impedance Techniques. *Journal of Power Sources* **1987**, *19* (4), 269–278.

(49) P. Garces, M. A. Climent and A. Aldaz, An. Quim. (Spain), Ser. A, 83 (1987) 9.

(50) M. A. Climent, P. Garces, M. Lopez-Segura and A. Aldaz, An. Quim. Ser. A, 83 (1987) 12.

(51) Skyllas-Kazacos, M.; Grossmith, F. Efficient Vanadium Redox Flow Cell. *Journal of The Electrochemical Society* **1987**, *134* (12), 2950.

(52) Rychcik, M.; Skyllas-Kazacos, M. Characteristics of a New All-Vanadium Redox Flow Battery. *Journal of Power Sources* **1988**, *22* (1), 59–67.

(53) M. Shimizu, N. Mori, M. Kuno, K. Mizunami and T. Shigematsu, Proc. Electrochem. Sot. 88-l 1 (1988) 249.

(54) L. Duic, Kern. Ind. (Serbo-Croatian), 37 (1988) 173. - Google Search https://www.google.es/search?q=L.+Duic%2C+Kern.+Znd.+(Serbo-Croatian)%2C+37+(1988)+173.&rlz=1C1KMZB_enES555ES555&oq=L.+Duic%2C+Kern.+Znd.+(Serbo-Croatian)%2C+37+(1988)+173.&aqs=chrome..69i57.777j0j9&sourceid=chrome&ie=UTF-8#q=L.+Duic,+Kern.+Ind.+(Serbo-Cr (accessed Jun 2, 2017).

(55) S. Takahashi, S. Higuchi, M. Futamata, 0. Nakamura, Y. Takada, I. Ogino, S. Ashimura and S. Okazaki, Osaka Kog. Gijatsu Shikensho Kiho, 39 (1988) 18. - Google Search https://www.google.es/search?q=S.+Takahashi%2C+S.+Higuchi%2C+M.+F

utamata%2C+0.+Nakamura%2C+Y.+Takada%2C+I.+Ogino%2C+S.+Ashimura+and+S.+Okazaki%2C+Osaka+Kog.+Gijatsu+Shikensho+Kiho%2C+39+(1988)+18.&rlz=1C1KMZB_enES555ES555&oq=S.+Takahashi%2C+S.+Higuchi%2C+ (accessed Jun 2, 2017).

(56) M. Shimizu, N. Mori and M. Shirotsuki, Jpn. Pat. 63 128 560 (Jun. 01,1988). - Google Search https://www.google.es/search?q=M.+Shimizu%2C+N.+Mori+and+M.+Shirotsuki%2C+Jpn.+Pat.+63+128+560+(Jun.+01%2C1988).&rlz=1C1KMZB_enES555ES555&oq=M.+Shimizu%2C+N.+Mori+and+M.+Shirotsuki%2C+Jpn.+Pat.+63+128+560+(Jun.+01%2C1988).&aqs=chrome..69i57.610j0j9&source (accessed Jun 2, 2017).

(57) F. Grossmith, P. Llewellyn, A. G. Fane and M. Skyllas-Kazacos, Proc. Electrochem. Sot., 88-l 1 (1988) 363.

(58) V-Fuel Pty Ltd. Status of Energy Storage Technologies as Enabling Systems for Renewable Energy from the Sun, Wind, Waves and Tides. 7.

(59) Zhong, S.; Kazacos, M.; Burford, R. P.; Skyllas-Kazacos, M. Fabrication and Activation Studies of Conducting Plastic Composite Electrodes for Redox Cells. *Journal of Power Sources* **1991**, *36* (1), 29–43.

(60) Sun, B.; Skyllas-Kazakos, M. Chemical Modification and Electrochemical Behaviour of Graphite Fibre in Acidic Vanadium Solution. *Electrochimica Acta* **1991**, *36* (3–4), 513–517.

(61) Sun, B.; Skyllas-Kazacos, M. Chemical Modification of Graphite Electrode Materials for Vanadium Redox Flow Battery Application—part II. Acid Treatments. *Electrochimica Acta* **1992**, *37* (13), 2459–2465.

(62) Sun, B.; Skyllas-Kazacos, M. Modification of Graphite Electrode Materials for Vanadium Redox Flow Battery Application—I. Thermal Treatment. *Electrochimica Acta* **1992**, *37* (7), 1253–1260.

(63) Zhong, S.; Padeste, C.; Kazacos, M.; Skyllas-Kazacos, M. Comparison of the Physical, Chemical and Electrochemical Properties of Rayon- and Polyacrylonitrile-Based Graphite Felt Electrodes. *Journal of Power Sources* **1993**, *45* (1), 29–41.

(64) Mohammadi, F.; Timbrell, P.; Zhong, S.; Padeste, C.; Skyllas-Kazacos, M. Overcharge in the Vanadium Redox Battery and Changes in Electrical Resistivity and Surface Functionality of Graphite-Felt Electrodes. *Journal of Power Sources* **1994**, *52* (1), 61–68.

(65) Haddadi-Asl, V.; Kazacos, M.; Skyllas-Kazacos, M. Conductive Carbon-Polypropylene Composite Electrodes for Vanadium Redox Battery. *Journal of Applied Electrochemistry* **1995**, *25* (1), 29–33.

(66) Li, X.; Zhang, H. H.; Mai, Z.; Zhang, H. H.; Vankelecom, I.; Lu, H.; Na, H.; Xing, W.; Ding, J. F.; Hu, J. Ion Exchange Membranes for Vanadium Redox Flow Battery (VRB) Applications. *Energy & Environmental Science* **2011**, *4* (4), 1147.

(67) Chieng, S. C.; Kazacos, M.; Skyllas-Kazacos, M. Preparation and Evaluation of Composite Membrane for Vanadium Redox Battery Applications. *Journal of Power Sources* **1992**, *39* (1), 11–19.

(68) Mohammadi, T.; Skyllas-Kazacos, M. Use of Polyelectrolyte for Incorporation

of Ion-Exchange Groups in Composite Membranes for Vanadium Redox Flow Battery Applications. *Journal of Power Sources* **1995**, *56* (1), 91–96.

(69) Mohammadi, T.; Kazacos, M. S. Modification of Anion-Exchange Membranes for Vanadium Redox Flow Battery Applications. *Journal of Power Sources* **1996**, *63* (2), 179–186.

(70) MOHAMMADI, T.; KAZACOS, M. S. Evaluation of the Chemical Stability of Some Membranes in Vanadium Solution. *Journal of Applied Electrochemistry* **1997**, *27* (2), 153–160.

(71) Sukkar, T.; Skyllas-Kazacos, M. Modification of Membranes Using Polyelectrolytes to Improve Water Transfer Properties in the Vanadium Redox Battery. *Journal of Membrane Science* **2003**, *222* (1), 249–264.

(72) Sukkar, T.; Skyllas-Kazacos, M. Membrane Stability Studies for Vanadium Redox Cell Applications. *Journal of Applied Electrochemistry* **2004**, *34* (2), 137–145.

(73) Leung, P.; Li, X.; León, C. P. de; Berlouis, L.; Low, C. T. J.; Walsh, F. C. Progress in Redox Flow Batteries, Remaining Challenges and Their Applications in Energy Storage. *RSC Advances* **2012**, *2* (27), 10125–10156.

(74) R. Zito, US Pat. 5612148, 1997 https://docs.google.com/viewer?url=patentimages.storage.googleapis.com/pdfs/US5612148.pdf (accessed Jun 2, 2017).

(75) Institution of Electrical Engineers., A.; Bartley, S.; Male, S.; Cooley, G. *Power Engineer.*; Institution of Electrical Engineers, 1999; Vol. 13.

(76) Walsh, F. C. Electrochemical Technology for Environmental Treatment and Clean Energy Conversion. *Pure and Applied Chemistry* **2001**, *73* (12), 1819–1837.

(77) Hazza, A.; Pletcher, D.; Wills, R.; Girenko, D. V.; Kovalyov, S. V.; Danilov, F. I. A Novel Flow Battery: A Lead Acid Battery Based on an Electrolyte with Soluble Lead(Ii). *Physical Chemistry Chemical Physics* **2004**, *6* (8), 1773.

(78) Pletcher, D.; Wills, R.; Wills, R.; Janney, P. A Novel Flow Battery: A Lead Acid Battery Based on an Electrolyte with Soluble Lead(Ii). *Physical Chemistry Chemical Physics* **2004**, *6* (8), 1779.

(79) Collins, J.; Kear, G.; Li, X.; Low, C. T. J.; Pletcher, D.; Tangirala, R.; Stratton-Campbell, D.; Walsh, F. C.; Zhang, C. A Novel Flow Battery: A Lead Acid Battery Based on an Electrolyte with Soluble Lead(II) Part VIII. The Cycling of a 10cm×10cm Flow Cell. *Journal of Power Sources* **2010**, *195* (6), 1731–1738.

(80) Cheng, J.; Zhang, L.; Yang, Y.-S.; Wen, Y.-H.; Cao, G.-P.; Wang, X.-D. Preliminary Study of Single Flow Zinc–nickel Battery. *Electrochemistry Communications* **2007**, *9* (11), 2639–2642.

(81) Zhang, L.; Cheng, J.; Yang, Y.; Wen, Y.; Wang, X.; Cao, G. Study of Zinc Electrodes for Single Flow Zinc/Nickel Battery Application. *Journal of Power Sources* **2008**, *179* (1), 381–387.

(82) Ito, Y.; Nyce, M.; Plivelich, R.; Klein, M.; Banerjee, S. *Gas Evolution in a Flow-Assisted Zinc–nickel Oxide Battery*; 2011; Vol. 196.

(83) Leung, P. K.; Ponce de León, C.; Walsh, F. C. An Undivided Zinc–cerium

Redox Flow Battery Operating at Room Temperature (295 K). *Electrochemistry Communications* **2011**, *13* (8), 770–773.

(84) Leung, P. K.; Ponce de Leon, C.; Walsh, F. C. The Influence of Operational Parameters on the Performance of an Undivided Zinc–cerium Flow Battery. *Electrochimica Acta* **2012**, *80*, 7–14.

(85) Duduta, M.; Ho, B.; Wood, V. C.; Limthongkul, P.; Brunini, V. E.; Carter, W. C.; Chiang, Y.-M. M. Semi-Solid Lithium Rechargeable Flow Battery. *Advanced Energy Materials* **2011**, *1* (4), 511–516.

(86) Lu, Y.; Goodenough, J. B.; Kim, Y. Aqueous Cathode for Next-Generation Alkali-Ion Batteries. *Journal of the American Chemical Society* **2011**, *133* (15), 5756–5759.

(87) Lu, Y.; Goodenough, J. B.; Na, H.; Liu, H.; Zhou, H.; Shao-Horn, Y. Rechargeable Alkali-Ion Cathode-Flow Battery. *Journal of Materials Chemistry* **2011**, *21* (27), 10113.

(88) Weber, A. Z.; Mench, M. M.; Meyers, J. P.; Ross, P. N.; Gostick, J. T.; Liu, Q. Redox Flow Batteries: A Review. *Journal of Applied Electrochemistry* **2011**, *41* (10), 1137–1164.

(89) Vázquez-Galván, J.; Flox, C.; Fàbrega, C.; Ventosa, E.; Parra, A.; Andreu, T.; Morante, J. R. R. R. R.; V?zquez-Galv?n, J.; Flox, C.; F?brega, C.; et al. Hydrogen-Treated Rutile TiO_2 Shell in Graphite-Core Structure as a Negative Electrode for High-Performance Vanadium Redox Flow Batteries. *ChemSusChem* **2017**, *10* (9), 2089–2098.

(90) Aaron, D.; Zhijiang, @bullet; @bullet, T.; Papandrew, A. B.; Zawodzinski, T. A. Polarization Curve Analysis of All-Vanadium Redox Flow Batteries. **2011**.

(91) Zhou, H.; Zhang, H.; Zhao, P.; Yi, B. A Comparative Study of Carbon Felt and Activated Carbon Based Electrodes for Sodium Polysulfide/Bromine Redox Flow Battery. *Electrochimica Acta* **2006**, *51* (28), 6304–6312.

(92) Thaller; H., L. Electrically Rechargeable Redox Flow Cells. **1974**.

(93) Thaller; H., L. Redox Flow Cell Energy Storage Systems. **1979**.

(94) Walsh, F. C. Electrochemical Technology for Environmental Treatment and Clean Energy Conversion*. *Pure Appl. Chem* **2001**, *73* (12), 1819–1837.

(95) Price, A.; Bartley, S.; Cooley, G.; Male, S. A Novel Approach to Utility-Scale Energy Storage. *Power Engineering Journal* **1999**, *13* (3), 122–129.

(96) Lessner, P. M.; McLarnon, F. R.; Winnick, J.; Cairns, E. J. Aqueous Polysulphide Flow-through Electrodes: Effects of Electrocatalyst and Electrolyte Composition on Performance. *Journal of Applied Electrochemistry* **1992**, *22* (10), 927–934.

(97) Yang, Z.; Zhang, J.; Kintner-Meyer, M. C. W.; Lu, X.; Choi, D.; Lemmon, J. P.; Liu, J. Electrochemical Energy Storage for Green Grid. *Chemical Reviews* **2011**, *111* (5), 3577–3613.

(98) Skyllas Kazacos M, Rychick M, Robins RG (1988) All-vana- dium redox battery. United States of America Patent https://docs.google.com/viewer?url=patentimages.storage.googleapis.com/pdfs/US4786567.pdf (accessed Jun 2, 2017).

(99) Rahman, F.; Skyllas-Kazacos, M. Vanadium Redox Battery: Positive Half-Cell Electrolyte Studies. *Journal of Power Sources* **2009**, *189* (2), 1212–1219.

(100) Sukkar, T.; Skyllas-Kazacos, M. Water Transfer Behaviour across Cation Exchange Membranes in the Vanadium Redox Battery. *Journal of Membrane Science* **2003**, *222* (1), 235–247.

(101) Zhao, P.; Zhang, H.; Zhou, H.; Chen, J.; Gao, S.; Yi, B. *Characteristics and Performance of 10kW Class All-Vanadium Redox-Flow Battery Stack*; 2006; Vol. 162.

(102) Skyllas-Kazacos, M. Thermal Stability of Concentrated V(V) Electrolytes in the Vanadium Redox Cell. *Journal of The Electrochemical Society* **1996**, *143* (4), L86.

(103) Skyllas-Kazacos, M. Novel Vanadium Chloride/Polyhalide Redox Flow Battery. *Journal of Power Sources* **2003**, *124* (1), 299–302.

(104) Skyllas-Kazacos, M.; Limantari, Y. Kinetics of the Chemical Dissolution of Vanadium Pentoxide in Acidic Bromide Solutions. *Journal of Applied Electrochemistry* **2004**, *34* (7), 681–685.

(105) Vafiadis, H.; Skyllas-Kazacos, M. Evaluation of Membranes for the Novel Vanadium Bromine Redox Flow Cell. *Journal of Membrane Science* **2006**, *279* (1), 394–402.

(106) Skyllas-Kazacos, M.; Kazacos, G.; Poon, G.; Verseema, H. Recent Advances with UNSW Vanadium-Based Redox Flow Batteries. *International Journal of Energy Research* **2010**, *34* (2), 182–189.

(107) Grigoriev, S. A.; Millet, P.; Porembsky, V. I.; Fateev, V. N. Development and Preliminary Testing of a Unitized Regenerative Fuel Cell Based on PEM Technology. *International Journal of Hydrogen Energy* **2011**, *36* (6), 4164–4168.

(108) Li, X.; Xiao, Y.; Shao, Z.; Yi, B. Mass Minimization of a Discrete Regenerative Fuel Cell (RFC) System for on-Board Energy Storage. *Journal of Power Sources* **2010**, *195* (15), 4811–4815.

(109) Fred Mitlitsky, *; Blake Myers, and; Weisberg, A. H. Regenerative Fuel Cell Systems. **1998**.

(110) Neyerlin, K. C.; Gu, W.; Jorne, J.; Gasteiger, H. A. Determination of Catalyst Unique Parameters for the Oxygen Reduction Reaction in a PEMFC. *Journal of The Electrochemical Society* **2006**, *153* (10), A1955.

(111) Kim, J. T.; Jorné, J. The Kinetics of a Chlorine Graphite Electrode in the Zinc-Chlorine Battery. *Journal of The Electrochemical Society* **1977**, *124* (10), 1473.

(112) Kosek, J. A.; Laconti, A. B. Advanced Hydrogen Electrode for a Hydrogen-Bromine Battery. *Journal of Power Sources* **1988**, *22* (3–4), 293–300.

(113) Livshits, V.; Ulus, A.; Peled, E. High-Power H2/Br2 Fuel Cell. *Electrochemistry Communications* **2006**, *8* (8), 1358–1362.

(114) Cathro, K. J.; Cedzynska, K.; Constable, D. C. Preparation and Performance of Plastic-Bonded-Carbon Bromine Electrodes. *Journal of Power Sources* **1987**, *19* (4), 337–356.

(115) Mader, M. J. A Mathematical Model of a Zn?Br[Sub 2] Cell on Charge. *Journal of The Electrochemical Society* **1986**, *133* (7), 1297.

(116) Redflow Energy Storage Solutions http://redflow.com/ (accessed Jun 19, 2017).

(117) Rechargeable Metal Halide Battery. **1971**.

(118) Hruska, L. W.; Savinell, R. F. Investigation of Factors Affecting Performance of the Iron-Redox Battery. *Journal of The Electrochemical Society* **1981**, *128* (1), 18.

(119) Sanz, L.; Lloyd, D.; Magdalena, E.; Palma, J.; Kontturi, K. Description and Performance of a Novel Aqueous All-Copper Redox Flow Battery. *Journal of Power Sources* **2014**, *268*, 121–128.

(120) Lloyd, D.; Vainikka, T.; Kontturi, K. The Development of an All Copper Hybrid Redox Flow Battery Using Deep Eutectic Solvents. *Electrochimica Acta* **2013**, *100*, 18–23.

(121) Sanz, L.; Palma, J.; García-Quismondo, E.; Anderson, M. The Effect of Chloride Ion Complexation on Reversibility and Redox Potential of the Cu(II)/Cu(I) Couple for Use in Redox Flow Batteries. *Journal of Power Sources* **2013**, *224*, 278–284.

(122) Raju, T.; Basha, C. A. Process Parameters and Kinetics for the Electrochemical Generation of Cerium(IV) Methanesulphonate from Cerium(III) Methanesulphonate. *Industrial & Engineering Chemistry Research* **2008**, *47* (22), 8947–8952.

(123) Matsuda, Y.; Tanaka, K.; Okada, M.; Takasu, Y.; Morita, M.; Matsumura-Inoue, T. A Rechargeable Redox Battery Utilizing Ruthenium Complexes with Non-Aqueous Organic Electrolyte. *Journal of Applied Electrochemistry 18* (6), 909–914.

(124) Chakrabarti, M. H.; Dryfe, R. A. W.; Roberts, E. P. L. Evaluation of Electrolytes for Redox Flow Battery Applications. *Electrochimica Acta* **2007**, *52* (5), 2189–2195.

(125) Yamamura, T.; Shiokawa, Y.; Yamana, H.; Moriyama, H. Electrochemical Investigation of Uranium ?-Diketonates for All-Uranium Redox Flow Battery. *Electrochimica Acta* **2002**, *48* (1), 43–50.

(126) Liu, Q.; Sleightholme, A. E. S.; Shinkle, A. A.; Li, Y.; Thompson, L. T. Non-Aqueous Vanadium Acetylacetonate Electrolyte for Redox Flow Batteries. *Electrochemistry Communications* **2009**, *11* (12), 2312–2315.

(127) Liu, Q.; Shinkle, A. A.; Li, Y.; Monroe, C. W.; Thompson, L. T.; Sleightholme, A. E. S. Non-Aqueous Chromium Acetylacetonate Electrolyte for Redox Flow Batteries. *Electrochemistry Communications* **2010**, *12* (11), 1634–1637.

(128) Sleightholme, A. E. S.; Shinkle, A. A.; Liu, Q.; Li, Y.; Monroe, C. W.; Thompson, L. T. Non-Aqueous Manganese Acetylacetonate Electrolyte for Redox Flow Batteries. *Journal of Power Sources* **2011**, *196* (13), 5742–5745.

(129) Sleightholme, A. E. S.; Shinkle, A. A.; Liu, Q.; Li, Y.; Monroe, C. W.; Thompson, L. T. Non - Aqueous Manganese Acetylacetonate Electrolyte for Redox Flow Batteries. *Journal of Power Sources* **2011**, *196*, 5742–5745.

(130) Kraytsberg, A.; Ein-Eli, Y. Review on Li?Air Batteries?Opportunities,

Limitations and Perspective. *Journal of Power Sources* **2011**, *196* (3), 886–893.

(131) CHIANG, Y.; CARTER, W. . C.; HO, B. Y.; DUDUTA, M. HIGH ENERGY DENSITY REDOX FLOW DEVICE. **2009**.

(132) Kazacos, M.; Cheng, M.; Skyllas-Kazacos, M. Vanadium Redox Cell Electrolyte Optimization Studies. *Journal of Applied Electrochemistry* **1990**, *20* (3), 463–467.

(133) Kazacos, M.; Skyllas-Kazacos, M. Performance Characteristics of Carbon Plastic Electrodes in the All-Vanadium Redox Cell. *Journal of The Electrochemical Society* **1989**, *136* (9), 2759.

(134) Skyllas-Kazacos, M.; Kasherman, D.; Hong, D. R.; Kazacos, M. Characteristics and Performance of 1 KW UNSW Vanadium Redox Battery. *Journal of Power Sources* **1991**, *35* (4), 399–404.

(135) Mohammadi, T.; Chieng, S. C.; Skyllas Kazacos, M. Water Transport Study across Commercial Ion Exchange Membranes in the Vanadium Redox Flow Battery. *Journal of Membrane Science* **1997**, *133* (2), 151–159.

(136) October 2011 No.73 | R&D | Sumitomo Electric Industries, Ltd. http://global-sei.com/technology/tr/bn73/ (accessed Jun 21, 2017).

(137) Xing, F.; Zhang, H.; Ma, X. Shunt Current Loss of the Vanadium Redox Flow Battery. *Journal of Power Sources* **2011**, *196* (24), 10753–10757.

(138) Shao, Y.; Wang, X.; Engelhard, M.; Wang, C.; Dai, S.; Liu, J.; Yang, Z.; Lin, Y. Nitrogen-Doped Mesoporous Carbon for Energy Storage in Vanadium Redox Flow Batteries. *Journal of Power Sources* **2010**, *195* (13), 4375–4379.

(139) Kim, S.; Tighe, T. B.; Schwenzer, B.; Yan, J.; Zhang, J.; Liu, J.; Yang, Z.; Hickner, M. A. Chemical and Mechanical Degradation of Sulfonated Poly(Sulfone) Membranes in Vanadium Redox Flow Batteries. *Journal of Applied Electrochemistry* **2011**, *41* (10), 1201–1213.

(140) Rahman, F.; Skyllas-Kazacos, M. Solubility of Vanadyl Sulfate in Concentrated Sulfuric Acid Solutions. *Journal of Power Sources* **1998**, *72* (2), 105–110.

(141) Teng, X.; Zhao, Y.; Xi, J.; Wu, Z.; Qiu, X.; Chen, L. Nafion/Organically Modified Silicate Hybrids Membrane for Vanadium Redox Flow Battery. *Journal of Power Sources* **2009**, *189* (2), 1240–1246.

(142) Skyllas-Kazacos, M.; Peng, C.; Cheng, M. Evaluation of Precipitation Inhibitors for Supersaturated Vanadyl Electrolytes for the Vanadium Redox Battery. *Electrochemical and Solid-State Letters* **1999**, *2* (3), 121.

(143) Kim, S.; Vijayakumar, M.; Wang, W.; Zhang, J.; Chen, B.; Nie, Z.; Chen, F.; Hu, J.; Li, L.; Yang, Z.; et al. Chloride Supporting Electrolytes for All-Vanadium Redox Flow Batteries. *Physical chemistry chemical physics : PCCP* **2011**, *13* (40), 18186–18193.

(144) Corcuera, S.; Skyllas-Kazacos, M. State-of-Charge Monitoring and Electrolyte Rebalancing Methods for the Vanadium Redox Flow Battery. *European Chemical Bulletin* **2012**, *1* (12), 511–519.

(145) Tang, A.; Bao, J.; Skyllas-Kazacos, M. Studies on Pressure Losses and Flow Rate Optimization in Vanadium Redox Flow Battery. *Journal of Power Sources*

2014, *248*, 154–162.

(146) Akhil, A. A.; Huff, G.; Currier, A. B.; Kaun, B. C.; Rastler, D. M.; Chen, S. B.; Cotter, A. L.; Bradshaw, D. T.; Gauntlett, W. D. SANDIA REPORT DOE / EPRI Electricity Storage Handbook in Collaboration with NRECA. **2015**, No. February.

(147) Chu, S.; Majumdar, A. Opportunities and Challenges for a Sustainable Energy Future. *Nature* **2012**, *488* (7411), 294–303.

(148) Carbajales-Dale, M.; Barnhart, C. J.; Benson, S. M. Can We Afford Storage? A Dynamic Net Energy Analysis of Renewable Electricity Generation Supported by Energy Storage. *Energy & Environmental Science* **2014**, *7* (5), 1538.

(149) *Medium-Term Renewable Energy Market Report 2016*; Medium-Term Renewable Energy Market Report; OECD, 2016.

(150) Doe. " RECOVERY ACT " FINANCIAL ASSISTANCE FUNDING OPPORTUNITY ANNOUNCEMENT U . S . Department of Energy - Headquarters Advanced Research Projects Agency – Energy (ARPA-E) Grid-Scale Rampable Intermittent Dispatchable Storage (GRIDS) Issue Date : Amended : *Energy* **2010**, 10.

(151) International Renewable Energy Agency (IRENA). *Electricity Storage and Renewables: Costs and Markets to 2030*; 2017.

(152) Darling, R. M.; Gallagher, K. G.; Kowalski, J. A.; Ha, S.; Brushett, F. R. Pathways to Low-Cost Electrochemical Energy Storage: A Comparison of Aqueous and Nonaqueous Flow Batteries. *Energy Environ. Sci.* **2014**, *7* (11), 3459–3477.

(153) Flox, C.; Skoumal, M.; Rubio-Garcia, J.; Andreu, T.; Morante, J. R. Strategies for Enhancing Electrochemical Activity of Carbon-Based Electrodes for All-Vanadium Redox Flow Batteries. *Applied Energy* **2013**, *109*, 344–351.

(154) Skoog, D. A.; Holler, F. J.; Crouch, S. R. *Principles of Instrumental Analysis*.

(155) Zawodzinski, T. A.; Sun, C.-N.; Aaron, D.; Hollmann, E.; Papandrew, A. B.; Mench, M. M. State of Charge Effects On the Performance of Vanadium Rfbs. *Meeting Abstracts* **2013**, *MA2013-02* (16), 1667–1667.

(156) Sun, C.-N.; Delnick, F. M.; Aaron, D. S.; Papandrew, A. B.; Mench, M. M.; Zawodzinski, T. A. Probing Electrode Losses in All-Vanadium Redox Flow Batteries with Impedance Spectroscopy. *ECS Electrochemistry Letters* **2013**, *2* (5), A43–A45.

(157) Liu, Q.; Turhan, A.; Zawodzinski, T. A.; Mench, M. M.; Zawodzinski, T. A.; Mench, M. M.; Mench, M. M.; Cui, G. L.; Hu, J. Z.; Graff, G.; et al. In Situ Potential Distribution Measurement in an All-Vanadium Flow Battery. *Chemical Communications* **2013**, *49* (56), 6292.

(158) You, D.; Zhang, H.; Chen, J. A Simple Model for the Vanadium Redox Battery. *Electrochimica Acta* **2009**, *54* (27), 6827–6836.

(159) Vijayakumar, M.; Li, L.; Graff, G.; Liu, J.; Zhang, H.; Yang, Z.; Hu, J. Z. Towards Understanding the Poor Thermal Stability of V5+ Electrolyte Solution in Vanadium Redox Flow Batteries. *Journal of Power Sources* **2011**, *196* (7), 3669–3672.

(160) High Energy Density Vanadium Electrolyte Solutions, Methods of Preparation Thereof and All-Vanadium Redox Cells and Batteries Containing High Energy Vanadium Electrolyte Solutions. **2002**.

(161) Flox, C.; Rubio-Garcia, J.; Skoumal, M.; Vázquez-Galván, J.; Ventosa, E.; Morante, J. R. Thermally Stable Positive Electrolytes with a Superior Performance in All-Vanadium Redox Flow Batteries. *ChemPlusChem* **2015**, *80* (2), 354–358.

(162) Li, S.; Huang, K.; Liu, S.; Fang, D.; Wu, X.; Lu, D.; Wu, T. Effect of Organic Additives on Positive Electrolyte for Vanadium Redox Battery. *Electrochimica Acta* **2011**, *56* (16), 5483–5487.

(163) Lei, Y.; Liu, S. -q.; Gao, C.; Liang, X. -x.; He, Z. -x.; Deng, Y. -h.; He, Z. Effect of Amino Acid Additives on the Positive Electrolyte of Vanadium Redox Flow Batteries. *Journal of the Electrochemical Society* **2013**, *160* (4), A722–A727.

(164) Wu, X.; Liu, S.; Wang, N.; Peng, S.; He, Z. Influence of Organic Additives on Electrochemical Properties of the Positive Electrolyte for All-Vanadium Redox Flow Battery. *Electrochimica Acta* **2012**, *78*, 475–482.

(165) Flox, C.; Rubio-García, J.; Skoumal, M.; Andreu, T.; Morante, J. R. Thermo–chemical Treatments Based on NH3/O2 for Improved Graphite-Based Fiber Electrodes in Vanadium Redox Flow Batteries. *Carbon* **2013**, *60*, 280–288.

(166) Chen, F.; Liu, J.; Chen, H.; Yan, C. Study on Hydrogen Evolution Reaction at a Graphite Electrode in the All-Vanadium Redox Flow Battery. **2012**, *7*, 3750–3764.

(167) Sun, C.-N.; Delnick, F. M.; Baggetto, L.; Veith, G. M.; Zawodzinski, T. a. Hydrogen Evolution at the Negative Electrode of the All-Vanadium Redox Flow Batteries. *Journal of Power Sources* **2014**, *248*, 560–564.

(168) Ventosa, E.; Skoumal, M.; Vázquez, F. J.; Flox, C.; Morante, J. R. Operando Studies of All-Vanadium Flow Batteries: Easy-to-Make Reference Electrode Based on Silver–silver Sulfate. *Journal of Power Sources* **2014**, *271*, 556–560.

(169) Li, B.; Gu, M.; Nie, Z.; Shao, Y.; Luo, Q.; Wei, X.; Li, X.; Xiao, J.; Wang, C.; Sprenkle, V.; et al. Bismuth Nanoparticle Decorating Graphite Felt as a High-Performance Electrode for an All-Vanadium Redox Flow Battery. *Nano letters* **2013**, *13* (3), 1330–1335.

(170) Li, B.; Gu, M.; Nie, Z.; Wei, X.; Wang, C.; Sprenkle, V.; Wang, W. Nanorod Niobium Oxide as Powerful Catalysts for an All Vanadium Redox Flow Battery. *Nano letters* **2014**, *14* (1), 158–165.

(171) Park, M.; Ryu, J.; Kim, Y.; Cho, J.; Hsueh, K. L.; Shieu, F. S.; Idrobo, J. C.; Pennycook, S. J.; Dai, H.; Sprenkle, V.; et al. Corn Protein-Derived Nitrogen-Doped Carbon Materials with Oxygen-Rich Functional Groups: A Highly Efficient Electrocatalyst for All-Vanadium Redox Flow Batteries. *Energy Environ. Sci.* **2014**, *7* (11), 3727–3735.

(172) Zhou, H.; Shen, Y.; Xi, J.; Qiu, X.; Chen, L. ZrO2-Nanoparticle-Modified Graphite Felt: Bifunctional Effects on Vanadium Flow Batteries. *ACS Applied Materials and Interfaces* **2016**, *8* (24), 15369–15378.

(173) Kim, K. J.; Lee, S.-W.; Yim, T.; Kim, J.-G. J. H.; Choi, J. W.; Kim, J.-G. J. H.;

Park, M.-S.; Kim, Y.-J. A New Strategy for Integrating Abundant Oxygen Functional Groups into Carbon Felt Electrode for Vanadium Redox Flow Batteries. *Scientific reports* **2014**, *4*, 6906.

(174) Park, M.; Jeon, I.-Y. Y.; Ryu, J.; Baek, J.-B. B.; Cho, J. Exploration of the Effective Location of Surface Oxygen Defects in Graphene-Based Electrocatalysts for All-Vanadium Redox-Flow Batteries. *Advanced Energy Materials* **2015**, *5* (5), 1–7.

(175) Park, M.; Jung, Y.; Kim, J.; Lee, H. il; Cho, J. Synergistic Effect of Carbon Nanofiber/Nanotube Composite Catalyst on Carbon Felt Electrode for High-Performance All-Vanadium Redox Flow Battery. *Nano Letters* **2013**, *13* (10), 4833–4839.

(176) Kim, K. J.; Park, M.-S.; Kim, J.-H.; Hwang, U.; Lee, N. J.; Jeong, G.; Kim, Y.-J.; Lin, Y. Novel Catalytic Effects of Mn3O4 for All Vanadium Redox Flow Batteries. *Chemical communications (Cambridge, England)* **2012**, *48* (44), 5455–5457.

(177) Yao, C.; Zhang, H.; Liu, T.; Li, X.; Liu, Z. Carbon Paper Coated with Supported Tungsten Trioxide as Novel Electrode for All-Vanadium Flow Battery. *Journal of Power Sources* **2012**, *218*, 455–461.

(178) Wu, X.; Xu, H.; Xu, P.; Shen, Y.; Lu, L.; Shi, J.; Fu, J.; Zhao, H.; Fu, J.; Shen, Y.; et al. PbO2-Modified Graphite Felt as the Positive Electrode for an All-Vanadium Redox Flow Battery. *Journal of Power Sources* **2014**, *250*, 274–278.

(179) Zhou, H.; Shen, Y.; Xi, J.; Qiu, X.; Chen, L. ZrO_2 -Nanoparticle-Modified Graphite Felt: Bifunctional Effects on Vanadium Flow Batteries. *ACS Applied Materials & Interfaces* **2016**, *8* (24), 15369–15378.

(180) Tseng, T.-M. T.-M. T.-M.; Huang, R.-H. R.-H.; Huang, C.-Y. C.-Y.; Hsueh, K.-L. K.-L.; Shieu, F.-S. F.-S. Improvement of Titanium Dioxide Addition on Carbon Black Composite for Negative Electrode in Vanadium Redox Flow Battery. *Journal of the Electrochemical Society* **2013**, *160* (8), A1269–A1275.

(181) Tseng, T.-M. T.-M. T.-M. T.-M.; Huang, R.-H. R.-H. R.-H.; Huang, C.-Y. C.-Y.; Liu, C.-C. C.-C. C.-C.; Hsueh, K.-L. K.-L. K.-L.; Shieu, F.-S. F.-S. F.-S. Carbon Felt Coated with Titanium Dioxide/Carbon Black Composite as Negative Electrode for Vanadium Redox Flow Battery. *Journal of the Electrochemical Society* **2014**, *161* (6), A1132–A1138.

(182) Diebold, U. The Surface Science of Titanium Dioxide. *Surface Science Reports* **2003**, *48* (5–8), 53–229.

(183) Chen, X.; Mao, S. S. Titanium Dioxide Nanomaterials: Synthesis, Properties, Modifications, and Applications. *Chemical reviews* **2007**, *107* (7), 2891–2959.

(184) Ryu, J.; Choi, W. Substrate-Specific Photocatalytic Activities of TiO2 and Multiactivity Test for Water Treatment Application. *Environmental science & technology* **2008**, *42* (1), 294–300.

(185) Fabrega, C.; Andreu, T.; Morante, J. R. Acidic and Basic Sites in Iron Modified Nano-TiO₂ for Gas Sensors. *Sensor Letters* **2008**, *6* (6), 1041–1044.

(186) Epifani, M.; Andreu, T.; Zamani, R.; Arbiol, J.; Comini, E.; Siciliano, P.; Faglia, G.; Morante, J. R. Pt Doping Triggers Growth of TiO2 Nanorods: Nanocomposite Synthesis and Gas-Sensing Properties. *CrystEngComm* **2012**, *14* (11), 3882.

(187) Lietti, L.; Forzatti, P.; Bregani, F. Steady-State and Transient Reactivity Study of TiO 2 -Supported V 2 O 5 - WO 3 De-NO x Catalysts : Relevance of the Vanadium - Tungsten Interaction on the Catalytic Activity. *Industrial & Engineering Chemistry Research* **1996**, *35*, 3884–3892.

(188) Tran, T.; McCormac, K.; Li, J.; Bi, Z.; Wu, J. Electrospun SnO2 and TiO2 Composite Nanofibers for Lithium Ion Batteries. *Electrochimica Acta* **2014**, *117*, 68–75.

(189) Ventosa, E.; Skoumal, M.; Vazquez, F. J.; Flox, C.; Arbiol, J.; Morante, J. R. Electron Bottleneck in the Charge/Discharge Mechanism of Lithium Titanates for Batteries. *ChemSusChem* **2015**, *8* (10), 1737–1744.

(190) Yan, Y.; Han, M.; Konkin, A.; Koppe, T.; Wang, D.; Andreu, T.; Chen, G.; Vetter, U.; Morante, J. R.; Schaaf, P. Slightly Hydrogenated TiO $_2$ with Enhanced Photocatalytic Performance. *Journal of Materials Chemistry A* **2014**, *2* (32), 12708.

(191) Manzanares, M.; Fàbrega, C.; Oriol Ossó, J.; Vega, L. F.; Andreu, T.; Morante, J. R. Engineering the TiO2 Outermost Layers Using Magnesium for Carbon Dioxide Photoreduction. *Applied Catalysis B: Environmental* **2014**, *150–151*, 57–62.

(192) Quaino, P.; Juarez, F.; Santos, E.; Schmickler, W. Volcano Plots in Hydrogen Electrocatalysis - Uses and Abuses. *Beilstein journal of nanotechnology* **2014**, *5* (1), 846–854.

(193) N?rskov, J. K.; Bligaard, T.; Logadottir, a.; Kitchin, J. R.; Chen, J. G.; Pandelov, S.; Stimming, U.; Nørskov, J. K.; Bligaard, T.; Logadottir, a.; et al. Trends in the Exchange Current for Hydrogen Evolution. *Journal of The Electrochemical Society* **2005**, *152* (3), J23.

(194) Trasatti, S. WORK FUNCTION , ELECTRONEGATIVITY , AND ELECTROCHEMICAL BEHAVIOUR OF METALS III . ELECTROLYTIC HYDROGEN EVOLUTION IN ACID SOLUTIONS Although the Dependence of Hydrogen Overvoltage (QH) on Electrode Material Was Experimentally Recognized at the Beginning. **1972**, *39*, 163–184.

(195) Islam, M. M.; Calatayud, M.; Pacchioni, G. Hydrogen Adsorption and Diffusion on the Anatase TiO 2 (101) Surface : A First-Principles Investigation. **2011**, *2* (101), 6809–6814.

(196) Barnard, A. S.; Zapol, P. Effects of Particle Morphology and Surface Hydrogenation on the Phase Stability of Ti O 2. *Physical Review B* **2004**, *70* (23), 235403.

(197) Yin, X.-L.; Calatayud, M.; Qiu, H.; Wang, Y.; Birkner, a; Minot, C.; Wöll, C. Diffusion versus Desorption: Complex Behavior of H Atoms on an Oxide Surface. *Chemphyschem : a European journal of chemical physics and physical chemistry* **2008**, *9* (2), 253–256.

(198) Morgan, B. J.; Watson, G. W. A Density Functional Theory + u Study of Oxygen Vacancy Formation at the (110), (100), (101), and (001) Surfaces of Rutile TiO2. *Journal of Physical Chemistry C* **2009**, *113* (17), 7322–7328.

(199) Wang, G.; Wang, H.; Ling, Y.; Tang, Y.; Yang, X.; Fitzmorris, R. C.; Wang, C.; Zhang, J. Z.; Li, Y. Hydrogen-Treated TiO2 Nanowire Arrays for Photoelectrochemical Water Splitting. *Nano Letters* **2011**, *11* (7), 3026–3033.

(200) Biesinger, M. C.; Lau, L. W. M.; Gerson, A. R.; Smart, R. S. C. Resolving Surface Chemical States in XPS Analysis of First Row Transition Metals, Oxides and Hydroxides: Sc, Ti, V, Cu and Zn. *Applied Surface Science* **2010**, *257* (3), 887–898.

(201) Pan, X.; Yang, M.-Q.; Fu, X.; Zhang, N.; Xu, Y.-J. Defective TiO2 with Oxygen Vacancies: Synthesis, Properties and Photocatalytic Applications. *Nanoscale* **2013**, *5* (9), 3601.

(202) Morgan, B. J.; Watson, G. W. Intrinsic N-Type Defect Formation in TiO2: A Comparison of Rutile and Anatase from GGA+U Calculations. *Journal of Physical Chemistry C* **2010**, *114* (5), 2321–2328.

(203) Wang, S.; Zhao, X.; Cochell, T.; Manthiram, A. Nitrogen-Doped Carbon Nanotube/Graphite Felts as Advanced Electrode Materials for Vanadium Redox Flow Batteries. *Journal of Physical Chemistry Letters* **2012**, *3* (16), 2164–2167.

(204) Wang , S.; Iyyamperumal , E.; Roy, A.; Xue, Y.; Yu, D.; Dai, L. Vertically Aligned BCN Nanotubes as Efficient Metal-Free Electrocatalysts for the Oxygen Reduction Reaction: A Synergetic Effect by Co-Doping with Boron and Nitrogen. *Angewandte Chemie International Edition* **2011**, *50* (49), 11756–11760.

(205) Gong, K.; Du, F.; Xia, Z.; Durstock, M.; Dai, L. Nitrogen-Doped Carbon Nanotube Arrays with High Electrocatalytic Activity for Oxygen Reduction. *Science (New York, N.Y.)* **2009**, *323* (5915), 760–764.

(206) Rao, C. V.; Cabrera, C. R.; Ishikawa, Y. In Search of the Active Site in Nitrogen-Doped Carbon Nanotube Electrodes for the Oxygen Reduction Reaction. *The Journal of Physical Chemistry Letters* **2010**, *1* (18), 2622–2627.

(207) Yu, D.; Nagelli, E.; Du, F.; Dai, L. Metal-Free Carbon Nanomaterials Become More Active than Metal Catalysts and Last Longer. *The Journal of Physical Chemistry Letters* **2010**, *1* (14), 2165–2173.

(208) Kim, K. J.; Kim, Y.-J. J.; Kim, J.-H. H.; Park, M.-S. S. The Effects of Surface Modification on Carbon Felt Electrodes for Use in Vanadium Redox Flow Batteries. *Materials Chemistry and Physics* **2011**, *131* (1–2), 547–553.

(209) Kabir, H.; Gyan, I. O.; Francis Cheng, I. Electrochemical Modification of a Pyrolytic Graphite Sheet for Improved Negative Electrode Performance in the Vanadium Redox Flow Battery. *Journal of Power Sources* **2017**, *342*, 31–37.

(210) Liu, T.; Li, X.; Xu, C.; Zhang, H. Activated Carbon Fiber Paper Based Electrodes with High Electrocatalytic Activity for Vanadium Flow Batteries with Improved Power Density. *ACS Applied Materials & Interfaces* **2017**, acsami.6b14478.

(211) Vohra, M. S.; Selimuzzaman, S. M.; Al-Suwaiyan, M. S. NH4 +-NH3 Removal from Simulated Wastewater Using UV-TiO2 Photocatalysis: Effect of Co-pollutants and PH. *Environmental Technology* **2010**, *31* (6), 641–654.

(212) Li, J.; Gao, L.; Sun, J.; Zhang, Q.; Guo, J.; Yan, D. Synthesis of Nanocrystalline Titanium Nitride Powders by Direct Nitridation of Titanium Oxide.

(213) Alexander, M. R.; Thompson, G. E.; Zhou, X.; Beamson, G.; Fairley, N. Quantification of Oxide Film Thickness at the Surface of Aluminium Using XPS. *Surface and Interface Analysis* **2002**, *34* (1), 485–489.

(214) Lu, Z. H.; McCaffrey, J. P.; Brar, B.; Wilk, G. D.; Wallace, R. M.; Feldman, L. C.; Tay, S. P. SiO2 Film Thickness Metrology by X-Ray Photoelectron Spectroscopy. *Applied Physics Letters* **1997**, *71* (19), 2764–2766.

(215) Amano, F.; Nakata, M.; Yamamoto, A.; Tanaka, T. Effect of Ti3+ Ions and Conduction Band Electrons on Photocatalytic and Photoelectrochemical Activity of Rutile Titania for Water Oxidation. *Journal of Physical Chemistry C* **2016**, *120* (12), 6467–6474.

(216) Henrich, V. E.; Cox, P. A. *The Surface Science of Metal Oxides*; Cambridge University Press, 1994.

(217) Zhang, Z.; Goodall, J. B. M.; Morgan, D. J.; Brown, S.; Clark, R. J. H.; Knowles, J. C.; Mordan, N. J.; Evans, J. R. G.; Carley, A. F.; Bowker, M.; et al. Photocatalytic Activities of N-Doped Nano-Titanias and Titanium Nitride. *Journal of the European Ceramic Society* **2009**, *29* (11), 2343–2353.

(218) Martínez-Ferrero, E.; Sakatani, Y.; Boissière, C.; Grosso, D.; Fuertes, A.; Fraxedas, J.; Sanchez, C. Nanostructured Titanium Oxynitride Porous Thin Films as Efficient Visible-Active Photocatalysts. *Advanced Functional Materials* **2007**, *17* (16), 3348–3354.

(219) Irie, H.; Watanabe, Y.; Hashimoto, K. Nitrogen-Concentration Dependence on Photocatalytic Activity of TiO 2-x N x Powders.

(220) Wu, Z.; Dong, F.; Zhao, W.; Guo, S. Visible Light Induced Electron Transfer Process over Nitrogen Doped TiO 2 Nanocrystals Prepared by Oxidation of Titanium Nitride. *Journal of Hazardous Materials* **2008**, *157*, 57–63.

(221) Vázquez Galván, J.; Flox, C.; Fabregas, C.; Ventosa, E.; Parra, A.; Andreu, T.; Morante, J. R. Hydrogen Treated Rutile TiO2 Shell in Graphite Core Structure as a Negative Electrode for High-Performance Vanadium Flow Batteries. *ChemSusChem* **2017**.

(222) Bard, A. J.; Faulkner, L. R.; York, N.; @bullet, C.; Brisbane, W.; Toronto, S. E. *ELECTROCHEMICAL METHODS Fundamentals and Applications*; 1944.

(223) Fink, H.; Friedl, J.; Stimming, U. Composition of the Electrode Determines Which Half-Cell's Rate Constant Is Higher in a Vanadium Flow Battery.

(224) Li, S. C.; Zhang, Z.; Sheppard, D.; Kay, B. D.; White, J. M.; Du, Y.; Lyubinetsky, I.; Henkelman, G.; Dohnálek, Z. Intrinsic Diffusion of Hydrogen on Rutile TiO2(110). *Journal of the American Chemical Society* **2008**, *130* (28), 9080–9088.

(225) Li, W.; Liu, J.; Yan, C. Multi-Walled Carbon Nanotubes Used as an Electrode Reaction Catalyst for VO2+/VO2+ for a Vanadium Redox Flow Battery. *Carbon* **2011**, *49* (11), 3463–3470.

(226) Wei, L.; Zhao, T. S.; Zeng, L.; Zeng, Y. K.; Jiang, H. R. Highly Catalytic and Stabilized Titanium Nitride Nanowire Array-Decorated Graphite Felt Electrodes for All Vanadium Redox Flow Batteries. *Journal of Power Sources*

2017, *341*, 318–326.

(227) Kim, K. J.; Park, M.-S.; Kim, Y.-J.; Kim, J. H.; Dou, S. X.; Skyllas-Kazacos, M.; Srinivasan, M. P.; Yan, Q.; Madhavi, S.; Sprenkle, V.; et al. A Technology Review of Electrodes and Reaction Mechanisms in Vanadium Redox Flow Batteries. **2015**, *3* (33), 16913–16933.

(228) Liu, M.; Xiang, Z.; Piao, J.; Shi, J.; Liang, Z. Electrochemistry of Vanadium Redox Couples on Nitrogen-Doped Carbon. *Electrochimica Acta* **2018**, *259*, 687–693.

(229) Jin, J.; Fu, X.; Liu, Q.; Liu, Y.; Wei, Z.; Niu, K.; Zhang, J. Identifying the Active Site in Nitrogen-Doped Graphene for the VO^{2+} /VO_2^{+} Redox Reaction. *ACS Nano* **2013**, *7* (6), 4764–4773.

(230) Kim, J.; Lim, H.; Jyoung, J.-Y.; Lee, E.-S.; Yi, J. S.; Lee, D. Effects of Doping Methods and Kinetic Relevance of N and O Atomic Co-Functionalization on Carbon Electrode for V(IV)/V(V) Redox Reactions in Vanadium Redox Flow Battery. *Electrochimica Acta* **2017**, *245*, 724–733.

(231) Xu, C.; Yang, X.; Li, X.; Liu, T.; Zhang, H. Ultrathin Free-Standing Electrospun Carbon Nanofibers Web as the Electrode of the Vanadium Flow Batteries. *Journal of Energy Chemistry* **2017**, *26* (4), 730–737.

(232) Wang, W. H.; Wang, X. D. Investigation of Ir-Modified Carbon Felt as the Positive Electrode of an All-Vanadium Redox Flow Battery. *Electrochimica Acta* **2007**, *52* (24), 6755–6762.

(233) Yue, L.; Li, W.; Sun, F.; Zhao, L.; Xing, L. Highly Hydroxylated Carbon Fibres as Electrode Materials of All-Vanadium Redox Flow Battery. *Carbon* **2010**, *48* (11), 3079–3090.

(234) Yun, N.; Park, J. J.; Park, O. O.; Lee, K. B.; Yang, J. H. Electrocatalytic Effect of NiO Nanoparticles Evenly Distributed on a Graphite Felt Electrode for Vanadium Redox Flow Batteries. *Electrochimica Acta* **2018**, *278*, 226–235.

(235) Bayeh, A. W.; Kabtamu, D. M.; Chang, Y.-C.; Chen, G.-C.; Chen, H.-Y.; Lin, G.-Y.; Liu, T.-R.; Wondimu, T. H.; Wang, K.-C.; Wang, C.-H. Synergistic Effects of a $TiNb_2O_7$ –reduced Graphene Oxide Nanocomposite Electrocatalyst for High-Performance All-Vanadium Redox Flow Batteries. *Journal of Materials Chemistry A* **2018**, *6* (28), 13908–13917.

(236) Wang, W.; Luo, Q.; Li, B.; Wei, X.; Li, L.; Yang, Z. Recent Progress in Redox Flow Battery Research and Development. *Advanced Functional Materials* **2013**, *23* (8), 970–986.

(237) Perry, M. L.; Weber, A. Z. Advanced Redox-Flow Batteries: A Perspective. *Journal of The Electrochemical Society* **2016**, *163* (1), A5064–A5067.

(238) Shah, A. A.; Watt-Smith, M. J.; Walsh, F. C. A Dynamic Performance Model for Redox-Flow Batteries Involving Soluble Species. *Electrochimica Acta* **2008**, *53* (27), 8087–8100.

(239) Watt-Smith, M. J.; Ridley, P.; Wills, R. G. A.; Shah, A. A.; Walsh, F. C. The Importance of Key Operational Variables and Electrolyte Monitoring to the Performance of an All Vanadium Redox Flow Battery. *Journal of Chemical Technology & Biotechnology* **2013**, *88* (1), 126–138.

(240) Winsberg, J.; Hagemann, T.; Janoschka, T.; Hager, M. D.; Schubert, U. S. Redox-Flow Batteries: From Metals to Organic Redox-Active Materials.

Angewandte Chemie - International Edition **2017**, *56* (3), 686–711.

(241) Roe, S.; Menictas, C.; Skyllas-Kazacos, M. A High Energy Density Vanadium Redox Flow Battery with 3 M Vanadium Electrolyte. *Journal of The Electrochemical Society* **2016**, *163* (1), A5023–A5028.

(242) Armand, M.; Tarascon, J.-M. Building Better Batteries. *Nature* **2008**, *451* (7179), 652–657.

(243) Barnhart, C. J.; Benson, S. M.; Cui, Y.; McGregor, P. G.; Mulheran, P. a.; Hall, P. J.; Zavadil, B. On the Importance of Reducing the Energetic and Material Demands of Electrical Energy Storage. *Energy & Environmental Science* **2013**, *6* (4), 1083.

(244) Lai, Q.; Zhang, H.; Li, X.; Zhang, L.; Cheng, Y. A Novel Single Flow Zinc?Bromine Battery with Improved Energy Density. *Journal of Power Sources* **2013**, *235*, 1–4.

(245) Wen, Y. H.; Zhang, H. M.; Qian, P.; Zhou, H. T.; Zhao, P.; Yi, B. L.; Yang, Y. S. Studies on Iron (Fe[Sup 3+]?Fe[Sup 2+])-Complex/Bromine (Br[Sub 2]?Br[Sup ?]) Redox Flow Cell in Sodium Acetate Solution. *Journal of The Electrochemical Society* **2006**, *153* (5), A929.

(246) Kim, J.-H.; Kim, K. J.; Park, M.-S.; Lee, N. J.; Hwang, U.; Kim, H.; Kim, Y.-J. Development of Metal-Based Electrodes for Non-Aqueous Redox Flow Batteries. *Electrochemistry Communications* **2011**, *13* (9), 997–1000.

(247) Wei, X.; Xu, W.; Vijayakumar, M.; Cosimbescu, L.; Liu, T.; Sprenkle, V.; Wang, W. TEMPO-Based Catholyte for High-Energy Density Nonaqueous Redox Flow Batteries. *Advanced Materials* **2014**, *26* (45), 7649–7653.

(248) Chen, Q.; Gerhardt, M. R.; Hartle, L.; Aziz, M. J. A Quinone-Bromide Flow Battery with 1 W/Cm2 Power Density. *Journal of the Electrochemical Society* **2015**, *163* (1), A5010–A5013.

(249) Huskinson, B.; Marshak, M. P.; Suh, C.; Er, S.; Gerhardt, M. R.; Galvin, C. J.; Chen, X.; Aspuru-Guzik, A.; Gordon, R. G.; Aziz, M. J. A Metal-Free Organic– –inorganic Aqueous Flow Battery. **2014**.

(250) Li, Z.; Li, S.; Liu, S.; Huang, K.; Fang, D.; Wang, F.; Peng, S. Electrochemical Properties of an All-Organic Redox Flow Battery Using 2,2,6,6-Tetramethyl-1-Piperidinyloxy and N-Methylphthalimide. *Electrochemical and Solid-State Letters* **2011**, *14* (12), A171.

(251) Potash, R. A.; McKone, J. R.; Conte, S.; Abru?a, H. D. On the Benefits of a Symmetric Redox Flow Battery. *Journal of The Electrochemical Society* **2016**, *163* (3), A338–A344.

(252) Bard, A. J.; Faulkner, L. R. *Electrochemical Methods : Fundamentals and Applications*; Wiley, 2001.

(253) Zhao, Y.; Si, S.; Liao, C. A Single Flow Zinc//Polyaniline Suspension Rechargeable Battery. *Journal of Power Sources* **2013**, *241*, 449–453.

(254) Takechi, K.; Kato, Y.; Hase, Y. A Highly Concentrated Catholyte Based on a Solvate Ionic Liquid for Rechargeable Flow Batteries. *Advanced Materials* **2015**, *27* (15), 2501–2506.

(255) Xu, Y.; Wen, Y.; Cheng, J.; Cao, G.; Yang, Y. Study on a Single Flow Acid Cd?Chloranil Battery. *Electrochemistry Communications* **2009**, *11* (7), 1422–

1424.

(256) Oh, S. H.; Lee, C.-W.; Chun, D. H.; Jeon, J.-D.; Shim, J.; Shin, K. H.; Yang, J. H.; Hennig, R. G.; Abruňa, H. D. A Metal-Free and All-Organic Redox Flow Battery with Polythiophene as the Electroactive Species. *J. Mater. Chem. A* **2014**, *2* (47), 19994–19998.

(257) Xu, Y.; Wen, Y.-H.; Cheng, J.; Cao, G.-P.; Yang, Y.-S. A Study of Tiron in Aqueous Solutions for Redox Flow Battery Application. *Electrochimica Acta* **2010**, *55* (3), 715–720.

(258) Huang, J.; Cheng, L.; Assary, R. S.; Wang, P.; Xue, Z.; Burrell, A. K.; Curtiss, L. A.; Zhang, L. Liquid Catholyte Molecules for Nonaqueous Redox Flow Batteries. *Advanced Energy Materials* **2015**, *5* (6), 1401782.

(259) Liu, T.; Wei, X.; Nie, Z.; Sprenkle, V.; Wang, W. A Total Organic Aqueous Redox Flow Battery Employing a Low Cost and Sustainable Methyl Viologen Anolyte and 4-HO-TEMPO Catholyte. *Advanced Energy Materials* **2016**, *6* (3), 1501449.

(260) Wei, X.; Xu, W.; Huang, J.; Zhang, L.; Walter, E.; Lawrence , C.; Vijayakumar, M.; Henderson, W. A.; Liu, T.; Cosimbescu, L.; et al. Radical Compatibility with Nonaqueous Electrolytes and Its Impact on an All-Organic Redox Flow Battery. *Angewandte Chemie International Edition* **2015**, *54* (30), 8684–8687.

(261) Zeng, Y. K.; Zhao, T. S.; An, L.; Zhou, X. L.; Wei, L. A Comparative Study of All-Vanadium and Iron-Chromium Redox Flow Batteries for Large-Scale Energy Storage. *Journal of Power Sources* **2015**, *300*, 438–443.

(262) Bachman, J. E.; Curtiss, L. A.; Assary, R. S. Investigation of the Redox Chemistry of Anthraquinone Derivatives Using Density Functional Theory. *The Journal of Physical Chemistry A* **2014**, *118* (38), 8852–8860.

(263) May Quan; Daniel Sanchez; Mark F. Wasylkiw, and; Smith*, D. K. Voltammetry of Quinones in Unbuffered Aqueous Solution: Reassessing the Roles of Proton Transfer and Hydrogen Bonding in the Aqueous Electrochemistry of Quinones. **2007**.

(264) Lin, K.; Chen, Q.; Gerhardt, M. R.; Tong, L.; Kim, S. B.; Eisenach, L.; Valle, A. W.; Hardee, D.; Gordon, R. G.; Aziz, M. J.; et al. Alkaline Quinone Flow Battery. *Science (New York, N.Y.)* **2015**, *349* (6255), 1529–1532.

(265) Zhang, S.; Li, X.; Chu, D. An Organic Electroactive Material for Flow Batteries. *Electrochimica Acta* **2016**, *190*, 737–743.

(266) Electrochemical Investigation of Quinone-Hydroquinone Couples in Molten Acetamide at 85°C. *Journal of Electroanalytical Chemistry and Interfacial Electrochemistry* **1985**, *187* (1), 187–195.

(267) Hale, J. M.; Parsons, R. Reduction of P-Quinones at a Dropping Mercury Electrode. *Transactions of the Faraday Society* **1963**, *59* (0), 1429.

(268) Understanding the Linear Correlation between Diffusion Coefficient and Molecular Weight. A Model to Estimate Diffusion Coefficients in Acetonitrile Solutions. *Electrochemistry Communications* **2011**, *13* (2), 129–132.

(269) Effect of Oxygen Plasma Treatment on the Electrochemical Performance of the Rayon and Polyacrylonitrile Based Carbon Felt for the Vanadium Redox Flow Battery Application. *Journal of Power Sources* **2016**, *332*, 240–248.

(270) Nitric Acid Activation of Graphite Granules to Increase the Performance of the Non-Catalyzed Oxygen Reduction Reaction (ORR) for MFC Applications. *Electrochemistry Communications* **2009**, *11* (7), 1547–1549.

(271) Zickler, G. A.; Smarsly, B.; Gierlinger, N.; Peterlik, H.; Paris, O. A Reconsideration of the Relationship between the Crystallite Size L a of Carbons Determined by X-Ray Diffraction and Raman Spectroscopy. **2006**.

(272) Langston, T. A.; Granata, R. D. Influence of Nitric Acid Treatment Time on the Mechanical and Surface Properties of High-Strength Carbon Fibers. *Journal of Composite Materials* **2014**, *48* (3), 259–276.

(273) Wedege, K.; Drazevic, E.; Konya, D.; Bentien, A. Organic Redox Species in Aqueous Flow Batteries: Redox Potentials, Solubility and Chemical Stability. *Nature Publishing Group* **2016**, No. December, 1–13.

(274) Janoschka, T.; Morgenstern, S.; Hiller, H.; Friebe, C.; Wolkersdörfer, K.; Häupler, B.; Hager, M. D.; Schubert, U. S. Synthesis and Characterization of TEMPO- and Viologen-Polymers for Water-Based Redox-Flow Batteries. *Polymer Chemistry* **2015**, *6* (45), 7801–7811.

(275) Janoschka, T.; Martin, N.; Martin, U.; Friebe, C.; Morgenstern, S.; Hiller, H.; Hager, M. D.; Schubert, U. S. An Aqueous, Polymer-Based Redox-Flow Battery Using Non-Corrosive, Safe, and Low-Cost Materials. *Nature* **2015**, *527* (7576), 78–81.

(276) Butler, J. A. V. Studies in Heterogeneous Equilibria. Part II.?The Kinetic Interpretation of the Nernst Theory of Electromotive Force. *Trans. Faraday Soc.* **1924**, *19* (March), 729–733.

(277) Butler, J. A. V. Studies in Heterogeneous Equilibria. Part III. A Kinetic Theory of Reversible Oxidation Potentials at Inert Electrodes. *Transactions of the Faraday Society* **1924**, *19* (March), 734.

(278) Anson, F. C. Double-Layer and Electrode Kinetics (Delahay, Paul). *Journal of Chemical Education* **1966**, *43* (1), 54.

(279) Vetter, K. J. *Electrochemical Kinetics : Theoretical Aspects.*; Elsevier Science, 1967.

(280) Gillen, R. D. Kinetics of Electrode Processes, Tibor Erdey-Gruz, Transl. by L. Simandi; Transl. Revised by D. A. Durham, Wiley, New York(1972). 482 Pages.$27.50. *AIChE Journal* **1973**, *19* (2), 412–412.

(281) Parsons, R. General Equations for the Kinetics of Electrode Processes. *Transactions of the Faraday Society* **1951**, *47* (0), 1332.

(282) *Modern Aspects of Electrochemistry No. 20*; Bockris, J. O., White, R. E., Conway, B. E., Eds.; Modern Aspects of Electrochemistry; Springer US: Boston, MA, 1989; Vol. 20.

(283) Mohilner, D. M.; Delahay, P. CURRENT-POTENTIAL CHARACTERISTICS FOR ELECTRODE PROCESSES WITH SPECIFIC ADSORPTION OF REACTANT AND/OR PRODUCT. *The Journal of Physical Chemistry* **1963**, *67* (3), 588–591.

(284) Gattrell, M.; Qian, J.; Stewart, C.; Graham, P.; MacDougall, B. The Electrochemical Reduction of VO2+ in Acidic Solution at High Overpotentials. *Electrochimica Acta* **2005**, *51* (3), 395–407.

(285) Curtiss, L. A.; Halley, J. W.; Hautman, J.; Hung, N. C.; Nagy, Z.; Rhee, Y.-J.; Yonco, R. M. Temperature Dependence of the Heterogeneous Ferrous-Ferric Electron Transfer Reaction Rate: Comparison of Experiment and Theory.

(286) and, M. H.; Fawcett*, W. R.; Hromadová, M.; Fawcett, W. R. Studies of Double-Layer Effects at Single Crystal Gold Electrodes II. The Reduction Kinetics of Hexaaquairon(III) Ion in Aqueous Solutions. **2000**.

(287) Randles, J. E. B.; Somerton, K. W. Kinetics of Rapid Electrode Reactions. Part 3.—Electron Exchange Reactions. *Trans. Faraday Soc.* **1952**, *48* (0), 937–950.

(288) Vetter, K. J. *Electrochemical Kinetics : Theoretical and Experimental Aspects ...*; Academic Press: New York N.Y, 1967.

(289) Faita, G.; Fiori, G.; Mussini, T. Electrochemical Processes of the Bromine/ Bromide System. *Electrochimica Acta* **1968**, *13* (8), 1765–1772.

(290) Mastragostino, M.; Gramellini, C. Kinetic Study of the Electrochemical Processes of the Bromine/Bromine Aqueous System on Vitreous Carbon Electrodes. *Electrochimica Acta* **1985**, *30* (3), 373–380.

(291) Schuldiner, S. Theory and Principles of Electrode Processes. *Journal of the American Chemical Society* **1966**, *88* (14), 3466–3466.

(292) Conway, B. *Theory and Principles of Electrode Processes*; Ronald Press Co.: New York, 1965.

(293) Bockris, J. O. (John O. .; Reddy, A. K. N.; Gamboa-Aldeco, M. *Modern Electrochemistry. Volume 2A, Fundamentals of Electrodics*; Kluwer Academic, 2002.

(294) Albery, W. J. Electrode Kinetics. *Philosophical Transactions of the Royal Society of London. Series A, Mathematical and Physical Sciences 302*, 221–235.

(295) C.J.M, C. J. A Guide to the Study of Electrode Kinetics. *Journal of Molecular Structure* **1973**, *17* (2), 448.

(296) Han, P.; Wang, H.; Liu, Z.; Chen, X.; Ma, W.; Yao, J.; Zhu, Y.; Cui, G. Graphene Oxide Nanoplatelets as Excellent Electrochemical Active Materials for VO2+/ and V2+/V3+ Redox Couples for a Vanadium Redox Flow Battery. *Carbon* **2011**, *49* (2), 693–700.

(297) Inoue, M.; Tsuzuki, Y.; Iizuka, Y.; Shimada, M. Carbon Fiber Electrode for Redox Flow Battery. *Journal of The Electrochemical Society* **1987**, *134* (3), 756.

(298) Ponce-de-Le?n, C.; Reade, G. W.; Whyte, I.; Male, S. E.; Walsh, F. C. Characterization of the Reaction Environment in a Filter-Press Redox Flow Reactor. *Electrochimica Acta* **2007**, *52* (19), 5815–5823.

(299) Electrically Rechargeable REDOX Flow Cell. **1975**.

(300) CHIANG, Y.-M.; BAZZARELLA, R. FUEL SYSTEM USING REDOX FLOW BATTERY. **2010**.

(301) van Brakel, J.; Heertjes, P. M. Analysis of Diffusion in Macroporous Media in Terms of a Porosity, a Tortuosity and a Constrictivity Factor. *International Journal of Heat and Mass Transfer* **1974**, *17* (9), 1093–1103.

(302) Carta, R.; Palmas, S.; Polcaro, A. M.; Tola, G. Behaviour of a Carbon Felt Flow by Electrodes Part I: Mass Transfer Characteristics. *Journal of Applied Electrochemistry* **1991**, *21* (9), 793–798.

(303) Dullien, F. A. L. *Porous Media : Fluid Transport and Pore Structure*; Academic Press, 1992.

(304) Gostick, J. T.; Fowler, M. W.; Pritzker, M. D.; Ioannidis, M. A.; Behra, L. M. In-Plane and through-Plane Gas Permeability of Carbon Fiber Electrode Backing Layers. *Journal of Power Sources* **2006**, *162* (1), 228–238.

(305) Newman, J. Optimization of Porosity and Thickness of a Battery Electrode by Means of a Reaction-Zone Model. *Journal of The Electrochemical Society* **1995**, *142* (1), 97.

(306) Roy, A.; Hickner, M. A.; Einsla, B. R.; Harrison, W. L.; McGrath, J. E. Synthesis and Characterization of Partially Disulfonated Hydroquinone-Based Poly(Arylene Ether Sulfone)s Random Copolymers for Application as Proton Exchange Membranes. *Journal of Polymer Science Part A: Polymer Chemistry* **2009**, *47* (2), 384–391.

(307) Sankir, M.; Kim, Y. S.; Pivovar, B. S.; McGrath, J. E. Proton Exchange Membrane for DMFC and H2/Air Fuel Cells: Synthesis and Characterization of Partially Fluorinated Disulfonated Poly(Arylene Ether Benzonitrile) Copolymers. *Journal of Membrane Science* **2007**, *299* (1–2), 8–18.

(308) Breitkopf, C.; Swider-Lyons, K. Modern Electrochemistry. In *Springer Handbook of Electrochemical Energy*; Springer Berlin Heidelberg: Berlin, Heidelberg, 2017; pp 11–30.

(309) Newman, J. S.; Thomas-Alyea, K. E. *Electrochemical Systems*; J. Wiley, 2004.

(310) Bird, R. B. (Robert B.; Stewart, W. E.; Lightfoot, E. N. *Transport Phenomena*; J. Wiley, 2007.

(311) Einstein, A. ??Ber Die von Der Molekularkinetischen Theorie Der W?Rme Geforderte Bewegung von in Ruhenden Fl?Ssigkeiten Suspendierten Teilchen. *Annalen der Physik* **1905**, *322* (8), 549–560.

(312) Wagner, E. Beiträge Zur Quantitativen Analyse Durch Elektrolyse. *Zeitschrift für Elektrotechnik und Elektrochemie* **1896**, *2* (28), 613–616.

(313) Bear, J. *Dynamics of Fluids in Porous Media*; Dover: New York :, 1988.

(314) Chen, Y. W. D.; Bard, A. J. Electrochemical and Spectrophotometric Studies of Iron Complexes with a Pentaaza Macrocyclic Ligand. *Inorganic Chemistry* **1984**, *23* (14), 2175–2181.

(315) Zhao, P.; Zhang, H.; Zhou, H.; Yi, B. Nickel Foam and Carbon Felt Applications for Sodium Polysulfide/Bromine Redox Flow Battery Electrodes. *Electrochimica Acta* **2005**, *51* (6), 1091–1098.

(316) Joerissen, L.; Garche, J.; Fabjan, C.; Tomazic, G. Possible Use of Vanadium Redox-Flow Batteries for Energy Storage in Small Grids and Stand-Alone Photovoltaic Systems. *Journal of Power Sources* **2004**, *127* (1–2), 98–104.

(317) Duarte, M. M. E.; Pilla, A. S.; Sieben, J. M.; Mayer, C. E. Platinum Particles Electrodeposition on Carbon Substrates. *Electrochemistry Communications* **2006**, *8* (1), 159–164.

(318) Yan, A.; Xiao, X.; Külaots, I.; Sheldon, B. W.; Hurt, R. H. Controlling Water Contact Angle on Carbon Surfaces from 5° to 167°. *Carbon* **2006**, *44* (14), 3116–3120.

(319) Li, L.; Kim, S.; Wang, W.; Vijayakumar, M.; Nie, Z.; Chen, B.; Zhang, J.; Xia, G.; Hu, J.; Graff, G.; et al. A Stable Vanadium Redox-Flow Battery with High Energy Density for Large-Scale Energy Storage. *Advanced Energy Materials* **2011**, *1* (3), 394–400.